JOURNAL OF SCIENCE

i

| Editorial Board |

| **Correspondence Address** |

Gazi University Graduate School of Natural and Applied Sciences
Emniyet Neighborhood, Bandırma Avenue, No:6/20B, 06560, Yenimahalle - ANKARA
B Block, Auxiliary Building

| **e-mail** |

gujsa06@gmail.com

| **web page** |

https://dergipark.org.tr/tr/pub/gujsa

Gazi University Journal of Science Part A: Engineering and Innovation
is a peer-reviewed journal.

| INDEXING |

TRDizin

ASOS indeks

Crossref

DRJI

Academic Resource Index ResearchBib

INDEX COPERNICUS INTERNATIONAL

ESJI www.ESJIndex.org — Eurasian Scientific Journal Index

Scilit

ROAD — DIRECTORY OF OPEN ACCESS SCHOLARLY RESOURCES

SIS Scientific Indexing Services

INFOBASE INDEX

SCI

scinapse

SOBIAD

EBSCOhost

HARVARD LIBRARY

| ACCESSIBILITY |

Google Scholar

CC BY SA

DergiPark AKADEMİK

| CONTENTS |

| CONTENTS |

x

Investigation of Chloride Anion Binding Properties of Glipizide Drug

Serap MERT[1,2,3*] 🆔

[1]*Kocaeli University, Department of Chemistry and Chemical Processing Technol., Kocaeli, Türkiye*
[2]*Kocaeli University, Department of Polymer Sci. and Technol., Kocaeli, Türkiye*
[3]*Kocaeli University, Center for Stem Cell and Gene Therapies Res. and Pract., Kocaeli, Türkiye*

Keywords	Abstract
Anion Receptor Sulphonylurea Glipizide ^{1}H-NMR Titration	This study addresses the anion binding property of Glipizide (GLP), an oral antidiabetic a second-generation drug member of the sulphonylurea (SU) family. GLP effectively interacts with Cl^- anion according to ^{1}H-NMR spectroscopic titrations of successive tetrabutylammonium chloride (TBACl) in deuterated chloroform ($CDCl_3$) and dimethyl sulfoxide (d_6-DMSO). Upon the addition of TBACl, the change in chemical shift was observed for both N-H protons of SU in $CDCl_3$, whereas it causes a difference in the shift of only one of N-H proton in SU in d_6-DMSO. In addition, the data obtained from ^{1}H-NMR spectroscopic titrations was analyzed by DynaFit program to calculate the binding constant (K_a) value between GLP and Cl^- anion. It was found that GLP binds Cl^- anion in $CDCl_3$ with higher affinity (K_a=77.37 M^{-1}, Fitplot for N-H_h proton at δ=6.47 ppm) than in d_6-DMSO (K_a=38.53 M^{-1}, Fitplot for N-H_h proton at δ=6.32 ppm).

Cite

1. INTRODUCTION

A variety of amides (Bondy & Loeb, 2003; Kang et al., 2006), sulfonamides (Huggins et al., 2009), (thio)ureas (Amendola et al., 2010; Li et al., 2010), squaramides (Cai et al., 2018; Marchetti et al., 2019) and sulfonylurea (SU)s (Barišić et al., 2021) can be used as neutral receptors because they displayed remarkable interaction with different anions such as Cl^- via H-bonding. Especially, aromatic synthetic SU derivatives displayed the characteristics of good anion binders with weakly basic anions (NO_3^-, HSO_4^-, Cl^-, Br^-, I^-) while N-Hs of SU compounds were deprotonated with strongly basic anions (dihydrogen phosphate and acetate), leading to hinder the anion binding possibilities of SUs in DMSO. However, anion binding and ligand deprotonation were noticed in deuterated acetonitrile (ACN) by adding dihydrogen phosphate or acetate salts. The different behaviors in deuterated ACN and DMSO and the detection of large differences between the binding constants have been attributed to the nature of the solvents due to the polarity difference affecting the ability of their H-bond acceptor (Barišić et al., 2021). Several distinctive signals of Glibenclamide (GLIB) were monitored in course of the titration by ^{1}H-NMR analyses to detect the interaction type and its strength between GLIB (Host) and various monomers such as tetrabutylammonium methacrylate (TBAM), acrylamide (AAM), and methacrylic acid (MAA) (Guest), and it was found that a very strong interaction between GLIB and TBAM was established due to the deprotonation of SU by the formation of GLIB dimers when compared to GLIB-AAM and GLIB-MAA. The molecularly imprinted polymer, prepared from TBAM, MAA, and ethylene glycol dimethacrylate (EDMA), displayed high selectivity for GLIB over Gliclazide (GLIC) and Glipizide (GLP), and very high-recoveries for GLIB from blood serum up to 92.4% over GLP and GLIC (Hasanah et al., 2015). Very strong interactions of GLIB with 4-vinylbenzyltrimethylammonium methacrylate (VBTMA) were also acquired with a 1:1 complex formation having stability constant $K_a > 10^5$ M^{-1} by ^{1}H-NMR titration. Similarly,

*Corresponding Author, e-mail: serap.mert@kocaeli.edu.tr

the imprinted polymers prepared from VBTMA exhibited high affinity and binding for GLIB, and selective extraction of GLIB with recoveries of up to 98% over GLIC and GLP from blood serum samples (Pessagno et al., 2018).

Glipizide, the second-generation SU family of the drug, is an oral hypoglycemic agent (Shuman, 1983; Pahwa et al., 2010) and highly effective in treating non-insulin-dependent diabetes mellitus (Lebovitz & Feinglos, 1983; Shuman, 1983). GLP, which helps the production of insulin from the pancreas and thus decreases glucose levels in blood, is rapidly absorbed and completely metabolized after its action (Brogden et al., 1979). GLP displays hypoglycemic (Pahwa et al., 2010), anticancer (Qi et al., 2014), and radical scavenging activities (by theoretical approach) (Hussan et al., 2022), and controlled release behaviors (Emami et al., 2014). Besides, a wide range of spectroscopic analyses of GLP has been performed in the literature (Ming et al., 2008; Adhikari et al., 2012; Prasad et al., 2013; Prakash & Iqbal, 2015; Ganesh et al., 2016; Jena et al., 2017; Ambadekar & Keni, 2018; Anwer et al., 2021).

The insulinotropic role of GLP is related to a high-affinity to SU receptor (SUR1), inhibiting the K_{ATP} channel on β cell plasma membrane, causing depolarization of the membrane potential, triggering $[Ca^{2+}]$ influx, and thus, insulin release is ensured. This lowers glucose levels in plasma and maintains this effect even with a short half-life (Norris, 1979; Shuman, 1983; Aguilar-Bryan et al., 1995; Best & Benington, 1998; Gribble & Reimann, 2002; Renström et al., 2002; Pahwa et al., 2010). Drug binding to granule membrane may also cause a change in the transport of Cl^- known to modulate islet electrical activation and insulin release (Best et al., 2004). Consequently, SUs are likely to have a further ionic effect on β cell. Thus, Cl^- is suggested to be important for islet function during the release of insulin provided by SUs drugs (Sehlin, 1981; Kinard & Satin, 1995; Best et al., 2004).

Cl^- anion and its transportation has crucial importance for biological systems such as the regulation of membrane potential, homeostasis, pH regulation, cellular proliferation, and cellular differentiation (Davis et al., 2007; Valdivieso & Santa-Coloma, 2019). Moreover, the abnormal chloride transportation was observed in various diseases including cystic fibrosis (Rowe et al., 2005). Considering the importance of Cl^- anion in biological systems (Rowe et al., 2005; Davis et al., 2007; Hosogi et al., 2014; Martin et al., 2018; Valdivieso & Santa-Coloma, 2019) and a relationship between Cl^- anion transport and insulin release (Sehlin, 1981; Kinard & Satin, 1995), Cl^- was chosen as the anionic guest to investigate the anion binding property of the antidiabetic drug GLP in the current work. Although there have been several attempts about anion binding studies related to SUs (Hasanah et al., 2015; Pessagno et al., 2018; Barišić et al., 2021) as mentioned above, as far as known, no Cl^- binding study on GLP drug, which may form supramolecular complexes through non-covalent interactions with Cl^-, has been performed before. The solution of GLP drug (as host) in $CDCl_3$ and d_6-DMSO was titrated with 0.2 to 26 equivalents of TBACl salt (guest), and the chemical shift change ($\Delta\delta$) of N-H protons in GLP was continuously monitored by ^{1}H-NMR analysis after each addition of TBACl salt. Finally, the association or binding constants ($K_a's$) were calculated for N-H protons in both deuterated solvents using the DynaFit software. This study has demonstrated that GLP, a drug with known antidiabetic properties, which can interact non-covalently with Cl^-, can be used as a potential agent in the transport and regulation of the concentration of Cl^- anion, which is very important for biological systems.

2. MATERIAL AND METHOD

Materials and Instruments: Glipizide (Santa Cruz Biotechnology) and tetrabutylammonium chloride (TBACl, 98% purity, Sigma-Aldrich) were used for ^{1}H-NMR spectroscopic titrations. Moisture sensitive TBACl was weighed in a glove bag filled with nitrogen atmosphere, and then, Bruker Avance III 400 MHz NMR spectrometer was used to perform spectroscopic titrations in $CDCl_3$ and d_6-DMSO.

NMR Analyses

^{1}H-NMR analyses of GLP in $CDCl_3$ and d_6-DMSO were performed, and signals of the protons of GLP in d_6-DMSO were found to be in agreement with the literature (Ming et al., 2008). The protons of GLP taken ^{1}H-NMR in $CDCl_3$ were accordingly assigned based on their chemical environments. ^{1}H-NMR (400 MHz, $CDCl_3$) δ 9.25 (s, 1H), 8.66 (s, 1H), 8.35 (t, 1H), 7.89 (t, J = 8 Hz., 1H), 7.82 (d, J = 8 Hz., 2H), 7.39 (d, J = 8 Hz.,

2H), 6.47 (d, J = 8 Hz., 1H), 3.75 (q, J = 8 Hz., 2H), 3.60 (m, 1H), 3.04 (t, J = 8 Hz., 2H), 2.64 (s, 3H), 1.56 – 1.84 (m, 5H), 1.36 – 1.13 (m, 5H).

^{1}H-NMR (400 MHz, d_6-DMSO) δ 10.31 (s, 1H), 9.09 (s, 1H), 8.82 (t, 1H), 8.60 (s, 1H), 7.79 (d, J = 8.1 Hz., 2H), 7.45 (d, J = 8.1 Hz., 2H), 6.33 (d, J = 8.1 Hz., 1H), 3.59 (m, 2H), 3.52 (s, 1H), 2.96 (t, J = 7.2 Hz., 2H), 2.58 (s, 3H), 1.72 – 1.41 (m, 5H), 1.37 – 0.95 (m, 5H). ^{13}C-NMR (101 MHz, DMSO-d_6) δ 163.05, 156.87, 150.59, 145.11, 142.86, 142.43, 142.07, 138.24, 129.20, 127.32, 48.09, 34.79, 32.30, 25.01, 24.21, 21.35.

Both H_h and H_n protons were observed in 0.0533 M solution of GLP in CDCl$_3$ before and after titration. However, H_h proton of GLP was visible at 6.33 ppm but H_n proton of SU somehow did not appear at 10.31 ppm at 0.0533 M solution of GLP drug in the ^{1}H-NMR spectrum before starting the titration in d_6-DMSO. The H_n proton was visible at 10.31 ppm in d_6-DMSO when 0.165 M GLP was used. However, the concentration at 0.165 M is too high to continue titration of TBACl up to 26 equiv. Therefore, H_h proton of GLP was monitored when ^{1}H-NMR of GLP was recorded in d_6-DMSO.

The solution of 1 M TBACl salt in CDCl$_3$ was added as an anionic guest in specific aliquots starting from 0.2 to 26 equiv. to a solution of 0.0533 M GLP receptor to evaluate the anion binding property of GLP. The changes in selected peaks of GLP were monitored by ^{1}H-NMR after each addition of Cl$^-$ anion. ^{1}H-NMR titrations experiments were also performed in d_6-DMSO to see the effect of the solvent nature on the binding ability of receptor to anion. Then, the data from these ^{1}H-NMR spectroscopic titrations was analyzed, and stoichiometric K_a of Cl$^-$ anion to GLP were calculated by open-access DynaFit software by fitting 1:1 model (Kuzmič, 2009; Thordarson, 2011; Ulatowski et al., 2016) as described in literature (Kuzmič, 2009; Mercurio et al., 2015; Zapata et al., 2017).

The concentration of GLP varied gradually from 0.0533 to 0.0203 M with subsequent addition of TBACl solution. By adding TBACl, the concentration of Cl$^-$ increased from 0 to 0.528 M at the end of titration. The shifts of N-H protons of SU throughout titration were recorded as ppm values. These three parameters (conc. of GLP and TBACl and ppm values of related protons) were used for the calculation of K_a, and plotting of fitplots, residual and relative sum of squares (SSQ/SSQ min.).

3. RESULTS AND DISCUSSION

The ^{1}H-NMR analysis of GLP drug (host) was performed in CDCl$_3$ and d_6-DMSO as a reference point before titration with TBACl salt (guest) in order to investigate Cl$^-$ anion recognition ability of GLP drug. The protons in the structure of GLP were labelled as shown in the spectrum in Figure 1A. The area under the peak of each proton signal was observed to be proportional to the number of hydrogen atoms in the structure of GLP. The difference in chemical shifts for both N-H protons of SU (H_h and H_n), amide N-H proton (H_l), aromatic protons (H_i and H_j) of the sulfonyl attached *para*-substituted ring, and the protons (H_k and H_m) in the pyrazine ring in CDCl$_3$ or d_6-DMSO (Figure 1 and Table 1) were analyzed after each TBACl addition from 0.2 to 26 equiv. to GLP drug.

The downfield shifts from 8.66 ppm to 10.98 ppm for H_n in Figure 2 and from 6.47 ppm to 7.41 ppm for H_h in Figure 3 were observed by adding TBACl up to 6 equiv. in CDCl$_3$ in ^{1}H-NMR spectra, respectively, indicating that the binding sites via the formation of a H-bonds (Ramalingam et al., 2008; Amendola et al., 2010; 2011; Bao et al., 2018; Picci et al., 2020; Barišić et al., 2021; Kumawat et al., 2021) between H_n and H_h protons of GLP and Cl$^-$ anion. Interestingly, when TBACl was continuously added from 8 to 26 equiv., slightly highfield shifts were observed from 10.98 ppm to 10.89 ppm for H_n and from 7.41 ppm to 7.33 ppm for H_h as shown in Figures 2 and 3 respectively. This might be interpreted as saturation of the H-bond interactions after the addition of more than six equiv. of TBACl and a very slight weakening of the H-bond interaction due to a partial increase in the electron density in N-H bond.

When the aromatic protons (H_i and H_j) of sulfonyl attached *para*-substituted ring were examined in CDCl$_3$, H_i was shifted to highfield slightly from 7.39 ppm to 7.13 ppm with successive addition of TBACl (from 0 to 26 equiv.) as shown in Figure 3, however, aromatic proton H_j was firstly shifted to downfield from 7.82 ppm to 7.95 ppm upon to 2 equiv. of TBACl, then, to highfield from 7.95 ppm to 7.77 ppm from 3 to 26 equiv. of TBACl in CDCl$_3$ as indicated in Figure 4. H-bonding between N-H_n proton adjacent to SU and Cl$^-$ anion affects

electron density of the aromatic ring directly attached to SU, and as a natural consequence of this interaction, slight differences in the chemical shifts of the H_i and H_j protons occur with the successive addition of TBACl in ^{1}H-NMR.

A)

B)

C)
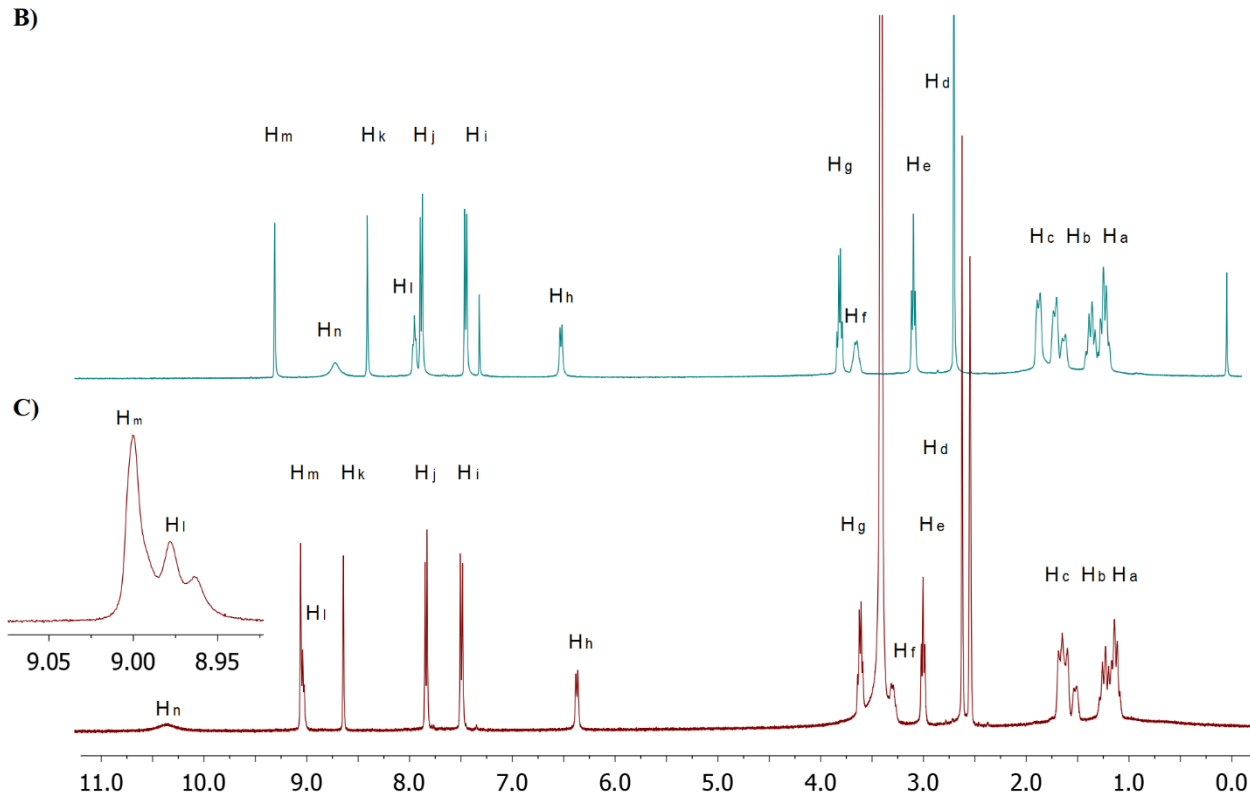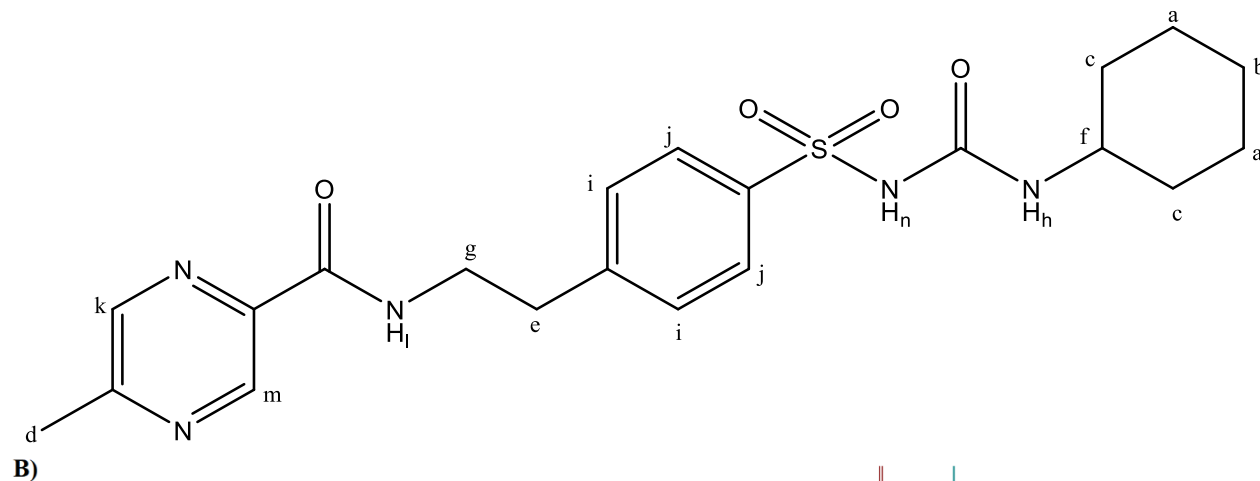
Figure 1. A) Structure of Glipizide, B) ^{1}H-NMR Spectra of Glipizide in CDCl₃ and C) in d₆-DMSO

Table 1. *Selected signals of protons from ^{1}H-NMR to monitor chemical shift changes in GLP in CDCl₃ and d₆-DMSO*

Solvent	h	i	j	k	l	m	n
CDCl₃	6.47 ppm	7.39 ppm	7.82 ppm	8.35 ppm	7.89 ppm	9.25 ppm	8.66 ppm
d₆-DMSO	6.33 ppm	7.45 ppm	7.79 ppm	8.60 ppm	8.82 ppm	9.09 ppm	10.31 ppm

The slight unexpected highfield change in chemical shifts of amide proton H_l from 7.89 to 7.75 ppm with the addition of 26 equiv. of TBACl in $CDCl_3$ indicated no H-bonding interaction between amide proton and Cl^- as shown in Figure 4. In a similar situation, where the complex stability of a single amide is low, but with the addition of urea functional group in addition to the amide in a compound, the ^{1}H-NMR titration results emphasize that Cl^- anion makes the H-bond with urea instead of amide (Barišić et al., 2022), which is compatible with the preference of Cl^- for N-H of SU over amide in our work.

When the shifts of H_m proton in the pyrazine ring, close to the amide group, were examined, very weak highfield shifts for H_m from 9.25 ppm to 9.02 ppm were noticed with the successive addition of 26 equiv. of TBACl in $CDCl_3$ as shown in Figure 2. However, when the shift of H_k proton on pyrazine ring, which is farther from the amide proton, was examined, H_k was unaffected up to the addition of 1 equivalent of TBACl in $CDCl_3$. Further addition of TBACl (1.2 to 26 equiv.) resulted in slight highfield shifts of the H_k signal from 8.34 ppm to 8.21 ppm as shown in Figure 4. The weak interaction between H_l proton of amide and Cl^- anion slightly affects resonance structure of the pyrazine ring, and thus, e^- density of the ring, leading to a slight change in chemical shifts of H_k and H_m protons in the pyrazine ring in ^{1}H-NMR with successive addition of TBACl.

When the titration of GLP drug with Cl^- was examined in d_6-DMSO as indicated in Figure 5, a significant downfield shift of only H_h from 6.32 ppm to 7.21 ppm by adding TBACl up to 8 equiv., indicating the existence of a H-bond (Ramalingam et al., 2008; Amendola et al., 2010; 2011; Bao et al., 2018; Picci et al., 2020; Kumawat et al., 2021) between GLP and Cl^- anion, as expected. H_h proton signal at 7.21 ppm almost remained unchanged when the 8 to 14 equiv. of TBACl was added. Then, a very slight highfield shift from 7.18 to 7.04 ppm was observed in the signal of N-H_h proton when TBACl is added from 16 to 26 equiv. (Figure 5).
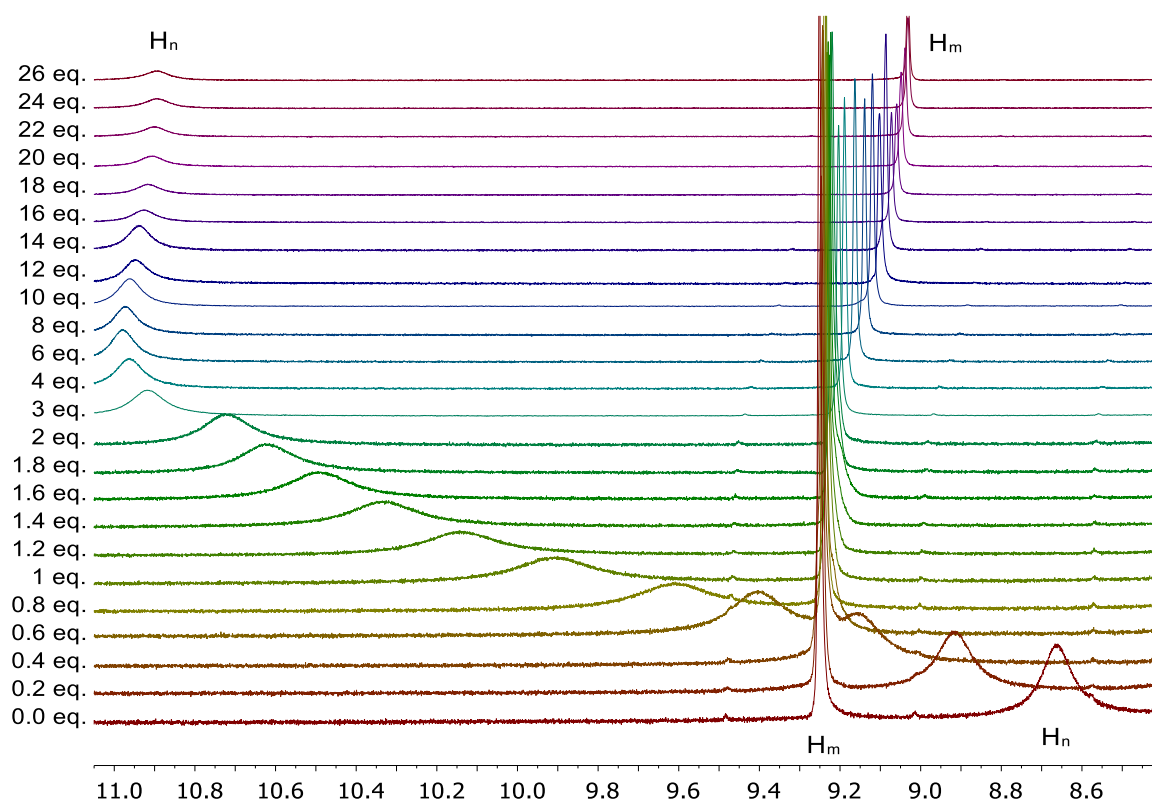
Figure 2. *Chemical shift of H_n, H_m in stack plots of ^{1}H-NMR spectra with the addition of TBACl (0–26 equiv) to GLP in $CDCl_3$ at 25°C*
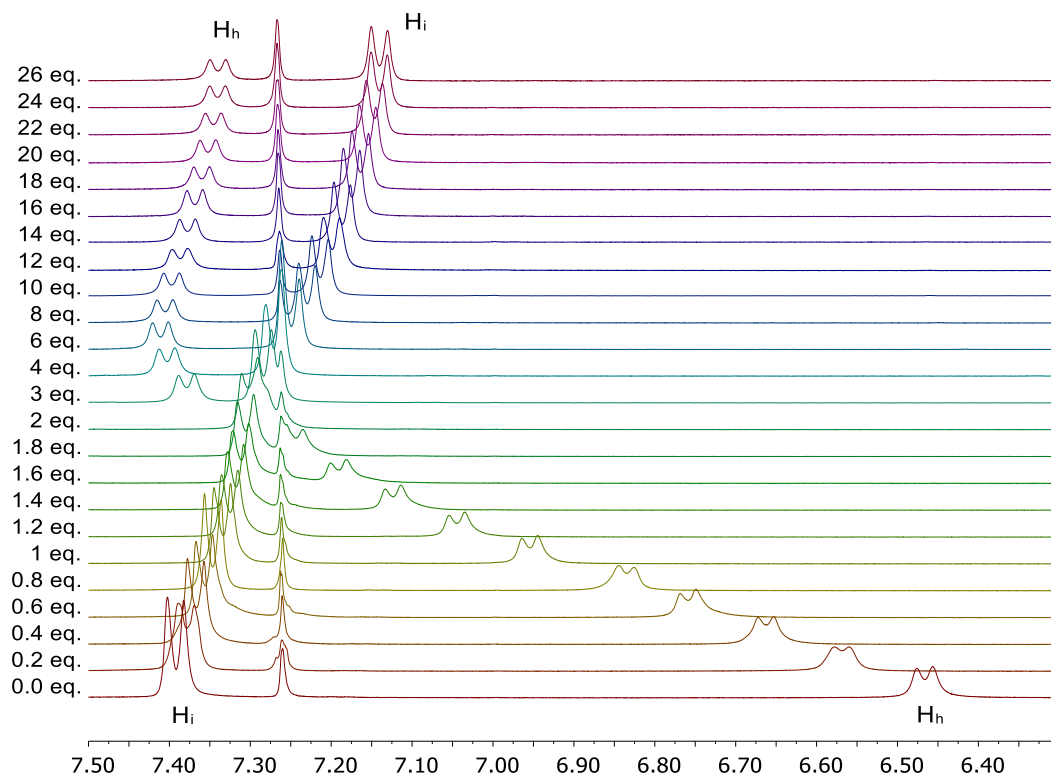
Figure 3. *Chemical shift of H_h, H_i in stack plots of ^{1}H-NMR spectra with the addition of TBACl (0–26 equiv)
to GLP in CDCl$_3$ at 25°C*
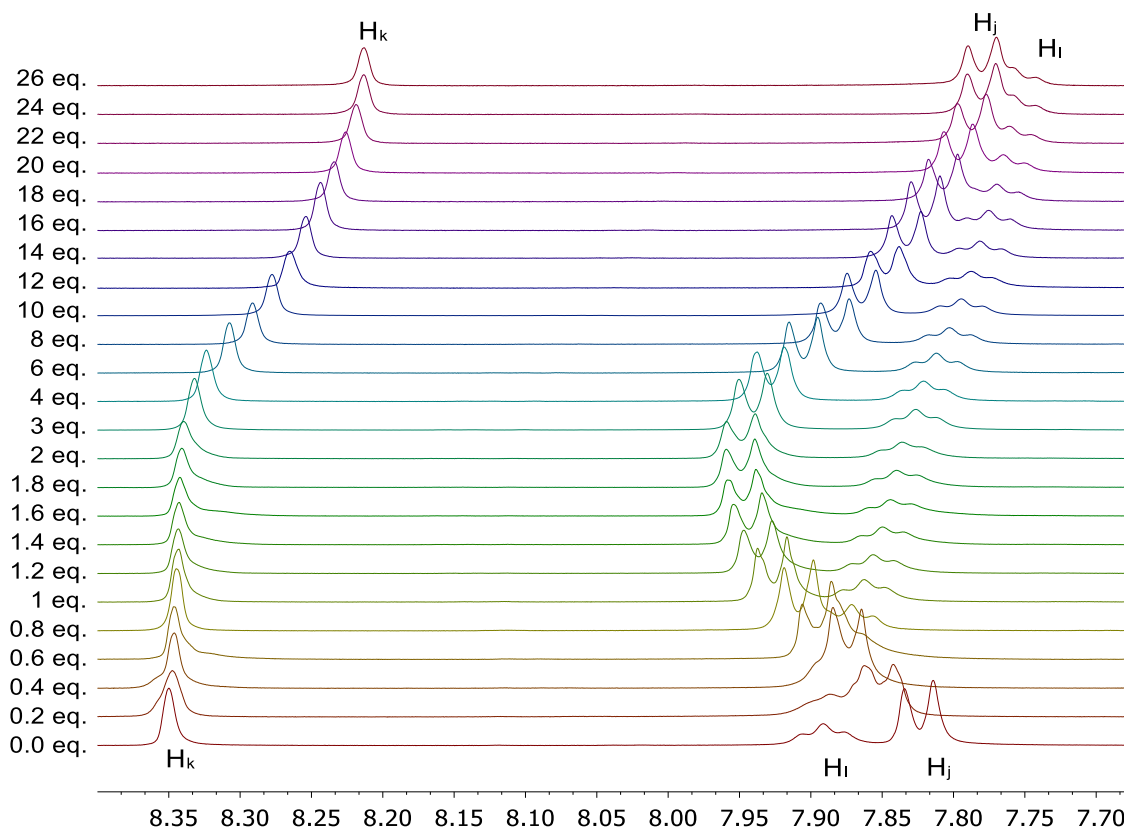
Figure 4. *Chemical shift of H_j, H_l, H_k in stack plots of ^{1}H-NMR spectra with the addition of TBACl (0–26
equiv) to GLP in CDCl$_3$ at 25°C*
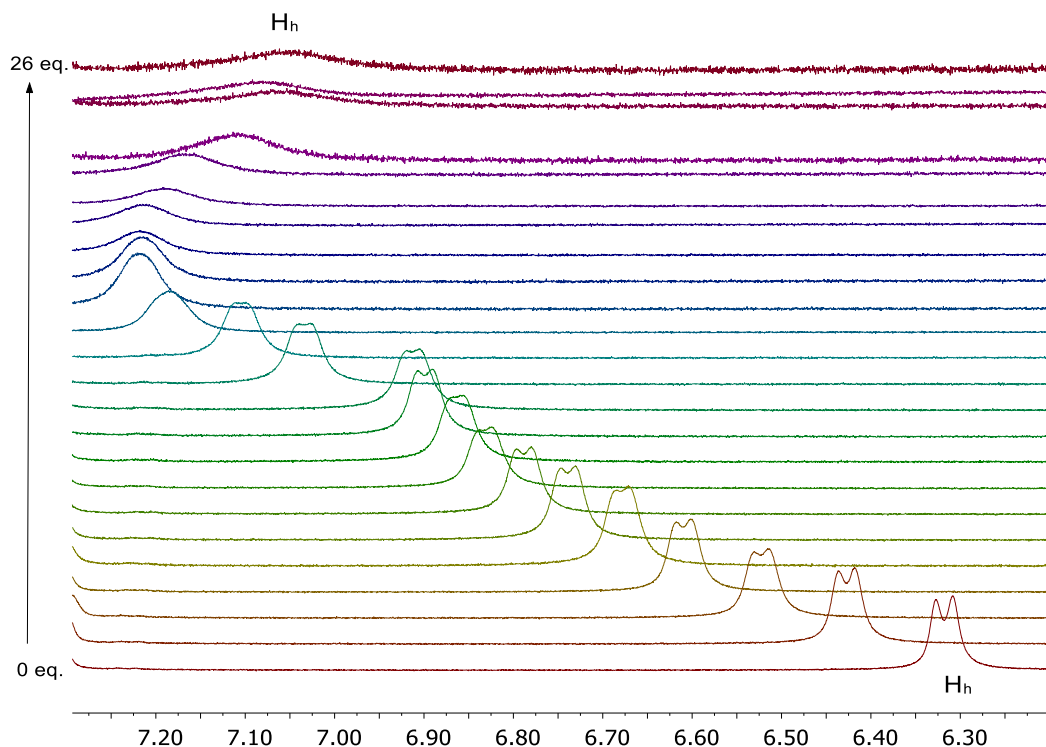
Figure 5. *Chemical shift of H_h in stack plots of ^1H-NMR spectra of GLP after the addition of TBACl (0 to 26 eqv.) in d_6-DMSO having <0.02% H_2O at 25°C*

The difference in H_n and H_h chemical shifts (Δδ) of GLP in response to increasing equiv. of Cl$^-$ anions in CDCl$_3$ and d_6-DMSO in ^1H-NMR was shown in Figure 6. Significant downfield changes of H_n and H_h in CDCl$_3$ and H_h in d_6-DMSO in ^1H-NMR confirm the binding site via the formation of H-bond between GLP and Cl$^-$. When only 3 equiv. of TBACl anion were added to the GLP solution, a very large chemical shift difference of 2.23 ppm for H_n in CDCl$_3$ reflects very strong H-bonding between H_n and Cl$^-$ anion (Figure 6). By adding 3 equiv. of TBACl to GLP solution, chemical shift differences of 0.91 ppm in CDCl$_3$ and of 0.71 ppm in d_6-DMSO were observed for H_h. No significant Δδ difference was observed for H_h when 8-18 equiv. of TBACl were added. The slightly different Δδ values at the initial stage of the titration (1-4 eq.) indicate the different strength of the H-bond interactions between GLP and Cl$^-$ anion due to the nature of the solvent. The reason why Δδ in H_n is larger than in H_h in CDCl$_3$ may be due to the direct bonding of N-H_n proton to the sulfonyl group.
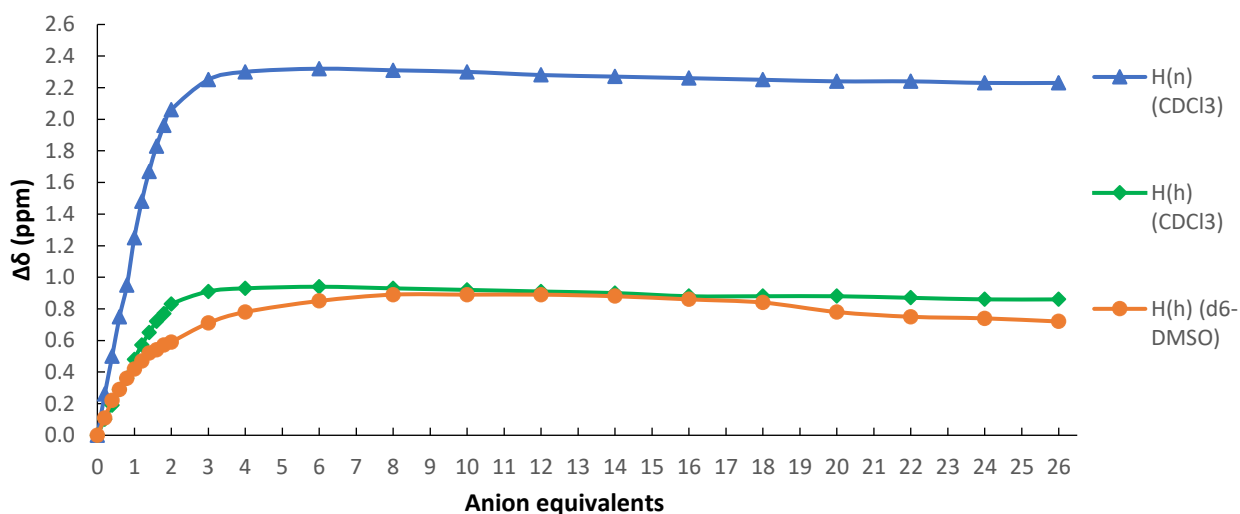
Figure 6. *Chemical shift differences of H_n and H_h of GLP with the successive addition of TBACl (0–26 equiv) in CDCl$_3$ and d_6-DMSO at 25°C*

Deprotonation of N-H of SU was not observed in our study while performing the titration experiments either in d_6-DMSO or in CDCl$_3$. When the titration experiment of GLIB, another derivative of GLP, with TBAM was carried out, the deprotonation of N-H bond in SU with the addition of TBAM was observed by disappearance of N-H peak in CDCl$_3$ or d_6-DMSO (Hasanah et al., 2015). The difference between deprotonation in the work of Hasanah et al. (2015) and anion binding in the current work is most probably related to the basicity of anions used during the titration because strong basic anions like acetate and dihydrogen phosphate could deprotonate N-H of SUs while weakly basic anions like NO$_3^-$, HSO$_4^-$, Cl$^-$, Br$^-$, I$^-$ showed high binding ability with SUs (Barišić et al., 2021).

The stoichiometric K_a value of GLP and Cl$^-$ anion according to the 1:1 model (Kuzmič, 2009; Thordarson, 2011; Ulatowski et al., 2016) were calculated as 77.59 M^{-1} for N-H$_n$ proton at δ= 8.66 ppm in CDCl$_3$ (Table 2) by analyzing of the titration data with DynaFit program (Kuzmič, 2009; Mercurio et al., 2015; Zapata et al., 2017). For the calculation of K_a values, three variants namely concentrations of GLP and TBACl, and chemical shift values of N-H protons of SU as ppm for each addition of TBACl were all used in the DynaFit program. Therefore fitplots, residual and relative sum of squares (SSQ/SSQ min.) obtained from DynaFit software using these variants were shown in Figures 7 and 8.

Although SU protons were unexpectedly shifted downfield at different rates (Figure 6) when titrated with TBACl, the K_a values were found very close to each other (77.59 M^{-1} for H$_n$ and 77.37 M^{-1} for H$_h$) in CDCl$_3$ by the DynaFit program. Confidence intervals for K_a values were 95% from DynaFit software. Moreover, ^{1}H-NMR spectroscopic titration showed that GLP can bind Cl$^-$ anion in CDCl$_3$ with 77.37 M^{-1} higher K_a value (for N-H$_h$ proton at δ = 6.47 ppm) than in d_6-DMSO, 38.53 M^{-1} (for N-H$_h$ proton at δ = 6.32 ppm) for the same N-H$_h$ proton. The reason why the K_a value calculated by the DynaFit program for H$_h$ in d_6-DMSO was considerably lower than in CDCl$_3$ was due to the nature of d_6-DMSO, competing with Cl$^-$ anion for H-bond with GLP receptor, and this situation partially inhibits the shifts of H$_h$ in ^{1}H-NMR spectrum. Even more H$_n$ proton of SU does not appear in ^{1}H-NMR spectrum before and during the titration, so K_a value of this proton could not be calculated in d_6-DMSO. The amide proton H$_l$ of GLP at 7.89 ppm was not analyzed with DynaFit program because it was not suitable for DynaFit analysis due to its shift to the upfield with the addition of TBACl in CDCl$_3$.

Table 2. *K_a values in different deuterated solvents*

	CDCl$_3$	$\Delta\delta^a$	$K_a^{a,c}$	d_6-DMSO	$\Delta\delta^b$	$K_a^{b,c}$
H$_h$	6.47 ppm	0,86	77.37	6.32 ppm	0,72	38.53
H$_n$	8.66 ppm	2.23	77.59	-		-

a: in CDCl$_3$, b: d_6-DMSO, c: binding constant generated using DynaFit software.

Fitplots, residual, and relative sum of squares (SSQ/SSQ min.) were obtained from DynaFit software by using a 1:1 model for the binding of Cl$^-$ with GLP in CDCl$_3$ as indicated in Figure 7. The randomness of the residual plot obtained from DynaFit program demonstrated the compatibility of the data with the program (Ulatowski et al., 2016). The program determines the corresponding number of independent least squares for all possible combinations (Kuzmič, 2009). The results were sorted by residuals (Figure 7B, 7E) and sum of squares (Figure 7C, 7F) to obtain a high confidence interval for the calculated K_a value. Confidence intervals for K_a values were given as 95% from DynaFit software. Furthermore, Cl$^-$ binding by GLP in d_6-DMSO was also studied using DynaFit program in a similar manner to that in CDCl$_3$ mentioned above (Figure 8). DynaFit scripts for each analysis were given in APPENDIX.
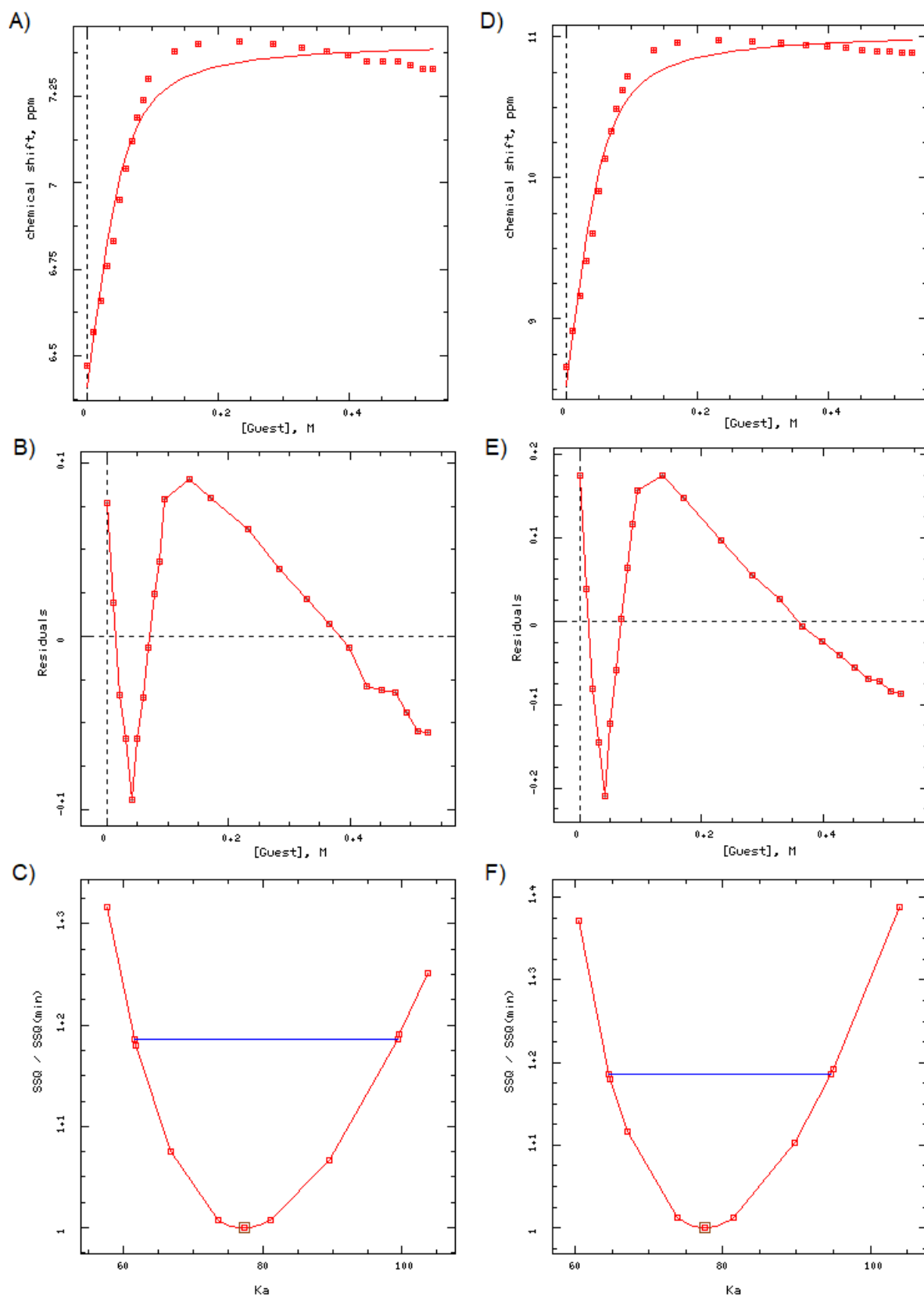
Figure 7. ^{1}*H-NMR spectroscopic titration in CDCl$_3$ A) Plot of downfield shifts of N-H$_h$ proton at δ = 6.47 ppm in GLP versus TBACl concentration B) Residual C) Relative sum of squares (SSQ/SSQ min.) K$_a$ = 77.37 M^{-1} (Fitplot for N-H$_h$ proton at δ = 6.47 ppm) D) Plot of downfield shifts of N-H$_n$ proton at δ = 8.66 ppm in GLP versus TBACl concentration E) Residual F) Relative sum of squares (SSQ/SSQ min.) K$_a$ = 77.59 M^{-1} (Fitplot for N-H$_n$ proton at δ = 8.66 ppm).*
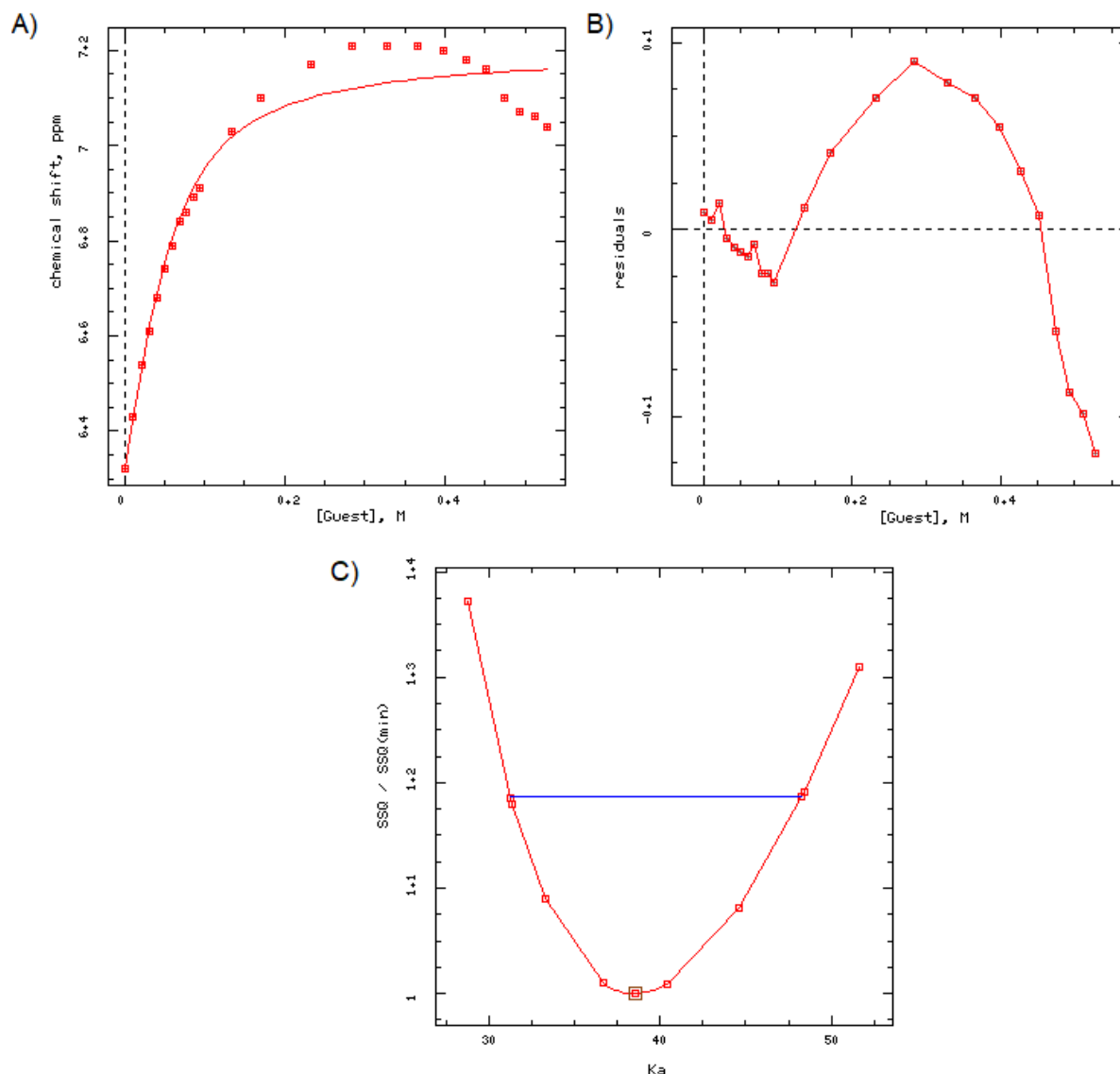
Figure 8. ^{1}H-NMR spectroscopic titration in d_6-DMSO **A)** Plot of downfield shifts of N-H$_h$ proton at $\delta = 6.32$ ppm in GLP versus TBACl concentration **B)** Residual **C)** Relative sum of squares (SSQ/SSQ min.) $K_a = 38.53$ M^{-1} (Fitplot for N-H$_h$ proton at $\delta = 6.32$ ppm).

4. CONCLUSION

In this study, the anion binding property of GLP was studied by ^{1}H-NMR spectroscopic titration with TBACl salt in CDCl$_3$ and d_6-DMSO. It was found that GLP could bind to Cl$^-$ anion in both deuterated solvents. Namely, the binding site via formation of H-bond between GLP and Cl$^-$ anion was confirmed by significant downfield changes of H$_n$ and H$_h$ in CDCl$_3$ and H$_h$ in d_6-DMSO in ^{1}H-NMR when N-H protons of SU (H$_h$ and H$_n$), amide N-H proton (H$_l$), aromatic protons (H$_i$ and H$_j$) of the sulfonyl attached *para*-substituted ring, and the protons (H$_k$ and H$_m$) in the pyrazine ring were examined with successive TBACl addition from 0.2 to 26 equiv. to GLP drug. An incredibly significant $\Delta\delta$ value of 2.25 ppm for H$_n$ in CDCl$_3$ was observed even only 3 equiv. of TBACl were added. On the other hand, a smaller $\Delta\delta$ values of 0.91 ppm in CDCl$_3$ and 0.71 ppm in d_6-DMSO were observed for H$_h$ when 3 equiv. of TBACl was added to related GLP solution. According to binding constant (K_a) value obtained by using DynaFit program for GLP and Cl$^-$ anion, it can be concluded that GLP can bind Cl$^-$ anion in CDCl$_3$ with higher affinity (K_a=77.37 M^{-1}, Fitplot for N-H$_h$ proton at $\delta = 6.47$ ppm) than in d_6-DMSO (K_a=38.53 M^{-1}, Fitplot for N-H$_h$ proton at $\delta = 6.32$ ppm) for N-H$_h$ proton. The difference between the binding constants between GLP and Cl$^-$ anion in CDCl$_3$ and d_6-DMSO might be associated with the nature of solvent.

CONFLICT OF INTEREST

The author declares no conflict of interest.

REFERENCES

Adhikari, L., Jagadev, S., Sahoo, S., Murthy, P. N., & Mishra, U. S. (2012). Devlopement and Validation of UV-Visible Spectrophotometric Method for Simultaneous Determination of pioglitazone Hydrochloride, Metformin Hydrochloride and Glipizide in its Bulk and Pharmaceutical Dosage Form (Tablet). *International Journal of Chem Tech Research*, *4*(2), 625-630.

Aguilar-Bryan, L., Nichols, C. G., Wechsler, S. W., Clement IV, J. P., Boyd III, A. E., González, G., Herrera-Sosa, H., Nguy, K., Bryan, J., & Nelson, D. A. (1995). Cloning of the β Cell High-Affinity Sulfonylurea Receptor: a Regulator of Insulin Secretion. *Science*, *268*(5209), 423-426. doi:10.1126/science.7716547

Ambadekar, S., & Keni, S. (2018). Fast and Economic Spectrophotometric Method for Metformin and Glipizide in Combination Tablet. *International Journal of Advances in Science Engineering and Technology*, *6*(1), 31-35.

Amendola, V., Bergamaschi, G., Boiocchi, M., Fabbrizzi, L., & Milani, M. (2010). The Squaramide versus Urea Contest for Anion Recognition. *Chemistry*, *16*(14), 4368-4380. doi:10.1002/chem.200903190

Amendola, V., Fabbrizzi, L., Mosca, L., & Schmidtchen, F.-P. (2011). Urea-, Squaramide-, and Sulfonamide-Based Anion Receptors: A Thermodynamic Study. *Chemistry*, *17*(21), 5972-5981. doi:10.1002/chem.201003411

Anwer, R., AlQumaizi, K. I., Haque, S., Somvanshi, P., Ahmad, N., AlOsaimi, S. M., & Fatma, T. (2021). Unravelling the Interaction of Glipizide with Human Serum Albumin Using Various Spectroscopic Techniques and Molecular Dynamics Studies. *Journal of Biomolecular Structure and Dynamics*, *39*(1), 336-347. doi:10.1080/07391102.2019.1711195

Bao, X., Wu, X., Berry, S. N., Howe, E. N. W., Chang, Y.-T., & Gale, P. A. (2018). Fluorescent squaramides as anion receptors and transmembrane anion transporters. *Chemical Communications*, *54*(11), 1363-1366. doi:10.1039/C7CC08706C

Barišić, D., Cindro, N., Vidović, N., Bregović, N., & Tomišić, V. (2021). Protonation and anion-binding properties of aromatic sulfonylurea derivatives. *RSC Advances*, *11*(39), 23992-24000. doi:10.1039/D1RA04738H

Barišić, D., Lešić, F., Tireli Vlašić, M., Užarević, K., Bregović, N., & Tomišić, V. (2022). Anion Binding by receptors containing NH donating groups – What do anions prefer?. *Tetrahedron*, *120*, 132875-132883. doi:10.1016/j.tet.2022.132875

Best, L., & Benington, S. (1998). Effects of sulphonylureas on the volume-sensitive anion channel in rat pancreatic *β*-cells. *British Journal of Pharmacology*, *125*(4), 874-878. doi:10.1038/sj.bjp.0702148

Best, L., Davies, S., & Brown, P. D. (2004). Tolbutamide potentiates the volume-regulated anion channel current in rat pancreatic beta cells. *Diabetologia*, *47*(11), 1990-1997. doi:10.1007/s00125-004-1559-4

Bondy, C. R., & Loeb, S. J. (2003). Amide based receptors for anions. *Coordination Chemistry Reviews*, *240*(1-2), 77-99. doi:10.1016/S0010-8545(02)00304-1

Brogden, R. N., Heel, R. C., Pakes, G. E., Speight, T. M., & Avery, G. S. (1979). Glipizide: A Review of its Pharmacological Properties and Therapeutic Use. *Drugs*, *18*(5), 329-353 doi:10.2165/00003495-197918050-00001

Cai, X.-J., Li, Z., & Chen, W.-H. (2018). Synthesis, Anion Recognition and Transmembrane Anion-transport Properties of Squaramides and Their Derivatives. *Mini-Reviews in Organic Chemistry*, *15*(2), 148-156. doi:10.2174/1570193X14666171114115629

Davis, A. P., Sheppard, D. N., & Smith, B. D. (2007). Development of synthetic membrane transporters for anions. *Chemical Society Reviews*, *36*(2), 348-357. doi:10.1039/B512651G

Emami, J., Boushehri, M. S. S., & Varshosaz, J. (2014). Preparation, characterization and optimization of glipizide controlled release nanoparticles. *Research in Pharmaceutical Sciences*, *9*(5), 301-314.

Ganesh, K., Nikitha, G., Sireesha, D., & Vasudha, B. (2016). Development and Validation of UV Spectrophotometric Method for Simultaneous Estimation of Metformin and Glipizide in Tablet Dosage Form. *International Journal of Applied Pharmaceutical Sciences and Research*, *1*(2), 56-59. doi:10.21477/ijapsr.v1i2.10176

Gribble, F. M., & Reimann, F. (2002). Pharmacological modulation of K_{ATP} channels. *Biochemical Society Transactions*, *30*(2), 333-339. doi:10.1042/bst0300333

Hasanah, A. N., Pessagno, F., Kartasasmita, R. E., Ibrahim, S., & Manesiotis, P. (2015). Tetrabutylammonium methacrylate as a novel receptor for selective extraction of sulphonylurea drugs from biological fluids using molecular imprinting. *Journal of Materials Chemistry B*, *3*(43), 8577-8583. doi:10.1039/C5TB01512J

Hosogi, S., Kusuzaki, K., Inui, T., Wang, X., & Marunaka, Y. (2014). Cytosolic chloride ion is a key factor in lysosomal acidification and function of autophagy in human gastric cancer cell. *Journal of Cellular and Molecular Medicine*, *18*(6), 1124-1133. doi:10.1111/jcmm.12257

Huggins, M. T., Butler, T., Barber, P., & Hunt, J. (2009). Synthesis and molecular recognition studies of pyrrole sulfonamides. *Chemical Communications*, (35), 5254-5256. doi:10.1039/B911985J

Hussan, K. P. S., Rahoof, K. A. A., Medammal, Z., Thayyil, M. S., & Babu, T. D. (2022). Theoretical insights into the radical scavenging activity of glipizide: DFT and molecular docking studies. *Free Radical Research*, *56*(1), 53-62. doi:10.1080/10715762.2022.2034803

Jena, B. R., Swain, S., Babu, S. M., Pradhan, D. P., & Sasikanth, K. (2017). UV spectrophotometric Method Development and Quantitative Estimation of Glipizide in Bulk and Pharmaceutical Dosage Forms. *International Journal of Drug Research and Technology*, *7*(3), 112-122.

Kang, S. O., Begum, R. A., & Bowman-James, K. (2006). Amide-Based Ligands for Anion Coordination. *Angewandte Chemie International Edition*, *45*(47), 7882-7894. doi:10.1002/anie.200602006

Kinard, T. A., & Satin, L. S. (1995). An ATP-Sensitive Cl⁻ Channel Current That Is Activated by Cell Swelling, cAMP, and Glyburide in Insulin-Secreting Cells. *Diabetes*, *44*(12), 1461-1466. doi:10.2337/diab.44.12.1461

Kumawat, L. K., Wynne, C., Cappello, E., Fisher, P., Brennan, L. E., Strofaldi, A., McManus, J. J., Hawes, C. S., Jolliffe, K. A., Gunnlaugsson, T., & Elmes, R. B. P. (2021). Squaramide-Based Self-Associating Amphiphiles for Anion Recognition. *ChemPlusChem*, *86*(8), 1058-1068. doi:10.1002/cplu.202100275

Kuzmič, P. (2009). DynaFit-A Software Package for Enzymology. In: M. L. Johnson, & L. Brand (Eds.), *Computer Methods Part B* (*Methods in Enzymology* book series, vol. 467), (pp. 247-280). doi:10.1016/S0076-6879(09)67010-5

Lebovitz, H. E., & Feinglos, M. N. (1983). Mechanism of Action of the Second-Generation Sulfonylurea Glipizide. *The American Journal of Medicine*, *75*(5), 46-54. doi:10.1016/0002-9343(83)90253-X

Li, A.-F., Wang, J.-H., Wang, F., & Jiang, Y.-B. (2010). Anion complexation and sensing using modified urea and thiourea-based receptors. *Chemical Society Reviews*, *39*(10), 3729-3745. doi:10.1039/B926160P

Marchetti, L. A., Kumawat, L. K., Mao, N., Stephens, J. C., & Elmes, R. B. P. (2019). The Versatility of Squaramides: From Supramolecular Chemistry to Chemical Biology. *Chem*, *5*(6), 1398-1485. doi:10.1016/j.chempr.2019.02.027

Martin, S. L., Saint-Criq, V., Hwang, T.-C., & Csanády, L. (2018). Ion channels as targets to treat cystic fibrosis lung disease. *Journal of Cystic Fibrosis*, *17*(2), S22-S27. doi:10.1016/j.jcf.2017.10.006

Mercurio, J. M., Caballero, A., Cookson, J., & Beer, P. D. (2015). A halogen- and hydrogen-bonding [2]catenane for anion recognition and sensing. *RSC Advances*, *5*(12), 9298-9306. doi:10.1039/C4RA15380D

Ming, X., Qi, Z.-C., Lian, H.-Z., & Wang, S.-K. (2008). Spectral Data Analyses and Structure Elucidation of Hypoglycemic Drug Glipizide. *Instrumentation Science & Technology*, *36*(5), 503-514. doi:10.1080/10739140802234956

Norris, E. (1979). Glipizide, a new second-generation sulfonylurea. In: R. A. Camerini-Davalos, B. Hanover (Eds.), *Treatment of EARLY DIABETES* (*Advances in Experimental Medicine and Biology* book series, vol.119), (pp. 427-434). doi:10.1007/978-1-4615-9110-8_62

Pahwa, R., Bohra, P., Sharma, P. C., Kumar, V., & Dureja, H. (2010). Glipizide: Some Analytical, Clinical and Therapeutic Vistas. *International Journal of Chemical Sciences*, *8*(1), 59-80.

Pessagno, F., Hasanah, A. N., & Manesiotis, P. (2018). Molecularly imprinted 'traps' for sulfonylureas prepared using polymerisable ion pairs. *RSC Advances*, *8*(26), 14212-14220. doi:10.1039/C8RA01135D

Picci, G., Kubicki, M., Garau, A., Lippolis, V., Mocci, R., Porcheddu, A., Quesada, R., Ricci, P. C., Scorciapino, M. A., & Caltagirone, C. (2020). Simple squaramide receptors for highly efficient anion binding in aqueous media and transmembrane transport. *Chemical Communications*, *56*(75), 11066-11069. doi:10.1039/D0CC04090H

Prakash, O., & Iqbal, S. A. (2015). FTIR, ^{1}H NMR, mass spectral, XRD and thermal characterization studies of Nd^{III} and Sm^{III} complexes of glipizide: An oral antidiabetic drug. *Journal of Indian Chemical Society*, *92*(1), 51-63. doi:10.5281/zenodo.5602962

Prasad, N., Issarani, R., & Nagori, B. P. (2013). Ultraviolet Spectrophotometric Method for Determination of Glipizide in Presence of Liposomal/Proliposomal Turbidity. *Journal of Spectroscopy*, *2013*, 836372. doi:10.1155/2013/836372

Qi, C., Zhou, Q., Li, B., Yang, Y., Cao, L., Ye, Y., Li, J., Ding, Y., Wang, H., Wang, J., He, X., Zhang, Q., Lan, T., Ka Ho Lee, K., Li, W., Song, X., Zhou, J., Yang, X., & Wang, L. (2014). Glipizide, an antidiabetic drug, suppresses tumor growth and metastasis by inhibiting angiogenesis. *Oncotarget*, *5*(20), 9966-9979. doi:10.18632/oncotarget.2483

Ramalingam, V., Domaradzki, M. E., Jang, S., & Muthyala, R. S. (2008). Carbonyl Groups as Molecular Valves to Regulate Chloride Binding to Squaramides. *Organic Letters*, *10*(15), 3315-3318. doi:10.1021/ol801204s

Renström, E., Barg, S., Thévenod, F., & Rorsman, P. (2002). Sulfonylurea-Mediated Stimulation of Insulin Exocytosis via an ATP-sensitive K$^+$ Channel-Independent Action. *Diabetes*, *51*(1), S33-S36. doi:10.2337/diabetes.51.2007.S33

Rowe, S. M., Miller, S., & Sorscher, E. J. (2005). Cystic Fibrosis. *New England Journal of Medicine*, *352*(19), 1992-2001. doi:10.1056/NEJMra043184

Sehlin, J. (1981). Are Cl$^-$ Mechanisms in Mouse Pancreatic Islets involved in Insulin Release?. *Upsala Journal of Medical Sciences*, *86*(2), 177-182. doi:10.3109/03009738109179226

Shuman, C. R. (1983). Glipizide: An Overview. *The American Journal of Medicine*, *75*(5), 55-59. doi:10.1016/0002-9343(83)90254-1

Thordarson, P. (2011). Determining association constants from titration experiments in supramolecular chemistry. *Chemical Society Reviews*, *40*(3), 1305-1323 doi:10.1039/C0CS00062K

Ulatowski, F., Dabrowa, K., Balakier, T., & Jurczak, J. (2016). Recognizing the Limited Applicability of Job Plots in Studying Host-Guest Interactions in Supramolecular Chemistry. *The Journal of Organic Chemistry*, *81*(5), 1746-1756. doi:10.1021/acs.joc.5b02909

Valdivieso, A. G., & Santa-Coloma, T. A. (2019). The chloride anion as a signaling effector. *Biological Reviews*, *94*(5), 1839-1856. doi:10.1111/brv.12536

Zapata, F., Benítez-Benítez, S. J., Sabater, P., Caballero, A., & Molina, P. (2017). Modulation of the Selectivity in Anions Recognition Processes by Combining Hydrogen- and Halogen-Bonding Interactions. *Molecules*, *22*(12), 2273. doi:10.3390/molecules22122273

APPENDIX

DynaFit Script (Kuzmič, 2009)

1. GLP in CDCl$_3$, H$_h$ at δ = 6.47 ppm

[task]

  data = equilibria

  task = fit

[mechanism]

  H + G   <= =>   H.G   :   Ka   assoc

 [constants]

  Ka = 1 ??

[responses]

  intensive ; ... NMR chemical shifts

[data]

  variable G, H

  plot titration ; ... [H] and [G] are varied simultaneously

  graph 1H ; proton chemical shifts

  set aH | response H = 6.47 ?, H.G = 7.33 ?

[output]

  directory ./examples/pt03/NMR/output/aa

[settings]

{Output}

  XAxisLabel = [Guest], M

  YAxisLabel = chemical shift, ppm

[end]

2. GLP in CDCl$_3$, H$_n$ at δ = 8.66 ppm

[task]

  data = equilibria

  task = fit

[mechanism]

  H + G   <= =>   H.G   :   Ka   assoc

[constants]

  Ka = 1 ??

[responses]

  intensive ; ... NMR chemical shifts

[data]

  variable G, H

  plot titration ; ... [H] and [G] are varied simultaneously

  graph 1H ; proton chemical shifts

  set aH | response H = 8.66 ?, H.G = 10.89 ?

[output]

  directory ./examples/pt03/NMR/output/aa

[settings]

{Output}

  XAxisLabel = [Guest], M

  YAxisLabel = Chemical shifts, ppm

[end]

3. GLP in d_6-DMSO H$_h$ at δ = 6.32 ppm

[task]

  data = equilibria

  task = fit

[mechanism]

  H + G   <= =>   H.G   :   Ka   assoc

[constants]

  Ka = 1 ??

[responses]

  intensive ; ... NMR chemical shifts

[data]

  variable G, H

  plot titration ; ... [H] and [G] are varied simultaneously

  graph 1H ; proton chemical shifts

  set aH | response H = 6.32 ?, H.G = 7.04 ?

[output]

  directory ./examples/pt03/NMR/output/aa

[settings]

{Output}

  XAxisLabel = [Guest], M

  YAxisLabel = chemical shift, ppm

[end]

The Effects of Undercut Depth and Length on Weldment Mechanical Properties

Memduh KURTULMUŞ[1*] (iD)

[1]Marmara University, Faculty of Applied Sciences, Department of Jewelery and Jewelery Design, İstanbul, Türkiye

Keywords	Abstract
Welding Defects Undercut Defect Undercut Geometry Static Stress Concentration Factor	Undercutting is a fusion welding defect that appears as a groove at the weld metal's toe. An undercut discontinuity forms when welding, particularly when the current is applied at an extremely rapid rate. It decreases the static and fatigue strength of the weld and produces stress concentration at the welding zone. The height of the reinforcement, the weld bead's contact angle, the undercut's breadth, depth, length, and root radius, as well as other factors, affect the stress concentration factor's size. In this study, two mild steel plates with a 20 mm thickness were welded together using gas metal arc welding. Each test plate was machined to have a 30° single bevel groove angle prior to welding. The butt welded plate underwent radiographic NDT testing. A weldment free of defect was created. The weldment was machined into typical test specimens for tensile strength. An undercut defect was simulated by drilling a groove through each tensile test sample. Grooves had different depths and lengths. After that, samples were put through a tensile test. The test findings allowed for the identification of the impacts of groove shape on tensile strength, ductility, and static stress concentration factor.

1. INTRODUCTION

In connecting the workpieces of a construction, a welding technology is commonly used. Butt welding joints are commonly used in welding operations. Welding discontinuities occur at the weld zone if optimum welding parameters are not used in the welding operation (Hou et al., 2020). An undercut is a common discontinuity which appears at the toe of the butt weld bead (Ottersböck et al., 2021). An undercut is a type of weld defect presents in a fusion weld process (Frostevarg & Kaplan 2014; Meng et al., 2017; Hu et al., 2018). These discontinuities, which look like grooves and notches, appear parallel to the weld bead. They locate on the boundary between the weld zone and the base metal. Figure 1 depicts the undercut defect formed in X-butt weld joints created using the submerged arc welding technique (Zong et al., 2016). There are generally two different undercut defects: Discontinuous and continuous undercuts. Discontinuous defects involve a change in the defect thickness along the weld bead. The inability of weld areas to be filled with liquid weld metal during solidification causes undercuts. The undercut defect develops while welding with an extraordinarily high welding current or welding at an abnormally high welding speed. (Zong et al., 2016).

When a structural component's shape is uneven and the flow of stress is interrupted, stress concentrations result. A geometric discontinuity which causes a localized increase in stress is called as a stress raiser (Juvinall & Marshek, 1991). Holes, grooves, notches, and changes in the cross-sectional area of the object are stress raisers. The elasticity theory and the measurements acquired using the photo-elasticity technique are used to determine the maximum stresses in the notches and discontinuities of the objects under a static load. The stress that will exist in defect free piece is named as the nominal stress. The degree of concentration of a discontinuity

under tensile loads can be expressed as a non-dimensional stress concentration factor K_t which is the ratio of the highest stress occurring at the toe of a stress raiser to the nominal stress (Juvinall & Marshek, 1991).
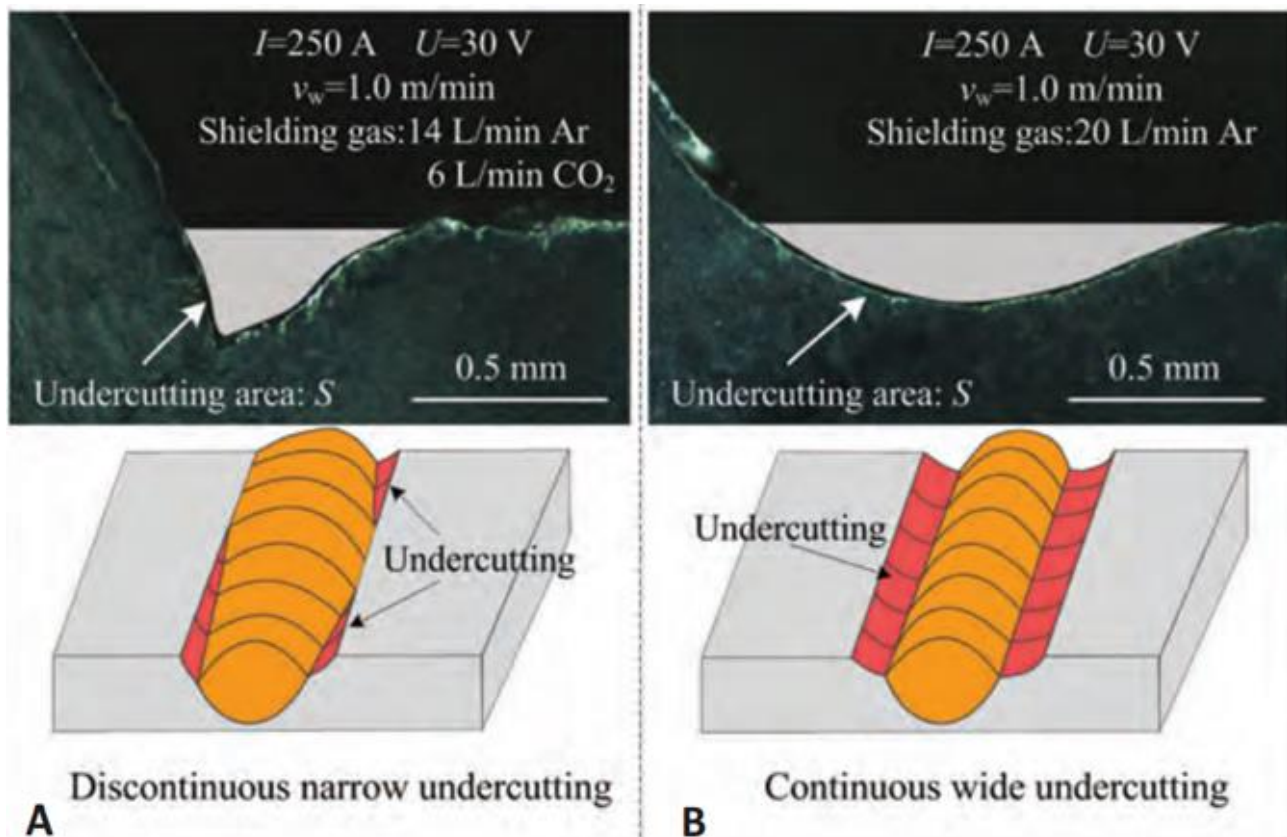
Figure 1. *Two different undercut discontinuities formed in butt weld joints made with gas metal arc welding* ***A)*** *Discontinuous narrow undercutting defect* ***B)*** *Continuous wide undercutting (Zong et al., 2016)*

The stress is concentrated at the bottom of an undercut because it has a notch-like effect (Juvinall & Marshek 1991) In butt welded joints, stress concentration occurs at the undercut which initiates a crack when the weldment is subjected to dynamic loads (Liinalampi et al., 2019; Molski & Tarasiuk, 2020; Kurtulmuş & Doğan, 2021; Kiraz et al., 2023). Fatigue cracks always start at stress raisers easily (Liinalampi et al., 2019). The K_t stress concentration coefficient in butt welds varies with the width, bottom radius, depth of the undercut and the weld contact angle (Cerit et al., 2010). Gill and his friends found that the stress concentration coefficient was dependent on the plate thickness, reinforcement height, weld bead width, and the weld bead contact angle (Gill & Singh, 2012). The effects of undercut length on the concentration of static stress were examined in a different study (Kurtulmuş & Doğan, 2021). An undercut defect causes a significant decrease both in the static strength (Kurtulmuş & Doğan, 2021) and the fatigue life of the structure (Liinalampi et al., 2019).

The effects of depth and length of continuous undercut defects on tensile strength, stress concentration coefficient (K_t) and ductility of weldments were experimentally investigated in this study. The mechanical properties of weldments were adversely affected with the undercut depths and lengths.

2. MATERIAL AND METHOD

In the experiments, two pieces of 1000x300x20 mm dimensioned EN 10025 S235JR (1.0037) unalloyed steel plates were used. On the longitudinal side of the plates a 30° bevel angel was machined. Angular distortion of the weldment was prevented by a reverse bending of the plates before the welding operations. Butt welding was done with an automatic CO_2 shielded gas metal arc (MAG) welding machine. In operations EN ISO 14341-A G3Si1 welding wires were used. Following each welding procedure, a penetrating liquid test was done. The produced weldment was radiographically examined to ensure that it was defect free.

Tensile test pieces perpendicular to the welding direction were cut from the weldment. The specimens were prepared according to ASTM standards (ASTM, 2015). The welding zone of each specimen was polished with sandpapers. The details of the weld zone became apparent by macro etching the specimens with nital solution. The contact angle of the weld bead was measured as 164°.

A notch resembling the undercut defect was formed at the base metal boundary parallel to the weld bead with a wire erosion device. A continuous notch was drilled on one side of the specimen. The tensile test specimens are shown in Figure 2. Each notch contained 1 mm width and 0.5 mm root radius. Three specimens having the same notch were prepared. The details of the notches are given at the Table 1. In the specimens the notch depth was 1, 2 or 3 mm and the notch length varied between 5, 10 and 20 mm. There are three tensile specimens for the welded state as well as the notched condition. The specimens of the sample group 1 didn't contain a notch.

Figure 2. *Photographs of tensile test specimens*

Table 1. *Details of the undercut grooves*

Sample No	Undercut depth, mm	Undercut length, mm
1	0	0
2	1	5
3	1	10
4	1	20
5	2	5
6	2	10
7	2	20
8	3	5
9	3	10
10	3	20

Tensile testing was conducted using a 50 tons capacity electronically controlled hydraulic test machine. The ultimate tensile strength and elongation percentage values were determined. Thirty experiments were conducted because there were three comparable test samples in ten separate experimental groups. By computing the simple average of three test results with a similar notch, the characteristics of each sample group were ascertained. By dividing the ultimate tensile strength of the notch-free first sample by the ultimate tensile strength of the sample group, the static stress concentration coefficient of each sample group was computed.

3. RESULTS AND DISCUSSION

The Table 2 displays the tensile test results and the computed static stress coefficient (K_t) values of samples. The following graphs were drawn by using the results of the Table 2.

Table 2. *The tensile test results, elongation % and the calculated static strength coefficient, K_t*

Sample No	Ultimate tensile strength MPa	Elongation %	Calculated Kt coefficient
1	551	30.1	1.00
2	507	28.4	1.08
3	501	24.3	1.10
4	492	17.9	1.12
5	498	19.2	1.11
6	487	16.5	1.13
7	466	9.8	1.18
8	497	18.2	1.11
9	464	14.3	1.19
10	422	8.0	1.31

Figure 3 shows the link between the length of the undercut with different undercut depths and the ultimate tensile strength of the weldment. In sample 2 the notch size is the smallest. The undercut length was 5 mm, and the notch depth was only 1 mm. Even this smallest notch caused a fall of the tensile strength from 551 MPa (Sample 1) to 501 MPa. The strength decreased 8%. The ultimate tensile strength of the weldment decreased to 492 MPa when the notch length increased from 5 mm to 20 mm. The strength decreases slightly with the undercut length. Figure 3 shows that the fall ratio in tensile strength with the undercut length is getting bigger with the notch depth. The strength decrease ratio was 8% for 5 mm long undercut, 9% for 10 mm length and 10% for 20 mm undercut length. The Table 3 was prepared by the results of the Table 2 to reveal the notch geometry factor on the tensile strength ratio. The data in Table 3 clearly shows that the notch depth and length play a significant role in the static strength of welds. The ultimate tensile strength of the weldment is further decreased when an undercut is longer and deeper. The largest stress reduction was achieved with an undercut length of 20 mm.
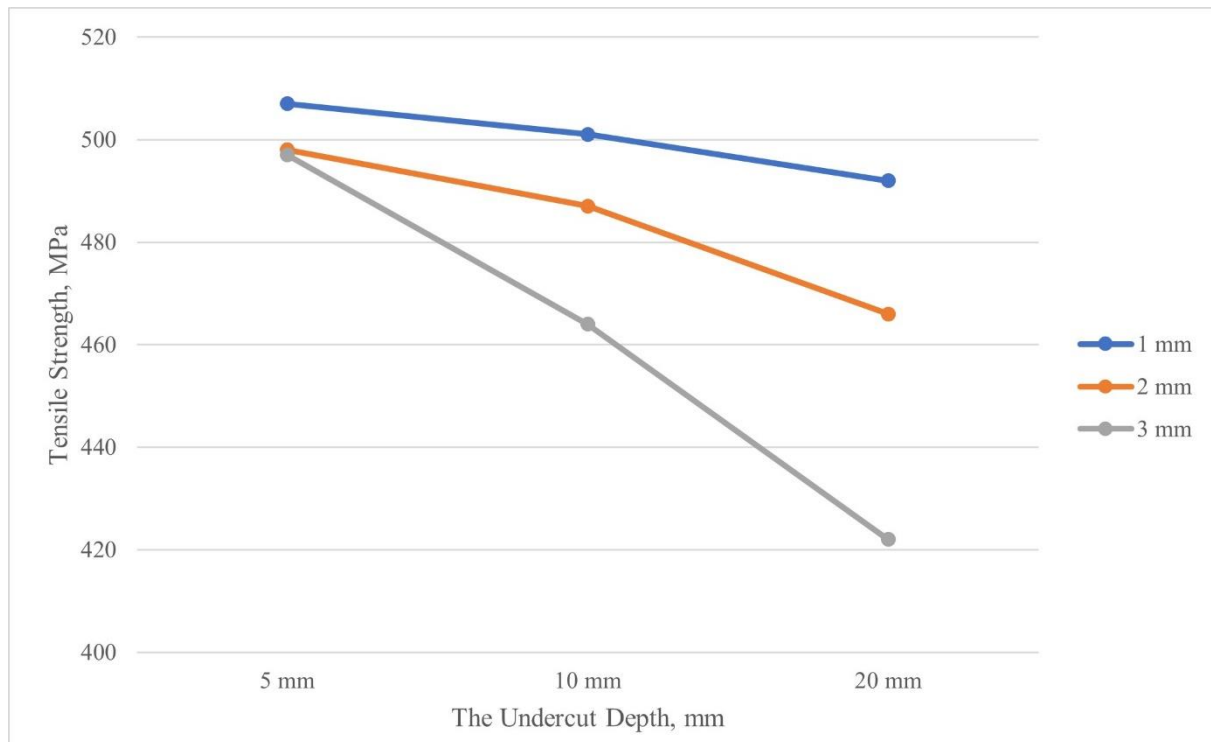
Figure 3. Variation of the ultimate tensile strength with the length of the undercut

Table 3. Variation of the ultimate tensile strength loss percentage with the undercut length and the undercut depth

Undercut depth, mm	*Undercut* length, mm		
	5	**10**	**20**
1	8%	9%	10%
2	10%	12%	15%
3	10%	16%	23%

Figure 4 shows how the length of the undercut affects the static stress coefficient (K_t) of the weld. The stress concentration coefficient was approximately equal for 5 mm undercut length of 1, 2 and 3 mm undercut depth. K_t increases in direct proportion to the length and depth of undercut because the ultimate tensile strength of notched welds decreases with increasing the notch size. The K_t increase was calculated for 20 mm undercut lengths. If Figures 3 and 4 are compared, it will be seen that the length and depth of the undercuts have a similar effect on the mechanical properties.

The relationship between the undercut length and the weldment's elongation ratio is seen in Figure 5. The size of the notch affects how ductile a weldment is. Figure 5 clearly differs from Figures 3 and 4 in several ways. When the undercut depth is increased from 1 mm to 2 mm in each notch length, a noticeable decrease in ductility is seen. However, there is a little loss in ductility when the undercut is deepened from 2 mm to 3 mm. The Table 4 was prepared by the results of the Table 2. This table shows how the notch geometry factor affects the weldments' ductility ratio. Examining the data reveals the impact of undercut depth on ductility loss in weldments with an undercut length of 5 mm. Weldment ductility is 6%, 36%, and 40% for undercut depths of 1, 2, and 3 mm, respectively. The ductility is reduced 6% for 1mm undercut depth. The reduction in elongation is 30% for increasing the notch depth from 1 mm to 2mm. The elongation fall is only 4% in increasing the depth from 2 mm to 3mm. Similar results were obtained in 10 mm and 20 mm undercut lengths.
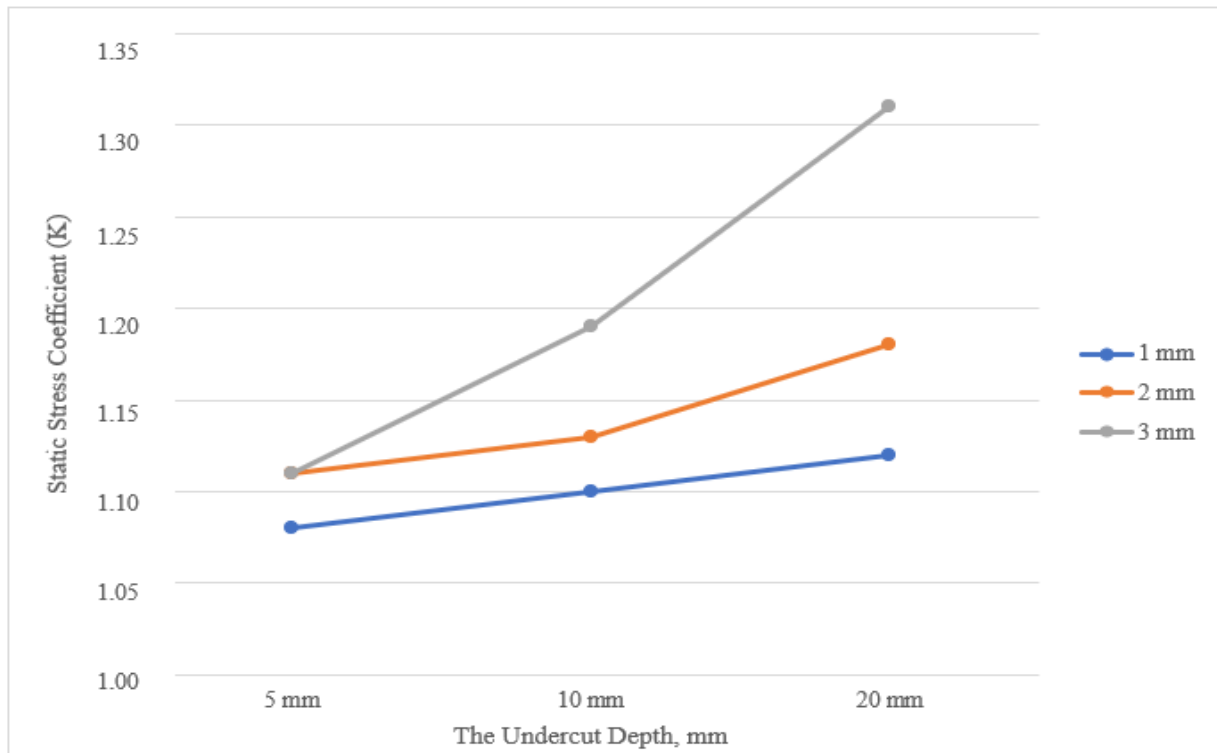
Figure 4. *Variation of the static stress concentration coefficient (K_t) with the undercut length*
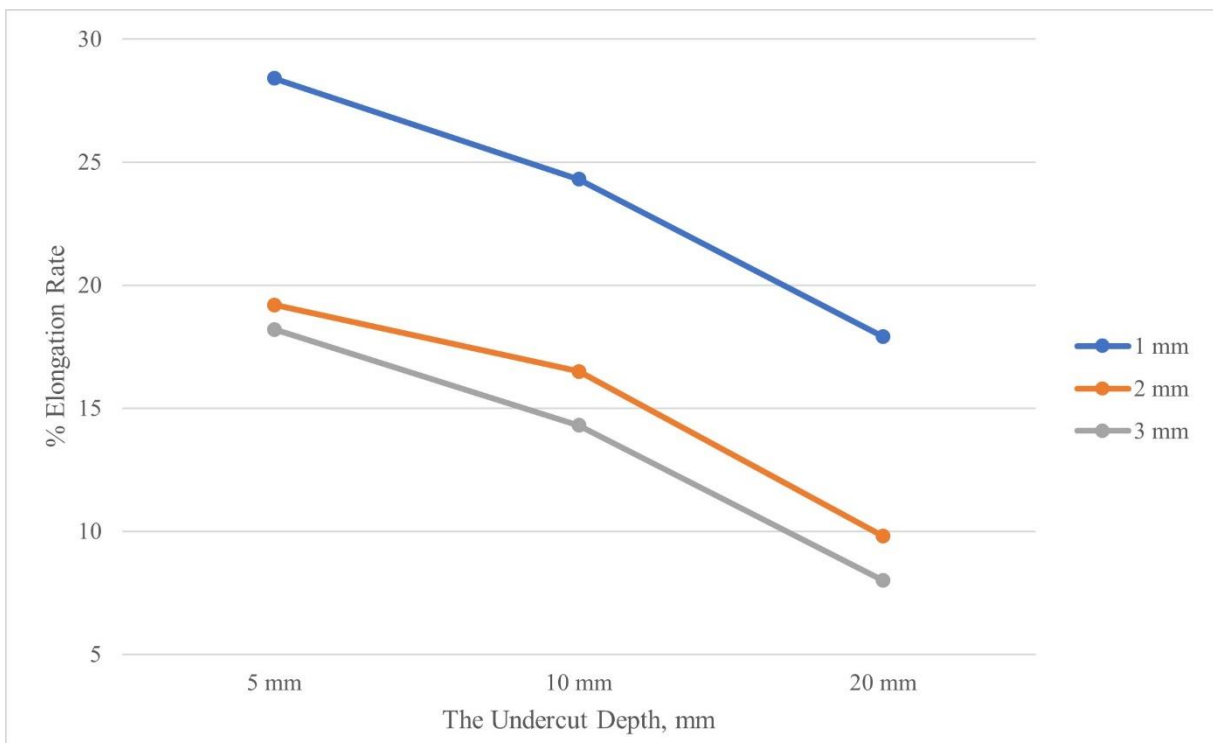
Figure 5. *Variation of weldment elongation % with the length of the undercut*

Table 4. *Variation of the elongation decrease percentage with the undercut length and the undercut depth*

Undercut depth, mm	*Undercut* length, mm		
	5	**10**	**20**
1	6%	19%	41%
2	26%	45%	68%
3	40%	52%	73%

4. CONCLUSION

The 60° V-butt welded joint was made by the MAG gas arc welding process on 20 mm thickness EN 10025 S235JR (1.0037) unalloyed steel plates. The following results were obtained from the tensile tests:

1. The ultimate tensile strength decreases with the undercut depth increase.

2. The ultimate tensile strength decreases with the undercut length increase

3. The stress concentration coefficient of the discontinuity grows as the undercut's depth or length increases.

4. The ductility decreases with the increase of undercut depth and length.

5. The highest ductility loss is obtained when the undercut depth is 2 mm.

6. The findings of this study led to the realization that a more precise equation is required in the literature in order to anticipate and identify the static stress concentration factor of undercut defects in future studies and researchs.

CONFLICT OF INTEREST

The author declares no conflict of interest.

REFERENCES

ASTM, American Society for Testing and Materials. (2015) Standard Test Methods for Tension Testing of Metallic Materials (ASTM E8/E8M-13a). ASTM International. doi:10.1520/E0008_E0008M-13A

Cerit, M., Kokumer, O., & Genel, K. (2010) Stress concentration effects of undercut defect and reinforcement metal in butt welded joint. *Engineering Failure Analysis*, *17*(2), 571-578. doi:10.1016/j.engfailanal.2009.10.010,

Frostevarg, J., & Kaplan, A. F. H. (2014) Undercuts in laser arc hybrid welding. *Physics Procedia*, *56*, 663-672. doi:10.1016/j.phpro.2014.08.071

Gill, J., & Singh, J. (2012) Effect of welding speed and heat input rate on stress concentration factor of butt welded joint of IS 2062 E 250 A steel. *International Journal of Advanced Engineering Research and Studies*, *1*(3), 98-100.

Hou, W., Zhang, D., Wei, Y., Guo, J., & Zhang, X. (2020) Review on computer aided weld defect detection from radiography images. *Applied Sciences, 10*(5), 1878. doi:10.3390/app10051878

Hu, Y., Xue, J., Dong, C., Jin, L., & Zhang, Z. (2018) Effect of additional shielding gas on welding seam formation during twin wire DP-MIG high-speed welding. *Applied Science*, *8*(9), 1658. doi:10.3390/app8091658

Juvinall, R. C., & Marshek, K. M. (1991). *Fundamentals of Machine Component Design* (2nd ed.). John Wiley and Sons, New York, USA.

Kiraz, A., Erkan, E. F., Canpolat, O., & Kökümer, O. (2023) Prediction of Stress Concentration Factor in Butt Welding Joints Using Artificial Neural Networks. *International Journal of Research in Industrial Engineering*, *12*(1), 43-52. doi:10.22105/riej.2023.349647.1322

Kurtulmuş, M., & Doğan, E. (2021) The effects of undercut geometry on the static stress concentration factor of welds. *Emerging Materials Research, 10*(3)*,* 272-277. doi:10.1680/jemmr.20.00100

Liinalampi, S., & Remes, H., & Romanoff, J. (2019) Influence of three-dimensional weld undercut geometry on fatigue-effective stress. *Welding in the World, 63*(2), 277-291. doi:10.1007/s40194-018-0658-7

Meng, X., Qin, G., & Zou, Z. (2017) Sensitivity of driving forces on molten pool behavior and defect formation in high-speed gas tungsten arc welding. *International Journal of Heat and Mass Transfer*, *107*, 1119-1128. doi:10.1016/j.ijheatmasstransfer.2016.11.025

Molski, K. L., & Tarasiuk, P. (2020) Stress Concentration Factors for Butt-Welded Plates Subjected to Tensile, Bending and Shearing Loads. *Materials*, *13*(8), 1798. doi:10.3390/ma13081798

Ottersböck, M. J., Leitner, M., & Stoschka, M. (2021) Characterisation of actual weld geometry and stress concentration of butt welds exhibiting local undercuts. *Engineering Structures*, *240*, 112266. doi:10.1016/j.engstruct.2021.112266

Zong, R., Chen, J., Wu, C., & Chen, M. (2016) Undercutting formation mechanism in gas metal arc welding. *Welding Journal,* 95, 174-184.

Genetic Algorithm based PID Tuning Software Design and Implementation for a DC Motor Control System

Zafer ORTATEPE[1*] iD

[1]*Pamukkale University, Department of Automotive Engineering, Denizli, Türkiye*

Keywords	Abstract
DC Motor Genetic Algorithm PID Tuning	This study presents the software and implementation for proportional-integral-derivative (PID) tuning of a DC motor control system using genetic algorithm (GA). The PID parameters for a specific control structure are optimized using GA in the proposed tuning procedure. Also, integral time absolute error (ITAE) is used as a fitness function to optimize the parameters. The robustness of the control system is compared with conventional mathematical method. Simulations are carried out in MATLAB/Simulink to compare the results of a DC motor control system. Simulation results show that in terms of overshoot, steady-state error, and settling time, GA-based PID tuning approach performed better than conventional method. Additionally, a sensitivity analysis is performed to evaluate how robust the proposed approach is to parameter variations. The analysis shows that compared to the conventional method, the GA-based PID tuning algorithm is more adaptable to variations in system parameters.

1. INTRODUCTION

Control systems play a significant role in many fields, from automotive to aerospace, robotics to industrial process control. One of the most used control methods in industry is proportional-integral-derivative (PID) controller. PID control, a closed-loop feedback technique, measures the error between a desired set point and the system's actual output continually and then modifies the control input to minimize this error. To maintain system stability and performance, it is essential to fine-tune of the PID parameters. However, conventional PID tuning methods can be time-consuming and require expert knowledge, making it challenging to tune the PID controller for complex systems (Borase et al., 2021).

In literature, a number of conventional PID tuning methods have been proposed, including Ziegler-Nichols (ZN) (Patel, 2020), Cohen-Coon (Taşören, 2021), and Tyreus-Luyben (Ibrahim et al., 2016) methods. These methods require expert knowledge of the system, and the tuning process can be time-consuming and challenging for complex systems.

To solve these drawbacks, some optimization techniques have been proposed to tune PID controllers, for instance particle swarm optimization (PSO) (Aranza et al., 2016) and differential evolution (DE) (Saad et al., 2012). A population-based optimization algorithm called PSO imitates its cooperative behavior of a swarm of particles. The PSO-based PID tuning method has been applied to various control systems, such as DC motor control (Alruim Alhasan & Güneş, 2017) and chemical processes (Fang et al., 2021). The other population-based optimization technique called DE imitates the natural process of crossover and mutation. DE-based PID

tuning methods have been applied to various control systems, such as HVAC systems (Rout et al., 2013) and mobile robots (Martinez-Soltero & Hernandez-Barragan, 2018).

GA is one of the most widely used optimization technique in engineering, including in control system design. It has been successfully implemented in various applications due to their ability to search a large parameter space and find optimal solutions (Malhotra et al., 2011). Moreover, GA-based PID tuning methods can automatically generate optimal PID parameters that achieve the desired system performance. The GA-based PID tuning method can handle complex systems and requires less expert knowledge, making it an attractive alternative to conventional PID tuning methods (de Figueiredo et al., 2023).

Different GA-based PID tuning techniques have been proposed by researchers. For instance, Islam et al. (2020) propose a GA-based PID tuning method that uses fuzzy logic to adjust crossover and mutation ratios. Method is implemented for a DC motor and the results showed that the transient-state response and steady-state error are reduced. Similarly, Jayachitra and Vinodha (2014) propose a GA-based PID tuning method that uses a weighted combination of objective functions. The method is applied to continuous stirred tank reactor and combination of all objective functions demonstrated its effectiveness in improving system performance. Tiwari et al. (2018) propose a PID control method for the DC motor control system that is based on a GA. MATLAB/Simulink is used to simulate performance of the system, and GA optimization is implemented using the MATLAB toolbox. The results showed that GA-based tuning method significantly improved the performance of control system compared to conventional ones. Moreover, in a DC motor control system, a hybrid optimization strategy for PID controller tuning is proposed by Flores-Morán et al. (2020). To improve the search capabilities of the optimization process, the GA method is combined with the PSO algorithm. The results showed that, in comparison to ZN approach, the hybrid optimization method greatly enhanced performance of DC motor control system. GA-based PID tuning approach is proposed by Galotto et al. (2007). For estimating the unknown parameters of the DC motor and fine-tuning the PID controller parameters, the authors employ the recursive least squares (RLS) approach. Results shows that the proposed method successfully improved the performance of the DC motor control system by optimizing the PID controller parameters. Korkmaz et al. (2012) propose variable parameter nonlinear PID controller and GA based PID controller to compare the results of the proposed controllers. According to the results, it can be deduced that both control methods are superior to the conventional ZN control method. However, it is seen that the GA-based control method gives slightly better results than the variable parameter nonlinear PID controller. Pereira and Pinto (2005) propose GA optimization technique to define the system identification and parameter tuning for the optimum adaptive control. In proposed system two independent GA are used respectively. When the results of the cascaded GA are compared with the conventional ZN method, it is emphasized that the GA-based system is superior. Wati and Hidayat (2013) propose GA-based PID parameters optimization for air heater temperature control. The experimental results demonstrate that the step response of GA-based PID controller performs better than conventional ZN tuning method. Meena and Devanshu (2017) propose a PID tuning method for process control by using GA. Comparing the proposed GA tuned plant's performance to that of a conventionally tuned plant, it can be seen that the GA tuned PID controller outperforms the conventionally designed PID controller.

Major gap in the literature regarding this subject is the lack of presentation of the full algorithms used in the above studies. This paper presents GA-based PID tuning method and its implementation for a DC motor control system. The proposed GA based tuning software is completely presented in this work, which is the key element that separates this study from others in the literature. The software is written in MATLAB, and the DC motor implementation has been done in MATLAB/Simulink.

The rest of the paper is arranged as follows: section 2 describes the mathematical model and transfer function of the DC motor. Section 3 analyzes conventional PID control method. Section 4 discusses the proposed GA-based PID tuning method and Section 5 gives its fully software. Section 6 describes the manual solution for single iteration. Section 7 gives the implementation of the proposed method for a DC motor control system. Finally, section 8 concludes the paper.

2. MATHEMATICAL MODEL OF DC MOTOR

A DC motor is a device that converts electrical energy into mechanical energy through its interaction of a magnetic field and current-carrying conductors. The DC motor can be modeled using mathematical equations that describe its behavior in terms of its physical parameters. Fundamental DC motor model is given in Figure 1. Mathematical model of DC motor in Laplace domain can be represented by the following equations:

$$e_a(s) = R_a I_a(s) + sL_a I_a(s) + e_b(s) \tag{1}$$

$$T_m(s) = K_i I_a(s) \tag{2}$$

$$T_m(s) = sJ_m \Omega_m(s) + B_m \Omega_m(s) + T_L(s) \tag{3}$$

$$e_b(s) = K_b \Omega_m(s) \tag{4}$$

The equations can be written as follows when the input and output of the system are defined as $e_a(s)$ and $\Omega_m(s)$.

$$I_a(s) = \frac{e_a(s) - e_b(s)}{sL_a + R_a} \tag{5}$$

$$\Omega_m(s) = \frac{T_m(s) - T_L(s)}{sJ_m + B_m} \tag{6}$$
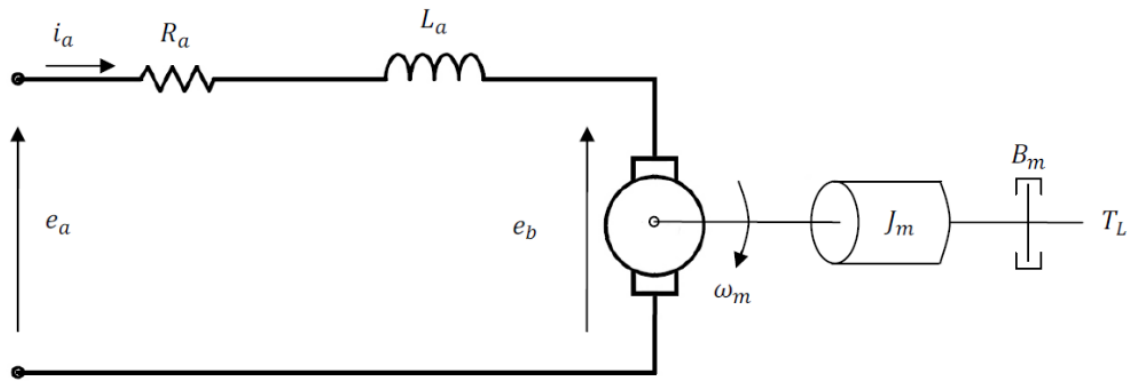
Figure 1. *DC motor model*

In the light of these equations, the DC motor control block diagram is shown in Figure 2.
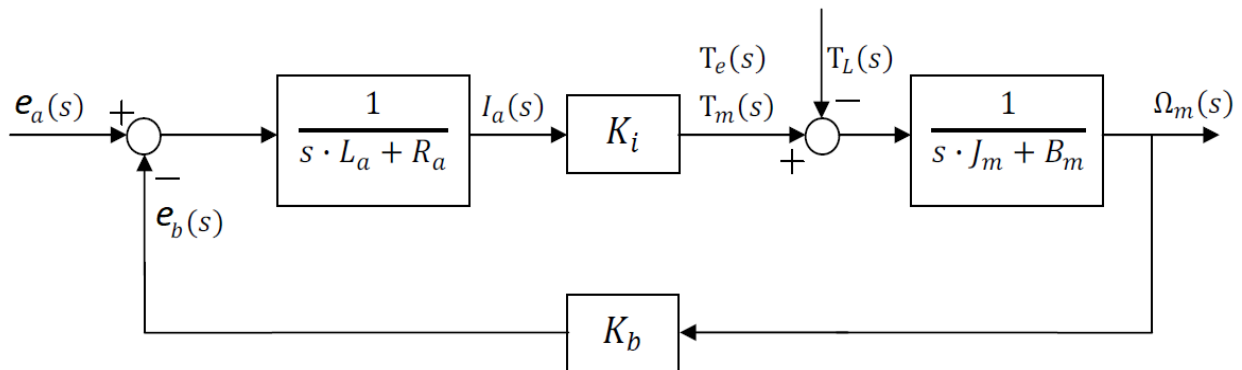
Figure 2. *Block diagram of the DC motor*

The transfer function of the DC motor must be modified to include the controller's effects when designing a controller for a DC motor control system. The resulting transfer function is:

$$\frac{\Omega_m(s)}{e_a(s)} = \frac{K_i}{s^2 J_m L_a + s(J_m R_a + L_a B_m) + R_a B_m + K_i K_b} \tag{7}$$

The electrical time constant is assumed to be zero due to the mechanical time constant of the system is much larger than the electrical time constant. So, if $L_a/R_a=0$, it must be $L_a=0$. In this case, overall transfer function of system is as follows:

$$\frac{\Omega_m(s)}{e_a(s)} = \frac{K_i}{s J_m R_a + R_a B_m + K_i K_b} \tag{8}$$

Since it is often assumed that $K_T = K_i = K_b$ in practice, the equation can be written as:

$$\frac{\Omega_m(s)}{e_a(s)} = \frac{K_T}{s J_m R_a + R_a B_m + K_T{}^2} \tag{9}$$

The system is similar to the general transfer function of the first-order system. So, let's bring the system to the general transfer function form of first-order systems with various arrangements.

$$\frac{K}{\tau s + 1} \cong \frac{\dfrac{K_T}{K_T{}^2 + R_a B_m}}{\dfrac{J_m R_a}{K_T{}^2 + R_a B_m} s + 1} \tag{10}$$

where K is the gain $K \cong \frac{K_T}{K_T{}^2 + R_a B_m}$ and τ is the time constant $\tau \cong \frac{J_m R_a}{K_T{}^2 + R_a B_m}$. The DC motor parameters used in this paper is given in Table 1.

Table 1. DC motor parameters used in this study

Parameters	Symbols	Values
Motor resistance	R_a	3.2Ω
Motor inductance	L_a	0H
Inertia moment	J_m	$0.082 \ kg.m^2$
Viscous friction coefficient	B_m	$0.0275 \ kg.m^2/s$
Motor torque constant	K_i	1.26 *N.m/A*
EMF constant	K_b	1.26 *V.s/rad*

As a result, the following is the DC motor's transfer function:

$$G_{S_S} = \frac{\Omega_m(s)}{e_a(s)} = \frac{0.752}{0.157s + 1} \tag{11}$$

3. PROPORTIONAL INTEGRAL DERIVATIVE (PID) CONTROL OF DC MOTOR

Due to their ability to precisely adjust speed and torque, DC motors are widely used in industrial applications. PID control is a popular technique for controlling motor speed. Besides, three elements are used in a closed loop PID control system: proportional, integral, and derivative. Proportional component adjusts the input voltage to the motor in proportion to the error between the desired and actual motor speed. Integral component integrates the error over time to compensate for any steady-state error. The motor's input voltage is changed by the derivative component to correspond with a measurement of the error's rate of change. PID controller transfer function is provided by:

$$G_{c_s} = K_P + \frac{K_I}{s} + K_D s \tag{12}$$

where K_P, K_I, and K_D are the proportional, integral, and derivative gains, respectively. "s" is the Laplace domain variable. A first-order system can be controlled by PID algorithm as if it is a second-order system, according to criteria such as desired overshoot and settling time. The criteria required in the controller design are determined as follows: Mp = %5 (overshoot ratio), Ts=0.4 s (settling time), ess = 0.02 (steady state error for ramp input signal). The formulations of these criteria are given as follows:

$$\%M_p = e^{-\frac{\xi}{\sqrt{1-\xi^2}}\pi}.100 \tag{13}$$

$$T_s = \frac{4}{\sigma} \qquad\qquad \sigma = \xi\omega_n \tag{14}$$

where ξ is the damping rate and ω_n is the damping frequency. When equations (13) and (14) are solved, $\xi = 0.69$ and $\omega_n = 14.4927$ are calculated. All of the system poles is given below:

$$s_{1,2} = -\xi\omega_n \mp \omega_n\sqrt{\xi^2 - 1} \tag{15}$$

$$\sigma = \xi\omega_n = 10 \tag{16}$$

$$\omega_n\sqrt{\xi^2 - 1} = 10.49 \tag{17}$$

$$s_{1,2} = -10 \mp j10.49 \tag{18}$$

Since e$_{ss}$ (∞) = 0.02

$$K_V = \frac{1}{e_{ss}} = \frac{1}{0.02} = 50 \tag{19}$$

$$K_V = \lim_{s\to 0} s G_{C_s} G_{S_s} \tag{20}$$

$$K_V = \lim_{s\to 0} s \left\{K_P + \frac{K_I}{s} + K_D s\right\}\left\{\frac{0.752}{0.157s + 1}\right\} \tag{21}$$

Finally, the integral coefficient of the control system is determined as $K_I = 37.6$. The characteristic equation of the system is defined as:

$$F(s) = 1 + G_{C_s} G_{S_s} = 0 \tag{22}$$

Therefore $G_{C_s} = -\frac{1}{G_{S_s}}$ can be obtained. Where G_{C_s} is the controller block and G_{S_s} is the DC motor transfer function block.

$$K_P + \frac{K_I}{s} + K_D s = -\frac{1}{\frac{0.752}{0.157s + 1}} \tag{23}$$

$$K_P + K_D(-10 + j10.49) = -\frac{0.157(-10 + j10.49) + 1}{0.752} - \frac{37.6}{-10 + j10.49} \tag{24}$$

Consequently, the proportional and derivative coefficients of the control system is determined as $K_P = 2.84$ and $K_D = 0.029$, respectively. A closed loop DC motor control system is given in Figure 3.
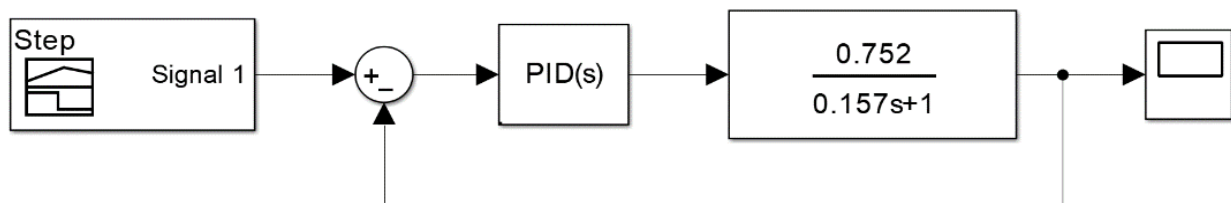
Figure 3. *Closed loop control system of the DC motor*

4. GENETIC ALGOTIRHM BASED PID TUNING SOFTWARE DESIGN

In this section, the software design for the GA-based PID tuning system is described. PID control method is widely used in closed loop systems. However, selection of the proportional, integral, and derivative gains is crucial to controller performance. To simplify the PID tuning process, a GA optimization algorithm is employed. The GA is an optimization method that draws inspiration from the genetics field's natural selection procedure. Crossover, mutation and selection processes are used to iteratively improve a starting population of potential solutions (PID gains). The following steps make up the software design:

Input and initialization: The DC motor transfer function, control targets, and PID limits are provided by the user as input to the software. Maximum number of generations, population size, mutation and crossover rates are also initialized.

Fitness evaluation: Fitness function is the objective metric used to evaluate each proposed solution's effectiveness. In this case, fitness function is integral time absolute error (ITAE) between the desired and actual motor speed over a certain time period.

Selection: The fittest members in the population are selected based on their fitness value. The tournament selection method is used, where pairs of individuals are randomly selected and compared based on their fitness value. The individual with highest fitness value is chosen for a next generation.

Crossover: Genetic information of two selected individuals is combined to generate new offspring. The one-point crossover strategy is applied, in which the genetic information beyond a predetermined point in the PID gain strings of two individuals are exchanged between them.

Mutation: Random changes in the genetic information of the offspring are introduced to diversify the population and avoid premature convergence.

Termination: When the maximum number of generations is reached or the fitness value of the best individual reaches a sufficient level, the GA process terminates.

Output and visualization: The optimal PID parameters for the DC motor control system are output by the software based on the fittest individual in the final generation. The software also provides a plot of the actual output value and the desired reference over time to visualize the performance of the system.

Overall, the software design enables the adjusting of PID parameters for DC motor control using a GA optimization algorithm. The next section describes the implementation of the software on a MATLAB platform.

5. GA BASED PID TUNING ALGORITHM

Initialization, fitness evaluation, selection, crossover, and mutation are the different parts of the algorithm. Initial parameters used in GA based PID software is given in Table 2.

Part 1 of the GA tuned PID tuning algorithm is given in Figure 4. In this part, the number of genes in each chromosome, upper and lower bounds of the parameters, size of each gene, and mutation and crossover rates are determined. A random population is generated within the specified limits for the initial population. The start and end bits of the K_D, K_P, and K_I genes in the chromosome are determined. If the random gene exceeds the upper limit, it is set to the upper limit and if it is below the lower limit, it is set to the lower limit. In addition, if the sign is negative, the sign bit is set to zero, and if it is positive, the sign bit is set to 9, and the absolute value of the genes is taken.

Part 2 of the GA based PID tuning algorithm is given in Figure 5. In this part, transfer function of DC motor is defined and the genes in the chromosome are placed into the transfer function. The integral of the system is taken, and the total error value is transferred to the objective fitness. Fitness function values are calculated from all objective fitness values, and the total fitness value is found and stored for use in the roulette wheel

method. The best individuals are selected using the roulette wheel method for crossover and best chromosomes move to the next generation.

```matlab
gene_number=3;
upper_limit=[0.5 5 50];
lower_limit=[0 0 0];
gene_size=[6 6 6]';
decimal=[2 2 2];
mutation_rate=0.01;
crossover_rate=0.7;
population_size=50;
generation=40;
loop=1;
g=1;
for i = 1:population_size
    for j = 1:gene_number
        gene(j,i,loop)=((rand*(upper_limit(j)-lower_limit(j)))+lower_limit(j));
    end
end
chromosome_size=sum(gene_size)+gene_number;
gene_start(1)=1;
for j=1:gene_number
gene_start(j+1)= gene_start(j)+gene_size(j)+1;
end
while loop <= generation
for i = 1:population_size
    for j = 1:gene_number
        if gene(j,i,loop)>upper_limit(j)
            gene(j,i,loop)=upper_limit(j);
            elseif gene(j,i,loop) < lower_limit(j)
            gene(j,i,loop)=lower_limit(j);
        end
        if gene(j,i,loop) < 0
            pop(gene_start(j),i)=0;
        else
            pop(gene_start(j),i)=9;
        end
        temporary_gene(j,i) = abs(gene(j,i,loop));
        temporary_gene(j,i) = temporary_gene(j,i)/10^(decimal(j)-1);
        for k = gene_start(j)+1:gene_start(j+1)-1,
            pop(k,i) = temporary_gene(j,i)-rem(temporary_gene(j,i),1);
            temporary_gene(j,i) = (temporary_gene(j,i)-pop(k,i))*10;
        end
    end
end
```

Figure 4. *Software design in a MATLAB environment (Part 1)*

Table 2. *Initial parameters of GA based PID software*

Parameters	Values
Population size	50
Generation	40
Number of gene	3
Limits of K_P	0-1
Limits of K_I	0-10
Limits of K_D	0-0.5
Size of gene	6, 6, 6
Mutation rate	0.01
Crossover rate	0.2

Part 3 of the GA tuned PID tuning algorithm is shown in Figure 6. In this part, the next step of the software is crossover and child chromosomes are generated from the parent chromosomes. During the process, chromosomes are randomly selected for crossover. If the crossover rate determined at the beginning of the software is greater than the randomly generated number between 0-1, crossover occurs, if it is small, it does not occur and the parent chromosomes are transferred to the child chromosomes exactly.

```
43 -        a=1;
44 -        sumfitness=0;
45 -        for t= 1:population_size
46 -        m=0:0.01:10;
47 -        numerator_1=0.752;
48 -        denumerator_1=[0.157 1];
49 -        sis1=tf(numerator_1,denumerator_1);
50 -        numerator_2=[gene(1,a,loop) gene(2,a,loop) gene(3,a,loop)];
51 -        a=a+1;
52 -        denumerator_2=[1 0];
53 -        sis2=tf(numerator_2,denumerator_2);
54 -        sistop=series(sis1,sis2);
55 -        new_sis=feedback(sistop,1);
56 -        y=step(new_sis,m);
57 -        error=0;
58 -            for i=1:1001
59 -                error=error+abs((y(i)-1)*0.01);
60 -            end
61 -        objective_fitness(t)=error;
62 -        end
63 -        best_obj_function=objective_fitness(1);
64 -        for h=1:population_size
65 -            if objective_fitness(h)<best_obj_function
66 -                best_obj_function=objective_fitness(h);
67 -            end
68 -        end
69 -        value(g)=best_obj_function;
70 -        g=g+1;
71 -        for t= 1:population_size
72 -        fitness(t)=1/objective_fitness(t);
73 -        sumfitness = sumfitness + fitness(t);
74 -        end
75 -        [bestfitness(loop),bestmember]=max(fitness);
76 -        bestindividual(:,loop)=gene(:,bestmember,loop);
77 -        average_fitness(loop) = sumfitness/population_size;
78 -        for i=1:population_size
79 -            pointer=rand*sumfitness;
80 -            members_number=1;
81 -            toplam=fitness(1);
82 -            while toplam < pointer
83 -                members_number=members_number+1;
84 -                toplam=toplam+fitness(members_number);
85 -            end
```

Figure 5. Software design in a MATLAB environment (Part 2)

In case of crossover, it is determined randomly from which bit the crossover starts. The bits of the selected chromosome from 1 to the determined place are transferred to the new child chromosome. The bits of another chromosome from the determined place to the end are transferred to the new child chromosome.

Thus, the child chromosome is formed by crossing the two randomly selected chromosomes from the randomly determined dividing point. Then the chromosomes mutate according to the mutation rate. If the mutation rate determined at the beginning is greater than the randomly generated number between 0 and 1, the mutation will occur, if it is small, it will not occur. Finally, new chromosomes are transferred to the gene pool and the cycle is increased by one.

Finally, the PID parameters produced by the software and the numerically calculated parameters in section 3 are applied to the DC motor transfer function and the relevant code lines are given in Figure 7.

```
86 -                  parent_chrom(:,i)=pop(:,members_number);
87 -          end
88 -          for s=1:population_size
89 -              q=s;
90 -              while q==s
91 -                  q = rand*population_size;
92 -                  q = q-rem(q,1)+1;
93 -              end
94 -              if crossover_rate > rand
95 -                  bolum = rand*chromosome_size;
96 -                  bolum = bolum-rem(bolum,1)+1;
97 -                  child(1:bolum,s)=parent_chrom(1:bolum,s);
98 -                  child(bolum+1:chromosome_size,s)=parent_chrom(bolum+1:chromosome_size,q);
99 -              else
100 -                 child(:,s)=parent_chrom(:,s);
101 -             end
102 -         end
103 -         for s=1:population_size
104 -             for p=1:chromosome_size
105 -                 if mutation_rate > rand
106 -                 rand_gen=rand*10;
107 -                 while child(p,s) == rand_gen-rem(rand_gen,1)
108 -                 rand_gen=rand*10;
109 -                 end
110 -                 child(p,s)=rand_gen-rem(rand_gen,1);
111 -                 end
112 -             end
113 -         end
114 -         pop=child;
115 -         loop=loop+1;
116 -         for i=1:population_size
117 -             for j=1:gene_number
118 -                 gene(j,i,loop)=0;
119 -                 bookmark=1;
120 -                 for k=gene_start(j)+1:gene_start(j+1)-1
121 -                     place=decimal(j)-bookmark;
122 -                     gene(j,i,loop)=gene(j,i,loop)+(pop(k,i))*10^place;
123 -                     bookmark=bookmark+1;
124 -                 end
125 -             end
126 -         end
127 -     end
```

***Figure 6.** Software design in a MATLAB environment (Part 3)*

```
128 -         t=0:0.01:10;
129 -         pay2=[response(1,1) response(2,1) response(3,1)];
130 -         payda2=[1 0];
131 -         sis2=tf(pay2,payda2);
132 -         sistop=series(sis1,sis2);
133 -         new_sis=feedback(sistop,1);
134 -         y=step(new_sis,t);
135 -         plot(t,y,'r:');
136 -         hold on
137 -         pay_2=[0.029 2.84 37.6];
138 -         payda_2=[1 0];
139 -         sis_2=tf(pay_2,payda_2);
140 -         sis_top=series(sis1,sis_2);
141 -         new_sis_=feedback(sis_top,1);
142 -         [y,x]=step(new_sis_,t);
143 -         plot(t,y,'g-');
```

***Figure 7.** Software design in a MATLAB environment (Part 4)*

6. MANUAL SOLUTION FOR A SINGLE ITERATION

In this section, the process of a single iteration of the system is demonstrated. Consider a system with three chromosomes, and assume that the first genes are generated by MATLAB as follows:

$$K_D = 13.5162; \quad 27.4001; \quad 16.1503$$

$$K_P = 2.5146; \quad 4.5713; \quad 29.8840$$

$$K_I = 6.8693; \quad 24.7745; \quad 2.3453$$

Then the calculation of the start and end points of the genes will subsequently be performed by the software.

$$gene\_start = 1 \quad 8 \quad 15 \quad 22$$

After the start and end points are determined, a gene pool equivalent to the length of the system is created.

$$chromosome\ 1 = 9135162; \quad 9025146; \quad 9068693$$

$$chromosome\ 2 = 9274001; \quad 9045713; \quad 9247745$$

$$chromosome\ 3 = 9161502; \quad 9298840; \quad 9023452$$

As evident from the gene pool, a value of 9 has been assigned to the starting bits, which are positive. If the signs were negative, the sign bits would have been 0. Subsequently, the objective function and fitness function are calculated for these chromosomes.

$$objective\ function = 2.2370; \quad 1.5646; \quad 0.5798$$

$$fitness = 0.4470; \quad 0.6392; \quad 1.7246$$

After calculating the fitness values, the well-performing genes are selected using the roulette wheel selection method, and a crossover pool is generated. This pool is stored in a matrix called parent_chrom.

$$chromosome\ 3 = 9161502; \quad 9298840; \quad 9023452$$

$$chromosome\ 1 = 9135162; \quad 9025146; \quad 9068693$$

$$chromosome\ 3 = 9161502; \quad 9298840; \quad 9023452$$

As can be seen, the well-performing genes are placed into the gene pool named parent_chrom. Subsequently, the crossover process takes place, and chromosomes are randomly selected and transferred to the child matrix from randomly chosen positions. This results in a gene exchange among the chromosomes.

After this process, the mutation stage is initiated, and it is decided whether each gene will undergo a mutation at a rate of 0.01. If a gene is to be mutated, a number between 0 and 10 is randomly generated and substituted for the corresponding gene. The resulting gene pool after mutation is as follows:

$$chromosome\ 3 = 9161502; \quad 9298840; \quad 9023452$$

$$chromosome\ 1\&3 = 9135162; \quad 90//98840; \quad 9023452$$

$$chromosome\ 3 = 9161502; \quad 9298840; \quad 9023452$$

Subsequently, the chromosomes named child undergo a mutation with a probability of 0.01. The resulting chromosomes after mutation are as follows:

$$new\ chromosome\ 1 = 9161502;\ \ 9298840;\ \ 9023452$$

$$new\ chromosome\ 2 = 9135162;\ \ 9098840;\ \ 9023452$$

$$new\ chromosome\ 3 = 9161502;\ \ 9298840;\ \ 9023452$$

If it is examined the new chromosomes, none of the bits have undergone a mutation with a probability of 0.01. However, this does not necessarily mean that there will never be any mutations. There were no mutations in the first generation.

After the mutation process, the chromosomes in this gene pool are converted to parameters and the second generation begins. After this step, the parameter values will be as in Table 3.

Table 3. PID parameters obtained from the first generation

	Chromosome 1	Chromosome 2	Chromosome 3
K_D	16.1502	13.5162	16.1502
K_P	29.8840	9.8840	29.8840
K_I	2.3452	2.3452	2.3452

7. RESULTS

The step responses of conventional PID and GA tuned PID are given in Figure 8. As calculated in the third section, parameters $K_D = 0.029$, $K_P = 2.84$ and $K_I = 37.6$ are selected for the conventional PID controller. Besides, when the GA-based PID tuning algorithm given in section 5 is run, the obtained PID parameters are $K_D = 0.012$, $K_P = 5$ and $K_I = 36.4872$, respectively. As can be seen from the figure, the parameters obtained from the GA-based PID algorithm are superior to the conventional PID calculation method in terms of overshoot and settling time.
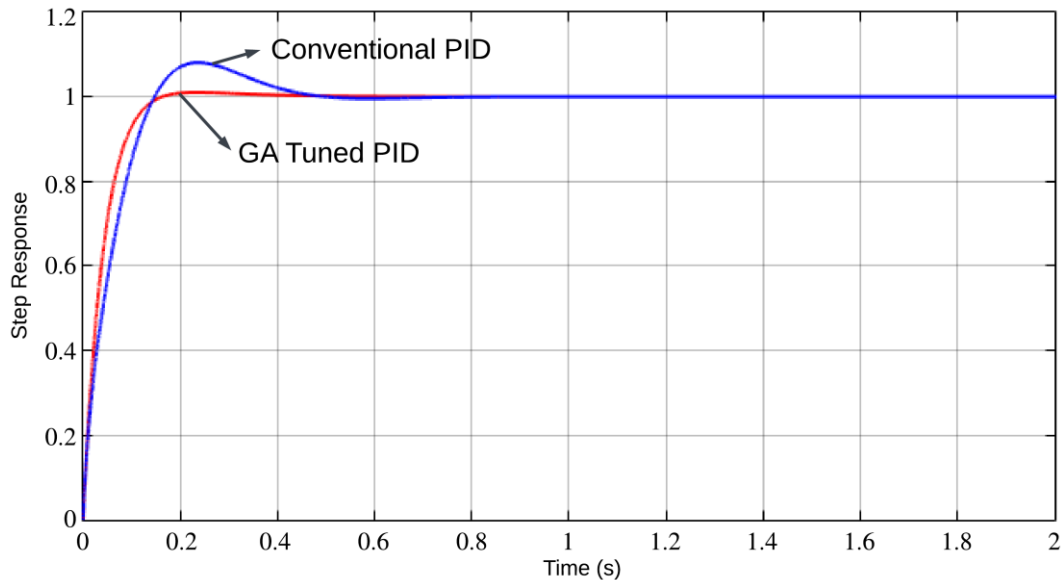
Figure 8. Step responses of conventional PID and GA-based PID control methods

The multi-step responses of conventional PID and GA-based PID is given in Figure 9. The same parameters as above are used for both conventional PID and GA-based PID. As can be seen from the figure, the parameters obtained from the GA-based PID algorithm are superior to the conventional PID calculation method in terms of overshoot and settling time for all unit steps.
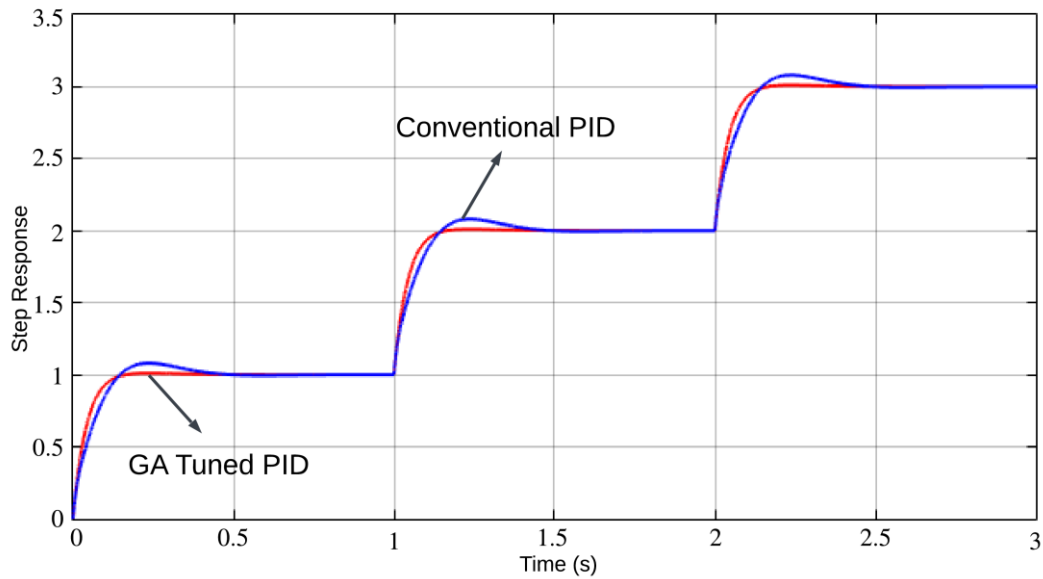
Figure 9. Multi-step responses of conventional PID and GA-based PID control methods

The step responses of conventional PID and two GA-based PID are given in Figure 10. Derivative, proportional and integral terms ($K_D = 0.029$, $K_P = 2.84$, $K_I = 37.6$) are selected for the conventional PID controller. Moreover, $K_D = 0.012$, $K_P = 5$ and $K_I = 36.4872$ are obtained GA-based PID tuning algorithm when the population size is 50 and iteration is 40 (response 1) and $K_D = 0$, $K_P = 5$ and $K_I = 34.1696$ are obtained when the population size is 100 and iteration is 80 (response 2), respectively. As can be seen from the figure, the algorithm gives better results in terms of overshoot and settling time as the number of populations and iterations increase. Moreover, all the parameters obtained from the GA-based PID algorithm are superior to the conventional method.
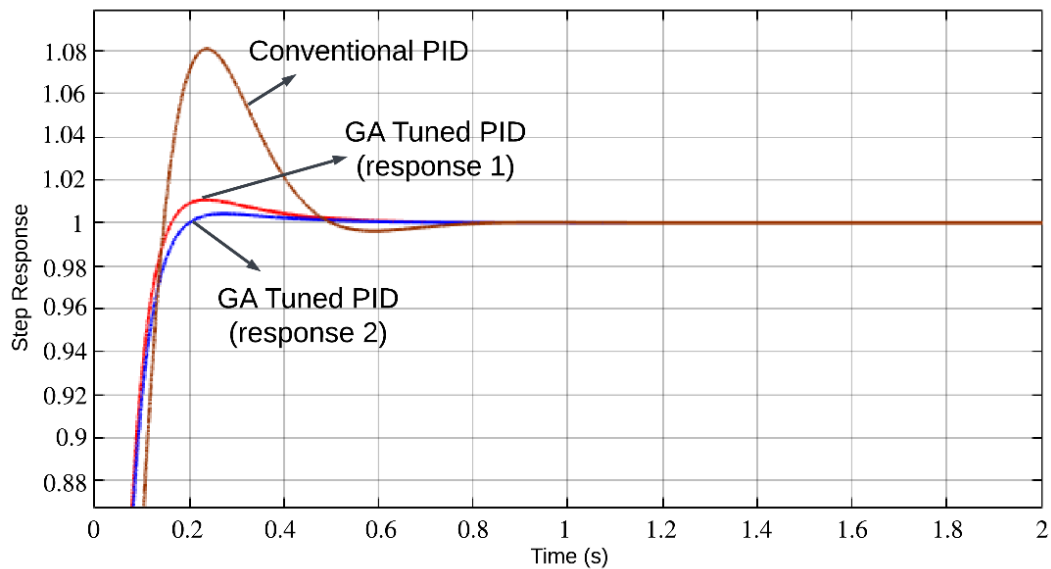
Figure 10. Step response of conventional and two GA-based PID control methods

The step response of conventional PID and GA tuned PID to the limitation of derivative, proportional and integral terms is given in Figure 11. In this simulation, all parameters are limited in the range of 0-50. Therefore, $K_D = 14.0465$, $K_P = 45.9608$ and $K_I = 50$ are obtained GA-based PID tuning algorithm when the population size is 50 and iteration is 40. Whereas, in all previous simulations, this limitation was set to $0 < K_D < 5$, $0 < K_P < 5$ and $0 < K_I < 50$. When the limits of the derivative and proportional terms are increased, the system responds quickly, but the settling time to the reference is too long. Therefore, the

boundaries of the terms specified in the algorithm should be evaluated separately for each system and appropriate limitations should be selected.
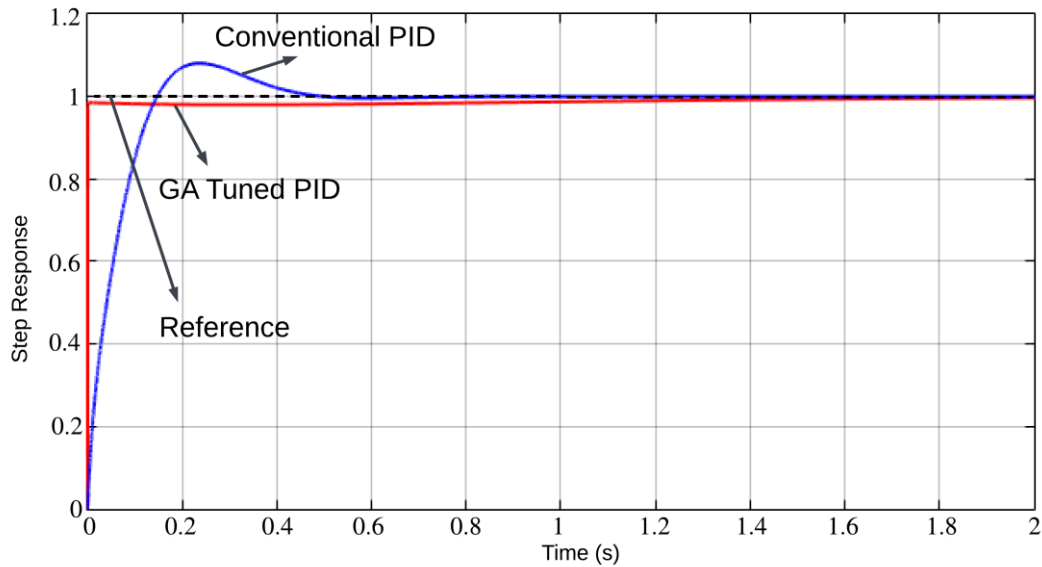
Figure 11. *Step response of conventional and GA tuned PID based DC motor*

Finally, the ramp signal responses of conventional PID and GA-based PID are given in Figure 12. Derivative, proportional and integral terms ($K_D = 0.029$, $K_P = 2.84$, $K_I = 37.6$) are selected for the conventional PID controller. Moreover, $K_D = 0.025$, $K_P = 3.95$ and $K_I = 43.832$ are obtained GA-based PID tuning algorithm when the population size is 50 and iteration is 40. As can be seen from the figure, the algorithm gives better results than conventional method in terms of overshoot and steady state error.
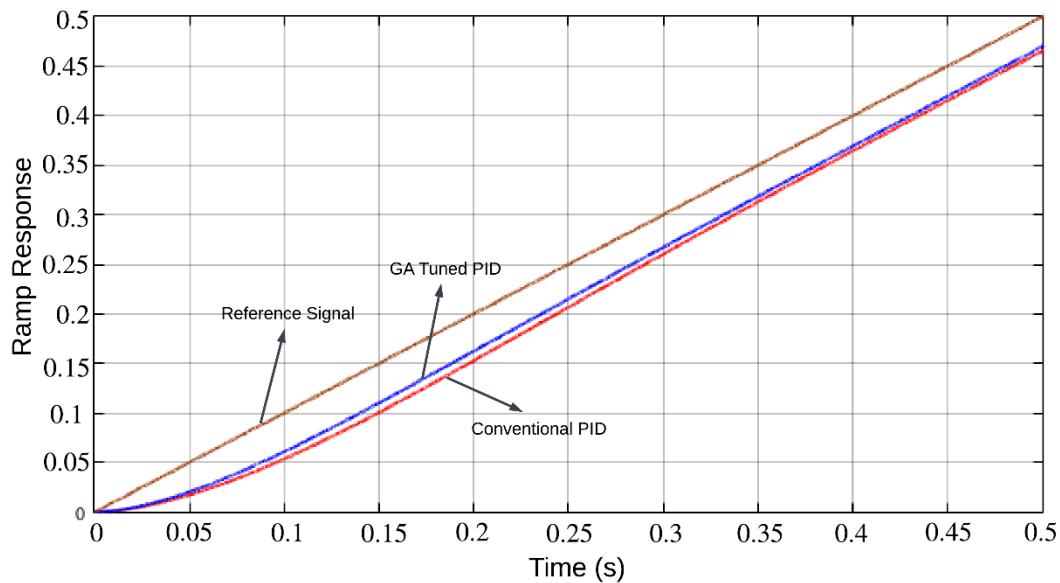
Figure 12. *Ramp signal response of conventional and GA tuned PID methods*

8. CONCLUSION

In this paper, GA based PID tuning software design and implementation for a DC motor control system is presented. To optimize the performance of DC motor control system, the proposed software architecture automates the process of adjusting proportional, integral, and derivative gains.

The output of the optimal proportional-integral-derivative (PID) parameters is examined following the conclusion of 40 iteration runs in a 50 population system. The overshoot is shortened, the steady-state error is minimized, and the settling time is greatly decreased, according to the GA-enhanced system. A comprehensive analysis of these results confirms that the PID-developed systems implemented in the industry can yield highly favorable outcomes. It is worth noting that increasing the generation and population size within the system could lead to even greater optimization of the outcomes. However, it is also necessary to take into account the fact that such increases will inevitably lead to a significant increase in processing time, potentially prolonging solution times.

CONFLICT OF INTEREST

The author declares no conflict of interest.

REFERENCES

Alruim Alhasan, H., & Güneş, M. (2017). A New Adaptive Particle Swarm Optimization Based on Self-Tuning of PID Controller for DC Motor System. *Çukurova University Journal of the Faculty of Engineering and Architecture, 32*(3), 243-249.

Aranza, M. F., Kustija, J., Trisno, B., & Hakim, D. L. (2016). Tunning PID controller using particle swarm optimization algorithm on automatic voltage regulator system. *IOP Conference Series: Materials Science and Engineering*, *128*, 012038. doi:10.1088/1757-899X/128/1/012038

Borase, R. P., Maghade, D. K., Sondkar, S. Y., & Pawar, S. N. (2021). A review of PID control, tuning methods and applications. *International Journal of Dynamics and Control*, *9*(2), 818-827. doi:10.1007/s40435-020-00665-4

Fang, H., Zhou, J., Wang, Z., Qiu, Z., Sun, Y., Lin, Y., Chen, K., Zhou, X., & Pan, M. (2022). Hybrid method integrating machine learning and particle swarm optimization for smart chemical process operations. *Frontiers of Chemical Science and Engineering*, *16*(2), 274-287. doi:10.1007/s11705-021-2043-0

de Figueiredo, R., Toso, B., & Schmith, J. (2023). Auto-Tuning PID Controller Based on Genetic Algorithm. In: M. Shamsuzzoha & G. L. Raja (Eds.), *Disturbance Rejection Control*. IntechOpen. doi:10.5772/INTECHOPEN.110143

Flores-Morán, E., Yánez-Pazmiño, W., Espín-Pazmiño, L., Carrera-Manosalvas, I., & Barzola-Monteses, J. (2020, October 13-16). *Particle Swarm Optimization and Genetic Algorithm PID for DC motor position controllers*. In: Proceedings of the 2020 IEEE ANDESCON, Quito, Ecuador. doi:10.1109/ANDESCON50619.2020.9272127

Galotto, L., Pinto, J. O. P., Bottura Filho, J. A., & Lambert-Torres, G. (2007, November 5-8). *Recursive least square and genetic algorithm based tool for PID controllers tuning*. In: Proceedings of the 2007 International Conference on Intelligent Systems Applications to Power Systems (ISAP), Kaohsiung, Taiwan. doi:10.1109/ISAP.2007.4441623

Ibrahim, O., Yahaya, N. Z. B., & Saad, N. (2016). PID Controller Response to Set-Point Change in DC-DC Converter Control. *International Journal of Power Electronics and Drive Systems (IJPEDS)*, *7*(2), 294-302. doi:10.11591/IJPEDS.V7.I2.PP294-302

Islam, Md. T., Karim, S. M. R., Sutradhar, A., & Miah, S. (2020). Fuzzy Logic and PID Controllers for DC Motor Using Genetic Algorithm. *International Journal of Control Science and Engineering*, *10*(2), 37-41. doi:10.5923/J.CONTROL.20201002.03

Jayachitra, A., & Vinodha, R. (2014). Genetic Algorithm Based PID Controller Tuning Approach for Continuous Stirred Tank Reactor. *Advances in Artificial Intelligence*, *2014*, 791230. doi:10.1155/2014/791230

Korkmaz, M., Aydoğdu, Ö., & Doğan, H. (2012, July 2-4). *Design and performance comparison of variable parameter nonlinear PID controller and genetic algorithm based PID controller*. In: Proceedings of the 2012 International Symposium on Innovations in Intelligent Systems and Applications (INISTA), Trabzon, Türkiye. doi:10.1109/INISTA.2012.6246935

Taşören, A. E. (2021). Design and Realization of Online Auto Tuning PID Controller Based on Cohen-Coon Method. European *Journal of Science and Technology*, 24 (Special Issue), 235-239. doi:10.31590/ejosat.897727

Malhotra, R., Singh, N., & Singh, Y. (2011). Genetic Algorithms: Concepts, Design for Optimization of Process Controllers. *Computer and Information Science*, *4*(2), 39-54. doi:10.5539/CIS.V4N2P39

Martinez-Soltero, E. G., & Hernandez-Barragan, J. (2018). Robot Navigation Based on Differential Evolution. *IFAC-PapersOnLine*, *51*(13), 350-354. doi:10.1016/J.IFACOL.2018.07.303

Meena, D. C., & Devanshu, A. (2017, January 19-20). *Genetic algorithm tuned PID controller for process control*. In: Proceedings of the 2017 International Conference on Inventive Systems and Control (ICISC), Coimbatore, India. doi:10.1109/ICISC.2017.8068639

Patel, V. V. (2020). Ziegler-Nichols Tuning Method: Understanding the PID Controller. *Resonance*, *25*(10), 1385-1397. doi:10.1007/s12045-020-1058-z

Pereira, D. S., & Pinto, J. O. P. (2005, July 24-28). *Genetic Algorithm based system identification and PID tuning for optimum adaptive control*. In: Proceedings of the 2005 IEEE/ASME International Conference on Advanced Intelligent Mechatronics, Monterey, CA, USA, (pp. 801-806). doi:10.1109/AIM.2005.1511081

Rout, U. K., Sahu, R. K., & Panda, S. (2013). Design and analysis of differential evolution algorithm based automatic generation control for interconnected power system. *Ain Shams Engineering Journal*, *4*(3), 409-421. doi:10.1016/J.ASEJ.2012.10.010

Saad, M. S., Jamaluddin, H., & Darus, I. Z. M. (2012). Implementation of PID controller tuning using differential evolution and genetic algorithms. *International Journal of Innovative Computing Information and Control*, 8(11), 7761-7779.

Tiwari, S., Bhatt, A., Unni, A. C., Singh, J. G., & Ongsakul, W. (2018, October 24-26). *Control of DC Motor Using Genetic Algorithm Based PID Controller*. In: Proceedings of the 2018 International Conference and Utility Exhibition on Green Energy for Sustainable Development (ICUE), Phuket, Thailand. doi:10.23919/ICUE-GESD.2018.8635662

Wati, D. A. R., & Hidayat, R. (2013, November 25-27). *Genetic algorithm-based PID parameters optimization for air heater temperature control*. In: Proceedings of the 2013 International Conference on Robotics, Biomimetics, Intelligent Computational Systems (ROBIONETICS), Jogjakarta, Indonesia, (pp. 30-34). doi:10.1109/ROBIONETICS.2013.6743573

An Investigation of the Impact of Distributed Generation Penetration on Directional Overcurrent Relay Coordination in a Distribution Network

Alisan AYVAZ[1*] iD

[1]Amasya University, Faculty of Engineering, Department of Electrical and Electronics Engineering, Amasya, Türkiye

Keywords	Abstract
DOCR Coordination Distributed Generators Voltage Profile Improvement Power Loss Reduction Gazelle Optimization Algorithm	Distributed generation units (DGs) are rapidly becoming widespread in distribution systems due to their advantages such as power loss reduction, voltage profile improvement, and economic returns. Many researchers seek new ways to maximize their these advantages. However, their impact on the fault current is a problem for the field of power system protection. The changes in the short-circuit currents due to DGs cause the miscoordination of the directional overcurrent relays (DOCRs). In this paper, the impact of distribution generation penetration on DOCR coordination is analyzed and investigated. Besides this negative impact of DGs, their contributions to reducing power loss and improving the voltage profile are also analyzed for different DG penetration levels. The gazelle optimization algorithm is utilized to solve the DOCR coordination problem studied in this paper. The method is performed on the distribution section of the IEEE 14-bus system. It is seen that a significant number of miscoordinations occur when even the DG penetration is increased by about 10%. With the increase in DG penetration, the number of miscoordinations does not increase proportionally, but there is a proportional increase in active and reactive power loss reduction and voltage profile improvement.

1. INTRODUCTION

Power system protection is being studied intensively by researchers as an important issue in order to deliver energy to consumers in a reliable way, to prevent damage to the power system due to possible short-circuit faults, and to avoid unnecessary energy interruptions in case of short-circuit faults. Among the power system protection elements, relays play the most important role in detecting the fault and taking the necessary action against the fault. Especially directional overcurrent relays (DOCRs) are commonly used in transmission and distribution networks due to their economic advantages (Shih et al., 2014). Directional overcurrent relays can be used for both primary (main) protection and secondary (backup) protection duties in power systems. The purpose of secondary protection is to provide a backup protection mechanism against failures that may occur in primary protection (Perveen et al., 2016). The important point here is that a certain time difference between the operating times of the relays in the primary and secondary protection duties, which is called coordination time interval (CTI), should be preserved for all relay pairs in the power system (Ayvaz, 2022). The CTI value is usually taken into account as a minimum of 0.3 seconds for electromechanical relays and a minimum of 0.1 seconds for digital relays. The main aim of solving the DOCR coordination problem is to reach the minimum total operating time of the relays without any violation of CTI values for all relay pairs.

The DOCR coordination problem is a non-linear optimization problem that has been solved by several optimization methods. These methods can be classified as mathematical programming methods, meta-heuristic

*Corresponding Author, e-mail: alisan.ayvaz@amasya.edu.tr

methods, and hybrid methods. Considering the recent studies, meta-heuristic optimization methods are popular methods that have been utilized to solve the DOCR coordination problem. Some of them are seagull optimization algorithm (SOA) (Abdelhamid et al., 2022), slime mould algorithm (SMA) (Draz et al., 2021), and jaya algorithm (JA) (Yu et al., 2019). The difficulty of solving the DOCR problem can be changeable based on the power system structure. For example, in radial systems, one relay in secondary protection generally corresponds to one relay in primary protection duty. This is different for meshed systems and more than one relay can be used for backup protection.

Distributed generation units (DGs) are used in distribution networks in renewable and non-renewable forms. Further, they can be classified according to their connection types as synchronous and inverter-based. Especially synchronous DGs have the most important position in the field of power system protection (Saleh et al., 2015). The effect of synchronous DGs on the fault current is much more than the inverter-based DGs (Ayvaz & Istemihan Genc, 2020). The synchronous DGs can change the direction and magnitude of the fault currents and cause the miscoordination of relays. In the literature, there are many published studies that propose new approaches to solve the DOCR coordination problem for distribution networks with DGs. The study carried out by Elmitwally et al. (2020) aims to find the optimal locations and sizes of fault current limiting devices taking into account the DOCR coordination on a power system with DGs. Narimani and Hashemi-Dezaki (2021) propose a new coordination method considering the stability of DGs. However, to the best of the Author's opinion, no study analyzes the number of DOCR coordination violations, power loss reduction, and voltage profile improvement for different DG penetration levels.

In this paper, an investigation study is proposed to analyze the impact of DG penetration on DOCR coordination, reduction in active and reactive power losses, and voltage profile improvement for a distribution network. To solve the DOCR coordination problem studied in this paper, the gazelle optimization algorithm (GOA) (Agushaka et al., 2023) is used. GOA is a recent meta-heuristic method inspired by the survival behavior of gazelles. GOA has been used for solving many other engineering problems, i.e. data clustering (Abualigah et al., 2022), and has shown superior performance.

The rest of the paper is organized as follows: the DOCR coordination problem formulation, power loss calculation function, and voltage deviation function are given in Section 2, the optimization results and the investigations based on these results are presented in Section 3, and Section 4 provides the conclusions.

2. MATERIAL AND METHOD

The objective function of the DOCR coordination problem considered in this study is given by (1).

$$OF = \sum_{m} \sum_{k=1}^{N} T_{k,m} \tag{1}$$

where, N is the total relay number in the distribution network. $T_{k,m}$ are the operation time of the relay k for the fault case m, respectively, and is calculated by using (2).

$$T_{k,m} = TMS_k \times \frac{\alpha}{\left(I_{f_m}/PS_k\right)^{\beta} - \gamma} \tag{2}$$

where, I_{f_m} is the fault current passing through the relay k for the fault case m, TMS_k expresses the time multiplier setting parameter of the relay k, and $\alpha, \beta,$ and γ are constants that determine the relay characteristic and take the values 0.14, 0.02, and 1, respectively, in general (Yu et al., 2019). PS_k is the time multiplier setting of the relay r.

The constraints of the DOCR problem are presented in (3)-(6).

$$CTI \leq T^{backup} - T^{main} \tag{3}$$

$$T_k^{min} \leq T_k \leq T_k^{max} \tag{4}$$

$$PS_k^{min} \leq PS_k \leq PS_k^{max} \tag{5}$$

$$TMS_k^{min} \leq TMS_k \leq TMS_k^{max} \tag{6}$$

The DOCR problem given by (1)-(6) is solved for a base DG penetration level using the gazelle optimization algorithm. This solution gives the optimal relay parameters, i.e. PS_k and TMS_k for all the relays in the system. Once the optimal solution is obtained for the base DG penetration level, i.e. 10% of the system's total power demand, the number of violations in DOCR coordination can be obtained for higher DG penetration levels to investigate the impact of DG penetration on the DOCR coordination. Further, the system's voltage profile and power loss are also obtained and analyzed for different DG penetration levels. Then, the variations in voltage profile, power loss, and the violation number corresponding to the increased DG penetration level are compared and investigated. To investigate the voltage profile improvement numerically, the voltage deviation function, as defined in (7), is used.

$$VD = \sum_{i=1}^{N_B}(1 - |V_i|)^2 \tag{7}$$

where, V_i is the voltage of ith bus (p.u.) and N_B is the number of buses in the power system.

On the other hand, the active and reactive power loss calculation formulas are given in (8) and (9), respectively.

$$\Delta P_{loss} = \sum P_{G\_tot} - \sum P_{D\_tot} \tag{8}$$

$$\Delta Q_{loss} = \sum Q_{G\_tot} - \sum Q_{D\_tot} \tag{9}$$

where, P_{G_tot}, P_{D_tot}, Q_{G_tot} and Q_{D_tot} are the total active power generation, total active power demand, total reactive power generation, and total reactive power demand in the system, respectively.

3. RESULTS AND DISCUSSION

The proposed study is performed on the distribution section of the IEEE 14-bus test system. The detailed system data can be found on the website Christie (1993). The system is modified by adding DGs to buses 6 and 7. The single-line diagram of the modified system is shown in Figure 1. It is assumed that each DG is synchronous type, has 5 MVA capacity, is normally operated at 0.9 at a lagging power factor, and has a 10% transient reactance. The total DG penetration is 10 MVA which corresponds to almost 10% of the total power demand of the system. In addition, each of them is connected to the system through a 20 MVA substation transformer with a 5% reactance. The short circuit power of the grid, i.e. slack bus, is assumed to be 500 MVA. The power flow analysis is performed using the Newton-Raphson method. The short-circuit calculations are made assuming a bolted three-phase-to-ground fault at the midpoint of the line. To calculate the fault currents, the bus impedance matrix (Z_{bus}) method is used (Grainger & Stevenson, 1994).

The control parameters of the GOA are used as their recommended settings given in (Agushaka et al., 2023). The maximum iteration number and population size are set to 1000 and 300, respectively. All the simulations and calculations are performed using MATLAB software. The upper and lower bounds of PS_k are calculated as follows (Fayoud et al., 2022):

$$1.25 \times I_{max\_load} \leq PS_k \leq (2/3) \times I_{min\_sc} \tag{10}$$

where, I_{min_sc} and I_{max_load} are the minimum fault current and maximum load current passing through the relay k, respectively. PS_k^{min} and PS_k^{max} are considered 0.5 and 2.5, respectively. TMS_k^{min} and TMS_k^{max} are

set to 0.05 and 1.1, respectively. The current transformer ratio of relays (R1, R2, R3, R6, R7, R10, R12, R13, R14, R16) and (R4, R5, R8, R9, R11, R15) is considered to be 300:1 and 100:1, respectively. For all the relay pairs, *CTI* is selected for 0.1 seconds.

In Table 1, the short circuit results are given for all the relay pairs. Since the pickup current of the backup relays R10 and R16 are higher than 2/3 of the fault currents passing through them, the corresponding relay pairs in Table 1 are ignored. Using the fault currents given in Table 1, the problem given by (1)-(6) is solved. The optimization results are presented in Table 2. The convergence curve of GOA for searching the minimum total relay operating time is seen in Figure 2. The total operating time is 22.9557 sec and there is no coordination violation for 10% DG penetration as a base case. Besides this level of DG penetration, 20% and 30% DG penetration levels are also considered for the investigations and analyses. The values of evaluation metrics considered in this study are given in Table 3 for different DG penetration levels. According to Table 3, the violation number of coordination is 7 and 8 for 20% and 30% DG penetration levels, respectively. It should be noted that, for 20% and 30% DG penetration levels, the problem given by (1)-(6) is not solved again and the relay settings obtained for 10% DG penetration level are considered. It can be interpreted that the DG penetration increases cause the higher fault currents and thus the coordination violations occur. Even a 10% change in DG penetration is enough to cause serious violations in coordination. In Table 4, the CTI values of relay pairs for different DG penetration levels are shown. The CTI values increase with the increase of penetration level for some relay pairs while they decrease for others. The relay pairs (R1, R3), (R2, R7), (R4, R2), (R9, R13), (R12, R10), (R14, R6), and (R16, R11) are priority relay pairs that cause coordination violations when the changes in DG penetration occur.
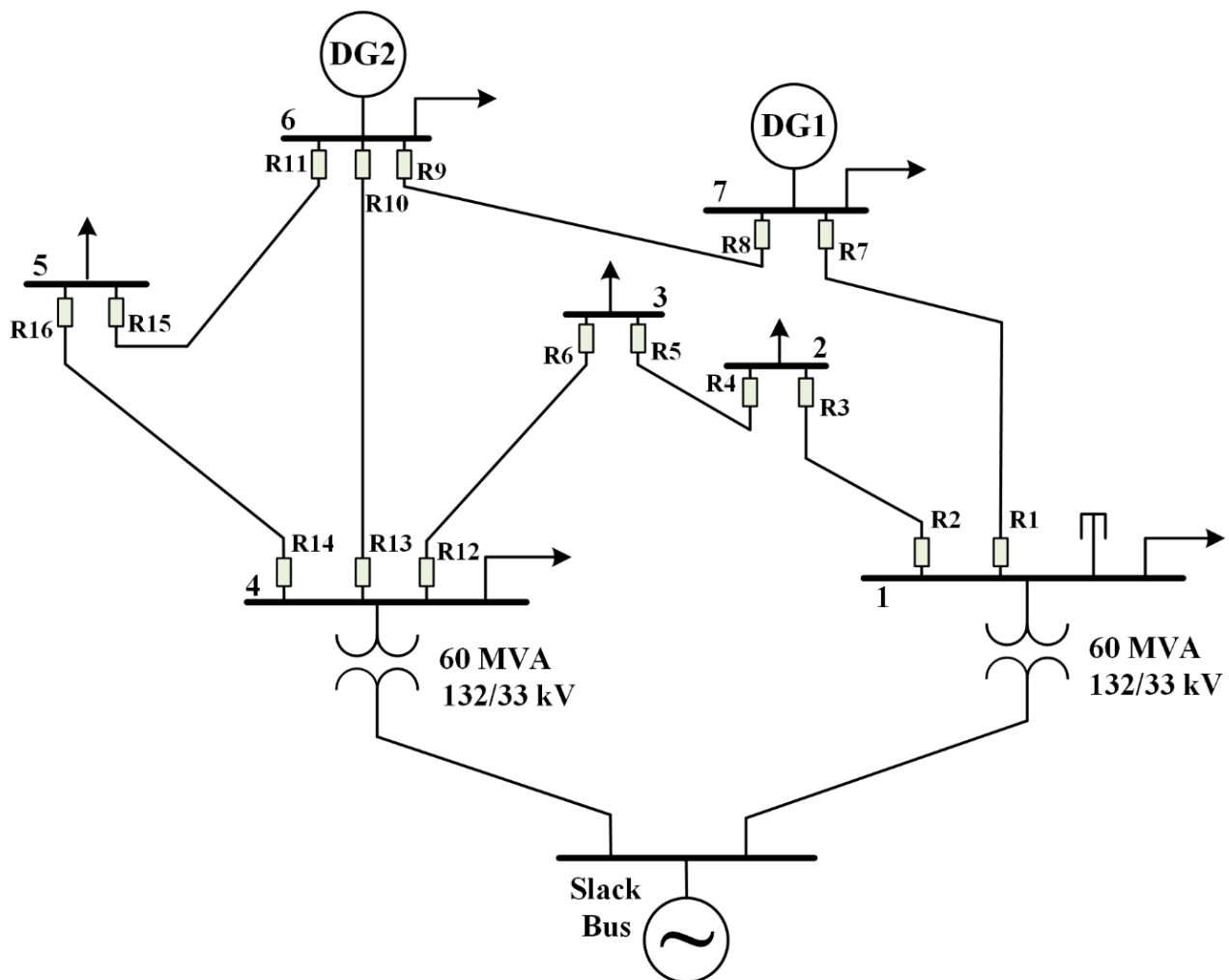
***Figure 1.** The modified IEEE 14-bus distribution system*

On the other hand, the total operating time decreases with the increase in DG penetration. This is because the high fault current reduces the relay's operating time according to (1). However, the reduction in total operating time causes the violations in coordination due to the occurrence of CTI values less than 0.1 sec as seen in Table 4. Considering the relay pair (R2, R7), the CTI is 0.8191 sec which is much higher than the limit value of 0.1 sec. However, with a 10% increase in DG penetration, for the relay pair (R2, R7), the CTI takes a negative value, i.e. -0.1248 sec, and a coordination violation occurs. Even this result alone shows the importance of analyzing the DG penetration on relay coordination.

Similar to the total operating time, the voltage deviation and power losses also reduce with the increase in DG penetration. The effect of DG penetration on active power loss is clearly visible. The active power loss reduces from 0.368 to 0.129 MW, which corresponds to a 65% variation when the DG penetration increases from 10% to 30%.

Table 1. *Fault currents passing through the main and backup relays*

Primary Relay	Current of Primary Relay (A)	Backup Relay	Current of Backup Relay (A)
R1	3380	R3	546
R2	4550	R7	948
R3	1311	R5	1311
R4	2906	R2	2906
R5	2115	R12	2115
R6	1599	R4	1599
R7	1790	R9	1133
R8	2048	R1	1442
R9	2663	R13	1680
R9	2663	R15	430
R10	1961	R8	1000
R10	1961	R15	250
R11	3097	R8	932
R11	3097	R13	1561
R12	3833	R10	758
R12	3833	R16	194*
R13	3907	R6	742
R13	3907	R16	220*
R14	3681	R6	678
R14	3681	R10	102*
R15	1596	R14	1596
R16	1224	R11	1224
*2/3 of the current value is lower than the relay's pickup current			

Table 2. *Optimal relay settings*

Relay	TMS	PS
R1	0.206	0.621
R2	0.296	0.760
R3	0.084	0.782
R4	0.401	0.509
R5	0.325	0.500
R6	0.119	0.560
R7	0.050	2.500
R8	0.187	1.578
R9	0.261	0.700
R10	0.143	0.897
R11	0.125	0.527
R12	0.376	0.500
R13	0.146	1.049
R14	0.222	0.545
R15	0.248	0.500
R16	0.050	0.526
OF (total operating time) = 22.9557 sec		
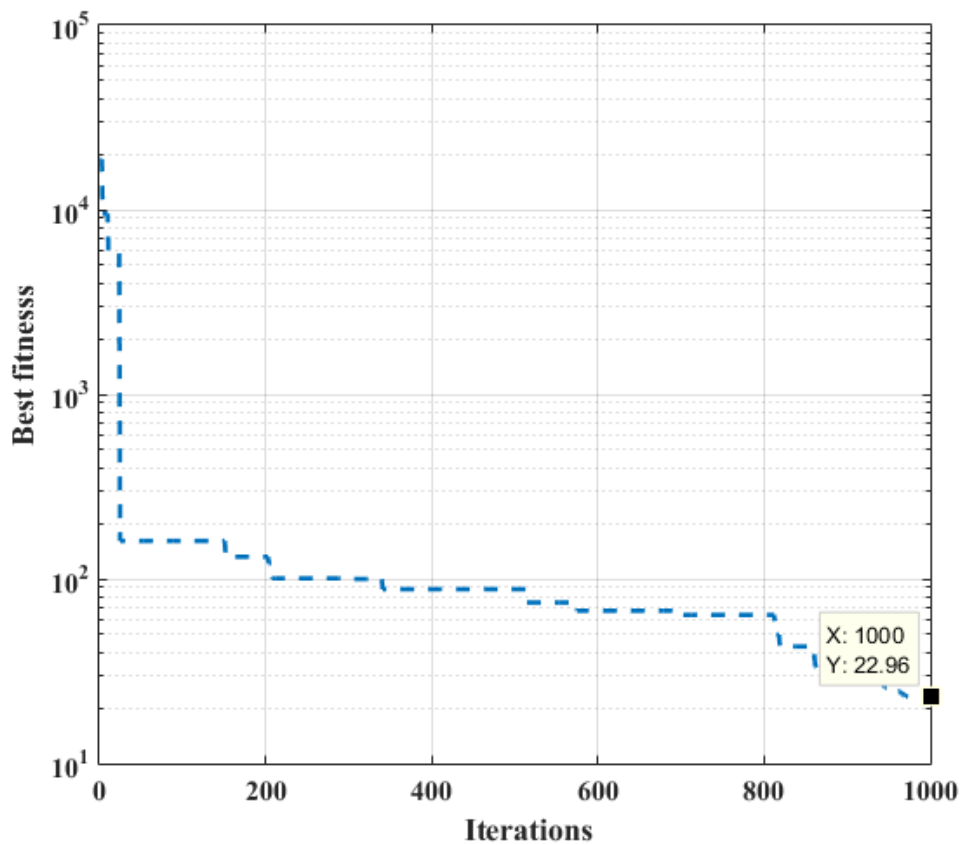
Figure 2. *The GOA convergence curve for searching the minimum total relay operating time*

Table 3. The evaluation metrics obtained for different DG penetration levels

Item	DG Penetration Level		
	10% (base case)	20%	30%
The Number of Violations in CTI	0	7	8
OF (sec)	22.9557	22.1752	22.1351
VDI (volt)	0.0120	0.0112	0.0105
ΔP_{loss} (MW)	0.368	0.204	0.129
ΔQ_{loss} (MVAr)	13.265	11.036	10.088

On the other hand, for the same increase that occurred in DG penetration, the voltage deviation reduces from 0.0120 to 0.0105 V, which corresponds to a 13% variation. However, considering the buses in the system individually, it can be interpreted that the increase in DG participation is quite effective in improving the voltage level of some buses. Figure 3 demonstrates the voltage profile of the system for different DG penetrations. The bus numbered 8 is the slack bus. From Figure 3, it is seen that, for buses 4, 5, 6, and 7, the voltage profile is significantly improved by increasing the DG penetration level. Especially considering the DG buses, i.e. buses 6 and 7, the voltage variation is higher than that of others. The numerical and graphical analyses show that power quality problems can be overcome by integrating DGs into modern power systems, especially in terms of voltage deviation and power losses. However, the DGs have a negative impact on protection coordination. For occurring coordination violations, there is no need for the highest DG penetration. Significant violations in coordination may even occur for low DG penetrations. Therefore, there is a need for new approaches to provide reliable DOCR coordination considering the DGs, which are increasingly common in modern power systems.

Table 4. CTI values of relay pairs for different DG penetration levels

Primary Relay	Backup Relay	DG Penetration Level		
		10%	20%	30%
R1	R3	0.2125	-0.0418	-0.0547
R2	R7	0.8191	-0.1248	-0.2080
R3	R5	0.3351	0.3358	0.3352
R4	R2	0.1277	0.0850	0.0800
R5	R12	0.3833	0.4262	0.4119
R6	R4	0.4231	0.3973	0.3941
R7	R9	0.2395	0.3931	0.4805
R8	R1	0.1900	0.5969	0.8361
R9	R13	0.1167	0.0470	0.0548
R9	R15	0.3038	0.2230	0.2304
R10	R8	0.2024	0.2134	0.2281
R10	R15	0.5644	0.3390	0.2995
R11	R8	0.5198	0.5391	0.5161
R11	R13	0.4233	1.2470	1.8760
R12	R10	0.1731	0.0422	-0.0878
R13	R6	0.1576	0.1012	0.0926
R14	R6	0.1060	0.0474	0.0420
R15	R14	0.1841	0.1281	0.1239
R16	R11	0.1014	0.0868	0.0950
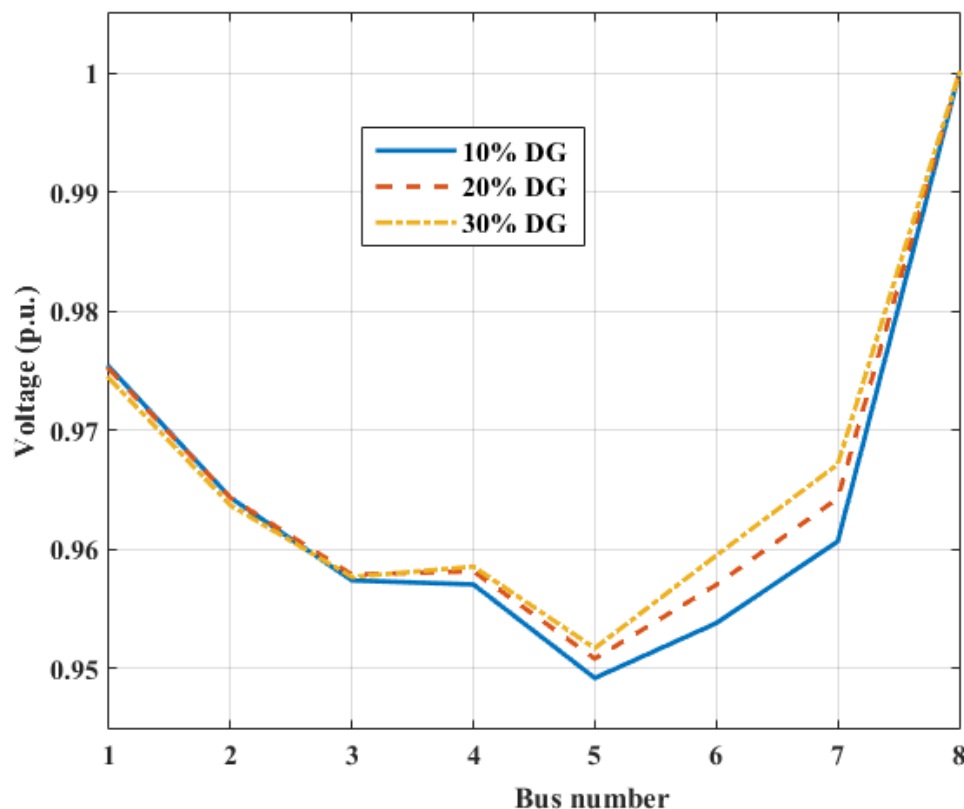
Figure 3. Voltage profile of the system for different DG penetration levels

4. CONCLUSION

In this paper, a novel investigation study is performed to evaluate the impact of DG penetration on DOCR coordination and power quality issues. First, the DOCR coordination problem is solved by using the base DG penetration level which corresponds to 10% of the total power demand of the considered distribution system. Based on this solution, the optimal relay settings are found without violating the CTI for all relay pairs. Then, for higher DP penetration levels, the number of coordination violations is obtained. It is shown that even a 10% increase in DG penetration causes a significant number of coordination violations. On the other hand, considering power quality issues, the more the DG penetration is increased, the more the voltage profile is improved and power losses are reduced. To provide reliable and accurate DOCR coordination and to overcome power quality issues, new coordination approaches are needed. The increase in DG penetration should not only be considered as the integration of new DGs into the system but also as intraday fluctuations in the power generation of renewable energy-based DGs. Therefore, there is a need for new DOCR coordination solutions that cover the DG's effect on coordination issues.

CONFLICT OF INTEREST

The author declares no conflict of interest.

REFERENCES

Abdelhamid, M., Houssein, E. H., Mahdy, M. A., Selim, A., & Kamel, S. (2022). An improved seagull optimization algorithm for optimal coordination of distance and directional over-current relays. *Expert Systems with Applications*, *200*, 116931. doi:10.1016/j.eswa.2022.116931

Abualigah, L., Diabat, A., & Zitar, R. A. (2022). Orthogonal learning Rosenbrock's direct rotation with the gazelle optimization algorithm for global optimization. *Mathematics*, *10*(23), 4509. doi:10.3390/math10234509

Agushaka, J. O., Ezugwu, A. E., & Abualigah, L. (2023). Gazelle optimization algorithm: a novel nature-inspired metaheuristic optimizer. *Neural Computing and Applications*, *35*(5), 4099-4131. doi:10.1007/s00521-022-07854-6

Ayvaz, A. (2022). *Optimal Coordination of Directional Overcurrent Relays Using Chameleon Swarm Algorithm*. In: 2nd International Black Sea Modern Scientific Research Congress, Rize, (pp. 63-71).

Ayvaz, A., & Istemihan Genc, V. M. (2020). Information-gap decision theory based transient stability constrained optimal power flow considering the uncertainties of wind energy resources. *IET Renewable Power Generation*, *14*(11), 1946-1955. doi:10.1049/iet-rpg.2019.1367

Christie, R. D. (1993). Power system test cases. (Accessed:10/07/2023) URL

Draz, A., Elkholy, M. M., & El-Fergany, A. A. (2021). Slime mould algorithm constrained by the relay operating time for optimal coordination of directional overcurrent relays using multiple standardized tripping curves. *Neural Computing and Applications*, *33*(18), 11875-11887. doi:10.1007/s00521-021-05879-x

Elmitwally, A., Kandil, M. S., Gouda, E., & Amer, A. (2020). Mitigation of DGs impact on variable-topology meshed network protection system by optimal fault current limiters considering overcurrent relay coordination. *Electric Power Systems Research*, *186*, 106417. doi:10.1016/j.epsr.2020.106417

Fayoud, A. B., Sharaf, H. M., & Ibrahim, D. K. (2022). Optimal coordination of DOCRs in interconnected networks using shifted user-defined two-level characteristics. *International Journal of Electrical Power & Energy Systems*, *142*(Part A), 108298. doi:10.1016/j.ijepes.2022.108298

Grainger, J., & Stevenson, W. (1994) *Power System Analysis*. McGraw-Hill.

Narimani, A., & Hashemi-Dezaki, H. (2021). Optimal stability-oriented protection coordination of smart grid's directional overcurrent relays based on optimized tripping characteristics in double-inverse model using high-set relay. *International Journal of Electrical Power & Energy Systems*, *133*, 107249. doi:10.1016/j.ijepes.2021.107249

Perveen, R., Kishor, N., & Mohanty, S. R. (2016). Fault detection and optimal coordination of overcurrent relay in offshore wind farm connected to onshore grid with VSC–HVDC. *International Transactions on Electrical Energy Systems*, *26*(4), 841-863. doi:10.1002/etep.2111

Saleh, K. A., Zeineldin, H. H., Al-Hinai, A., & El-Saadany, E. F. (2015). Optimal coordination of directional overcurrent relays using a new time–current–voltage characteristic. *IEEE Transactions on Power Delivery*, *30*(2), 537-544. doi:10.1109/TPWRD.2014.2341666

Shih, M. Y., Enríquez, A. C., & Treviño, L. M. T. (2014). On-line coordination of directional overcurrent relays: Performance evaluation among optimization algorithms. *Electric Power Systems Research*, *110*, 122-132. doi:10.1016/j.epsr.2014.01.013

Yu, J., Kim, C.-H., & Rhee, S.-B. (2019). Oppositional Jaya algorithm with distance-adaptive coefficient in solving directional over current relays coordination problem. *IEEE Access*, 7, 150729-150742. doi:10.1109/ACCESS.2019.2947626

Edge Computing for Computer Games by Offloading Physics Computation

Fatih Mustafa KURT[1] Bahri Atay ÖZGÖVDE[1*]

[1]*Boğaziçi University, Department of Computer Engineering, İstanbul, Türkiye*

Keywords	Abstract
Edge Gaming Edge Computing Physics Simulation Task Offloading Computer Games Game Engine	Realistic graphics and smooth experience in computer games come with the cost of increased computational requirements on the end-user devices. Emerging Cloud Gaming that enables executing the games on thin devices comes with its disadvantages such as susceptibility to network latency and the incurred cloud computing cost for the game service provider. The monolithic architecture of the game engines also presents an issue for cloud gaming where scaling efficiency in the cloud turns out to be limited. This paper proposes using edge computing principles to offload a subset of the local computations executed by games to a nearby edge server typically assigned for gaming applications. Specifically, we focus on physics computations since depending on the number of objects and their interactions modes this part may have considerable computational cost. In order to demonstrate the effectiveness of our approach we developed an edge gaming framework called Edge Physics Simulation (EPS) using the open-source game engine Bevy and the Rapier physics engine. We come up with an experiment setup in which a game scene with a high number of objects is executed using both standard local computation approach and using the proposed EPS method. In the experiments up to 8000 objects of varying shape complexities are employed to trigger significant computational load due to the collision detection process. Assessment metrics used are average physics computation time, resource consumption of local device and, the breakdown of the physics duration into its critical components such as network time, simulation time and compression time. Our results show that EPS significantly reduces physics time compared to local execution. For the highest number of objects 75% reduction in physics computation time is reported where breakdown of physics time is further analyzed.

1. INTRODUCTION

Today's game engines are complex pieces of software encompassing multiple components with unique functionalities to provide immersive gameplay close to real life. For example, the visual appearance of real life is resembled in the games by the rendering component, the audio component produces sounds of the environment and actions, and the physics laws are applied to the objects by the physics engine. Game engines achieve these immersive gameplays by producing continuous or discrete outputs and presenting them to the user, such as displaying frames from the game world, playing sound from the speakers, and vibrating the controller. In addition to producing these outputs, game engines are also required to perform these operations in a limited time. Depending on the exact game universe and mechanics implemented, these requirements can vary across game genres (Efe & Önal, 2020).

Immersive gameplay requires a smooth experience, which means producing image frames at a high rate. In order to accomplish this experience, both game software should be optimized, and the devices that run the games should be computationally powerful enough. This constraint puts pressure on the game engine, the game developer, and the hardware itself. Typically, the limiting factor in this situation becomes the end-user device.

Newer computer games, despite efficiency measures taken by the developers, turn out to be resource hungry. Users with insufficient computational capacity, therefore, are refrained from executing their preferred games. This also creates a burden on the game software companies as they can address only a subset of their potential users.

Cloud Computing is a helpful method to let thin devices execute services that require high computing power. There are emerging solutions that provide gaming services under the concept of Cloud Gaming. Cloud gaming enables players to play games on thin devices by receiving the inputs from the device, executing the game in the cloud, and sending the output as a video stream back to the device. However, this method has certain drawbacks. First, the latency between the device and the server makes cloud gaming less applicable outside the advanced internet infrastructures. Secondly, it has a monolithic architecture where all the games run on only one machine and do not attempt to utilize end-user devices.

As a solution to the strict execution time requirements of services, edge computing can minimize the latency substantially compared to cloud computing (Cao et al., 2020). Edge computing allows low latencies between the server and the devices by locating powerful servers at the edge of the network in the proximity of end-users. Edge computing uses the computation offloading technique, which is the delegation of a computational task from the client machine to an edge-enabled server machine. Multiple factors affect the decision of which part of the game engine should be offloaded, such as computational requirements and memory accesses. Offloading lightweight tasks that do not require high computing power may not be worth its communication overhead. In this respect, computationally heavy tasks are good candidates for offloading. However, tasks unavoidably occur in the local software's call graph and may require interacting with other parts of the engine multiple times. Therefore, a component that accesses the core data of the engine frequently may not be a good candidate to offload. However, most physics engines have their context separated from the game context, making them feasible for computation offloading.

There is an immense literature on edge computing and its application domains. Edge computing principles have been successfully applied to a wide range of use cases ranging from IoT to autonomous driving (Cruz et al., 2022). Nevertheless, edge computing for computer games still needs to be explored to its full potential, as most studies focus on cloud gaming. Therefore, the challenges and opportunities of edge gaming require further exploration. This study specifically focuses on offloading the physics process in an edge computing setting. Distributed coordination, state management of game and physics engines, and communication and synchronization approaches are explored.

In this paper, we propose an edge gaming framework named Edge Physics Simulation (EPS) for computer games that involve heavy physics computation. We aim to relieve the computational burden on the end user device and delegate physics tasks to an edge server. To demonstrate the performance of our method, we implement an experiment setup that involves the open-source Bevy game engine and the open-source Rapier physics engine (Bevy, 2023; Rapier, 2023). In the proposed setting, the game engine runs on a thin user device, and the physics engine runs on the edge server. The results of the experiments show that the proposed solution reduces the average calculation time for the physics by up to 75% compared to the solution that executes physics on the thin device.

The contributions of the study can be summarized as:

- A novel gaming framework is proposed in which edge computing principles are applied to the computer games vertical.
- Gamescene is processed in a distributed fashion in which the game context and physics context take place on different hardware environments. An open-source implementation is provided based on Bevy game engine.
- A multi-faceted performance assessment is carried out via extensive experiments where the number of game objects and their shape complexities and over-the-network compression rates are varied.
- Considerable physics execution speed-up is reported, which indicates edge computing as a valid research direction for computer games.

The organization of this paper follows as: Section 2 summarizes a recent selection of the related works about edge gaming and cloud gaming alternatives. Then, Section 3 defines the proposed edge gaming framework explains the components in the solution architecture. In Section 4, the experimental setup and the properties of the testbed are focused on. Section 5 presents the results of the experiments and discusses them. Finally, Section 6 concludes the paper by summarizing the results and listing possible future works.

2. RELATED WORKS

The game engine is a crucial software component in game development and design. Although commercially well-known game engines exist such as Unity, Unreal, and CryEngine, the realm of game engines is much broader (CryEngine, 2023; Unity, 2023; Unreal, 2023). In a recent study, Vagavolu et al. (2021) present a dataset of open-source game engines where the authors analyze the software development activities of 526 game engine projects in the dataset. Similarly, Politowski et al. (2021) discuss the game engines from the perspective of a software framework in which authors compare the characteristics of 282 game engines, including a survey with 124 game engine developers.

Before developing an edge computing framework for computer games, the inner details of a typical game engine need to be analyzed to understand the overall technical challenges better. In this respect, some of the earlier works attempted to dissect the popular game engine Unity3D into its main modules, such as input, rendering, scripting, and physics engine; they analyze CPU consumptions of each module tested with different games with have different resource requirements (Messaoudi et al., 2015). As a common pattern, the rendering module is the most demanding module for the CPU resource. In addition to CPU consumption, the GPU consumption of the rendering's submodules is also analyzed. For a complete discussion of the technical perspectives on game engines, Gregory (2018) provides an excellent reference where all sub-systems of a typical game engine are focused individually and explored in depth.

A popular approach for augmenting the capabilities of end-user gaming devices is cloud gaming. Cloud gaming differs from the edge computing approach in that game software as a whole generally gets executed in the data center (Huang et al., 2014). Bhojan et al. (2020) propose an architecture for cloud gaming and report server resource consumption when number of players in the system varies. Chen et al. (2019) in which authors emphasize the distinction between cloud gaming and video-on-demand (VoD) applications and further propose an adaptive real-time streaming policy using the deep reinforcement learning tool that considers both the quality of service (QoS) and quality of experience (QoE) in cloud gaming scenarios.

A related but technically distinct technical approach for edge gaming is defined in 5G architecture via mobile edge computing (MEC) (Artuñedo Guillen et al., 2020). Nowak et al. (2021) provide a detailed survey on 5G-MEC use cases and a technical summary of research in computer games exploiting 5G to enhance the gamer experience. The authors provide a wide range of examples from the gaming sector and discuss the direction in which 5G can leverage gaming applications from various points. A specific example is reported by Cao et al. (2022) in which authors propose a heuristic algorithm to minimize QoE impairments under given constraints.

Since the rendering consumes most of the CPU resource, offloading the rendering part to a powerful server can help users play the games on resource-limited devices. Bulman and Garraghan (2020) propose a unified Graphics API that is mapped to OpenGL or Vulkan Graphics frameworks depending on the hardware capabilities of the user device (OpenGL, 2023; Vulkan, 2023). With this approach, unified API can offload some of the calls to the cloud when the performance of the device degrades. The authors show that this method can achieve 33% more frames per second when the commands are distributed over the cloud and device with a 50-50 ratio (Bulman & Garraghan, 2020).

Virtual reality (VR) and augmented reality (AR) technologies provide a novel opportunity to enhance computer game interaction modes for the end users. However, the constrained hardware devices involved in AR & VR scenarios necessitate edge computing for a smooth game experience. Nyamtiga et al. (2022) carried out a detailed empirical study on an experimental VR offloading testbed where the performance of the system is evaluated using three different VR games. The authors demonstrate the advantages and the tradeoffs involved in using the reduction in computational load and power consumption on the client device. Another study that focuses on the VR edge computing approach is described by Mehrabi et al. (2021), in which online heuristic

Fatih Mustafa KURT, Bahri Atay ÖZGÖVDE

algorithms are proposed for the tradeoff between average video quality and delivery latency. The authors perform a series of simulation-based experiments for performance analysis and report a 22% improvement in video delivery and 8% in video quality.

Another offloading approach, proposed by Messaoudi et al. (2018), partitions the game scene into game objects such as the player character environment; then, in turn, it performs offloading of logic execution and rendering of these game objects to the server depending on the required device resources, data transfer time, and dependencies of the code. As a result of offloading, the server streams OpenGL ES commands back to the device to complete the rendering (Messaoudi et al., 2018).

A similar method for offloading computationally heavy tasks to the cloud for a soft body physics simulator is suggested and implemented by Danevičius et al. (2018) This method defines a task set that can be executed locally or offloaded to the cloud for the simulation program and partitions them as running on the local device or being offloaded to the cloud. This decision is made concerning multiple factors, such as the computation speed of the local device and cloud, the size of the inputs and outputs of the task, and network bandwidth and latency. An intelligent offloading management component uses these factors to decide if the task should be offloaded or not. Even though the study suggests offloading a program that runs a physics simulation, its goals heavily differ from our proposal's goals, such as separating the physics calculations from the game engine completely.

It is also possible to design all the game engine components modularly. The authors of SMASH propose a distributed game engine that is flexible enough to run the game entirely on the local or distribute its components over the network (Maggiorini et al., 2016). The architecture of SMASH resembles microkernels where the engine components interact internally by sending messages over a bus. A component with a SMASH-compatible interface can be added to the engine and can be used by other components. Another distributed game architecture is proposed by Mazzuca (2022) that implements a prototype for the rendering component. The implementation sends scene information to the rendering service over a UDP socket. The rendering service renders the scene and streams encoded video to the device (Mazzuca, 2022).

In order to apply edge computing principles to computer gaming scenarios, computational offloading should be implemented involving the game engine itself. This is not a straightforward task, as existing game engines are typically not designed with edge computing in mind. Our initial exploration with the open-source game engine Godot showed that distributing game engine functionality over a client-server model is cumbersome as the call graph of the overall code does not allow for minimizing communication overhead and latency (Godot, 2023). A suitable game engine for our purposes should have flexible and modular architecture, allowing a re-design with the minimum effort possible. When these requirements are considered, Bevy game engine turned out to be a valid choice for developing a game engine architecture compatible with edge computing.

Bevy promotes itself as a data-driven game engine that is open-source, free to use, and written in Rust programming language (Bevy, 2023; Rust, 2023). It has active development going on and is being developed by the contributions of its community and its members. Being easy to modify and easy to play with its core components are the reasons for choosing Bevy instead of other open-source game engines. The Rust programming language was also a compelling reason to use the Bevy. Rust presents itself as a system-programming language that aims to be both performant, reliable, and productive (Rust, 2023). As a benefit of ownership-based memory management and being memory-safe, developing edge physics was both fun and easy for a network-based application. Another reason for choosing Bevy is the Entity Component System (ECS) paradigm used to represent the objects in the game world.

3. SYSTEM DEFINITION

In order to apply edge computing principles in a gaming scenario, we propose an architecture that offloads physics computation, which is part of the typical local execution öf game software. Figure 1 shows the main components of a game engine. Game engines may or may not have a default physics engine included in their software stack. Since the design and implementation of a physics engine is an expertise by itself, there is a variety of third-party physics engines that can be incorporated into the game engines (Bullet, 2023; Havok, 2023; PhysX, 2023). When an independent physics engine is employed within the game engine, there is a clear

separation of physics related computation procedures from the rest of the game engine software, where physics functionality is presented through a well-defined physics application programming interface (API).
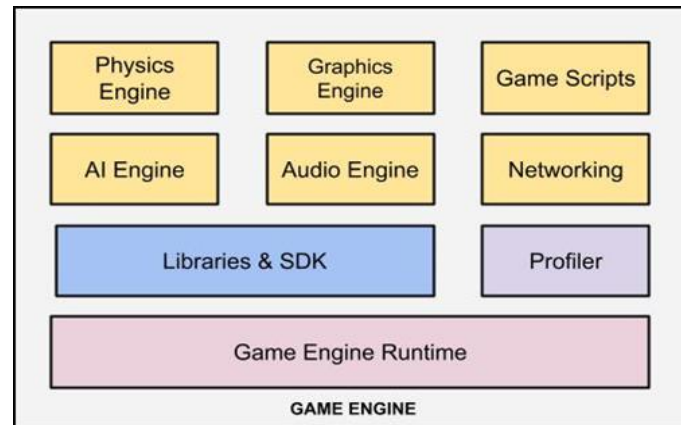
Figure 1. Components and Modules of a Typical Game Engine

In this respect, the proposed system architecture contains a distributed flow of game execution in which gamer device (local device) and an edge server (remote device) both take part via a computation offloading sequence. Figure 2 depicts the architecture of Edge Physics Simulation (EPS) framework. As dictated by the edge computing scenarios in general a fast local access networking technology is assumed to connect gamer devices to the edge server. Edge server is not dedicated to client, therefore multiple devices can connect to edge server to take offloading service.
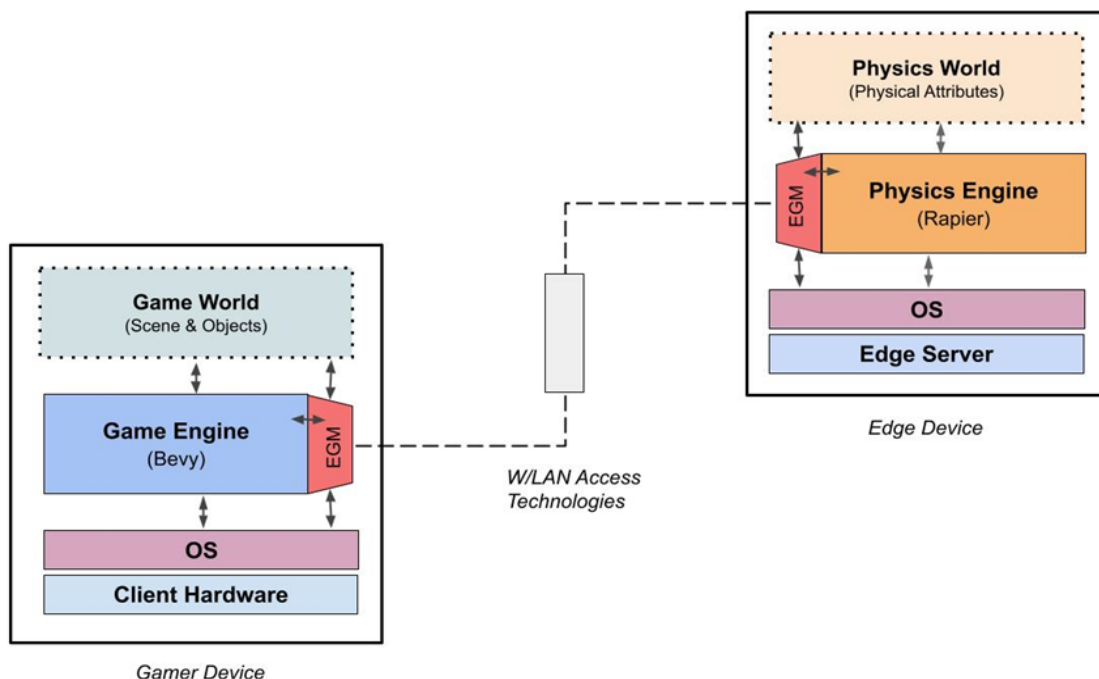
Figure 2. Edge Physics Simulation (EPS) Architecture (EGM: Edge Gaming Manager)

In our implementation, we used the Bevy game engine and Rapier physics engine as the core modules. The reasons behind our choice are: (i) both systems are open source and actively maintained by a decent community of developers, (ii) they do not impose any licensing fees, (iii) last but not least, the software architecture of these systems allowed flexible modification opportunities during the development and testing phases of our study. Edge Gaming Manager (EGM) is a special module developed in this study responsible for accessing internal data structures and attributes of the objects, supplying device connectivity for offloading and network payload size control using configurable compression techniques.

3.1. Bevy Game Engine

At its core, Bevy is built around a "game world" and a system scheduler. The game world is a jargon to denote the structure that holds the data that will be used within the game loop. This data includes entities, components of the entities, and resources such as a timer that tracks the past time intervals in the game, meshes to be used in the rendering and game state. On the other hand, the. On the other hand, the system scheduler schedules the systems in the ECS architecture and executes them on the game world. Here, the term "system" refers to a process that acts on "entities" with selected "components". For further technical details of the ECS, Hatledal et al. (2021) give definitions for ECS units and present a simulation framework implementation based on ECS software paradigm.

Systems can be grouped together by putting them into a System Set. Systems in the set can be chained for sequential execution, or the execution order can be left to the scheduler. In addition to chaining the systems, System Sets themselves can further be chained to define an execution order between them. If there is no order given at development time, the scheduler will try to execute systems concurrently to employ parallelism in a way that will avoid modifying a resource by two systems simultaneously. A simplified overview for the System Sets that are available in the Bevy by default and their execution order can be seen in Figure 3. From beginning to end, the execution of these sets represents the game loop
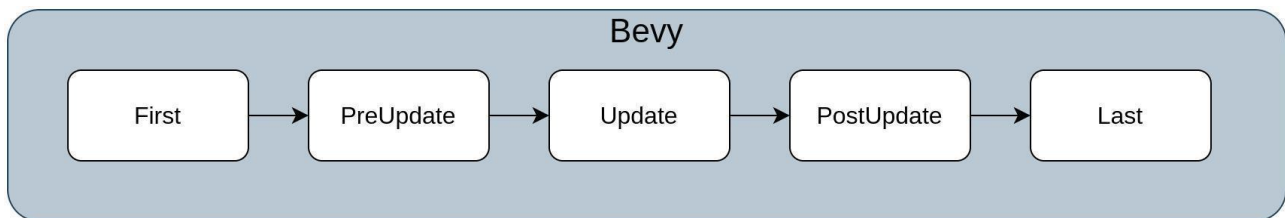
Figure 3. Bevy's Default System Sets

Aside from its core units, Bevy provides additional plugins to implement other features, such as rendering and audio. Each plugin modifies the game world by inserting resources and instructs the scheduler on executing its systems. For example, the input plugin schedules its systems to be run at the PreUpdate set in order to let other systems that will be run at the Update set read the user inputs. Plugin-based architecture makes Bevy a modular game engine such that a plugin can be swapped with another implementation of the feature, assuming it provides a compatible interface to the plugins that depend on it. Even the core without any additional plugins is a valuable tool for developing an application that requires a scheduler.

3.2. Rapier Physics Engine

Although Bevy implements fundamental components of a game engine as plugins, it does not have a physics engine that is available out of the box. However, there are certain physics plugins that integrate independently developed physics engines into the Bevy. Bevy Rapier is such a plugin that enables the integration of the Rapier physics engine into the Bevy game engine without much effort (Bevy Rapier, 2023).

As a standalone physics engine, Rapier contains its own world (context) to perform physics simulations. To integrate Rapier into Bevy, the Bevy Rapier plugin defines three main system sets that perform (i) syncing Bevy's game world to Rapier physics world, (ii) simulating the physics for one step, and (iii) transferring the changed values in the physics world to the Bevy's original game world. Here, the word "world" means the context, and Bevy's plugin software interface stores Rapier's context in the game world as a resource. The integration of Bevy's System Sets and the plugin's System Sets can be seen in Figure 4.
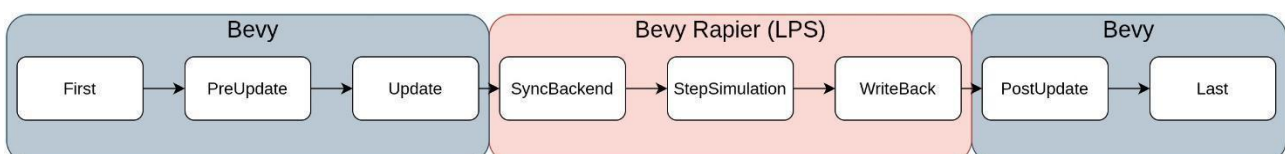
Figure 4. Integration of Bevy Rapier Plugin's System Sets

3.3. Proposed Solution

Standard installation and execution procedures let the Rapier plugin, which is named Local Physics Simulation (LPS), execute everything on the local device. This causes heavy physics simulations to become the performance bottleneck of the game loop and results in increased frame times. As a remedy, we propose Edge Physics Simulation (EPS), which offloads physics-based computation to an edge server.

The idea originates from the existence of the two different worlds (contexts) that belong to Rapier and Bevy that are synchronized two times in each frame. This approach has already reduced the number of interactions between the two worlds to a minimum and enabled the separation of these two execution tracks on different computational environments.

In the EPS architecture, a separate controller named Edge Gaming Manager (EGM) separate from the original game, is developed and deployed to an edge server. In the edge server, both the simulation step and the context are moved into EGM. At the startup, EGM listens on a TCP port and waits for a new connection. For the game, it tries to connect to the EGM when it is started. This is achieved by a peer EGM instance on the user device, as shown in Figure 2. When a connection from the game is established, EGM reads the synchronization data over the connection, simulates the physics for one step using rapier functionality, and sends the new positions and the rotations of the objects to the game. These three steps are executed in a loop until the underlying connection gets broken or the game sends a shutdown message. In the game, the execution order of the Bevy Rapier's System Sets is modified to minimize the time that is taken to receive the response. For example, while Edge is performing the StepSimulation step, Client also continues the execution of the PostUpdate and the Last sets. A visual representation of the architecture is shown in Figure 5.
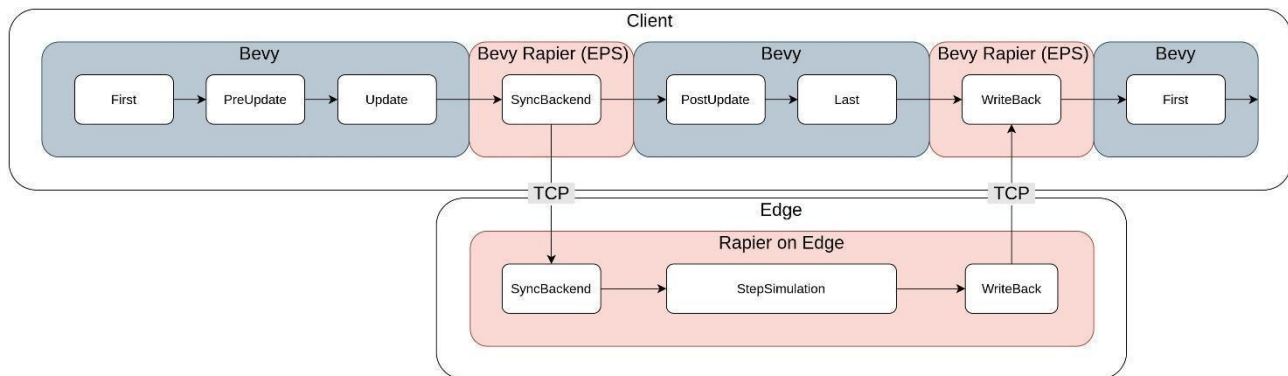
Figure 5. Proposed Solution's Architecture

The EPS should provide smooth gameplay even if there is no demanding physics calculations from the game. Moreover, it is also essential to utilize the underlying network connection efficiently. For this reason, reducing the time that is spent in the network should be minimized. EPS uses DEFLATE compression algorithm in order to reduce the size of the data sent over the network (Deutsch, 1996). DEFLATE employs different compression levels that range from 1 to 9 and inform the algorithm to favor faster compression times or smaller compressed sizes, respectively. When applicable, it also disables the buffering algorithm applied to TCP socket by the operating systems, such as Nagle's algorithm, to minimize the latency (Nagle, 1984).

4. EXPERIMENTS

An experiment setup is designed to enable performance evaluation of the two different approaches in a comparative manner. One solution is the Edge Physics Simulation (EPS), in which the client offloads its physics simulation to the edge server for each frame. Another solution is the Local Physics Simulation (LPS), in which all the simulation is executed on the client. For EPS solution, the experiments are conducted on one edge machine and one client machine, whereas LPS contains only the client machine. Details of the implementation platform will be discussed in the following subsection.

During the experiments, the rendering component of the game is disabled due to the client's weak GPU. When the rendering is enabled, the frame time increases and starts fluctuating. Therefore, instead of measuring the

Frames per Second (FPS) for comparison, the physics time taken to perform the StepSimulation step is measured and compared for each solution. For the EPS solution, physics time also contains data transmission time over the network and StepSimulation step. Figure 6 visualizes the physics time measurement for each solution..

(a)

(b)
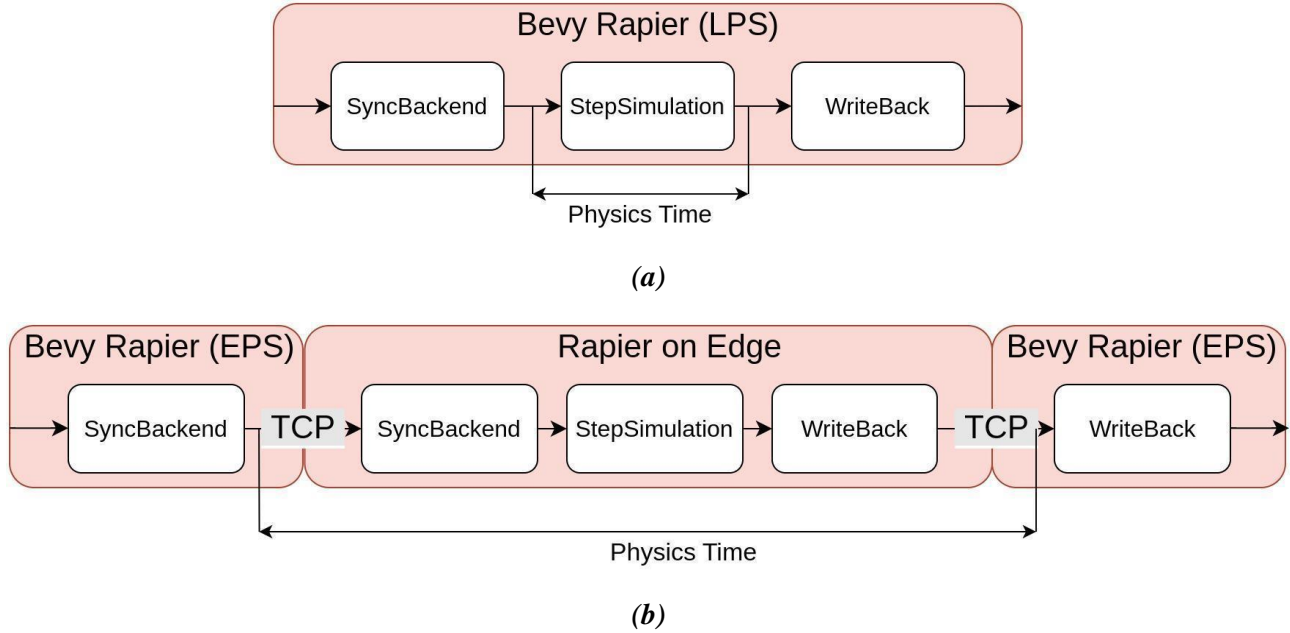
Figure 6. *a) LPS (Local Physics Simulation) Physics Time, b) EPS (Edge Physics Simulation) Physics Time*

The experiments are based on a scenario that has a multitude of physical objects stacked up on each other to form a grid pattern in a confined space. In this setting, a ball with high velocity initially triggers the objects, and objects fall due to gravity, and considerable inter-object collision takes place. Elasticity and coefficient of friction values are adjusted to maintain the continuous movement of objects. Figure 7 and Figure 8 visually depict snapshots from the experiments in which Figure 7 shows the initial condition.
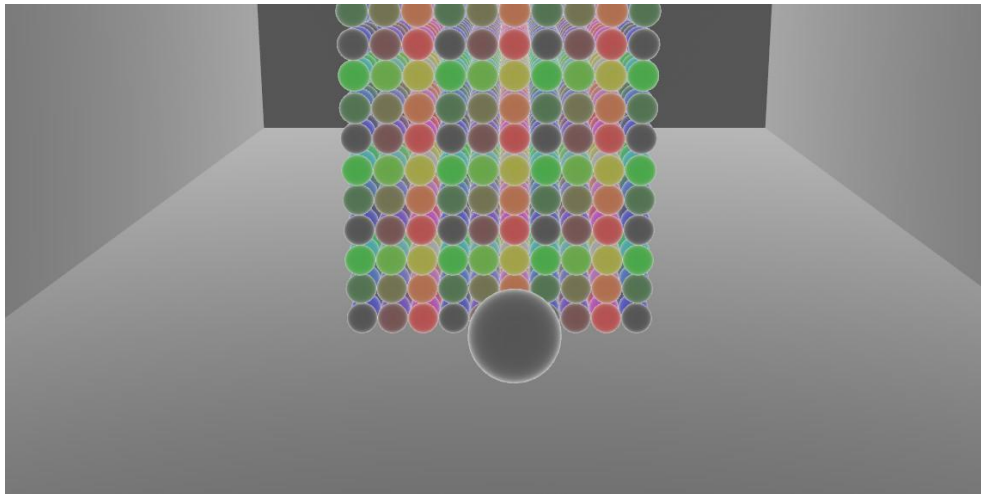
Figure 7. *Appearance of the Scene at Initial State*
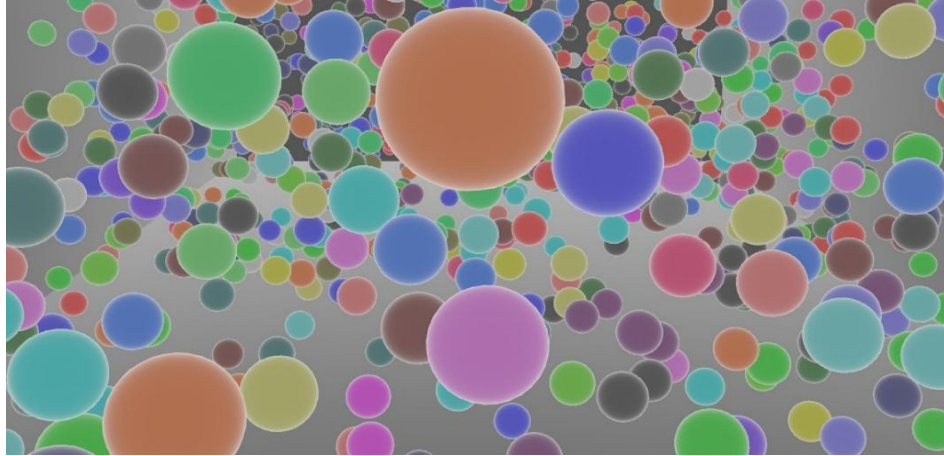
Figure 8. *Appearance of the Scene at the Steady State*

Parameters for each experiment run are defined in terms of the:

- number of objects used for the simulation,
- shape of the objects,
- whether edge gaming is enabled or not (i.e. EPS vs. LPS),
- compression level used in the communication, and
- whether Continuous Collision Detection (CCD) is enabled or not.

CCD is a special collision detection algorithm that considers the positions of the objects between frames. CCD provides much more accurate collision detection behavior, especially when objects are small and have high velocity. However, this comes with an extra computational cost; therefore, game programmers need to switch this feature on only when necessary. Table 1 summarizes the values used in the experiments for the relevant parameters. Visual appearances of the shapes are shown in Figure 9. These parameters affect the computational load taking place in the game scene and allow us to model different game profiles requiring different levels of physics computations. Each experiment run gets executed for 15 seconds. After an exploratory phase of the experiments, it was seen that this duration was sufficient for the system to reach a steady state. Please note that when the local execution is used, there is no compression option since no data is sent over the network.

Table 1. *Experiment Parameters*

Parameter	Values
Solution Approach	Local, Edge
Number of Objects	500, 1000, 2000, 4000, 8000
Collision Detection Algorithm	Discrete CD, Continuous CD
Compression Levels	No compression, Level 1, Level 3
Object Shapes	ball, capsule, cuboid, complex

| **(a)** | **(b)** | **(c)** | **(d)** |
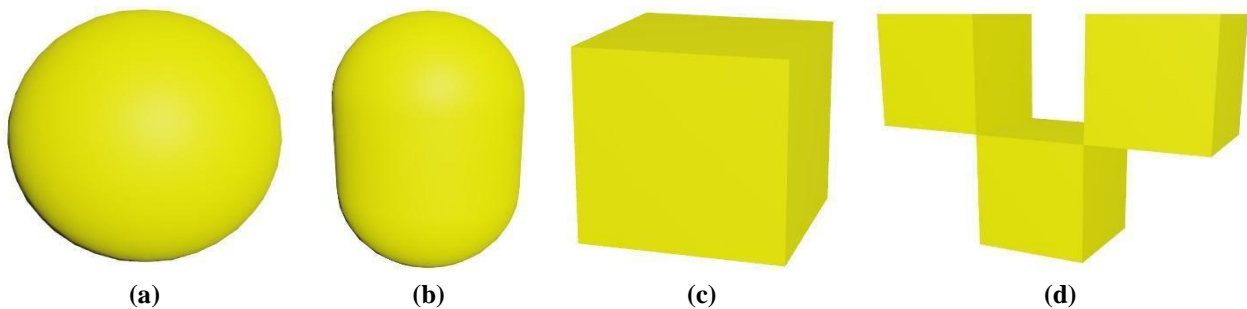
Figure 9. *Visual Appearances of Shapes **a)** Ball **b)** Capsule **c)** Cuboid **d)** Complex*

There are also other parameters belonging to the physics engine that affect the experiment's behavior and computational load. However, values for these parameters are kept constant for all the experiments. Table 2 summarizes these parameters and the values chosen for them.

Table 2. Constant Experiment Parameters

Parameter	Values
Density of Object	0.477 kg/cm^3
Elasticity Coefficient of Object	1.1
Friction Force	0.0 N
Gravity	9.81 m/s^2

When the combinations of different values for each option are considered, there are 160 different configurations to be tested. Moreover, each configuration is tested 2 times to check if they produce similar results. Displaying each possible configuration in this paper is impossible due to space considerations. Instead, a subset of the configurations that gives a clear understanding of the general behavior of the solutions is shown in Section 5.

4.1. Implementation Platform

To implement the experiment platform, two different machines are used as an edge server and a client device. For the EPS solution, these machines are connected over a Local Area Network (LAN) with 100 Mbit ethernet connections using a modem. Figure 10 presents a diagram that describes the platform visually.
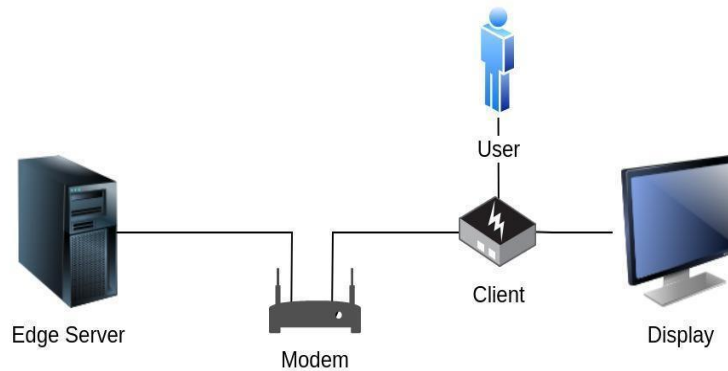
Figure 10. Diagram of the platform used for the implementation

The flow in this diagram for generating one frame can be explained as: The client accepts input from the user, processes it, and sends updated components of the entities to the Edge Server. After completion of the physics calculation, the client receives the latest state of the entities from the edge server and outputs the result to the Display. In this platform, the Edge Server is a PC that contains powerful hardware compared to the client device. On the other hand, the Raspberry Pi 4B device is used as the client. The hardware and software configurations of the machines are summarized in Table 3.

Table 3. Machine Configurations

Machine	Hardware			Software	
	CPU	Memory	Connection	OS-Arch-Distribution	libc
Client	4 core Cortex-A72@1.8 GHz	4GB LPDDR4@3200 MHz	100 Mbit Ethernet	Linux - aarch64 - Arch Linux	Glibc 2.35
Edge	6 core AMD Ryzen 5600X@3.7 GHz	32GB DDR4@3200 MHz	100 Mbit Ethernet	Linux - x86_64 - Gentoo	Glibc 2.37

4.2. Data Collection from Experiments

Evaluating and analyzing the experiments requires collecting related information from the application and its environment during the experiments. For the application part, some diagnostics are placed into the source code of both the client application and the physics server. These diagnostics collect data from the application state for every frame. Logs are collected and stored inside a file by another application specifically developed for this case. The diagnostics that include information from the physics server are collected in the physics server and sent back to the client for each frame. A summary of the data collected and processed during the experiments is depicted in Table 4. Other than the diagnostics data collected, the CPU usage data is also collected by another process.

Table 4. Edge Gaming Experiment Data Summary

Diagnostic	Description
Time	Time passed since application startup
Frame Count	Number of frames generated since startup
Frame Time	Time taken to generate current frame
Physics Time	Time taken to complete physics computation
Network Time	Time spent in the network communication
Sent Bytes	Number of bytes sent to edge server
Sent Compressed Bytes	Number of actual bytes that are sent over the network. For **No Compression** case, this is equal to **Sent Bytes**
Received Bytes	Number of bytes expected to be received from edge server
Received Compressed Bytes	Number of actual bytes that are received over the network. For **No Compression** case, this is equal to **Received Bytes**
Compression Time in Client	Time taken to compress payload on the client
Decompression Time in Client	Time taken to decompress payload on the client
Compression Time in Server	Time taken to compress payload on the server
Decompression Time in Server	Time taken to decompress payload on the server

5. RESULTS AND DISCUSSION

The two solutions discussed, namely EPS and LPS, are investigated concerning two different criteria: execution performance and resource consumption. The execution performances of the solutions are identified by their physics time durations, whereas the resource consumptions are identified by their CPU usage. For EPS solution, bandwidth usage of the network is also considered to be a metric for resource consumption.

5.1. Physics Time

In order to obtain a general overview, the performances of EPS and LPS are compared with respect to their physics execution time under different configurations. In the first set of experiment runs, the effect of the number of objects on the scene is explored. In order to underline the physics computation, the object shape is chosen as "complex" so that extra collision geometry is involved. For other experiment parameters, CCD (Continuous Collision Detection) mode is switched off, and for the EPS part, the compression level is set to 1. Figure 11 shows the performances of LPS and EPS comparatively. The performance gap increases for a larger number of objects in the scene in favor of the edge-based solution.
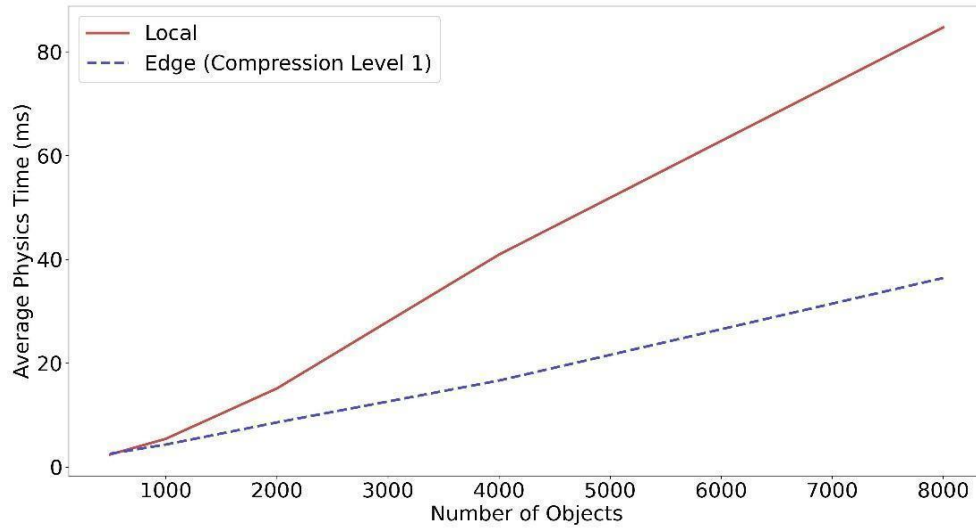
Figure 11. *Average Physics Time for solutions, shape = complex, CCD = off*

Apart from reporting the mean physics time values, it is also meaningful to see how physics time in every frame evolves during the experiments. In Figure 12, the characteristics of the scenario can be seen. Initially, physics time is small since all the objects are idle. When the ball on the ground hits the objects, a spike in physics time is observed. After a small amount of time from the collision, the physics time converges to a steady state with small variations over time. This convergence is because the number of collisions that happen in one step becomes steady due to gas molecules like the perpetual movement of the objects. As expected from Figure 11, Figure 12 reveals that edge-based proposed solution (EPS) outperforms local computing (LPS) at all times.
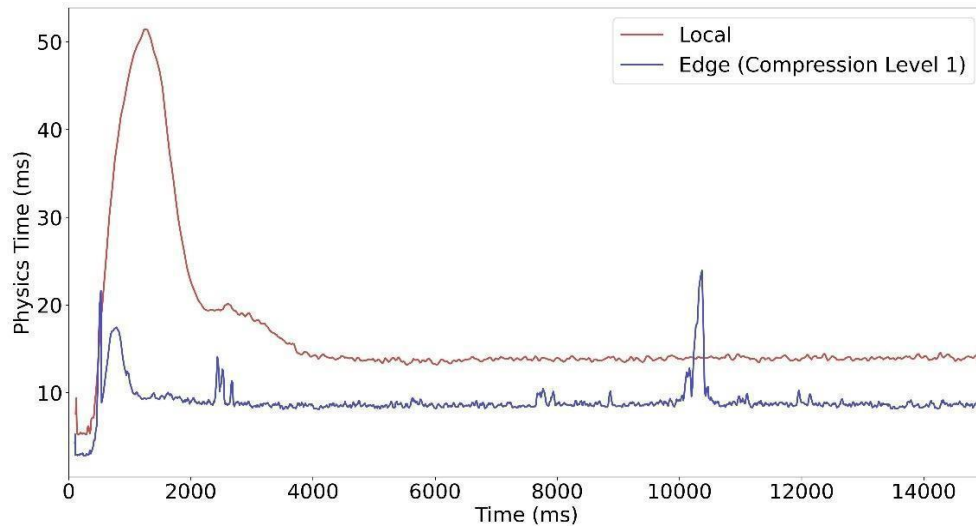
Figure 12. *Time series visualization of physics computation time. Each data point belongs to successive frames over time. (Objects=2000, Shape Type = Complex, CCD=off)*

To explore the EPS model in more detail, the extra computational load incurred by collision detection modality is experimented by turning CCD mode on and off. These two configurations illustrate the characteristics of the solution under different computational requirements for the physics calculations. Figure 13 clearly shows the effect of the CCD where turning on the CCD mode changes the linear behavior of the solution under different number of objects. The non-linearity of Average Physics Time where CCD mode is turned on indicates that the behavior of the EPS solution is mostly dependent on the physics calculation performed under the hood.
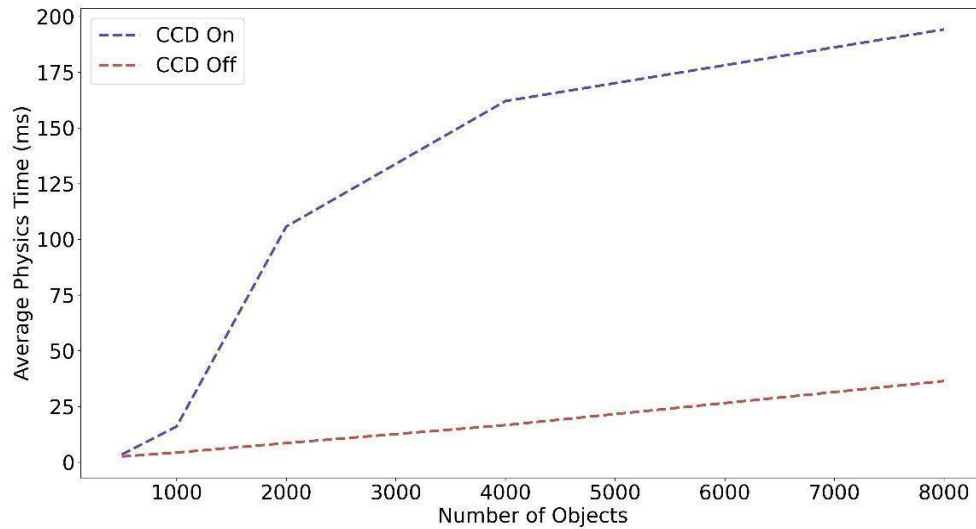
Figure 13. *Average Physics Time for EPS where CCD is toggled for the configurations*

The performance of edge computing approaches is determined not only by the computation time on the server but also by the time spent over the network. In this respect, our proposed solution employs data compression techniques further to minimize the data context transfer time for physics offloading. Compression, however, comes with a new trade-off where higher compression levels result in lower data size at the expense of increased computation overhead. The compression algorithm used in the experiments allows for ten different compression levels where level=1 has the fastest computation time, and level=10 has the maximum compression rate (Deutsch, 1996).

To explore the trade-off brought by compression, a series of experiments is executed with different compression rates for over-the-network transfer. Figure 14 depicts how local solution (LPS) compares to edge solution (EPS) with different compression rates. For a clear visual representation, the figure presents normalized values for physics time. For a very low number of game objects, edge computing turns out to be not effective. However, as the number of game objects increased, all variants of edge computing solutions outperformed local computation based approach. It is apparent that compression enhances performance. The best-performing compression rate occurs at level=1, meaning that extra time required for more complex compression does not pay off. Results belonging to all possible compression configurations are not included in Figure 14 to avoid a cluttered view where compression levels 1 and 3 are sufficient to understand the general trend.
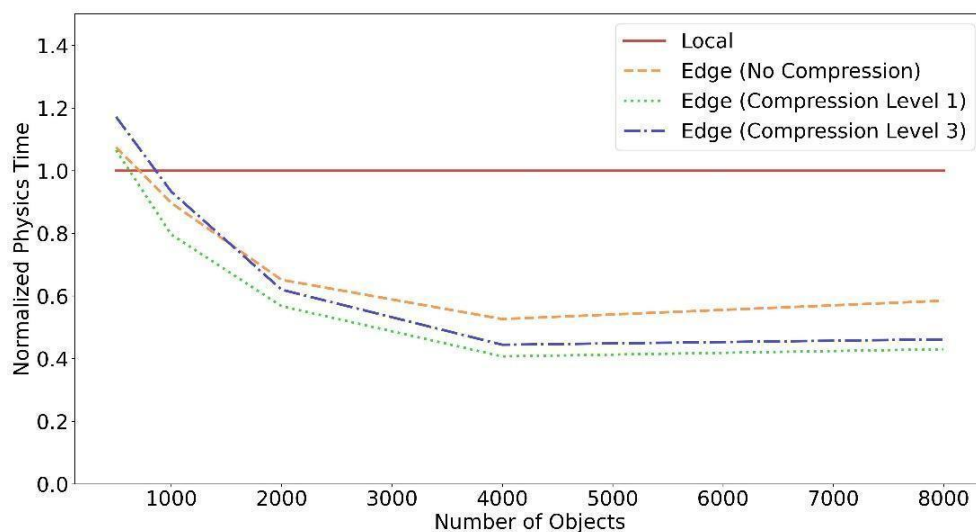
Figure 14. *Normalized physics computation time to depict the effect of compression rates. (Local physics computation is normalized to 1)*

To better understand the reported physics time for the edge-based solution, Figure 15 shows the breakdown of the overall physics time in terms of network transfer time, physics simulation time, and data compression time. Timings are reported for one physics simulation step of EPS where level 1 compression and complex shape are used, as CCD is turned off. The figure shows that network time takes most of the physics time at the lower number of objects. This network overhead can be eliminated using higher-speed connections such as gigabit ethernet. As the number of objects increases, the simulation and compression times increase to a point where network time takes less than half of the physics time.
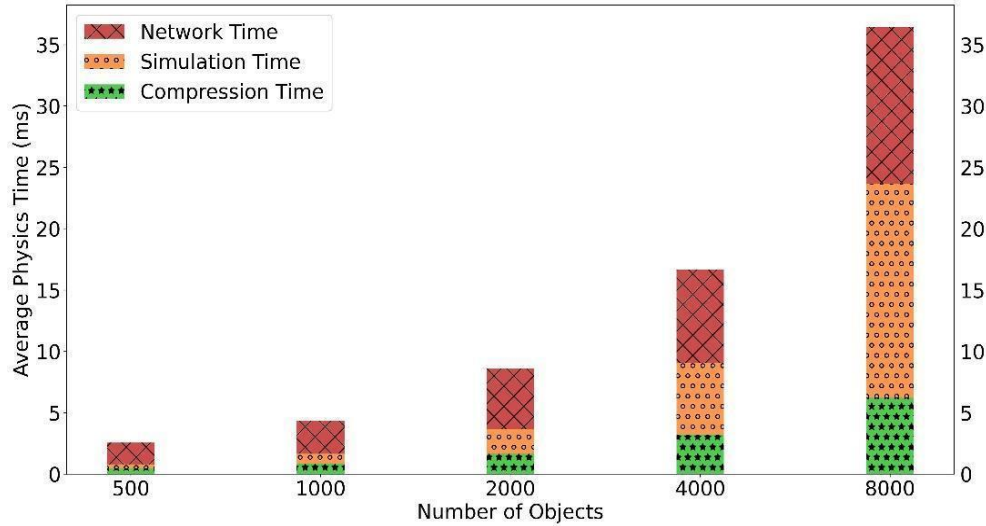
Figure 15. Breakdown of Physics Time, shape = complex, CCD = off

5.2. Resource Consumption

In order to compare the resource consumption of the edge and local computation-based solutions, CPU utilization statistics of the game execution processes are recorded. Note that LPS (Local Physics Simulation) involves the execution of both the Bevy game engine and the Rapier physics engine as a bundle. In contrast, EPS (Edge Physics Simulation) includes our proposed modified setup for offloading physics computation.

Figure 16 shows that the edge-based solution lowers the CPU utilization of the client considerably. This observation parallels the general edge computing paradigm, where applications can be run on low-end devices. As the number of objects increases, the usage of the EPS decreases. This behavior is because the time spent on the edge server and on the I/O increases as the number of objects increases. This blocks the client and keeps it idle most of the time.
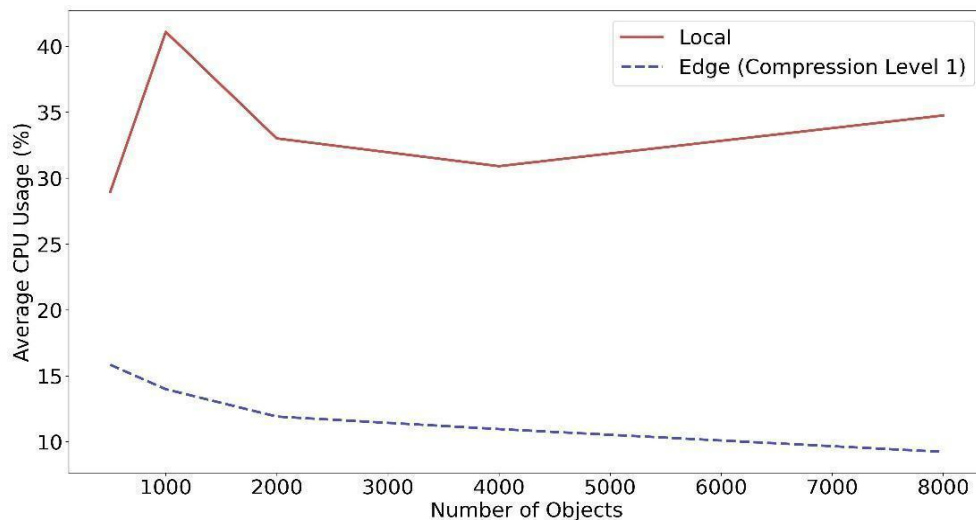
Figure 16. Average CPU Usage for solutions, shape = complex, CCD = off

One could imagine that CPU usage for the LPS solution should be similar across the experiments. On the contrary, Figure 16 shows that configurations for *500* and *1000* objects have very different CPU usage. The usages only become similar after the *2000* number of objects. This shows that Rapier's physics engine employs parallelism in its implementation. However, this implementation hits scaling issues under different configurations.

In Figure 17, there are three different metrics for the bandwidth usage. The first, *Uplink*, represents the data transmitted from the client to the edge, whereas the second, *Downlink*, represents the data received from the edge. Since the objects are spawned at the beginning of the experiment, the client uses the Uplink only at that time. Throughout the experiment, Uplink stays close to *0*. For the Downlink, as seen in Figure 12, it becomes steady over time except for some significant drops that also affect the frame time.
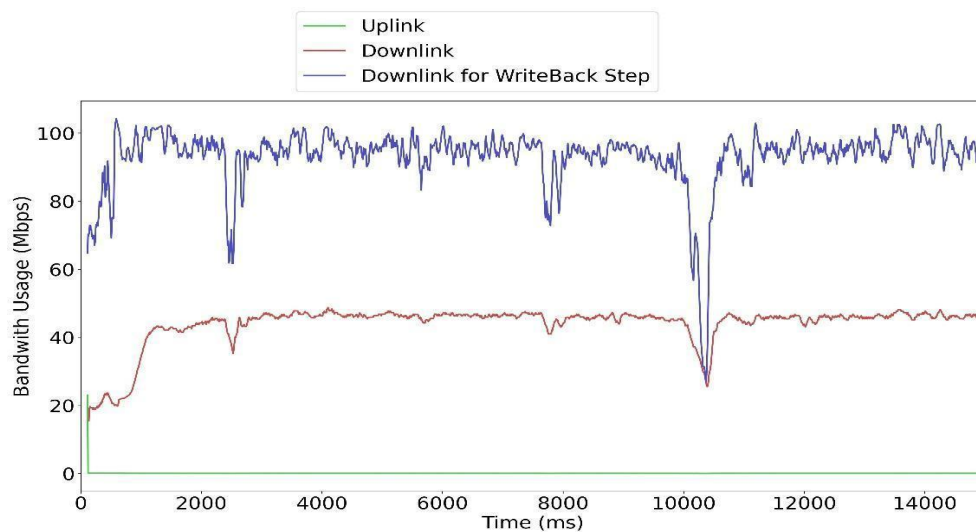
Figure 17. *Bandwidth Usage over time, number of objects = 2000, shape = complex, CCD = off*

The experiments are executed in a network environment with a 100Mbps line rate. Downlink figures stay much below this because communication between two machines does not occur during the whole frame. We include one additional metric, *Downlink for WriteBack Step*, as a correction factor. This metric takes into account the time that is passed in the *WriteBack* step. This clearly shows that the connection speed limit is reached during this step.

After performing multiple comparisons between two solutions under different configurations, it can be said that the proposed solution EPS provides substantially shorter physics simulation time compared to default LPS and reduces CPU usage when a weak client and a powerful edge server are used. The performance of EPS can also be improved further by increasing the bandwidth of the network, such as employing a higher-speed connection.

6. CONCLUSION

Computer games belong to the group of the most resource-demanding software in the modern era. Gamers continuously face a hardware challenge as newer games typically require more computational capacity. As a remedy, this study proposes an edge gaming architecture called Edge Physics Simulation (EPS) that offloads physics computation tasks to the edge server. EPS further enhances task offloading operation by incorporating a compression mechanism that can be tuned. To demonstrate the performance of EPS, an edge gaming setup is implemented by employing an open-source Bevy game engine and Rapier physics engine. A series of experiments are conducted covering various system parameters, including the number of objects on the game scene, the complexity of the object shapes, collusion detection algorithm type, and the level of compression. By looking at the results of the experiments, it is shown that the edge computing based implementation can speed up the physics calculation up to 75% compared to its local-only counterpart. The speed-up figures reported are significant and show the feasibility of edge computing for computer games. As such, EPS will enable users to play their games on hardware with relatively low resources.

As future work, we aim to focus on other critical components of a typical game engine that can potentially be distributed over the network, such as rendering and AI modules. This will enable a full-fledged edge gaming setup in which low-resource devices are able to execute games with high computational requirements. Also, we plan to examine the effect of client hardware resources on the overall system performance. This will enable us to model different user equipment profiles, such as mobile phones, tablets, and older generation PCs.

CONFLICT OF INTEREST

The authors declare no conflict of interest.

REFERENCES

Bevy (2023). A refreshingly simple data-driven game engine built in Rust, Free and Open Source Forever. (Accessed:15/06/2023) URL

Bevy Rapier (2023). Official Rapier plugin for the Bevy game engine. (Accessed:15/06/2023) URL

Bhojan, A., Ng, S. P., Ng, J., & Ooi, W. T. (2020). CloudyGame: Enabling cloud gaming on the edge with dynamic asset streaming and shared game instances. *Multimedia Tools and Applications*, *79*(43-44), 32503-32523. doi:10.1007/s11042-020-09612-z

Bullet (2023). Real-time collision detection and multi-physics simulation for VR, games, visual effects, robotics, machine learning. (Accessed:10/08/2023) URL

Bulman, J., & Garraghan, P. (2020). *A Cloud Gaming Framework for Dynamic Graphical Rendering Towards Achieving Distributed Game Engines*. In: Proceedings of the 12th USENIX Workshop on Hot Topics in Cloud Computing (HotCloud 20), Virtual Event.

Cao, K., Liu Y., Meng G. & Sun, Q. (2020). An Overview on Edge Computing Research. *IEEE Access*, *8*, 85714-85728. doi:10.1109/ACCESS.2020.2991734

Cao, T., Jin, Y., Hu, X., Zhang, S., Qian, Z., Ye, B., & Lu, S. (2022). Adaptive provisioning for mobile cloud gaming at edges. *Computer Networks*, *205*, 108704. doi:10.1016/j.comnet.2021.108704

Chen, H., Zhang, X., Xu, Y., Ren, J., Fan, J., Ma, Z., & Zhang, W. (2019). T-Gaming: A Cost-Efficient Cloud Gaming System at Scale. *IEEE Transactions on Parallel and Distributed Systems*, *30*(12), 2849-2865. doi:10.1109/TPDS.2019.2922205

Cruz, P., Achir, N., & Viana, A. C. (2022). On the Edge of the Deployment: A Survey on Multi-access Edge Computing. *ACM Computing Surveys*, *55*(5), 1-34. doi:10.1145/3529758

CryEngine (2023). The complete solution for next generation game development by Crytek. (Accessed:10/08/2023) URL

Danevičius, E., Maskeliūnas, R., Damaševičius, R., Połap, D., & Woźniak, M (2018). A Soft Body Physics Simulator with Computational Offloading to the Cloud. *Information*, *9*(12), 318. doi:10.3390/info9120318

Deutsch, P. (1996, May). DEFLATE Compressed Data Format Specification version 1.3. Network Working Group. (Accessed:10/08/2023) URL

Efe, A., & Önal, E. (2020). ONLINE Game Security: A Case Study of an MMO Strategy Game. *Gazi University Journal of Science Part A: Engineering and Innovation*, *7*(2), 43-57.

Godot (2023). Free and open source 2D and 3D game engine. (Accessed:31/07/2023) URL

Gregory, J. (2018). *Game Engine Architecture*. CRC Press.

Artuñedo Guillen, D., Sayadi, B., Bisson, P., Wary, J. P., Lonsethagen, H., Antón, C., de la Oliva, A., Kaloxylos, A., & Frascolla, V. (2020). *Edge computing for 5G networks* - white paper. Zenodo. doi:10.5281/zenodo.3698117

Hatledal, L. I., Chu, Y., Styve, A., & Zhang, H. (2021). Vico: An entity-component-system based co-simulation framework. *Simulation Modelling Practice and Theory*, *108*, 102243. doi:10.1016/j.simpat.2020.102243

Havok (2023). Havok Physics, Make game worlds real. (Accessed:10/08/2023) URL

Huang, C.-Y., Chen, K.-T., Chen, D.-Y., Hsu, H.-J., & Hsu, C.-H. (2014). GamingAnywhere: The first open source cloud gaming system. *ACM Transactions on Multimedia Computing, Communications, and Applications*, *10*(1s), 10. doi:10.1145/2537855

Maggiorini, D., Ripamonti, L. A., Zanon, E., Bujari, A., & Palazzi, C. E. (2016). *SMASH: A distributed game engine architecture*. In: IEEE Symposium on Computers and Communication (ISCC 2016), (pp. 196-201), Messina.

Mazzuca, L. (2022). *Distributed Cloud Gaming Pipeline*. MSc Thesis, Universidad Complutense de Madrid.

Mehrabi, A, Siekkinen, M., Kämäräinen, T., & yl¨-J¨¨ski, A. (2021). Multi-Tier CloudVR: Leveraging Edge Computing in Remote Rendered Virtual Reality. *TrACM Transactions on Multimedia Computing, Communications, and Applications*, *17*(2), 49. doi:10.1145/3429441

Messaoudi, F., Ksentini, A., & Simon, G. (2015). *Dissecting games engines: The case of Unity3D*. In: International Workshop on Network and Systems Support for Games (NetGames 2015), (pp. 1-6), Zagreb.

Messaoudi, F., Ksentini, A., & Bertin, P. (2018). *Toward a Mobile Gaming Based-Computation Offloading*. In: IEEE International Conference on Communications (ICC 2018), (pp. 1-7), Kansas City.

Nagle, J. (1984). Congestion Control in IP/TCP Internetworks. Network Working Group. (Accessed:10/08/2023) URL

Nowak, T. W., Sepczuk, M., Kotulski, Z., Niewolski, W., Artych, R., Bocianiak, K., Osko, T., & Wary, J.-P. (2021). Verticals in 5G MEC-Use Cases and Security Challenges. *IEEE Access*, *9*, 87251-87298. doi:10.1109/ACCESS.2021.3088374

Nyamtiga, B. W., Hermawan, A. A., Luckyarno, Y. F., Kim, T.-W., Jung, D.-Y., Kwak, J. S., & Yun, J.-H. (2022). Edge-Computing-Assisted Virtual Reality Computation Offloading: An Empirical Study. *IEEE Access*, *10*, 95892-95907. doi:10.1109/ACCESS.2022.3205120

OpenGL (2023). The Industry's Foundation for High Performance Graphics. (Accessed:15/06/2023) URL

Politowski, C., Petrillo, F., Montandon, J. E., Valente, M. T., & Guéhéneuc, Y.-G. (2021). Are game engines software frameworks? A three-perspective study. *Journal of Systems and Software*, *171*, 110846. doi:10.1016/j.jss.2020.110846

Physx (2023). NVIDIA PhysX® is an open source, scalable, multi-platform physics simulation solution supporting a wide range of devices, from smartphones to high-end multicore CPUs and GPUs. (Accessed:10/08/2023) URL

Rapier (2023). Fast 2D and 3D physics engine for the Rust programming language. (Accessed:15/06/2023) URL

Rust (2023). A language empowering everyone to build reliable and efficient software. (Accessed:15/06/2023) URL

Unity (2023). Unity Real-Time Development Platform 3D, 2D, VR & AR Engine. (Accessed:10/08/2023) URL

Unreal (2023). The world's most open and advanced real-time 3D creation tool. (Accessed:10/08/2023) URL

Vagavolu, D., Agrahari, V., Chimalakonda, S., & Venigalla, A., S., M. (2021). *GE526: A Dataset of Open-Source Game Engines*. In: IEEE/ACM 18th International Conference on Mining Software Repositories (MSR 2021), (pp. 605-609), Madrid.

Vulkan (2023). Cross platform 3D Graphics. (Accessed:15/06/2023) URL

Optimization of Green Synthesis Parameters of Silver Nanoparticles with Factorial Design for Dye Removal

Gülçin DEMİREL BAYIK[1*] iD　Busenur BAYKAL[1] iD

[1]Zonguldak Bulent Ecevit University, Department of Environmental Engineering, Zonguldak, Türkiye

Keywords	Abstract
Silver Nanoparticles Factorial Design Green Synthesis Dye Removal Adsorption	In this study production of silver nanoparticles (AgNPs) from collard greens were optimized by the design of experiments (DOE). A 2^4 full factorial design was employed to evaluate the effects on two responses. The optimized values for AgNP production were 1:7 leaf to water, 1:4 extract to $AgNO_3$, 5 molar $AgNO_3$, and a leaf size of <1 mm. For dye removal efficiency, the optimized values were changed to 1:15 of leaf to water and 1:10 of extract to $AgNO_3$, while the other two parameters remained the same. SEM (scanning electron microscopy) showed that optimizing the process for dye removal led to smaller AgNP production with increased surface area, resulting in higher absorbency. ANOVA (analysis of variance) tables were used to interpret each parameter's main and effects on interaction. Additionally, reaction rate kinetics were estimated, and dye removal showed a slightly higher R-square of pseudo second-order than NP production, which fits the pseudo first-order reaction model.

Cite

1. INTRODUCTION

Nanotechnology refers to the process of creating and manufacturing materials and technologies at the nanoscale. The fabrication of nanoparticles utilizing various metals, including zinc oxide, copper oxide, gold, and silver is one of the most exciting fields of nanotechnology study. By precisely controlling the size, shape, and chemical composition of nanoparticles, scientists can produce distinct materials with tailored properties suitable for various applications. This innovative technology is advancing rapidly and has the potential to revolutionize various industries (Golli et al., 2023). Silver nanoparticles (AgNPs) have gained substantial interest in different research areas with their outstanding electrical conductivity, catalytic characteristics, and antibacterial capabilities (Min et al., 2023).

AgNPs can be produced in several ways, involving physical, chemical, and biological methods. Because of its environmentally benign and sustainable approach, green synthesis for AgNPs has been an important research subject in the field of AgNP synthesis. This approach has various advantages, including low energy usage and the use of mild reaction conditions, making it a preferred choice among researchers (Nie et al., 2023). Plants are one of the biological agents used in the green synthesis of NPs. Due to their natural phytochemical structure, which includes terpenes, flavonoids, and antioxidants that play role in reducing process for nanoparticle production (Jeevanandam et al., 2016).

Nanoparticles posess a variety of physicochemical features, including an increased surface-to-volume ratio, smaller size, catalytic potential, thermal and electrical conductivity, and optical absorption. Catalysts, active food packaging materials, environmental remedies, antimicrobial activity, filters, chemical sensors, medical

*Corresponding Author, e-mail: gulcin.demirel@beun.edu.tr

imaging, and nanocomposites can all be made from metal nanoparticles with adjustable sizes, shapes, and compositions (Iravani, 2011; Silva et al., 2015; Rastogi et al., 2017). Silver nanoparticles (AgNPs) constitute a common type of metal nanoparticle used in cosmetics, water treatment, medicine, and pharmaceuticals (Rastogi et al., 2017).

Environmental applications for nanomaterials include removing bacteria, heavy metals, and aromatic polycyclic hydrocarbons (PAHs), the degradation of carbon tetrachloride, a key function in the desulfurization process, and the remediation of pesticides, chlorinated organic solvents, and dye-contaminated water bodies (Kumar Das et al., 2022). Among numerous water pollutants, chemical dyes are a significant contributor to industrial water pollution and a significant environmental risk. Three common water contaminants have been recognized as carcinogenic and mutagenic: Congo red (CR), Rhodamine B (RhB), and Methylene blue (MB). MB becomes absorbed in suspended particles and is unable to evaporate or decompose in water, although it does not bioaccumulate in aquatic animals, according to the US Environmental Protection Agency (EPA) (Ngoc et al., 2022). Synthetic dyes deriving from different industries like textile, plastic, paper, and food industries are treated by conventional methods such as adsorption, advanced oxidation, photocatalytic oxidation, radiation, and membrane separation (Wang et al., 2018; Jiang et al., 2019; David & Moldovan, 2020). Among these methods, the adsorption method is well known for being advantageous because it is cost-effective and easy to manage (Çimen et al., 2019; Yaghoobi et al., 2023). Choosing a high-performance adsorbent is critical to achieving a successful and effective adsorption process. A recent study indicates that porous metal oxides are effective solid adsorbents for water contaminants. These materials are advantageous in adsorption process because they have a large surface area and they have many chemically active sites, and functionalization capability (Lee et al., 2013).

In this study, design of experiments (DOE) has been used as a method to assess the effects of two optimization conditions on the two responses, namely NP production quantity and dye removal efficiency. The synthesis of AgNPs was accomplished by reacting collard green leaf (*Brassica oleracea acephala*) with AgNO$_3$ to reduce silver ions. A two-level full factorial design (FFD) was employed, where all possible combinations of parameter levels were examined to analyze the results.

2. MATERIAL AND METHOD

Experimental Design

The experimental program was created using a full factorial design with three replicates. The the influence of four distinct parameters on the amount of produced Ag nanoparticles (AgNP) was investigated. Minitab 18 statistical software was used to design and analyze the process. Four parameters with two levels were used in the design. The parameters were the ratio of water to plant leaf (LW) in the extraction stage, the ratio of extract to AgNO$_3$ (EAgNO3), the molarity of AgNO3 (Mol), and the plant leaf size (LS). Response factors were selected as the amount of AgNPs synthesized (g) and dye removal efficiency (%). A total of 48 experiments with 3 replicates were designed with the two levels are shown in Table 1.

Table 1. Experimental design parameters

Parameter	Unit	Low Level (-1)	High Level (+1)
Leaf:water (LW)	g/ml	1:7	1:15
Extract:AgNO₃ solution (EAg)	ml/ml	1:4	1:10
Molarity AgNO₃(Mol)	Mol	1	5
Leaf size(LS)	mm	<1	2
Response			
NP amount produced	g		
Dye removal	%		

Plant Biomass and Extraction Procedure

Black collard greens were harvested from gardens in Anatolia's western Black Sea region, Zonguldak, Turkey. First tap water was used to clean the plant leaves, then they were soaked in distilled water to purify any pollutants, and finally dried at ambient temperature in the lab. After drying, the leaves were then chopped and sieved through an 18 mesh sieve. They were then placed in plastic bags until they were used.

12 g of dried leaves were placed to a 250 mL beaker, followed by 180 mL of distilled water to achieve a certain leaf-to-water ratio. For 10-15 minutes, the beaker was whirled in a magnetic stirrer at 100°C until the solution color was turned from yellow to brown. After cooling down, it was passed through a vacuum filter.

Ag Nanoparticle Synthesis and Characterization

Previously prepared plant extracts were reacted with a specific amount of $AgNO_3$ to achieve the necessary ratio. The development of nanoparticles was noticed by a color change from brown to pale yellow and then back to brown after the nanoparticles formed. The nanoparticle formation was determined with a Schimadzu UV-1800 spectrophotometer between 300-700 nm for 24 hours. After the reaction, the reaction solution was dried in an incubator at 105 °C for 24 hours. The beaker was then cleaned with distilled water and vacuum-filtered using filter paper from Whatman No. 1. Filter sheets were dried in an incubator at 105°C for two hours. The characterization of the structure and molecular morphology were achieved by scanning electron microscopy (SEM).

Batch Adsorption Test

Dye removal studies were carried out in batch reactors using 50 mL beakers containing 0.5 mg/L Methylene Blue (MB). The beaker was filled with 0.02 g of AgNP, and the samples were kept under sunlight. After 24 h, samples were taken, and color was measured at 664nm in the spectrophotometer. The methylene blue uptake on the NPs and percentage of removal were calculated by:

$$qe = ((Co − Ct) × V)/W \tag{1}$$

$$Removal\ (\%) = (Co − Ct)/Co × 100 \tag{2}$$

Here, Co indicates the beginning concentration (mg/L), Ct the concentration at time t (mg/L), V the volume of solution (L), and W the weight of NPs (g).

3. RESULTS AND DISCUSSION

Analysis of Factorial Design

Figure 1 represents synthesized nanoparticles with observed color changes indicating nanoparticle formation and an increase in absorption peaks in the direction of the arrow from 5 min to 24 h.
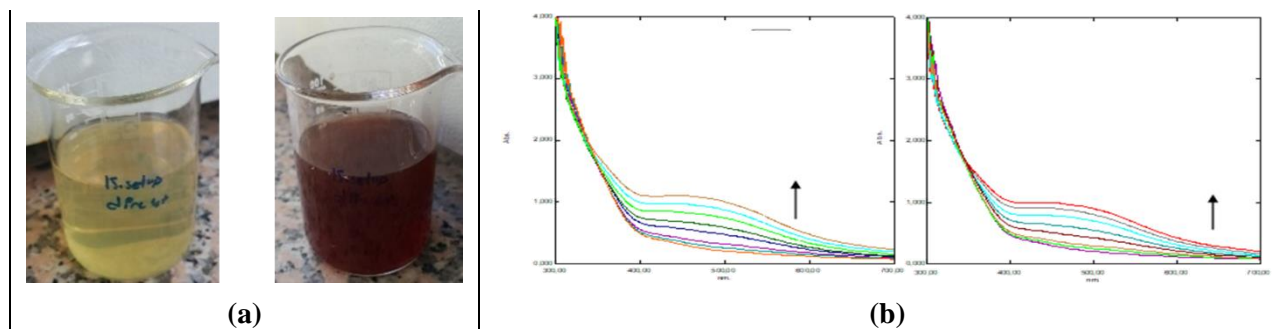

(a)   **(b)**

Figure 1. Color change and absorption peaks during nanopartcile synthesis
a) color change from pale yellow to brown b) UV absorption peaks between 5 min-24 h.

Surface plasmon resonance (SPR) occurs in AgNPs containing free electrons, resulting in the creation of an absorbance band (Noginov et al., 2007). This distinct property enables silver-containing metal nanoparticles to absorb in the ultraviolet-visible (UV-VIS) region. As a result, SPR is a useful instrument for monitoring the reduction of Ag+ ions. Because of surface plasmon resonances, the absorption spectra of AgNPs exhibit maximal absorption within the region of 400-500 nm during the process (Akter et al., 2018; Imanzadeh & Hadi, 2018). When examining the UV spectrum presented in Figure 1, it becomes evident that the band gap corresponding to surface plasmon resonance (SPR) varies within the range of 430-460 nm. This variation in the SPR band gap coincides with the formation of nanoparticles, as observed in the spectrum.

Based on a factorial design of four independent parameters at two levels in triplicate, a total of 48 runs of NP production and dye removal experiments were performed. The responses were given as an averaged mean in Table 2.

Table 2. Summary of the full factorial design

Run	Leaf:Water (g/ml)	Extract:AgNO₃ (ml/ml)	Mol AgNO₃ (mmol)	Leaf Size (mm)	Response (gr NP)	Response Removal (%)
1	1:7	1:4	1	1	0.2165	38.83
2	1:7	1:10	1	1	0.1091	63.91
3	1:15	1:10	1	1	0.1299	45.90
4	1:15	1:4	5	1	0.2567	43.23
5	1:7	1:10	5	1	0.2471	43.54
6	1:7	1:4	1	2	0.2030	44.62
7	1:15	1:4	1	2	0.1676	61.11
8	1:7	1:10	1	2	0.1212	54.44
9	1:15	1:10	1	2	0.0634	
10	1:7	1:4	5	2	0.2968	35.47
11	1:7	1:10	5	2	0.2838	53.16
12	1:15	1:10	5	2	0.2197	49.88
13	1:15	1:4	1	1	0.1888	51.87
14	1:15	1:4	5	2	0.2810	62.67
15	1:7	1:4	5	1	0.3974	56.12
16	1:7	1:4	1	2	0.203	44.62

An ANOVA test has been performed to establish the statistical significance of the model's and variables' fit. Tables 3 and 4 show ANOVA tables for nanoparticulate formation and dye removal. In the ANOVA table, DF indicates the degree of freedom, ADJ SS refers to the sum of squares, ADJ MS indicates mean squares, F represents the distribution factor, and p refers to the significance factor. A statistically significant parameter should have a p-value less than 0.05 at a 95% confidence level. The reaction factor with the highest F value was the most effective. The ANOVA tables reveal that the design model fits the data (p0.05) and that all parameters in nanoparticulate formation and dye removal efficiency are statistically significant, with the exception of the LW ratio, which has a p value of >0.05 in Table 3. The 2-way interactions LW x EAg, LW x Mol, and EAg x Mol, as well as the 3-way interactions LW x EAg x Mol, LW x Mol x LS, and EAg x Mol x LS, all have p-values of 0.05, indicating statistically significant effects. Contributions from two-way and three-way interactions account for 2.65 and 5.84 percent of total contributions, respectively. The term molarity had the highest contribution, with 58.77 for NP production. In the case of dye removal efficiency, all the 2-way and 3-way interactions are statistically significant with a p-value of < 0.05. The prob > F value was greater than 0.050, indicating insignificant terms could be eliminated from the model. Contrary to NP production, the contribution of 2-way and 3-way interactions to the removal response is quite high, 45.42% and 47.11%, respectively.

Table 3. *ANOVA for selected factorial model response of produced nanoparticles*

| Source	DF	Adj SS	Adj MS	F-Value	P-Value	Percent Contribution
Model	15	0.307912	0.020527	48.84	0.000	95.94
Linear	4	0.275584	0.068896	163.92	0.000	85.87
LW (Leaf:water)	1	0.020087	0.020087	47.79	0.000	6.26
EAg (Extract:AgNO$_3$)	1	0.065023	0.065023	154.70	0.000	20.26
Mol (Molarity AgNO$_3$)	1	0.188626	0.188626	448.79	0.000	58.77
LS (Leaf Size)	1	0.003810	0.003810	9.06	0.005	1.19
2-Way Interactions	6	0.008520	0.001420	3.38	0.011	2.65
LW*EAg	1	0.002087	0.002087	4.97	0.033	0.65
LW*Mol	1	0.003172	0.003172	7.55	0.010	0.99
LW*LS	1	0.000036	0.000036	0.09	0.771	0.01
EAg*Mol	1	0.002072	0.002072	4.93	0.034	0.65
EAg*LS	1	0.001087	0.001087	2.59	0.118	0.34
Mol*LS	1	0.000204	0.000204	0.48	0.491	0.06
3-Way Interactions	4	0.018744	0.004686	11.15	0.000	5.84
LW*EAg*Mol	1	0.000546	0.000546	1.30	0.263	0.17
LW*EAg*LS	1	0.011187	0.011187	26.62	0.000	3.49
LW*Mol*LS	1	0.004565	0.004565	10.86	0.002	1.42
EAg*Mol*LS	1	0.002478	0.002478	5.90	0.021	0.77
4-Way Interactions	1	0.002064	0.002064	4.91	0.034	0.64
LW*EAg*Mol*LS	1	0.002064	0.002064	4.91	0.034	0.64
Error	31	0.013029	0.000420			4.06
Total	46	0.320942				100.00

The model's R^2 value is 95.94%, which is adequate for describing the observed data. The modified R-squared statistic is 93.98%.

Figure 2 depicts the residuals analysis performed to confirm the ANOVA assumptions. Normal probability plots of standardized residuals fit quite well against the standardized residuals, as seen in the figure, indicating that the model prediction statistically fits the data. Figure 2 also depicts standardized residuals in relation to experimental runs, standardized residuals in relation to estimated values, histogram plots of the standardized residuals, and a normal probability map of the residuals' analysis results. The data showed no trend in the distribution of the standardized residual vs the fitted value, indicating that the constant variance assumption was valid. As a result, both the normality and constant variance assumptions were met.

Table 4. *ANOVA for selected factorial model response of dye removal*

Source	DF	Adj SS	Adj MS	F-Value	P-Value	Percent Contribution
Model	14	3542.25	253.02	10.89	0.000	83.56
Linear	4	719.65	179.91	7.74	0.000	16.98
LW	1	80.92	80.92	3.48	0.072	1.91
EAg	1	173.83	173.83	7.48	0.010	4.10
Mol	1	509.41	509.41	21.92	0.000	12.02
LS	1	491.05	491.05	21.13	0.000	11.58
2-Way Interactions	6	1925.33	320.89	13.81	0.000	45.42
LW*EAg	1	1419.11	1419.11	61.08	0.000	33.48
LW*Mol	1	951.17	951.17	40.94	0.000	22.44
LW*LS	1	173.02	173.02	7.45	0.011	4.08
EAg*Mol	1	403.36	403.36	17.36	0.000	9.51
EAg*LS	1	828.37	828.37	35.65	0.000	19.54
Mol*LS	1	259.38	259.38	11.16	0.002	6.12
3-Way Interactions	4	1996.95	499.24	21.49	0.000	47.11
LW*EAg*Mol	1	1468.75	1468.75	63.21	0.000	34.65
LW*EAg*LS	1	1442.12	1442.12	62.07	0.000	34.02
LW*Mol*LS	1	424.54	424.54	18.27	0.000	10.01
EAg*Mol*LS	1	777.03	777.03	33.44	0.000	18.33
Error	30	697.03	23.23			16.44
Total	44	4239.28				100.00

The model's R^2 value is 83.56%, and the corrected R-squared statistic is 75.88%.
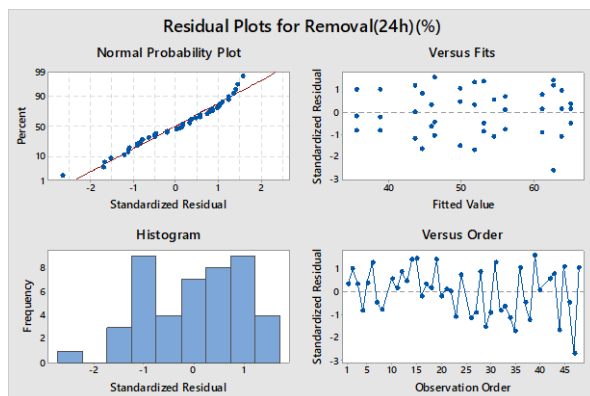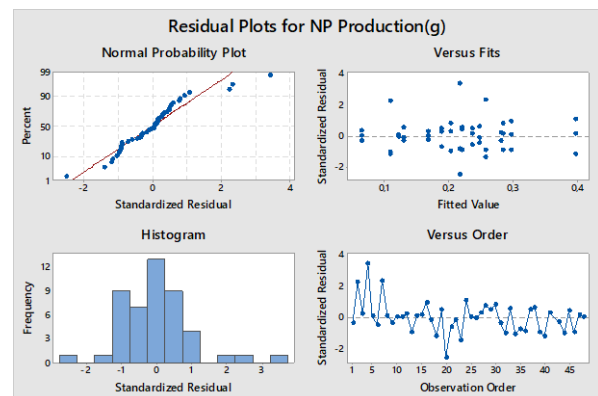
(a)   (b)

Figure 2. *Analysis of residuals **a)** for response removal **b)** for response NP production*

Figures 3 and 4 show the normal probability plots of the standardized effects for NP production and dye removal, respectively, to help analyze each factor and its interaction. There are two distinct regions on each of the two plots: one below 50%, where the factors and their interactions demonstrated significant negative coefficients, and one above 50%, where the factors and their interactions demonstrated significant positive coefficients. When the data in the ANOVA tables is compared to the graphs in Figures 3 and 4, it is apparent that the molarity of $AgNO_3$ is the most important component in the NP formation process. The extract to $AgNO_3$ ratio is the second crucial element. The third important factor is the ratio of leaf to water, and finally, 2-way interactions among LW, EAg, and Mol are important. According to the graphs and ANOVA tables, the variable LS shows a significant adverse impact on NP production. While the two-way interactions between LS and other parameters are insignificant, the three-way interactions between LS and other parameters have a significant negative influence on NP production. The synergical effect of LWxEAgxMol is the most significant term in the dye removal effectiveness of produced nanoparticles, followed by the interaction of EAgxLS and the main influence of Mol. The 2- way interactions of EAgxMol, LWxMol, and LWEAg and the 3-way interactions of LWxMolxLS, EAgxMolxLS, and LWxEAgxLS are also significant terms with negative coefficients.
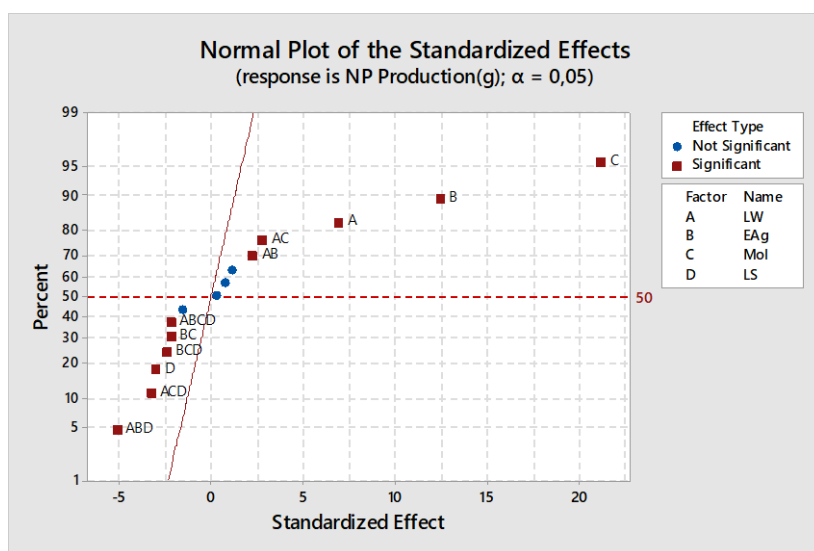

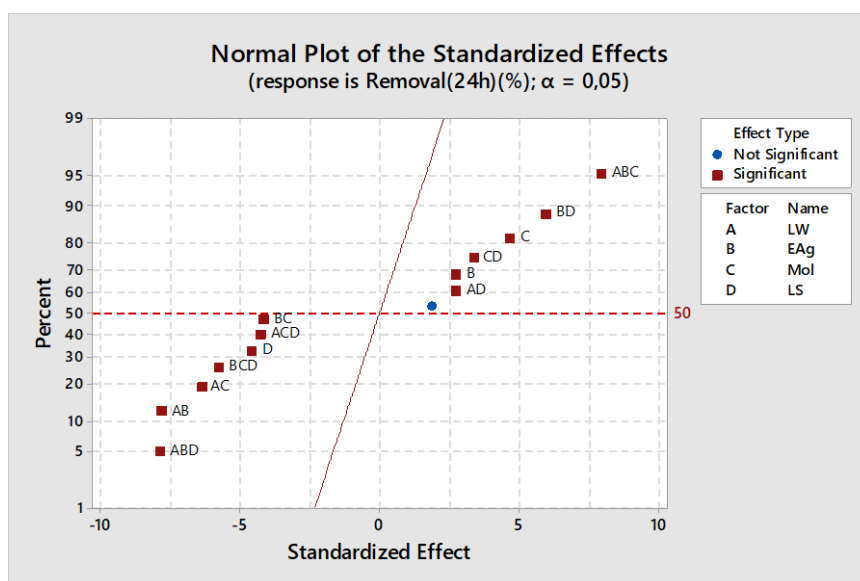*Figure 3.* The standardized effects for NP production

Figure 4. The standardized effects for dye removal

Regression equations of the NP generation and dye removal are given together with all of the main and interaction effects of all factors in Equation 1 and Equation 2.

NP Produced (gr)= 0,21359 + 0,02077 LW + 0,03738 EAg + 0,06366 Mol - 0,00905 LS + 0,00670 LW*EAg + 0,00826 LW*Mol + 0,00088 LW*LS - 0,00667 EAg*Mol - 0,00483 EAg*LS + 0,00209 Mol*LS + 0,00342 LW*EAg*Mol - 0,01550 LW*EAg*LS - 0,00990 LW*Mol*LS - 0,00730 EAg*Mol*LS - 0,00666 LW*EAg*Mol*LS   (3)

Removal efficiency (24 hour) (%) = 46,927 + 1,836 LW + 2,691 EAg + 4,607 Mol - 4,523 LS - 7,690 LW*EAg - 6,295 LW*Mol + 2,685 LW*LS - 4,100 EAg*Mol + 5,875 EAg*LS + 3,288 Mol*LS + 7,823 LW*EAg*Mol - 7,752 LW*EAg*LS - 4,206 LW*Mol*LS - 5,690 EAg*Mol*LS   (4)

Table 5 displays the outcomes of the experimental data optimization. The factors mol $AgNO_3$ and leaf size are the same for boyh responses. At the optimum conditions for maximum NP production (LW 1:7; EAg 1:4), a removal efficiency of 56.12% was achieved. When the ratio of leaf to water was increased to 1:15 and the extract to $AgNO_3$ to 1:10, the removal efficiency reached a maximum value of 65.52%.

Table 5. *Optimum AgNPs synthesis conditions*

Responses	Leaf:Water (LW)	Extract:AgNO$_3$ (EAg)	Mol AgNO$_3$ (Mol)	Leaf Size (LS)	Maximum Yield
NP Production (g)	1:7	1:4	5	<1	0.397
Dye Removal (%)	1:15	1:10	5	<1	65.52

A fast response rate, a short contacting time, and a high capacity for adsorption are essential for an efficient adsorption process. Adsorption features are better understood when reaction rate equations are used to explain the variance in the effective number of functioning sites on the adsorbent surface throughout adsorption (Liu et al., 2019). Equations 5-6 provide the linear form of the pseudo-first-order and pseudo-second-order kinetic models, respectively.

$$ln\,(qe - qt) = lnqe - k_1 t \qquad (5)$$

$$\frac{t}{qt} = \frac{1}{k_2\,qe^2} + \frac{1}{qe} \qquad (6)$$

Here k_1 is the pseudo-first-order rate constant, k_2 is the pseudo-second-order rate constant, qe is the quantity of dye adsorbed at equilibrium per unit weight of the adsorbent (mg g^{-1} min^{-1}) and qt is the amount of solute adsorbed (mg g^{-1}min^{-1}) at a time 't', and t is the time (min).

Figure 5 presents linear fits of the pseudo-first order and pseudo-second order kinetics, and Table 6 presents the derived corresponding factors. The elimination of methylene blue best fits the pseudo-first-order model under the conditions required to optimize NP production, with an R^2 of 0.979. Although the R^2 of pseudo first order and pseudo second order reaction kinetics are nearly the same, pseudo second order is slightly higher (0.981) for NPs produced under optimal conditions to enhance dye elimination. The rate constants of pseudo-first-order reactions are greater than those of pseudo-second-order reactions. The pseudo-first-order approach implies that the adsorption rate corresponds to the difference between the saturation concentration (qe) and the rate of solute uptake with time t (qt). The pseudo-second-order equation, on the contrary, assumes that the sorption is governed by a chemical adsorption process governed by electron sharing or transfer (Zhang et al., 2016). Bhargavi et al. (2015) studied the color black G (CBG) removal with ZnO nanoparticles, and they claim that the adsorption was best explained by the pseudo-first-order kinetics. MgO NPs adsorbed two different dyes, Reactive Blue 19 and Reactive Red, 198, representing azo and anthraquinone dyes. The kinetic tests of both dyes revealed a pseudo-second-order model (Moussavi & Mahmoudi, 2009). The pseudo-second-order kinetic method was used for removing the anionic dye known as methyl orange using Co_3O_4 nanoparticles (Uddin & Baig, 2019).
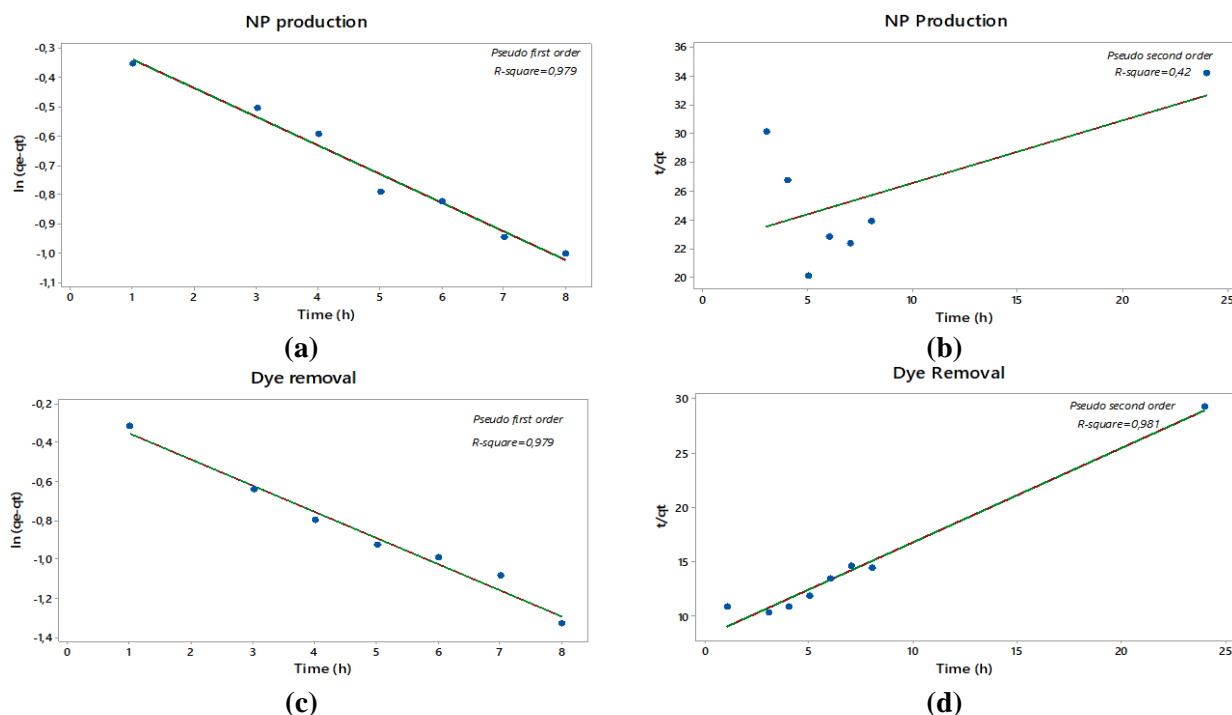
Figure 5. *Linear form of the reaction models fitted for the responses*
*NP production **a**) pseudo first order **b**) pseudo second order and*
*dye removal **c**) pseudo first order **d**) pseudo second order*

Table 6. *Reaction rate constants for pseudo-first-order and pseudo-second-order model*

	Pseudo first order		Pseudo second order	
	qe (mg/g)	K1 (min⁻¹)	qe(mg/g)	K2 (min⁻¹)
Maximum NP production	0,79	0,01224	2,29	0,0086
Maximum dye removal	0,80	0,01675	1,15	0,0092

Characterization of the produced nanoparticles

The scanning electron microscope (SEM) technique has been performed to identify the morphological structure of the silver nanoparticles. The SEM images of the particles produced under the optimized conditions of response NP production and dye removal are given in Figure 6. The figures show that the produced nanoparticles are unevenly distributed in size and have irregular shapes.

The particle size distribution of NPs optimized for dye removal is wide, based on SEM size measurements, showing the presence of smaller particles that contribute to a higher removal effectiveness. The information provided suggests that there is a difference in the size of NPs observed under 100000x magnification between the production experiments and the dye removal experiments. The size of the NPs observed during the production experiments was 71-219 μm, while the size of the NPs detected during the dye removal studies was 49-75 μm. The smaller NPs with a wider size distribution can provide more surface area for interactions with the dye molecules, leading to a higher removal efficiency. Silver nanoparticles with a large surface area act as a fitting catalyst for the electron transfer reaction of methylene blue molecules (Vidhu & Philip, 2014; VenkataRao et al., 2020)

Particle size and surface area analysis was conducted by a mastersizer. This analytical approach characterizes particle size distribution and gives useful information about the surface area of nanoparticles. Plant-mediated silver nanoparticles are often polydispersed due to the existence of a variety of reducing compounds in the plant extract. This results significant heterogeneity in shape and size of the nanoparticles (Bala & Rani, 2020).
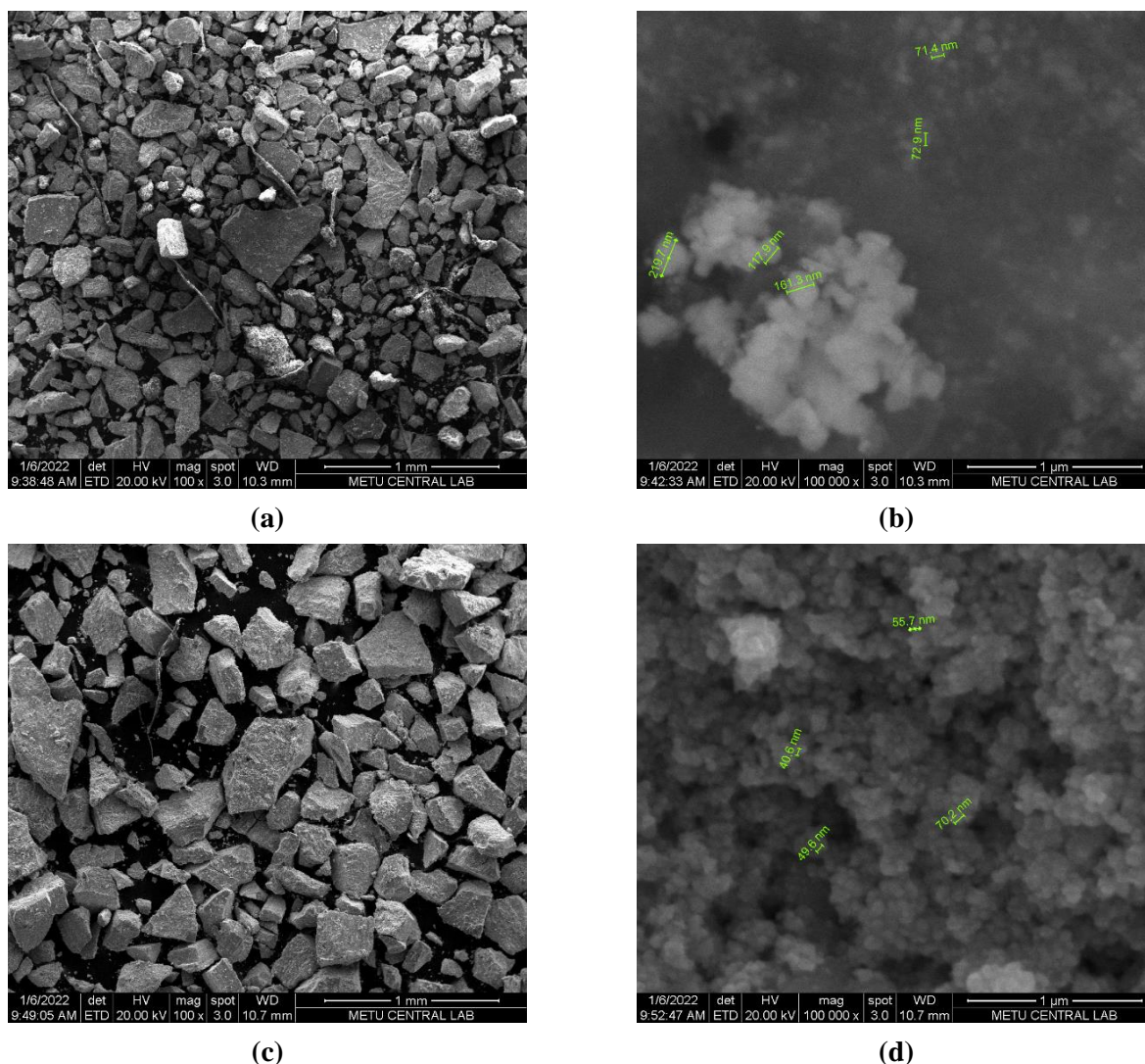
Figure 6. *SEM images of the NPs produced at the optimum conditions of*
a), b) NP production c), d) dye removal

Figure 7 shows that under conditions where nanoparticle production is maximized, the particle sizes exhibit a narrower distribution within a specific range. However, under conditions where the dye removal efficiency is maximized, the particle size variation spans a wider range. The specific surface areas are measured as 0.0833 and 0.202 m²/g for NP production and dye removal, respectively. The existence of smaller particles under dye removal circumstances leads to a more even distribution of particle sizes, which gives a larger surface area. This increased surface area allows for greater dye removal effectiveness. The smaller particles provide greater activity locations for dye molecules to interact with, increasing the overall efficacy of the removal process.

Researchers have investigated the parameters influencing nanoparticle synthesis, which include pH, extract concentration, and metal salt concentration. The relationship between the morphological properties of nanoparticles and synthesis conditions was evaluated. Venugobal and Anandalakshmi (2016) have produced silver nanoparticles from Commiphora caudata leaf extract. Their research concludes that, the absorbance of the generated nanoparticles increases with the percentage of the extract of leaves. The maximum absorbance was recorded at increased leaf extract concentrations (5 ml). Because of the higher leaf concentrate, symmetrical nanoparticles were generated (Venugobal & Anandalakshmi, 2016). A different study utilised Acalypha hispida to modify the physicochemical properties of the silver nanoparticles. Silver nanoparticles produced within 20-50 nm have a spherical shape that is reliant on the quantity of plant extract (Sithara et al., 2017). It has been found that when the volume of plant extract increases, the absorption peak changes towards longer wavelengths, indicating the existence of large-sized nanoparticles (Rajput et al., 2020). As a result, bigger particles were generated in this investigation as the concentration of the reactive extract of plants rose.
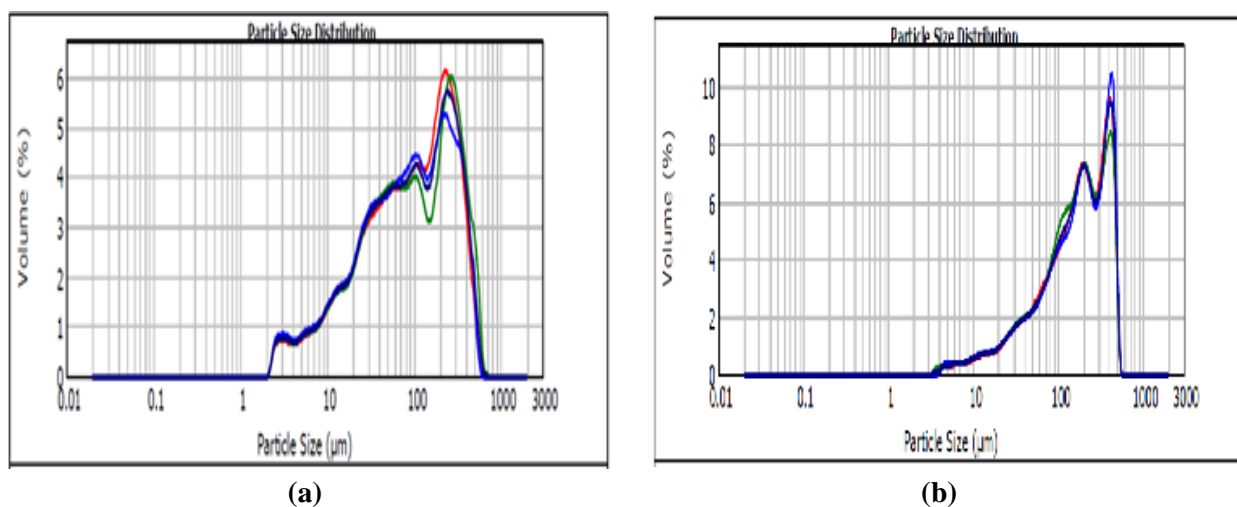
(a)   **(b)**

Figure 7. *Particle size partitioning of the NPs produced at the optimum conditions of*
***a)** NP production, **b)** dye removal*

Silver ion concentration has a considerable influence on the size, shape, and also the extent of silver nanoparticle production. *Syzygium cumini* (*S.cumini*) fruit extract was utilized to synthesize biogenic new silver nanoparticles (AgNP) in a single pot, and it was discovered that there was a direct proportional relationship between metal salt concentration and nanoparticle creation. They discovered a unique SPR band at natural concentrations (0.5 mM-1 mM). As the salt concentration was increased over 1 mM, however, a red (bathochromic) shifting appeared, which suggests an appearance of large-sized and polydisperse nanoparticles (Parmar et al., 2019). Increasing the concentration of $AgNO_3$ was found to increase the synthesis of AgNP. A deformed peak was observed above a concentration of 5 mM of $AgNO_3$. At increasing $AgNO_3$ concentrations, absorption spectra switched to longer wavelengths (426-450 nm), demonstrating increased AgNP production (red-shifted) (Rajput et al., 2020). Saini et al. (2019) discovered during their research on C. corylifolium that the synthesis rate of AgNPs increased with higher concentrations of $AgNO_3$, and the absorption spectra shifted towards longer wavelengths (Abdelghany et al., 2018). In this study, the nanoparticles' dominant size was found to be greater than 70 nm both for NP production and dye removal because the experimental design optimized the concentration of $AgNO_3$ to 5mM.

4. CONCLUSION

The current study used a full factorial design (FFD) to optimize the green synthesis parameters of silver nanoparticle (AgNP) production in order to increase dye removal efficiency. The study has evaluated four parameters, namely the ratio of water to plant leaf, the ratio of extract to AgNO3, the molarity of $AgNO_3$, and the plant leaf size, at two levels each, to determine their effect on the amount of synthesized AgNPs and dye removal efficiency. According to the findings, the factors had a substantial impact on AgNP production and dye removal efficiency. The characterization of synthesized NP were carried out by SEM and mastersizer analysis The analysis confirmed that the sizes of synthesized AgNPs are different for two conditions, which in turn results in differences in dye removal efficiencies. The dye removal efficiency of green-synthesized AgNPs is considerably high, even it was applied at a low dosage (0.02 g). The kinetic analysis confirmed that methylene blue adsorption on AgNPs follows pseudo-first-order reaction kinetics with concentration difference as a driving force. Overall, the research presents a useful framework for optimizing green AgNP production and their prospective uses in water treatment.

ACKNOWLEDGEMENT

CONFLICT OF INTEREST

The authors declare no conflict of interest.

REFERENCES

Abdelghany, T. M., Al-Rajhi, A. M. H., Al Abboud, M. A., Alawlaqi, M. M., Ganash Magdah, A., Helmy, E. A. M., & Mabrouk, A. S. (2018). Recent Advances in Green Synthesis of Silver Nanoparticles and Their Applications: About Future Directions. A Review. *BioNanoScience*, *8*(1), 5-16. doi:10.1007/s12668-017-0413-3

Akter, M., Rahman, Md. M., Ullah, A. K. M. A., Sikder, Md. T., Hosokawa, T., Saito, T., & Kurasaki, M. (2018). Brassica rapa var. japonica Leaf Extract Mediated Green Synthesis of Crystalline Silver Nanoparticles and Evaluation of Their Stability, Cytotoxicity and Antibacterial Activity. *Journal of Inorganic and Organometallic Polymers and Materials*, *28*(4), 1483-1493. doi:10.1007/s10904-018-0818-7

Bala, A., & Rani, G. (2020). A review on phytosynthesis, affecting factors and characterization techniques of silver nanoparticles designed by green approach. *International Nano Letters*, *10*(3), 159-176. doi:10.1007/s40089-020-00309-7

Bhargavi, R. J., Maheshwari, U., & Gupta, S. (2015). Synthesis and use of alumina nanoparticles as an adsorbent for the removal of Zn(II) and CBG dye from wastewater. *International Journal of Industrial Chemistry*, *6*(1), 31-41. doi:10.1007/s40090-014-0029-1

Çimen, B., Şengül, S., Ergüt, M., & Özer, A. (2019). Green Synthesis and Characterization of CuO Nanoparticles: Telon Blue AGLF and Methylene Blue Adsorption. Sinop University Journal of Natural Sciences, *4*(1), 1-20. doi:10.33484/sinopfbd.315643

David, L., & Moldovan, B. (2020). Green Synthesis of Biogenic Silver Nanoparticles for Efficient Catalytic Removal of Harmful Organic Dyes. *Nanomaterials*, *10*(2), 202. doi:10.3390/nano10020202

Golli, R., Thummaneni, C., Pabbathi, D. D., Srungarapu, T., Jayasri, G., & Vangalapati, M. (2023). *Silver nanoparticles synthesized by Brassica oleracea (Broccoli) acting as antifungal agent against Candida albicans*. In: M. Seenuvasan, & D. M. Sangeetha (Eds.), Proceedings of the Second Global Conference on Recent Advances in Sustainable Materials 2022. Materials Today: Proceedings, (vol. 80, part 2, pp. 1495-1500). doi:10.1016/j.matpr.2023.01.284

Imanzadeh, G., & Hadi, R. (2018). Brassica Oleraceae, A Versatile Plant For Green Synthesis of Silver Nanoparticles. *Iranian Chemical Communication*, *6*(1), 70-77.

Iravani, S. (2011). Green synthesis of metal nanoparticles using plants. *Green Chemistry*, *13*(10), 2638-2650. doi:10.1039/C1GC15386B

Jeevanandam, J., Chan, Y. S., & Danquah, M. K. (2016). Biosynthesis of metal and metal oxide nanoparticles. *ChemBioEng Reviews*, *3*(2), 55-67. doi:10.1002/cben.201500018

Jiang, C., Wang, X., Qin, D., Da, W., Hou, B., Hao, C., & Wu, J. (2019). Construction of magnetic lignin-based adsorbent and its adsorption properties for dyes. *Journal of Hazardous Materials*, *369*, 50-61. doi:10.1016/j.jhazmat.2019.02.021

Kumar Das, P., Mohanty, C., Krishna Purohit, G., Mishra, S., & Palo, S. (2022). Nanoparticle assisted environmental remediation: Applications, toxicological implications and recommendations for a sustainable environment. *Environmental Nanotechnology, Monitoring & Management*, *18*, 100679. doi:10.1016/j.enmm.2022.100679

Lee, H. U., Lee, S. C., Lee, Y.-C., Vrtnik, S., Kim, C., Lee, S., Lee, Y. B., Nam, B., Lee, J. W., Park, S. Y., Lee, S. M., & Lee, J. (2013). Sea-urchin-like iron oxide nanostructures for water treatment. *Journal of Hazardous Materials*, *262*, 130-136. doi:10.1016/j.jhazmat.2013.08.014

Liu, X., Tian, J., Li, Y., Sun, N., Mi, S., Xie, Y., & Chen, Z. (2019). Enhanced dyes adsorption from wastewater via Fe3O4 nanoparticles functionalized activated carbon. *Journal of Hazardous Materials*, *373*, 397-407. doi:10.1016/j.jhazmat.2019.03.103

Min, K. H., Shin, J. W., Ki, M.-R., & Pack, S. P. (2023). Green synthesis of silver nanoparticles on biosilica diatomite: Well-dispersed particle formation and reusability. *Process Biochemistry*, *125*, 232-238. doi:10.1016/j.procbio.2022.12.018

Moussavi, G., & Mahmoudi, M. (2009). Removal of azo and anthraquinone reactive dyes from industrial wastewaters using MgO nanoparticles. *Journal of Hazardous Materials*, *168*(2–3), 806-812. doi:10.1016/j.jhazmat.2009.02.097

Ngoc, P. K., Mac, T. K., Nguyen, H. T., Viet, D. T., Thanh, T. D., Van Vinh, P., Phan, B. T., Duong, A. T., & Das, R. (2022). Superior organic dye removal by $CoCr_2O_4$ nanoparticles: Adsorption kinetics and isotherm. *Journal of Science: Advanced Materials and Devices*, *7*(2), 100438. doi:10.1016/j.jsamd.2022.100438

Nie, P., Zhao, Y., & Xu, H. (2023). Synthesis, applications, toxicity and toxicity mechanisms of silver nanoparticles: A review. *Ecotoxicology and Environmental Safety*, *253*, 114636. doi:10.1016/j.ecoenv.2023.114636

Noginov, M. A., Zhu, G., Bahoura, M., Adegoke, J., Small, C., Ritzo, B. A., Drachev, V. P., & Shalaev, V. M. (2007). The effect of gain and absorption on surface plasmons in metal nanoparticles. *Applied Physics B: Lasers and Optics*, *86*(3), 455-460. doi:10.1007/s00340-006-2401-0

Rastogi, A., Zivcak, M., Sytar, O., Kalaji, H. M., He, X., Mbarki, S., & Brestic, M. (2017). Impact of Metal and Metal Oxide Nanoparticles on Plant: A Critical Review. *Frontiers in Chemistry*, *5*, 78. doi:10.3389/fchem.2017.00078

Rajput, S., Kumar, D., & Agrawal, V. (2020). Green synthesis of silver nanoparticles using Indian Belladonna extract and their potential antioxidant, anti-inflammatory, anticancer and larvicidal activities. *Plant Cell Reports*, *39*(7), 921-939. doi:10.1007/s00299-020-02539-7

Parmar, A., Kaur, G., Kapil, S., Sharma, V., Choudhary, M. K., & Sharma, S. (2019). Novel biogenic silver nanoparticles as invigorated catalytic and antibacterial tool: A cleaner approach towards environmental remediation and combating bacterial invasion. *Materials Chemistry and Physics*, *238*, 121861. doi:10.1016/j.matchemphys.2019.121861

Silva, L. P., Reis, I. G., & Bonatto, C. C. (2015). Green Synthesis of Metal Nanoparticles by Plants: Current Trends and Challenges. In: V. A. Basiuk & E. V Basiuk (Eds.), *Green Processes for Nanotechnology: From Inorganic to Bioinspired Nanomaterials*, (pp. 259-275). Springer. doi:10.1007/978-3-319-15461-9_9

Sithara, R., Selvakumar, P., Arun, C., Anandan, S., & Sivashanmugam, P. (2017). Economical synthesis of silver nanoparticles using leaf extract of Acalypha hispida and its application in the detection of Mn(II) ions. *Journal of Advanced Research*, *8*(6), 561-568. doi:10.1016/j.jare.2017.07.001

Uddin, M. K., & Baig, U. (2019). Synthesis of Co_3O_4 nanoparticles and their performance towards methyl orange dye removal: Characterisation, adsorption and response surface methodology. *Journal of Cleaner Production*, *211*, 1141-1153. doi:10.1016/j.jclepro.2018.11.232

VenkataRao, P., SaiTarun, G., Govardhani, Ch., Manasa, B., Joy, P. J., & Vangalapati, M. (2020). *Biosorption of congo red dye from aqueous solutions using synthesized silver nano particles of Grevillea robusta : Kinetic studies*. In: S. K. Singh, E. T. Akinlabi, K. Kumar, J. P. Davim, & K. K. Saxena (Eds.), Proceedings of the 10th International Conference of Materials Processing and Characterization. Materials Today: Proceedings, (vol. 26, part 2, pp. 3009-3014). doi:10.1016/j.matpr.2020.02.626

Venugobal, J., & Anandalakshmi, K. (2016). Green Synthesis of Silver Nanoparticles Using Commiphora caudata Leaves Extract and the Study of Bactericidal Efficiency. *Journal of Cluster Science*, *27*(5), 1683-1699. doi:10.1007/s10876-016-1032-9

Vidhu, V. K., & Philip, D. (2014). Catalytic degradation of organic dyes using biosynthesized silver nanoparticles. *Micron*, *56*, 54-62. doi:10.1016/j.micron.2013.10.006

Wang, J., Zhang, Q., Shao, X., Ma, J., & Tian, G. (2018). Properties of magnetic carbon nanomaterials and application in removal organic dyes. *Chemosphere*, *207*, 377-384. doi:10.1016/j.chemosphere.2018.05.109

Yaghoobi, M., Asjadi, F., & Sanikhani, M. (2023). A facile one-step green hydrothermal synthesis of paramagnetic Fe3O4 nanoparticles with highly efficient dye removal. *Journal of the Taiwan Institute of Chemical Engineers*, *144*, 104774. doi:10.1016/j.jtice.2023.104774

Zhang, F., Chen, X., Wu, F., & Ji, Y. (2016). High adsorption capability and selectivity of ZnO nanoparticles for dye removal. *Colloids and Surfaces A: Physicochemical and Engineering Aspects*, *509*, 474-483. doi:10.1016/j.colsurfa.2016.09.059

Effect of Annealing and Doping Process of the Zn$_{1-x}$Ti$_x$O Films

Tuğba ÇORLU[1,2] Sezen TEKIN[3*] Irmak KARADUMAN ER[3] Selim ACAR[2]

[1]Suleyman Demirel University, Innovative Technologies Application and Research Center, Isparta, Türkiye
[2]Gazi University, Faculty of Science, Department of Physics, Ankara, Türkiye
[3]Çankırı Karatekin University, Eldivan Medical Services Vocational School, Department of Medical Services and Techniques, Çankırı, Türkiye

Keywords	Abstract
Ti-doped ZnO SILAR Annealing Characterization	In this study, undoped and Ti-doped ZnO thin films grown by SILAR (Successive Ionic Layer Adsorption and Reaction) method were investigated using XRD, SEM, linear absorbance and electrical characterization. The effect of doping ratio was determined changing Ti ratios from 0.05 to 0.20. In addition, the films with the same additive ratio were annealed at 300°C for 15 minutes in nitrogen environment. Thus, the effects of both annealing and doping ratio on the thin films produced were examined in detail. When the current-voltage graphs are examined, it is observed that there is a decrease in the resistance values with doping. The best additive effect was observed for Zn0.90Ti0.10O film and the structures formed after this additive ratio returned to their initial morphology.

1. INTRODUCTION

Many studies have been carried out and model systems have been developed to improve the previously known properties of basic physical and chemical properties related to thin film performance and structure in various applications and to increase the progress in this field. The combined results of all these emerging experimental and theoretical investigations form the basis for the development of new thin film systems and shaping their structure and performance.

Thin films must have appropriate thickness, information and characteristic properties in order to exhibit the expected functions. For this purpose, the production studies of higher quality thin films are carried out trying different deposition methods and production on different substrate materials. Different methods are used to control the properties of thin films. One of these methods is the placement of impurity atoms to the structure. The impurity atoms must be smaller or equal in diameter than the host ions, and at the same time, the doping atoms must have an extra electron compared to these ions. This situation is not only one of the most important conditions for doping, but also means fewer crystal defects, since in such a case the lattice tension is less and it also leads to high electrochemical stability.

Titanium (Ti) was chosen as the impurity for ZnO thin films in this study. It has partially filled d shells, and it can replace the ions of the host semiconductor, so that the titanium can easily settle into the structure. In addition, Ti fully complies with the conditions mentioned below. Both ionic and covalent diameters (0.068 nm and 0.136 nm) are closest to those of zinc (0.072 nm and 0.131 nm). In this way, any structural changes or microstructural defects cannot be observed after settling impurity into the structure. Titanium doping has many effects on the properties of zinc oxide. One of them is that the extra free electrons from Ti reduce the electrical

resistance and increase the conductivity (Hsu et al., 2016). The fact that Ti provides two extra free electrons also ensures that doping at a lower concentration is sufficient to achieve a high degree of conductivity, which is costly (Hsu et al., 2016). Another plus of this situation is that due to the improvement of the electrical properties, the response of the structure also increases, and the decrease in the resistance causes more sensor response in general (Shewale & Yu, 2016). In addition, the addition of Ti impurity atoms can reduce the crystal size of the samples and improve the specific surface areas of the samples concerned (Darmadi et al., 2020). Another benefit of Ti doping is that it increases the device capacitance and reduces the reactivity to humidity in the environment. Being a chemically stable material makes it suitable for biochemical detection (Lee et al., 2018). However, one of the most important points to be considered during doping is the amount of titanium to be used, because if the additive is too much, it may settle in the interatomic regions in the structure and the desired properties may not be achieved (Lee et al., 2018).

Various physical and chemical based methods are used to grow thin films. However, these physically-based methods require high costs and superior device performance. Chemical-based methods are more preferred because they are affordable, fast, environmentally friendly and can be found easily. There are some studies about the Ti-doped ZnO samples with different grown methods and investigate physical and chemical methods. Samuel et al. (2022) have predetermined pure and Ti-doped ZnO samples with the hydrazine assisted wet chemical route and searched their physical and chemical properties. Rilda et al. (2023) have been synthesized with the sol-gel process using mediated Aspergillus niger with the four stages of Ti-doped ZnO (Ti/ZnO). The growth and investigation of Ti-doped ZnO nanoparticles subjected to vacuum annealing using solid state reaction by Soniya and Kaleemulla (2023). The basis of the SILAR (Successive Ionic Layer Adsorption and Reaction) method is based on sequential ionic layer adsorption and reaction. In order to avoid homogeneous precipitation on the film, rinsing with deionized water is applied at regular intervals. The originality in this method is the adsorption (deposition) of one substance onto another substance on the substrate. Deposition is achieved by the contact of two different phases. The formation of the film is based on a process resulting from van-der Waals forces or chemical attraction forces that occur between the substrate and the ions in the solution. In this process, factors such as temperature, base feature and surface area, growth rate, pressure and density directly affect the yield. One of the advantages of the SILAR method is enabling the use of temperature-sensitive materials such as insulators, semiconductor metals and polyester. In this way, corrosion and oxidation of the substrate is prevented. Increasing the quality of thin films produced by this method; concentration, solution pH, adsorption, reaction and rinse time parameters. In addition, the thin-film growth technique based on the deposition technique is based on ion-based deposition that occurs in the nucleation regions on the substrate surfaces. The unnecessity of high-quality vacuum and substrate is one of the most important advantages that distinguish the SILAR technique from other expensive techniques. Ade et al. (2021) has reported the doped-ZnO samples produced with SILAR method and the effect of doping on the physical and chemical properties of ZnO samples. In this study, ZnO thin films were grown by the SILAR method with different Ti doping changed from 0.5 % to 0.20 %. The morphological, structural, optical and electrical properties of produced thin films were investigated. In addition, the films with the same additive ratio were annealed at 300 °C for 15 minutes in nitrogen environment. Thus, the effects of both annealing and doping were examined in detail.

2. MATERIAL AND METHOD

2.1. Preparation of Interdigital Electrodes

Initially, glass substrates, for using Ag IDEs, were cut 8 mm wide and 25 mm long. The substrates were cleaned with 20 ml acetone, methanol, and distilled water for 30 min by using an ultrasonic cleaner for each solution, respectively. Substrates dried with dry air were placed on a laser-cut mask with an electrode thickness of 1 mm. Ag metal targets were used to grow IDEs on prepared glass substrates by a thermal evaporation system. Finally, the grown IDEs were annealed at 300 °C in a nitrogen gas environment.

2.2. Preparation of Thin Films

Ti-doped ZnO thin films have been grown by the SILAR method on the glass substrates which the interdigitated Ag electrodes (Ag-IDE) have been evaporated to a side of the substrate. To grow titanium-doped and pure zinc oxide nanostructures, aqueous zinc–ammonia complex ions ($[Zn(NH_3)^4]^{2+}$) and aqueous

titanium–ammonia complex ions ($[Ti(NH_3)^4]^{2+}$) have been chosen as the cation precursors, in which trace metal basis of $ZnCl_2$ (99.9%, Sigma-Aldrich) of 0.1 M as a source for Zn, TiO_2 (99%, Merck) of 0.1 M as a source for Ti and aqueous ammonia solution (NH_3 -28%, Sigma-Aldrich) have been used. Deionized water has been used as a solvent. In order to obtain the ($[Zn(NH_3)^4]^{2+}$) and ($[Ti(NH_3)^4]^{2+}$) complex, $ZnCl_2$, TiO_2, NH_3 and deionized water were mixed in appropriate proportions. All the growth process parameters of nanostructures through the SILAR method are given below, respectively. The glass substrate was kept in the ($[Zn(NH_3)_4]^{2+}$) solution for the product undoped ZnO thin film, which was prepared before, for 15 seconds, firstly. The substrate, which was removed from the solution, was kept in distilled water at 80°C during 7s. The substrates, which were in air during 60 s after hot water, were then immersed in distilled water at 25°C and kept there during 30 s. Thus, a cycle is completed (Figure 1). The same process was used to produce titanium-doped thin films. Differently in the production times of undoped ZnO, the glass substrates were kept in the prepared Ti-doped ZnO solution for 20 seconds, while this time was set as 7 seconds for hot water and 40 seconds for pure water at room temperature. This process was completed with forty cycles. After the growth process samples were dried at room temperature for a day. After taking structural, morphological and electrical characterization they annealed at nitrogen environment for 30 minutes. Structural analysis of thin films was evaluated using the Bragg Brentano method by Bruker D8 Advance Twin-Twin X-ray diffractometer (XRD), scanning electron microscope (SEM, FEI Quanta FEG 250), a UV–Vis–NIR spectrophotometer (Jasco V-770 UV-Vis-NIR) and a Keithley 2400 sourcemeter.
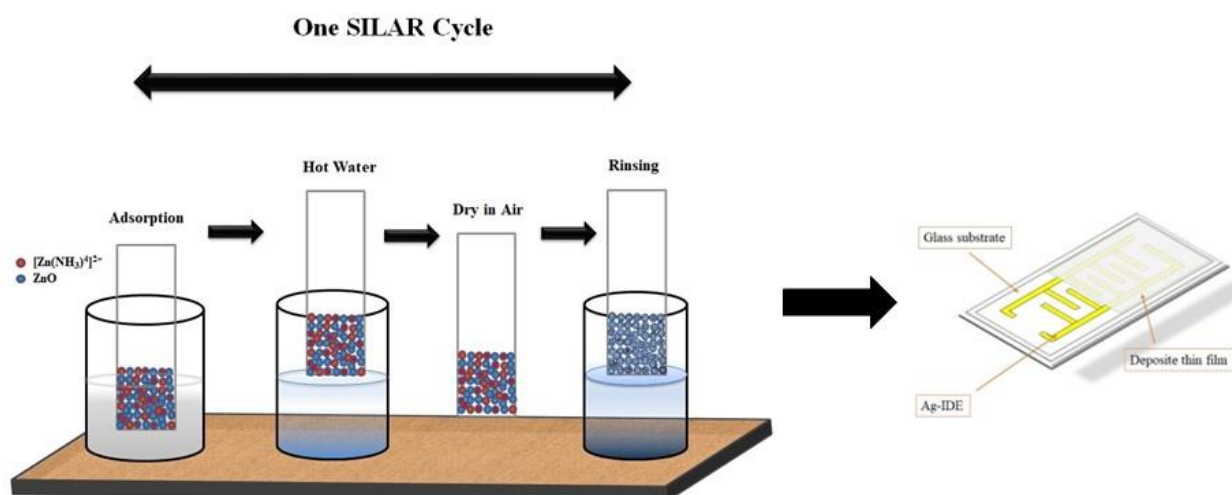

Figure 1. The schematic diagram of SILAR method

3. RESULTS AND DISCUSSION

From Figure 2 to Figure 6 show the SEM images of as-grown and annealed thin films. It was seen that nanorod-like structures were formed as the additive ratio increases in the samples. However, with the $Zn_{0.85}OTi_{0.15}O$ sample, a return to the initial ZnO shape was observed and nanoball-like structures were observed. It was understood that the most suitable doping ratio is 0.10 %. Ti contribution in the $Zn_{0.90}OTi_{0.10}O$ sample. The small-sized nanoball-like particles were seen to be agglomerated, for the pure ZnO thin film. In the SEM images taken from a longer distance, it was seen that the samples were homogeneously distributed and enlarged on the surface. With increasing doping ratio, they have formed as clusters and decrease in the grain size can be observed with increase in annealing temperature. Ade et al. (2021) have grown pure and Ti(1, 3 and 5%)-doped ZnO thin films by the successive ionic layer adsorption and reaction (SILAR) method and an decrease in particle size with doping.
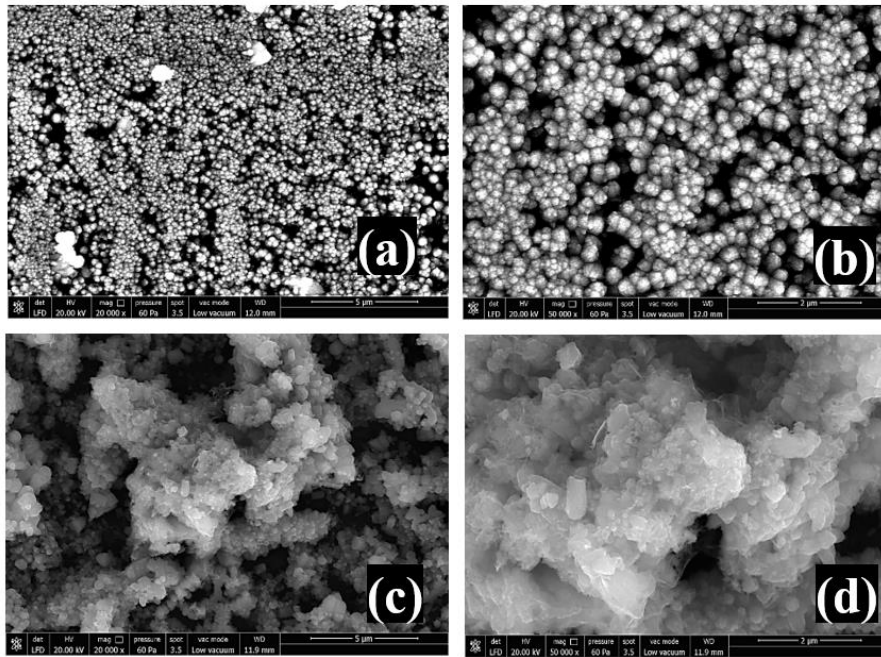
Figure 2. The SEM images of ZnO thin films *a*), *b)* as-grown and *c*), *d)* heat-treated
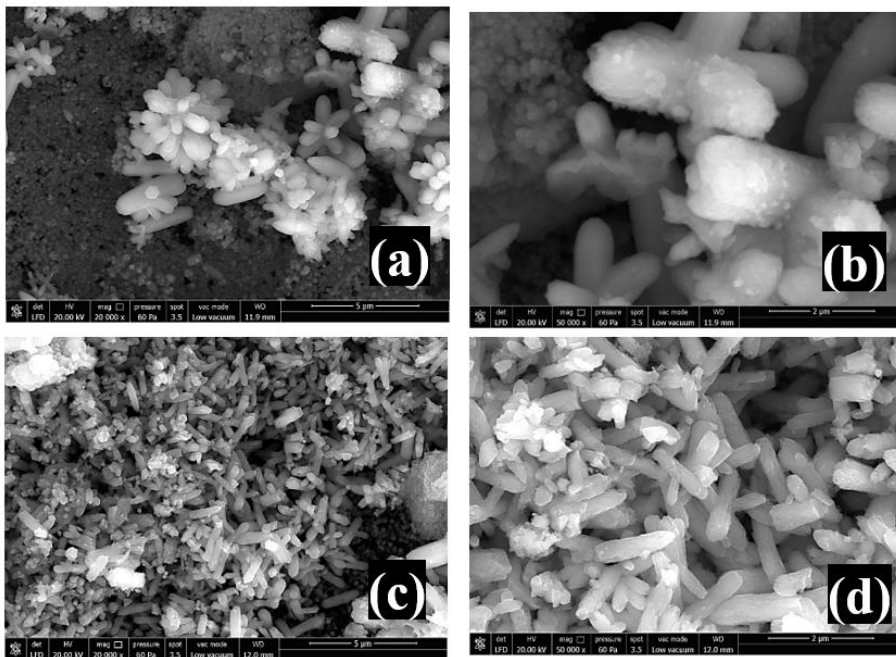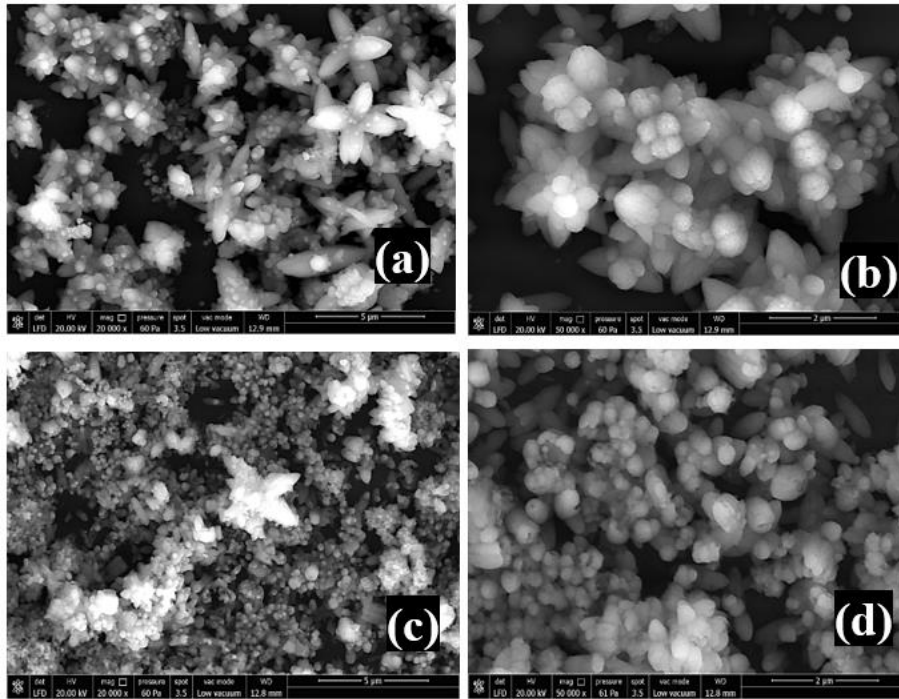

Figure 3. The SEM images of $Zn_{0.95}Ti_{0.05}O$ thin films *a*), *b)* as-grown and *c*), *d)* annealed

Figure 4. *The SEM images of* $Zn_{0.90}Ti_{0.10}O$ *thin films* ***a), b)*** *as-grown and* ***c), d)*** *annealed*
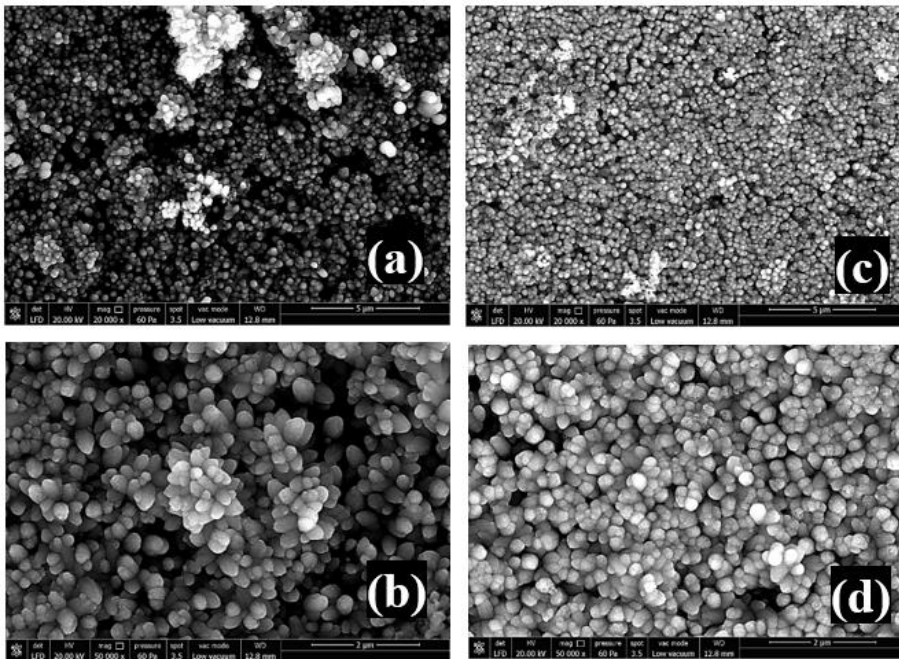

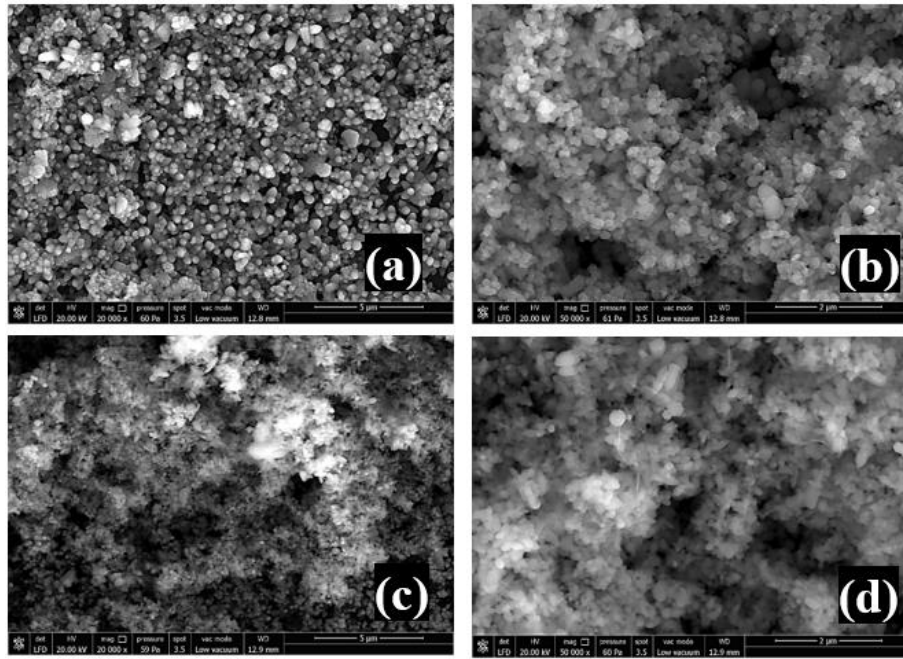**Figure 5.** *The SEM images of* $Zn_{0.85}Ti_{0.15}O$ *thin films* ***a), b)*** *as-grown and* ***c), d)*** *annealed*

Figure 6. *The SEM images of $Zn_{0.80}Ti_{0.20}O$ thin films **a), b)** as-grown and **c), d)** annealed*

Figure 7-11 depict the XRD analysis of as-grown and annealed thin films. When the diffraction patterns of the films are examined, the widths and intensities of the peaks differ at each annealing temperature. If the intensities of the peaks in the diffraction patterns are large and the widths are narrow, it means that the crystallization is good in the films, while the intensities of the peaks are small and the widths are large, it means that the crystallization is not good in the films. It was seen that the intensities of the thin films produced are large and the widths are narrow. Crystallization was clearly observed in the produced films. All the films exhibited polycrystalline behavior the PDF 01-071-6424 (Valdés et. al. 2009). Only the peaks belong to the Ti elements which is indexed PDF 00-021-1272 (Li et al., 2014) were seen for $Zn_{0.80}Ti_{0.20}O$ thin film. As the annealing temperature has been implemented, improvements in thin film structures and increases in peak intensities were observed. With the annealing process, the additive atoms settle into the structure and the placed additive atoms increase the crystallization.
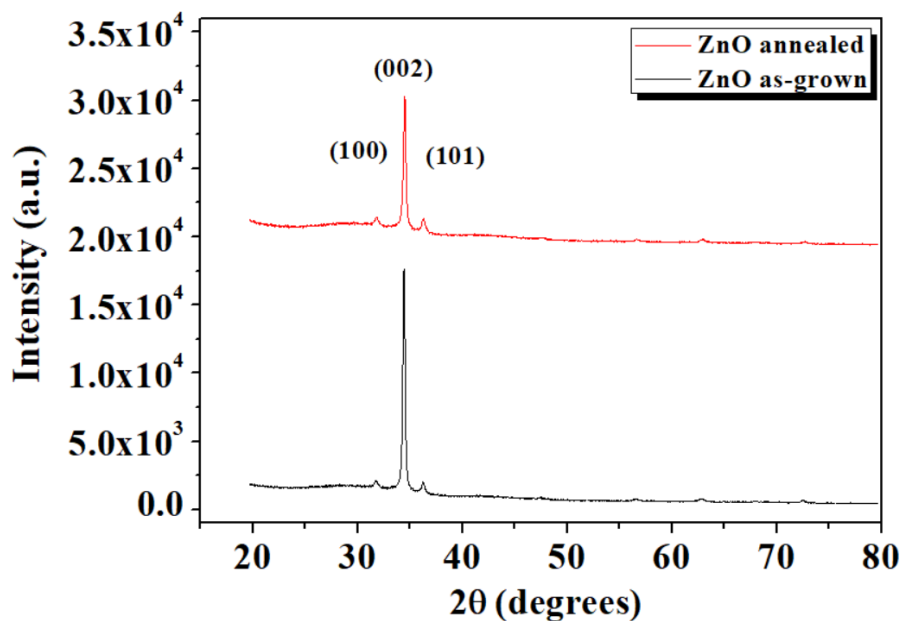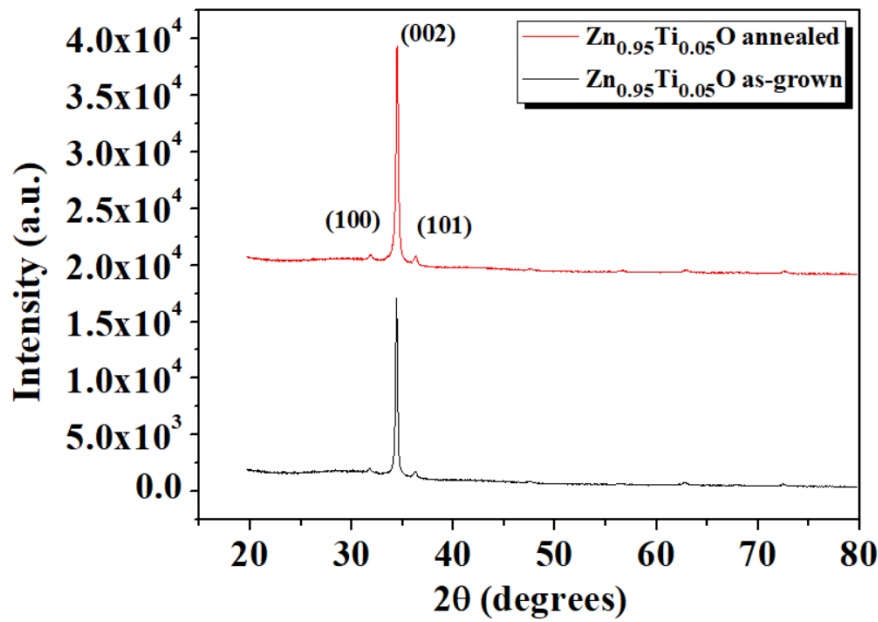

Figure 7. *The XRD analyses of ZnO thin films*

Figure 8. The XRD analyses of $Zn_{0.95}Ti_{0.05}O$ thin films
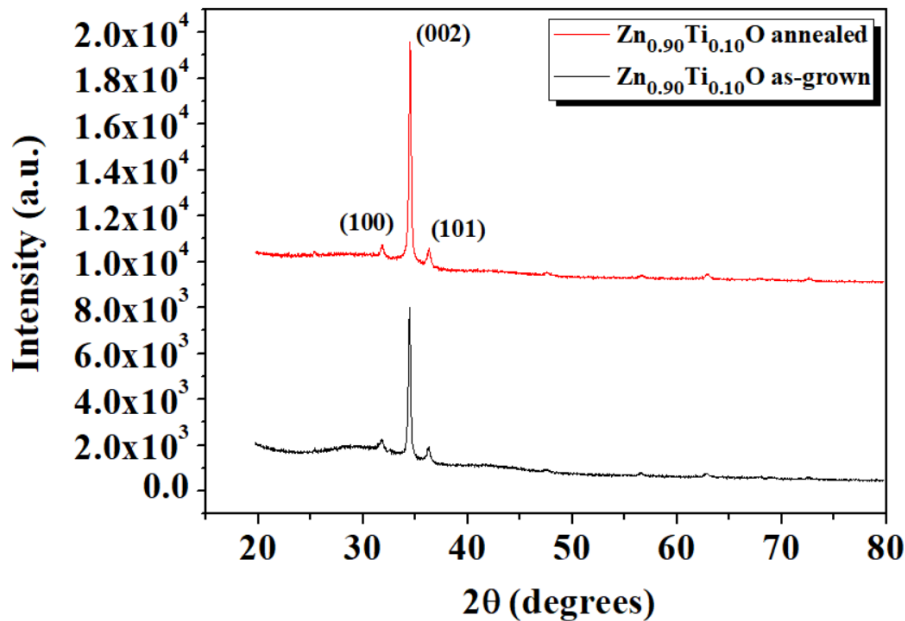
Figure 9. The XRD analyses of $Zn_{0.90}Ti_{0.10}O$ thin films

The crystalline size and dislocation density of produced films are given in Figure 12 and Figure 13. The crystalline for the as-grown samples was calculated as 38.9, 36.8, 36, 34.8 and 34.2 nm for ZnO, $Zn_{0.95}Ti_{0.05}O$, $Zn_{0.90}Ti_{0.10}O$, $Zn_{0.85}Ti_{0.15}O$ and $Zn_{0.80}Ti_{0.20}O$, respectively. The calculations were characterized with Debye-Scherrer's formula (Samuel et al., 2022), and Soniya and Kaleemulla (2023) observed the same results. It may be due to the fact that Ti ions replace Zn ions and do not disrupt the crystal structure. Since the radius of the Ti and Zn ion is 0.68 Å (Ti^{+4}) and 0.74 Å (Zn^{+2}), it can be assumed that the dopant atoms settle in the main unit cell without any deterioration (Soniya & Kaleemulla, 2023). In addition, the crystalline for the annealed samples was calculated as 40, 38.6, 38.2, 37.8 and 37.6 nm for ZnO, $Zn_{0.95}Ti_{0.05}O$, $Zn_{0.90}Ti_{0.10}O$, $Zn_{0.85}Ti_{0.15}O$ and $Zn_{0.80}Ti_{0.20}O$, respectively. The grain size reduction can be mainly attributed to the internal stress increases due to the structural and chemical disorder that causes the system to become unstable when the Ti4+ content in the stable ZnO system increases (Soltabayev et al., 2023).
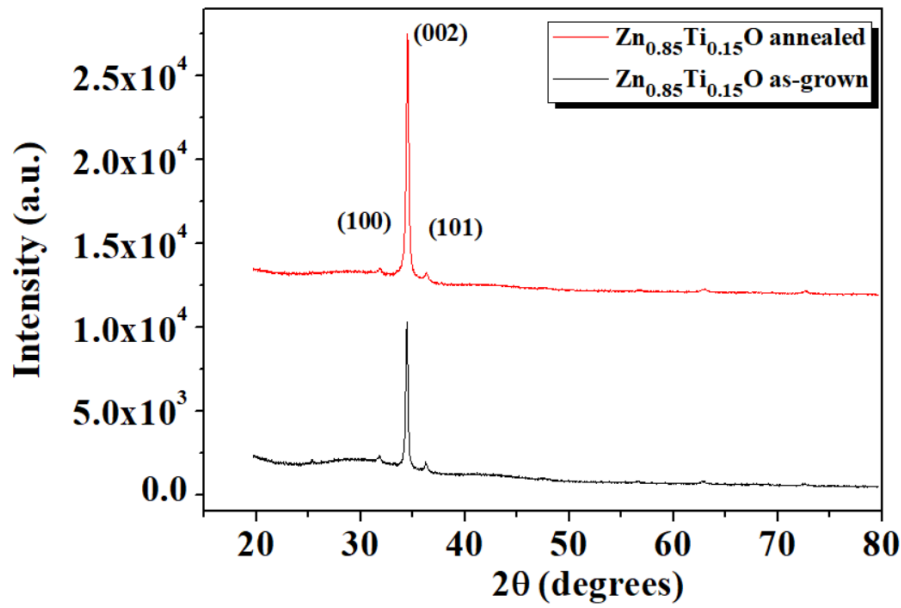
Figure 10. The XRD analyses of $Zn_{0.85}Ti_{0.15}O$ thin films
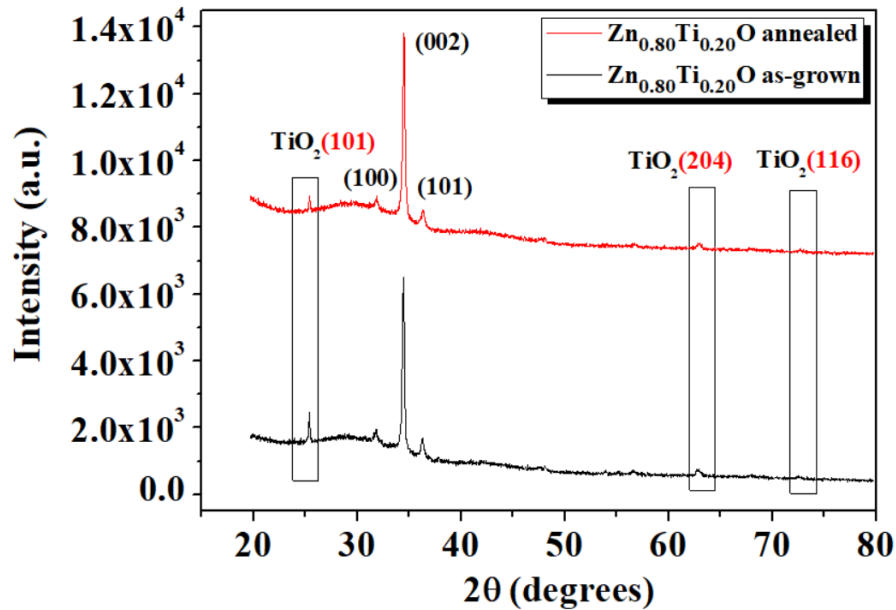
Figure 11. The XRD analyses of $Zn_{0.80}Ti_{0.20}O$ thin films

Figure 14 and Figure 15 present the linear absorbance of as-grown and annealed $Zn_xTi_{1-x}O$ thin films, respectively. The band gap values of as grown samples were calculated 3.35, 3.38, 3.40, 3.39 and 3.38 eV for ZnO, $Zn_{0.95}Ti_{0.05}O$, $Zn_{0.90}Ti_{0.10}O$, $Zn_{0.85}Ti_{0.15}O$ and $Zn_{0.80}Ti_{0.20}O$, respectively. The calculations were made by Tauc Plot (Tekin & Karaduman Er, 2022). Results depended on doping and annealing is in agreement with literature (Pawar et al., 2018). The band gap values in annealed samples were calculated 3.23, 3.28, 3.28, 3.26 and 3.27 eV for ZnO, $Zn_{0.95}Ti_{0.05}O$, $Zn_{0.90}Ti_{0.10}O$, $Zn_{0.85}Ti_{0.15}O$ and $Zn_{0.80}Ti_{0.20}O$, respectively.
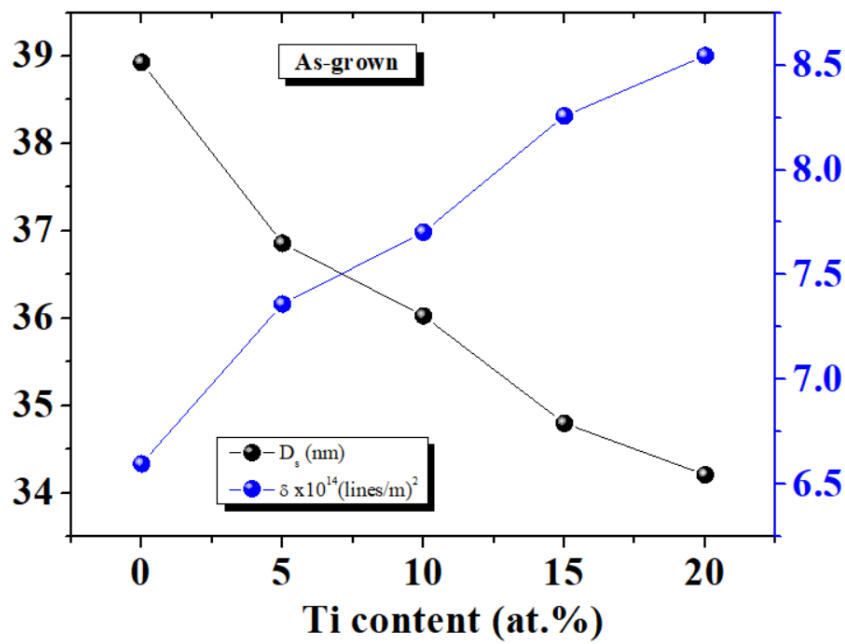
Figure 12. *The D and δ of $Zn_xTi_{1-x}O$ thin films; as-grown*
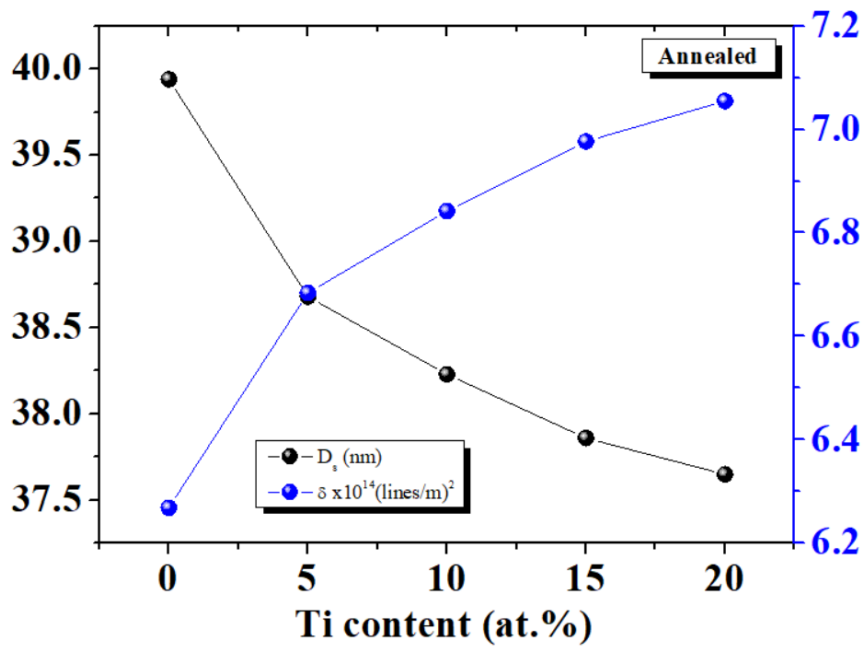
Figure 13. *The D and δ of $Zn_xTi_{1-x}O$ thin films; annealed*

The I-V graphs of $Zn_xTi_{1-x}O$ thin films are given at Figure 16 and Figure 17. Two probe methods were used for the electrical characterization of the prepared thin films at room temperature. As can be seen from the graph, the samples exhibited the I–V characteristic and Ohmic behavior. The resistance values of as-grown films at 5 V were calculated as 2220, 1779, 1633, 1179 and 956 kΩ for ZnO, $Zn_{0.95}Ti_{0.05}O$, $Zn_{0.90}Ti_{0.10}O$, $Zn_{0.85}Ti_{0.15}O$ and $Zn_{0.80}Ti_{0.20}O$, respectively. If the glass taken directly from the furnace is left to cool at normal temperature, it will crack with the effect of thermal shock, so the annealing process was continued in the furnace and the samples were cooled simultaneously with the cooling of the furnace. The resulting internal stresses were eliminated. Thus, decreases in resistance values were observed with annealing. The resistance values of annealed films were calculated as 907, 734, 678, 485 and 394 kΩ for ZnO, $Zn_{0.95}Ti_{0.05}O$, $Zn_{0.90}Ti_{0.10}O$, $Zn_{0.85}Ti_{0.15}O$ and $Zn_{0.80}Ti_{0.20}O$, respectively (at 5 V).
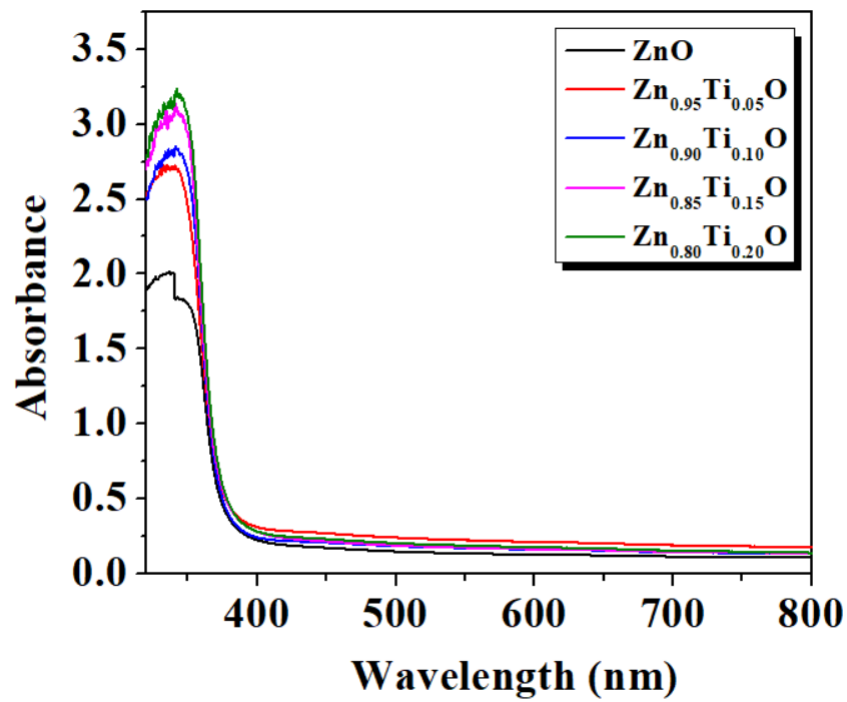
Figure 14. The UV-absorbance analyses of $Zn_xTi_{1-x}O$ thin films
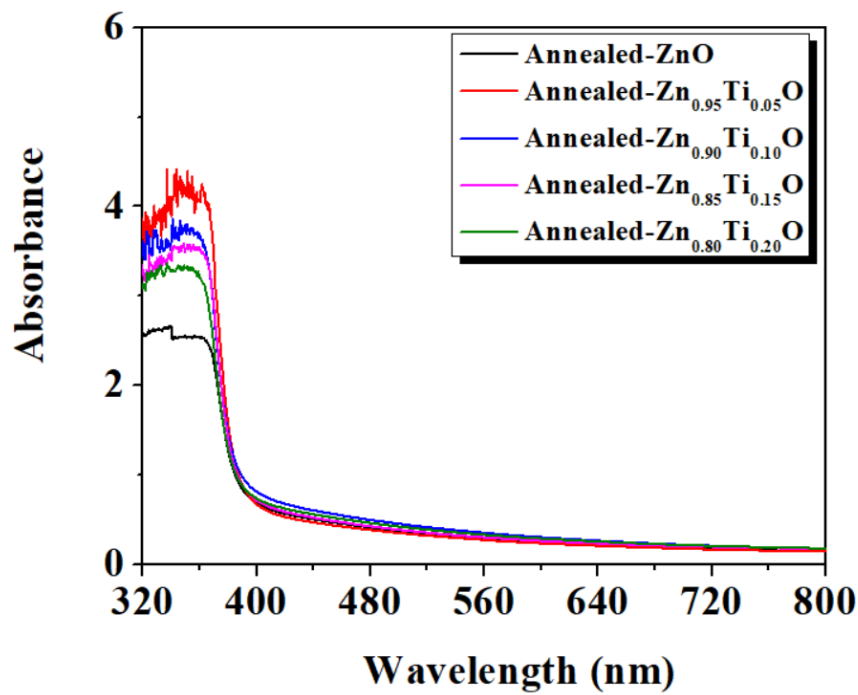
Figure 15. The UV-absorbance analyses of $Zn_xTi_{1-x}O$ thin films
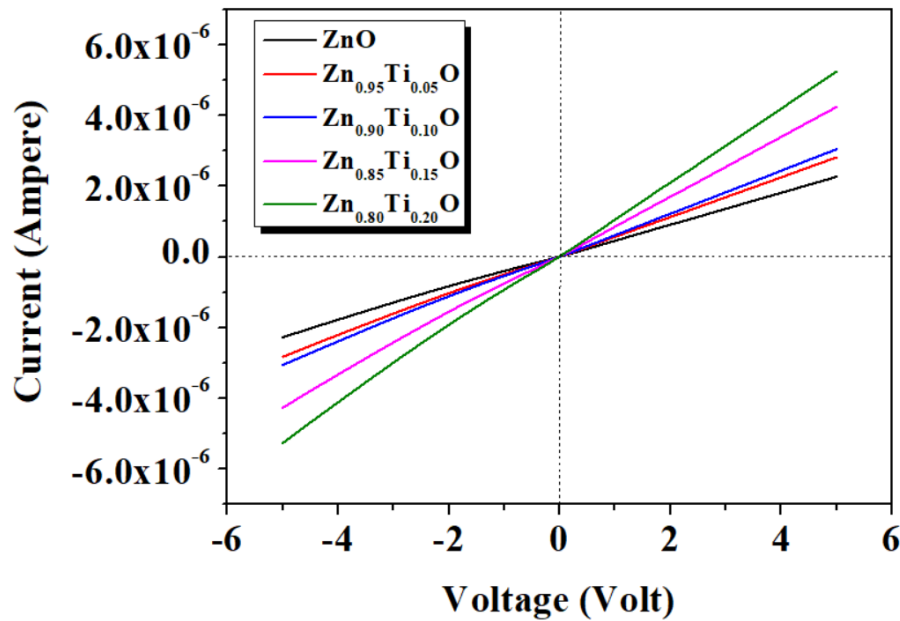
Figure 16. The I-V graphs of $Zn_xTi_{1-x}O$ thin films
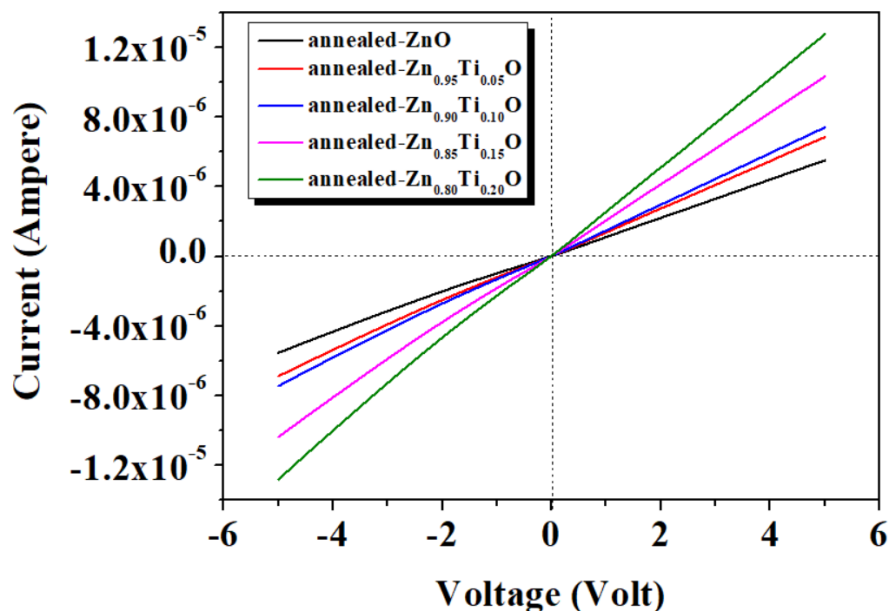
Figure 17. The I-V graphs of $Zn_xTi_{1-x}O$ thin films

4. CONCLUSION

In this study, the variation of structural, electrical and linear absorption properties with both doping rate and annealing was investigated. In the SEM images, it is seen that the samples are homogeneously distributed on the surface and all the films exhibit polycrystalline behavior. The XRD analyzes are showed that the Ti is incorporated into the structure and does not cause deterioration. However, different TiO2 phases are seen for the Zn0.80Ti0.20O sample. It is seen that there is an increase in the deterioration of the structure of the residual Ti additive. Starting from here, it is thought that 0.15 % contribution is the maximum contribution. This is due to the migration of atoms, which helps incorporation of Ti and oxygen atoms into the lattice regions. As the temperature increased, improvements in thin film structures and increases in peak intensities were observed. As can be seen from the graph, the samples exhibit the I–V characteristic and Ohmic behavior.

ACKNOWLEDGEMENT

CONFLICT OF INTEREST

The authors declare no conflict of interest.

REFERENCES

Ade, R., Kumar, S. S., Valanarasu, S., Kumar, S. S., Sasikumar, S., Ganesh, V., Bitla, Y., Algarni, H., & Yahia, I. S. (2021). Enhanced optoelectronic properties of Ti-doped ZnO nanorods for photodetector applications. *Ceramics International*, *47*(17), 24031-24038. doi:10.1016/j.ceramint.2021.05.112

Darmadi, I., Taufik, A., & Saleh, R. (2020). Analysis of optical and structural properties of Ti_doped ZnO nanoparticles synthesized by co-precipitation method. *Journal of Physics: Conference Series*, *1442*(1), 012021. doi:10.1088/1742-6596/1442/1/012021

Hsu, S.-F., Weng, M.-H., Chou, J.-H., Fang, C.-H., & Yang R.-Y. (2016). Effect on the Ti-target arc current on the properties of Ti-doped ZnO thin films prepared by dual-target cathodic arc plasma deposition. *Ceramics International*, *42*(13), 14438-14442. doi:10.1016/j.ceramint.2016.06.043

Lee, M. L., Wang, J. C., Kao, C. H., Chen, H., Lin, C. Y., Chang, C. W., Mahanty, R. K., Lin, C. F., & Chang, K. M. (2018). Comparison of ZnO and Ti-doped ZnO sensing membrane applied in electrolyte-insulator-semiconductor structure. *Ceramics International*, *44*(6), 6081-6088. doi:10.1016/j.ceramint.2017.12.239

Li, W., Liang, R., Hu, A., Huang, Z., & Zhou, Y. N. (2014). Generation of oxygen vacancies in visible light activated one-dimensional iodine TiO_2 photocatalysts. *RSC Advances*, *4*(70), 36959-36966. doi:10.1039/C4RA04768K

Pawar, S. T., Chavan, G. T., Prakshale, V. M., Jadkar, S. R., Kamble, S. S., Maldar, N. N., & Deshmukh, L. P. (2018). Probing into the optical and electrical properties of hybrid $Zn_{1-x}Co_xSe$ thin films. *Journal of Materials Science: Materials in Electronics*, *29*(5), 3704-3714. doi:10.1007/s10854-017-8302-7

Rilda, Y., Valeri, A., Syukri, S., Agustien, A., Pardi, H., & Sofyan, N. (2023). Biosynthesis, characterization, and antibacterial activity of Ti-doped ZnO (Ti/ZnO) using mediated Aspergillus niger. *South African Journal of Chemical Engineering*, *45*, 10-19. doi:10.1016/j.sajce.2023.04.001

Samuel, J., Suresh, S., Shabna, S., Sherlin Vinita, V., Joslin Ananth, N., Shajin Shinu, P. M., Mariappan, A., simon, T., Samson, Y., & Biju, C. S. (2022). Characterization and antibacterial activity of Ti doped ZnO nanorods prepared by hydrazine assisted wet chemical route. *Physica E: Low-dimensional Systems and Nanostructures*, *143*, 115374. doi:10.1016/j.physe.2022.115374

Shewale, P. S., & Yu, Y. S. (2016). H_2S gas sensing properties of undoped and Ti doped ZnO thin films deposited by chemical spray pyrolysis. *Journal of Alloys and Compounds*, *684*, 428-437. doi:10.1016/j.jallcom.2016.05.178

Soltabayev, B., Ajjaq, A., Yergaliuly, G., Kadyrov, Y., Turlybekuly, A., Acar, S., & Mentbayeva, A. (2023). Ultrasensitive nitric oxide gas sensors based on Ti-doped ZnO nanofilms prepared by RF magnetron sputtering system. *Journal of Alloys and Compounds*, *953*, 170125. doi:10.1016/j.jallcom.2023.170125

Soniya, P. G., & Kaleemulla, S. (2023), Properties of Ti doped ZnO nanoparticles under solid state reaction method involving vacuum annealing. *Physica B: Condensed Matter*, *649*, 414409. doi:10.1016/j.physb.2022.414409

Tekin, S., & Karaduman Er, I. (2022). The structural, morphological, optical and gas-sensing properties of Mn3O4 thin films grown by successive ionic layer adsorption and reaction technique. *Journal of Materials Science: Materials in Electronics*, *33*(18), 14519-14534. doi:10.1007/s10854-022-08372-w

Investigation of Surface Dose Accuracy of Two Dose Calculation Algorithms Using Thermoluminescent Dosimeters

Osman Vefa GÜL[1*] iD

[1]Selçuk University, Faculty of Medicine, Department of Radiation Oncology, Selçuklu, Konya, Türkiye

Keywords	Abstract
Surface Dose Thermoluminescent Dosimetry Algorithm	Accurate estimation of the surface dose in radiotherapy is very important in reducing skin reactions. This study aims to evaluate the accuracy of two different treatment planning algorithms in calculating the surface dose in a specially designed phantom using thermoluminescent dosimetry (TLD). In this study, a special phantom was designed for surface dose measurement. The phantom surface consisted of an adhesive bolus for the adhesion of TLDs. 121 TLDs were placed 1 cm apart on the bolus surface. In TPS, irradiation plans were created at different fields and source-surface distances (SSD). Dose calculations were made with Anisotropic Algorithm algorithms (AAA) and Pencil Beam Convolution (PBC) algorithms for all plans. The mean dose was measured for each point. For each of the 4x4, 6x6, 8x8, 10x10, and 12x12 cm2 domains, the TLDs within the domain were approximately 1 cm inward from the edge. To measure the effect of SSD on surface dose, the isocenter point was located at depths of 0 cm, 2.5 cm and 5.0 cm, respectively. The surface dose at each depth was measured with TLDs. The doses calculated by the AAA and PBC algorithms were compared with the doses measured by TLDs. The AAA algorithm overestimates the surface dose by 4% compared to the TLD measurement for the 4x4 field. The surface dose calculation of the PBC algorithm was found to be high when compared to TLD measurements for all SSDs and fields. There was a significant difference between the PBC algorithm dose calculation and TLD measurements in all fields and SSDs (p<0.001). It was observed that the AAA algorithm performed better in calculating the surface dose than the PBC algorithm. AAA and PBC algorithm users are advised to be more careful about surface dose calculation.

1. INTRODUCTION

Radiation is the transport of energy in the form of waves or particles (Lejosne et al., 2022; Aydemir et al., 2023). Radiation that has the energy to remove electrons from the atom's orbit is called ionizing radiation. Radiation therapy, is aimed to destroy cancer cells by using particle or wave radiation. Ionizing radiation is used in radiotherapy, which plays a primary role in treating cancer patients. The main purpose of radiotherapy is to protect critical organs in the best possible way while delivering the required dose to the target volume (Simoni et al., 2021). Modern treatment techniques are used together with the developing technology in radiation therapy (Matsumoto et al., 2021). All current treatment techniques require a treatment planning process based on computed tomography (CT) images. Thanks to the treatment planning processes, the absorbed dose in the target volume and organs at risk can be estimated by the treatment planning systems (TPS). TPSs use different dose calculation algorithms. It is vital that these algorithms accurately estimate the dose. Algorithms used in radiotherapy successfully estimate the in-field and organ-at-risk (OAR) doses but cannot successfully calculate the out-of-field and surface doses.

*Corresponding Author, e-mail: vefagul@selcuk.edu.tr

The failure of dose calculation algorithms in the superficial region is due to electron instability, multi-leaf collimators (MLC) leakage, and beamformers such as secondary collimators and blocks. It does not take into account the radiation scattered from the patient (Chakarova et al., 2012). The absorption of photon rays used in radiation therapy in the surface region varies depending on many parameters. These parameters include field size, distance from the beam source, and beam angle (Panettieri et al., 2009). Photon energies used in radiotherapy are absorbed as a result of Compton scattering. The photon beams transfer some of their energy to the orbiting electrons, and the electrons gain motion energy. The activated electrons transfer their energy to the tissue and are absorbed. As a result of this absorption, secondary radiation is transferred to the tissue. Secondary radiations generated on the surface significantly affect the skin dose (Ravikumar & Ravichandran, 2000; Mowery & Singh, 2023). Contaminated electrons in the head of the therapy device can be caused by components such as primary collimator, flattening filter, monitor ion chambers, target, and treatment set-up parameters such as field size, wedge filter, block carrier tray, patient fixation tools, and source-skin distance (SSD) (Tsapaki & Bayford, 2015; Ng et al., 2022). While the patient is irradiated, the SSD is very important for the skin dose. Skin side effects are common during radiation therapy (Ramseier et al., 2020; Córdoba et al., 2021). Side effects on the skin due to radiation adversely affect the patient's quality of life (Wang & Tepper, 2021). The field size is also one of the critical parameters affecting the skin dose. Increasing the area size causes an increase in dose in the build-up region. High-energy photons release their maximum dose (dmax) more profoundly than the surface, depending on their energies. This is called the skin-sparing effect of high-energy photon beams. Although TPS can accurately estimate the dose given to the target volume and OARs, studies have shown that TPS cannot accurately calculate the surface dose (Danckaert et al., 2023). The accuracy of TPSs in calculating surface dose has been reported by various researchers on inhomogeneous phantoms There is a lack of confidence in the surface dose calculation of TPS. Surface dose measurements require special dosimetric methods. The most important of these dosimetric equipment is in vivo dosimetry. Various measurement methods such as film dosimetry, Thermoluminescent dosimeter (TLD), diode dosimetry, semiconductor detectors and ion chambers have been developed for in-vivo dosimetry.

Few studies report comparisons of measured skin doses with doses calculated by TPS. This study aims to evaluate the accuracy of two different treatment planning algorithms in calculating the surface dose in a specially designed phantom using thermoluminescence dosimetry.

2. MATERIAL AND METHOD

Phantom Design

The necessary phantom setup was created to examine the surface doses for modern radiotherapy techniques. For this setup, 10 PTW brand RW3 solid-water phantoms (PTW, Physikalisch Technische Werkstätten, Freiburg, Germany) in 40x40 dimensions were placed on each other. The RW3 phantom can be used for dose measurements for high-energy photon and electron energies. RW3 material contains $2.1 \pm 0.2\%$ TiO_2 mixed polystyrene (C_8H_8), its mass density is 1.045 g/cm^3, and its electron density is 3.386×10^{23} e/g (Guardiola et al., 2022). A 0.5 cm thick gel layer-type adhesive bolus was fixed on these solid phantoms. The type of bolus used was Superflab. 121 TLD chips were placed on the adhesive bolus at 1 cm intervals. Tissue equivalent TLD-100 chips were used to identify measurement points that were easily visible during TPS. Since TLD-100 chips are tissue-equivalent materials, no artefacts occurred. Thus, 121 measurement points were determined on the phantom in a field of 11×11 cm^2. The phantom created for point dose measurement is shown in Figure 1. CT images of the created phantom were obtained with a slice thickness of 1 mm. The obtained DICOM images were transferred to TPS.

Radiotherapy Planning

This study used the Varian DHX (Varian Medical Systems, USA) model linear accelerator device. This device; is a high-tech radiotherapy device that can perform applications such as three-dimensional conformal radiotherapy (3DCRT). In the current Varian DHX device, in the Millennium 80 MLC system, each bank has 40 pairs of leaves and the predicted MLC leaf width in the isocenter is 1 cm. While the SSD distance is 100 cm, the maximum space size opened is 40 cm x 40 cm^2. The planning system of this device used in irradiation is Eclipse TPS. This planning system is used to plan the radiotherapy treatments of cancer patients. Eclipse TPS makes dose calculations using a three-dimensional tomography image. Eclipse software is widely used

for planning external treatments using photon, electron and proton beams. In our current research, two different algorithms of Eclipse TPS (Varian Medical Systems, Palo Alto, CA) were used. These were the Pencil Beam Convolution (PBC) and Analytical Anisotropic Algorithm algorithms (AAA). The PBC algorithm is obtained as a result of the integration of all point-spread kernels along the infinite beam path of the photons in the phantom. AAA has been developed for the accuracy of dose distributions and scattered dose calculation in external beam therapy, especially in heterogeneous environments. The current research created beam plans with AAA and PBC algorithms. These plans were for 4x4, 6x6, 8x8, 10x10 and 12x12 cm^2 fields. For each beam field, 100 monitor units (MU) of radiation were applied at 0-degree angle of the Gantry. In addition, irradiation was performed on three different SSDs for different fields determined. The SSD used in the irradiation was 100, 97.5 and 95 cm, respectively. X-ray was applied at 300 MU/min. The beam plans created for different field sizes are shown in Figure 2. The planning made with AAA and PBC algorithms determined 9,25,49,81, and 121 measurement points for 4x4, 6x6, 8x8, 10x10 and 12x12 cm^2 areas, respectively. The point dose was read for each of the determined measuring points.
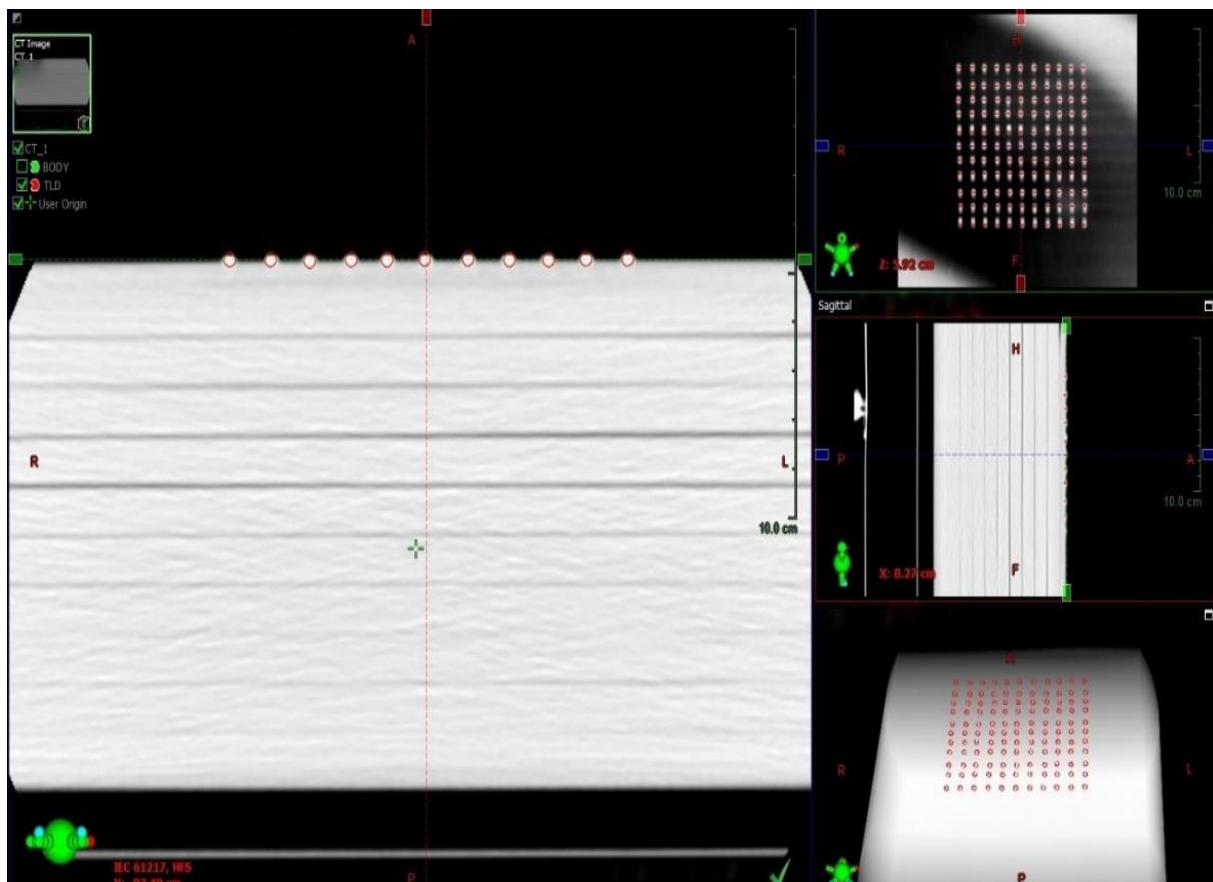
Figure 1. Phantom created for point dose measurement

Calibration of TLDs

Confirmation of the dose calculated by TPS in the surface region was done using thermoluminescence dosimetry (TLD). TLD-100 chips with dimensions of 3.2 mm x 3.2 mm x 0.9 mm were used for surface dose measurement. 190 TLD-100 crystals were used for calibration. First, TLD-100 crystals were numbered and fired in a TLD oven for 1 hour at 400 ºC and 2 hours at 100 ºC. TLDs were irradiated with 6 MV photon energy in Varian DHX linear accelerator device with one cGy equal to 1MU. Then, preheating was done at 100 ºC for 10 minutes in a TLD oven. TLD-100 crystals were read on the Harshaw 3500 TLD reader. Reading calibration factor (RCF) and element correction coefficient (ECC) factors were found for TLDs. Afterwards, 125 TLD-100s with similar dose responses and reproducibility within ±3% were selected among the ECC values found. TLDs included in the study were irradiated from 80 cGy to 200 cGy, and the calibration curve was drawn. The calibration curve for TLD-100 chips is shown in Figure 3.
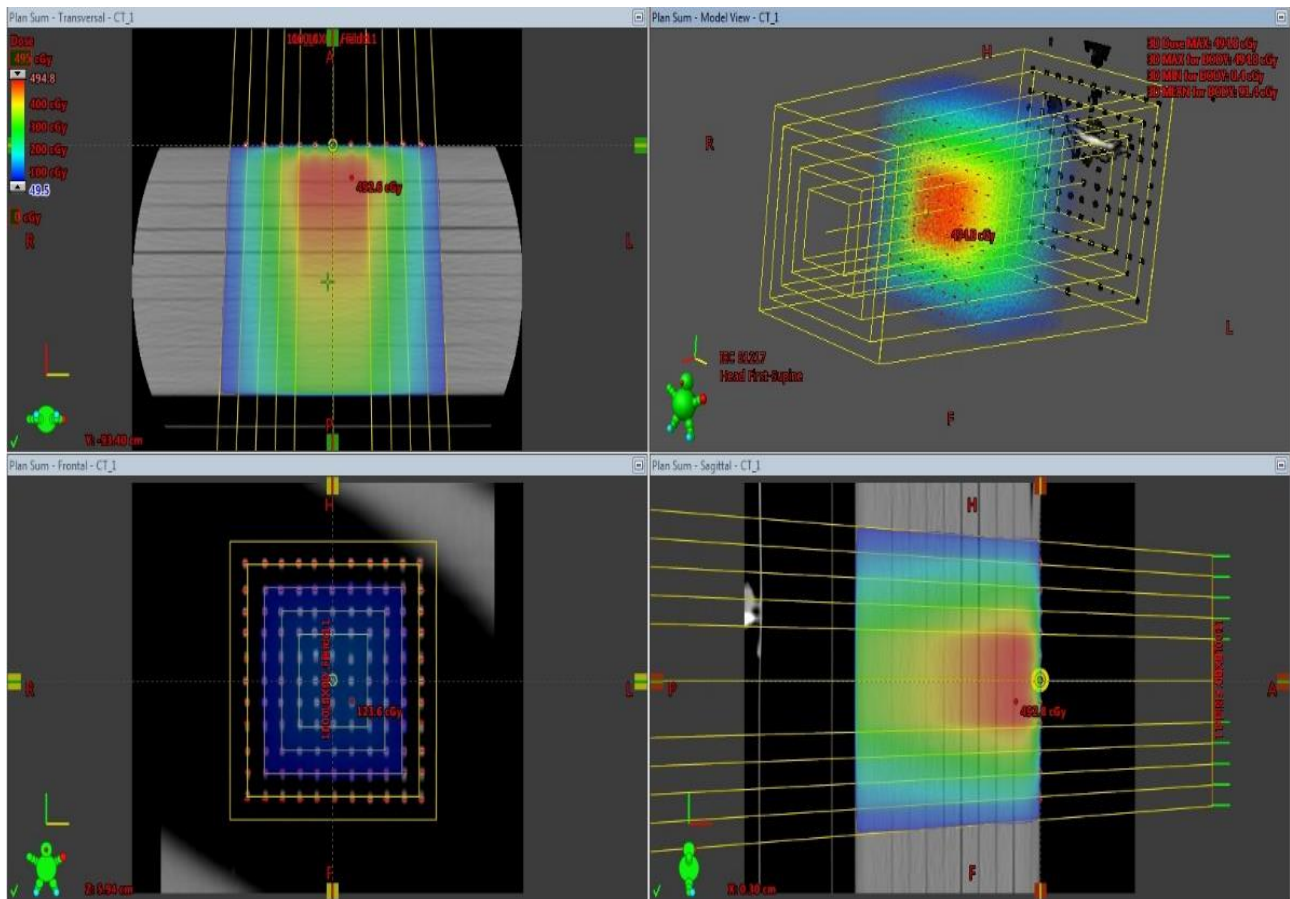
Figure 2. *Beam plans created for different field sizes*
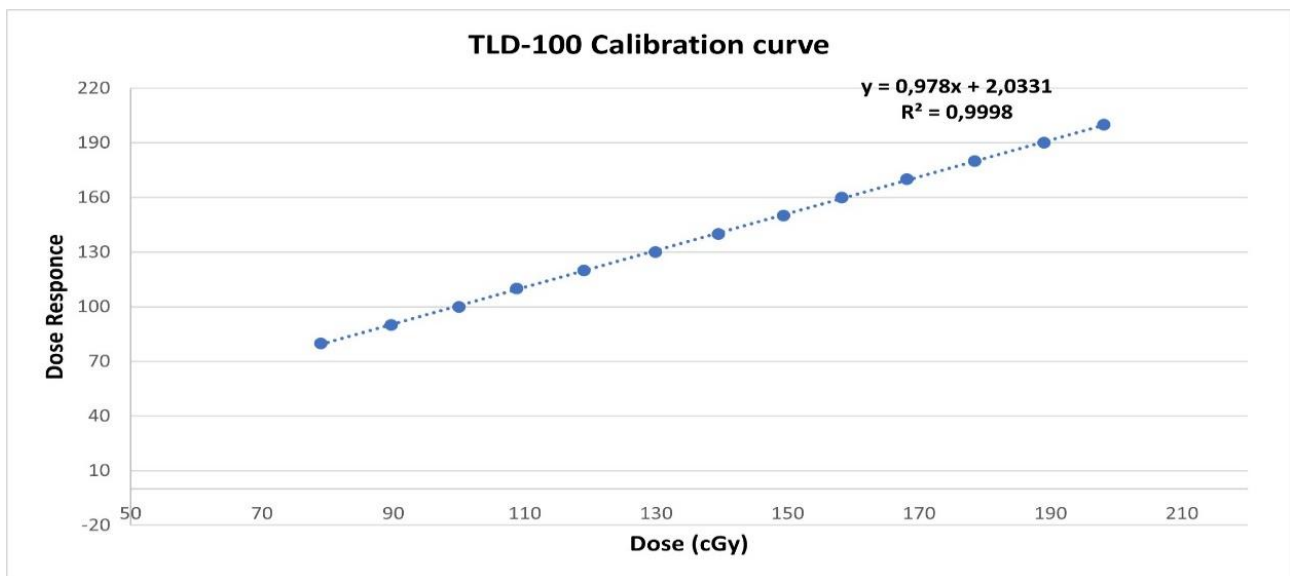
Figure 3. *Calibration curve for TLD-100 chips*

Surface Dose Measurement with TLDs

Necessary calibration procedures were performed before proceeding to the measurements in the linear accelerator. Surface doses were measured by TLD according to SSD and field sizes were determined in TPS. The mean dose was measured for each point. For each of the 4x4, 6x6, 8x8, 10x10 and 12x12 cm² fields, the TLDs within the field were approximately 1 cm inward from the edge. To measure the effect of SSD on the

surface dose, the isocenter point was placed at 0 cm, 2.5 cm and 5.0 cm depths, respectively. The surface dose at each depth was measured with TLDs. Each measurement was repeated three times to minimize uncertainty.

Statistical Analysis

Study Statistical Package for Social Sciences, version 25.0 (SPSS, Inc., Chicago, IL) was used for data analysis of the current study. The percentage differences between the point doses calculated by the AAA and PBC algorithms and those measured by TLD were evaluated. Paired Sample t-test for comparison of point doses. used.

3. RESULTS AND DISCUSSION

The dose distributions at the measurement points were calculated with AAA and PBC algorithms for different areas and SSDs. Dose distributions at predetermined points were measured with TLDs. Each measurement was repeated three times to minimize uncertainty. The dose distributions calculated by TPS and measured by TLD are shown in Tables 1, 2, and 3 for SSD 100, 97.5 and 95 cm, respectively. Tables 1, 2, and 3 summarise the percentage difference between Eclipse TPS and TLD doses. It was observed that the surface dose increased as the field increased for all SSDs. The AAA algorithm overestimates the surface dose by 4% compared to the TLD measurement for the 4x4 field. The surface dose calculation of the PBC algorithm was found to be high when compared to TLD measurements for all SSDs and fields. There was a significant difference between the PBC algorithm dose calculation and TLD measurements in all fields and SSDs ($p<0.001$). The highest difference between the PBC algorithm and TLD measurements was 10.23% for SSD=100 and 12x12 field size.

Table 1. Surface doses calculated by Eclipse TPS and measured by TLD for SSD 100 cm

Field size (cm^2)	TLD (cGy)	AAA (cGy)	PBC(cGy)	TLD & AAA		TLD & PBC	
				Diff (%)	p-value	Diff (%)	p-value
4x4	30.24±0.11	31.51±0.23	29.36±0.15	-4.03	<0.001	2.99	<0.001
6x6	33.48±0.08	34.60±0.19	32.25±0.12	-3.24	<0.001	3.81	<0.001
8x8	35.35±0.48	34.97±0.09	33.86±0.08	1.09	<0.001	4.40	<0.001
10x10	38.86±0.20	38.17±1.60	36.66±0.20	1.81	<0.001	6.00	<0.001
12x12	41.59±0.39	39.99±0.17	37.73±0.23	4.00	<0.001	10.23	<0.001

Table 2. Surface doses calculated by Eclipse TPS and measured by TLD for SSD 97.5 cm

Field size (cm^2)	TLD (cGy)	AAA (cGy)	PBC(cGy)	TLD & AAA		TLD & PBC	
				Diff (%)	p-value	Diff (%)	p-value
4x4	31.52±0.09	33.02±0.10	30.44±0.01	-4.54	<0.001	3.54	<0.001
6x6	35.06±0.54	35.39±0.16	32.26±0.21	-0.93	0.007	8.68	<0.001
8x8	38.26±0.38	38.24±0.12	36.36±0.07	0.05	0.798	5.22	<0.001
10x10	42.04±0.22	40.99±0.07	39.73±0.09	2.56	<0.001	5.81	<0.001
12x12	43.49±0.42	42.99±0.06	41.98±0.08	1.63	<0.001	3.60	<0.001

Table 3. Surface doses calculated by Eclipse TPS and measured by TLD for SSD 95 cm

Field size (cm^2)	TLD (cGy)	AAA (cGy)	PBC(cGy)	TLD & AAA		TLD & PBC	
				Diff (%)	p-value	Diff (%)	p-value
4x4	32.41±0.41	34.07±0.06	31.58±0.44	-4.87	<0.001	2.63	0.004
6x6	37.94±0.17	38.02±0.09	35.74±0.27	-0.21	0.073	6.16	<0.001
8x8	42.79±0.05	42.18±0.44	40.91±0.12	1.44	<0.001	4.60	<0.001
10x10	44.68±0.46	43.51±0.30	41.97±0.07	2.69	<0.001	6.46	<0.001
12x12	46.92±0.26	44.90±0.07	43.54±0.21	4.50	<0.001	7.76	<0.001

Mahur et al. (2022) aimed to evaluate the accuracy of the doses calculated by TPS in the surface area of a head and neck phantom they designed, using EBT3 Gafchromic film. In their study, they showed that there was a 16.72% difference between TPS and Gafchromic film measurements for the 3DCRT technique (Mahur et al., 2022). In the current study, all measurements were made with TLDs. Accordingly, the highest difference between Eclipse TPS and TLD measurements was 10.23% for the PBC algorithm. For the AAA algorithm, this difference was 4.87%. In parallel with Mahur et al. (2022), it was observed that TPS could not calculate the surface dose with full accuracy. Oinam and Singh (2010) examined the accuracy of dose calculation in the build-up region of the AAA and PBC algorithms using TLD. They took point dose measurements at different depths near the surface of the head and neck phantom. Oinam and Singh (2010) found a difference of 4.71% and 2.09% for AAA and PBC algorithms, respectively, according to their TLD measurements at a depth of 2 mm from the surface. In this dosimetric study, the surface dose within the build-up region was examined. Accordingly, for all dose measurements, the difference between doses calculated by the AAA algorithm and measured by TLDs was 2.51%. This difference was 5.46% for the PBC algorithm. It was observed that the AAA algorithm was more successful in calculating the surface dose than the PBC algorithm. Wong et al. (2012) evaluated the accuracy of the surface dose estimated by a clinically used TPS on a customised chest wall phantom with TLD measurements. They reported no significant difference between point doses measured by TLD and calculated by TPS, with a difference of up to 2.21% between TPS and TLD doses (Wong et al., 2012). There was no significant difference between TLD measurements and the AAA algorithm in the 8x8 field for SSD 97.5 and the 6x6 field for SSD 95. In parallel with Wong et al. (2012), there was no significant difference in TPS and TLD measurements at different depths and fields. Cao et al. (2017) aimed to evaluate the shallow dose calculation accuracy of four commonly used algorithms with Monte Carlo (MC) simulation and film measurements. When compared with the film measurements, they reported a difference of 4.07% and 22.15% between the AAA and PBC algorithms. They emphasized that caution should be exercised when using AAA and PBC algorithms in superficial dose calculation (Cao et al., 2017). In parallel with Cao et al. (2017), a significant difference was observed between TLD measurements and surface doses calculated by TPS. In particular, it was observed that the PBC algorithm underestimated the surface dose. It was seen that the AAA algorithm can calculate high or low according to the field size. In parallel with Cao et al. (2017), centres using the AAA and PBC algorithms are recommended to be careful about the surface dose.

4. CONCLUSION

This study aimed to give information about the accuracy of surface dose estimation of the commonly used AAA and PBC algorithms in radiotherapy TPS. It was observed that the AAA algorithm performed better in calculating the surface dose than the PBC algorithm. Surface dose calculation performances of AAA and PBC algorithms vary depending on area and SSD. Accurate knowledge of the surface dose can help prevent acute reactions and delayed effects. AAA and PBC algorithm users are advised to be more careful about surface dose calculation.

CONFLICT OF INTEREST

The author declares no conflict of interest.

REFERENCES

Aydemir, G. A., Akay, D., Tataroğlu, A., & Ocak, S. B. (2023). Electrical and optical properties of p-Si based structures with lead oxide interfaces. *Materials Science and Engineering: B*, *294*, 116552. doi:10.1016/j.mseb.2023.116552

Cao, Y., Yang, X., Yang, Z., Qiu, X., Lv, Z., Lei, M., Liu, G., Zhang, Z., & Hu, Y. (2017). Superficial dose evaluation of four dose calculation algorithms. *Radiation Physics and Chemistry*, *137*, 23-28. doi:10.1016/j.radphyschem.2016.02.032

Chakarova, R., Gustafsson, M., Back, A., Drugge, N., Palm, Å., Lindberg, A., & Berglund, M. (2012). Superficial dose distribution in breast for tangential radiation treatment, Monte Carlo evaluation of Eclipse algorithms in case of phantom and patient geometries. *Radiotherapy and Oncology*, *102*(1), 102-107. doi:10.1016/j.radonc.2011.06.021

Córdoba, E. E., Lacunza, E., & Güerci, A. M. (2021). Clinical factors affecting the determination of radiotherapy-induced skin toxicity in breast cancer. *Radiation Oncology Journal*, *39*(4), 315-323. doi:10.3857/roj.2020.00395

Danckaert, W., Ost, P., & De Wagter, C. (2023). Accuracy and reliability of a commercial treatment planning system in nontarget regions in modern prostate radiotherapy. *Journal of Applied Clinical Medical Physics*, *24*(8). doi:10.1002/acm2.14003

Guardiola, C., Bachiller-Perea, D., Kole, E. M. M., Fleta, C., Quirion, D., De Marzi, L., & Gómez, F. (2022). First experimental measurements of 2D microdosimetry maps in proton therapy. *Medical Physics*, *50*(1), 570-581. doi:10.1002/mp.15945

Lejosne, S., Allison, H. J., Blum, L. W., Drozdov, A. Y., Hartinger, M. D., Hudson, M. K., Jaynes, A. N., Ozeke, L., Roussos, E., & Zhao, H. (2022). Differentiating Between the Leading Processes for Electron Radiation Belt Acceleration. *Frontiers in Astronomy and Space Sciences*, 9. doi:10.3389/fspas.2022.896245

Mahur, M., Singh, M., Semwal, M., & Gurjar, O. (2022). Evaluation of surface dose calculations using monaco treatment planning system in an indigenously developed head and neck phantom. *Medical Journal of Dr. D.Y. Patil Vidyapeeth*. doi:10.4103/mjdrdypu.mjdrdypu_827_21

Matsumoto, T., Toya, R., Shimohigashi, Y., Watakabe, T., Matsuyama, T., Saito, T., Fukugawa, Y., Kai, Y., & Oya, N. (2021). Plan Quality Comparisons Between 3D-CRT, IMRT, and VMAT Based on 4D-CT for Gastric MALT Lymphoma. *Anticancer Research*, *41*(8), 3941-3947. doi:10.21873/anticanres.15190

Mowery, M. L., & Singh, V. (2023). *X-ray Production Technical Evaluation*. StatPearls. Treasure Island (FL).

Ng, K.-H., Ung, N. M., & Hill, R. (2022). *Problems and Solutions in Medical Physics: Radiotherapy Physics*. CRC Press.

Oinam, A. S., & Singh, L. (2010). Verification of IMRT dose calculations using AAA and PBC algorithms in dose buildup regions. *Journal of Applied Clinical Medical Physics*, *11*(4), 105-121. doi:10.1120/jacmp.v11i4.3351

Panettieri, V., Barsoum, P., Westermark, M., Brualla, L., & Lax, I. (2009). AAA and PBC calculation accuracy in the surface build-up region in tangential beam treatments. Phantom and breast case study with the Monte Carlo code PENELOPE. *Radiotherapy and Oncology*, *93*(1), 94-101. doi:10.1016/j.radonc.2009.05.010

Ramseier, J. Y., Ferreira, M. N., & Leventhal, J. S. (2020). Dermatologic toxicities associated with radiation therapy in women with breast cancer. *International Journal of Women's Dermatology*, *6*(5), 349-356. doi:10.1016/j.ijwd.2020.07.015

Ravikumar, M., & Ravichandran, R. (2000). Dose measurements in the build-up region for the photon beams from Clinac-1800 dual energy medical linear accelerator. *Strahlentherapie und Onkologie*, *176*(5), 223-228. doi:10.1007/s000660050004

Simoni, N., Micera, R., Paiella, S., Guariglia, S., Zivelonghi, E., Malleo, G., Rossi, G., Addari, L., Giuliani, T., Pollini, T., Cavedon, C., Salvia, R., Milella, M., Bassi, C., & Mazzarotto, R. (2021). Hypofractionated Stereotactic Body Radiation Therapy With Simultaneous Integrated Boost and Simultaneous Integrated

Protection in Pancreatic Ductal Adenocarcinoma. *Clinical Oncology*, *33*(1), e31-e38. doi:10.1016/j.clon.2020.06.019

Tsapaki, V., & Bayford, R. (2015). Medical Physics: Forming and testing solutions to clinical problems. *Physica Medica*, *31*(7), 738-740. doi:10.1016/j.ejmp.2015.05.017

Wang, K., & Tepper, J. E. (2021). Radiation therapy-associated toxicity: Etiology, management, and prevention. *CA: A Cancer Journal for Clinicians*, *71*(5), 437-454. doi:10.3322/caac.21689

Wong, S., Back, M., Tan, P. W., Lee, K. M., Baggarley, S., & Lu, J. J. (2012). Can radiation therapy treatment planning system accurately predict surface doses in postmastectomy radiation therapy patients? *Medical Dosimetry*, *37*(2), 163-169. doi:10.1016/j.meddos.2011.06.006

A GIS-MCDA-Based Analysis for Spatial Ecotourism Suitability Assessment in Saudi Arabia's Hail Province

Samera AL SALAH[1*] (iD)

[1]*King Abdulaziz University, Faculty of Arts & Humanities, Department of Geography and GIS, Jeddah, Saudi Arabia*

Keywords	Abstract
Ecotourism Suitability Map Geographic Information System GIS-MCDA Hail Saudi Arabia	Ecotourism was developed to combine culture, education, and tourism, but it has now evolved into a fundamental idea for global ecological sustainability. Ecotourism has the potential to help protect natural assets while also fostering beneficial synergies among tourism sector agents, visitors, and local residents. Low-density communities gain from rising interest in low-impact tourist products that assist the local economy. Based on this approach, the current research aims to assess the potential of existing natural and rural characteristics in the Hail area, situated in the center of Saudi Arabia, to underpin the development of sustainable tourist goods. In the research, natural ecotourism locations in Saudi Arabia's Hail province were evaluated for their spatial suitability. The methodology of the research included a number of steps and procedures, beginning with the creation of a geographic database on the area's natural resources for tourists. After extracting data from various sources and determining the criteria for the spatial suitability of natural tourist sites, which are represented in a set of natural and human criteria that directly affect the success of any tourist site based on the standards of the Saudi Commission for Tourism and National Heritage, the Ministry of Municipal and Rural Affairs and Housing, and standards derived from literary references, a total of 27 highly suitable sites were identified. Based on GIS (Geographic Information System)-based multicriteria decision analysis (GIS-MCDA) methodology, nine criteria were identified and represented in the form of layers, which were merged with each other through the overlay mechanism, after assigning a weight to each criterion based on its importance, to create a map identifying relevant natural environment tourist locations in the research region. The locate region for ecotourism, which covers 24501.225 km2, produced by the suitability modeler tool within ArcGIS Pro software and defined by the presence of ecotourism sites that fulfill the needs and standards of environmental tourism sites according to four degrees of suitability (high, moderate, marginal, and low). From a total of 64 sites, 27 exhibit a high suitability for ecotourism, accounting for 42.18% of all sites. While the number of sites with a moderate suitability rating reached 37 sites, representing 57.81% of all sites.

1. INTRODUCTION

The significance of tourism stems from the concept that it is one of the activities that contributes to the achievement of scientific, social, cultural, and economic objectives, as it allows for the identification of various places and their specific geographical laboratories. Tourism boosts individual productivity, increases the interconnection of social relationships, and raises cultural and social awareness at the communal level. Individually, tourism helps to reduce job demands and create a lifestyle change by broadening the individual's perspectives and awareness and learning about different civilizations, cultures, and customs. Therefore, it has become an area for many scientific research in several fields of the social sciences. Geography evolved as one of the most significant sciences for studying this phenomenon from its numerous perspectives in its spatial

*Corresponding Author, e-mail: salsalih@kau.edu.sa

context, as well as its interactions and influences with other geographical phenomena. Traveling responsibly to natural regions that preserves the environment, supports community well-being, and includes interpretation and education is known as ecotourism (Primavera et al., 2019). It may use the many natural and cultural ecosystem services that Hail offer to enhance local livelihoods. Tourism geography or ecotourism is concerned with the study of tourism and its associated activities with a specific focus on the characteristics of location, linkages, and reciprocal impacts of these activities. ecotourism emphasizes the spatial extension and spatial relationships of phenomena caused by travel and leisure, as well as the geographical components of the three pillars of tourism activity: reception (tourist supply environment), sending areas (demand environment), and tourist transportation.

Ecotourism combines conservation, community, and sustainable travel. This implies that people who develop, engage in, and sell ecotourism activities should follow the ecotourism principles outlined below:

- Reduce the physical, social, behavioral, and psychological consequences.
- Increase cultural and environmental knowledge and respect.
- Ensure that both guests and hosts have a great experience.
- Make direct financial rewards available for conservation.
- Create financial advantages for both the local community and private enterprise.
- Visitors should have memorable interpretive experiences that help them become more sensitive to the political, environmental, and social climates of the host nations.
- Create, build, and manage low-impact facilities.
- Recognize Indigenous Peoples' rights and spiritual beliefs in your community and collaborate with them to generate empowerment.

The Hail area is rich in natural tourist components such as mountain tourism, valleys, sand, natural flora, and climatic appropriateness, suggesting that this unique system is available throughout most months of the year. The findings also suggested that the relatively natural features that maintain these unique locations for future generations and the population of the area, secondarily, need care and attention by tourist planners first.

The natural plant is one of the cornerstones of the tourism industry and one of the natural components that play an important role in tourist attractions due to the Hail area's inherent aesthetic value, cultural significance, and use as a location for numerous significant tourism and recreation activities in such environments that are distinct in nature, emptiness, and continuous extension. It is also one of the most unique tourist ranges in the field of tourism, based on natural plant patterns. Perennial and seasonal vegetation make up the two primary types of vegetation in the Hail area.

The Hail province has various historical monuments, including the remains of Barzan Palace, which was built in 1808 under the reign of Muhammad bin Abdul Mohsen Al Ali and consists of two towers. The Seduction Gate is a park with numerous structures used for weddings and parties. The Al-Qishla Palace was built of mud during the reign of Abdul Aziz bin Musaed. The Aesthetic water bladder model is located near Tabarjal's Al-Sumail roundabout on the international route. The Machar Park, with a total area of 20,000 square meters, is one of the governorate's best-known parks. Shuaib Jaw in the Aja Mountains, Al-Riya Resort at the beginning of the Aqdah Road, an artistic model of incense burners and pampering, the Hatim Al-Ta'i burner in Jabal Al-Samra, Al-Magwa Tourist and Recreational Park, and Aeref Castle in the midst of Hail are the other sights. Despite the province's potential natural resources, a lack of tourism planning and suitability analysis prevents potential tourism investment from being realized. The primary goal of this study is to evaluate land suitability in the Hail region for ecotourism, using the GIS (Geographic Information System)-based multi- criteria decision analysis (GIS-MCDA) method within the GIS platform. GIS-MCDA methodology was used in suitability assessment (Modica et al., 2014; Bakirman & Gumusay, 2020; Doljak et al., 2021; Mentzafou et al., 2021). Based on geographical evaluation and the integration of many spatial layers, the study's research attempts to highlight locations best suited for ecotourism and develop maps of potential sites across the region.

2. STUDY AREA AND MATERIALS

2.1. Study Area

For the purposes of this study, the province of Hail was considered the base unit, and their suitability for the practice of ecotourism activities was determined by integrating a set of criteria and support for the development of tourist activities based on ecotourism principles, using the ArcGIS Pro software.

Hail province is a region in the Kingdom of Saudi Arabia. It is the eighth-largest, lying between 25° 30' and 29° N latitude and 39° and 44° 30' E longitude, encompassing a total surface area of 117,0151 km² and a population of 731,000 people in 2019. The municipality of Hail is made up of five municipalities: Hail, Baqa, Alghazalah,

Asshinan, and Hail (Figure 1) The Nefud Al-Kebir and the Aja Mountains are close to the Hail city (Great Sand Dune Desert). Hail has long been protected from outside invasion by these insurmountable mountains and the equally famed desert. Hail is an agricultural oasis that produces grain, dates, and fruit, with the irrigated gardens of the Hail Province accounting for a substantial percentage of the Kingdom's wheat output. Hail has a diverse geography with distinctive characteristics such as caverns, mountains, plains, and volcanoes, with enormous potential for adventure and sports activities to complement existing events such as the Hail Rally and Hail Season (Figure 1).

The study of the tourist area's physical location and the degree to which it is connected to the surrounding area and other major cities through transportation and communication lines have a clear impact on the region's tourism potential; for example, if the area is easily accessible from and to other locations, it offers constant communication and frequency. The higher the demand for a tourism region, the more conveniently and affordably it may be accessible to travelers and leisure seekers.

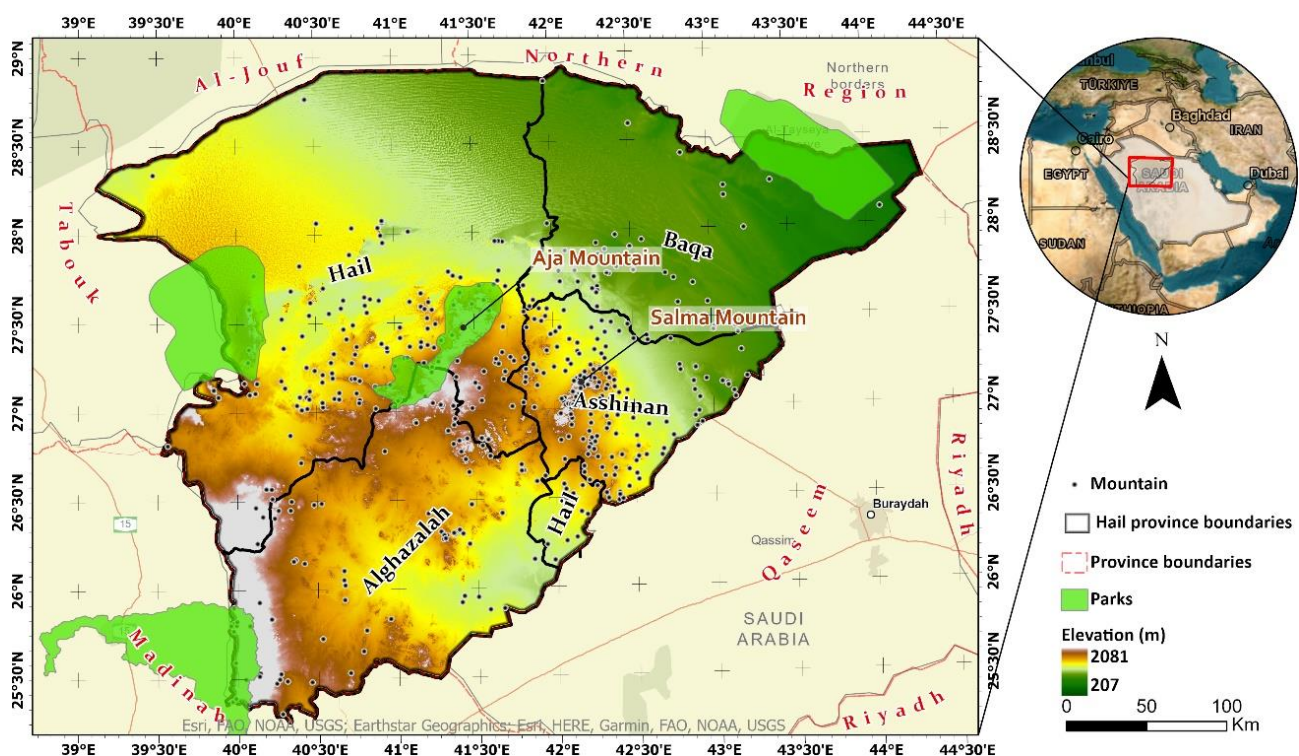***Figure 1.*** *Location of the study area*

2.2. Data Sources and Analysis

The collected spatial datasets include 9 criteria comprising environmental, topographical, ecological, and natural areas with various measurement scales and are therefore normalized for comparison. Various geographic and attribute datasets were developed and aggregated from the sources listed below (Table 1).

Several topographical (elevation, and slope), ecological (flora and fauna habitats, and protected zones), and land use (road network, towns, and utilities) resources were used to construct several criteria in order to perform a suitability site study for ecotourism. Sentinel-2 satellite data and the Normalized Difference Vegetation Index (NDVI) were used to study the geographical differences in vegetation cover in the Hail province in 2022. Google Earth Engine (GEE) was employed for this purpose. A multi-petabyte collection of geospatial information and satellite imagery is combined with planetary-scale analytical tools in Google Earth Engine. The Earth Engine is used by scientists, researchers, and developers to identify changes, chart trends, and measure variations on the surface of the planet. While still free for use in education and research, Earth Engine is now accessible for commercial usage. The produced map was transferred into ArcGIS Pro 2.8.4 after preparing the code in GEE and producing the NDVI in 2022.

Table 1. *Data sources*

Data Layers	Sources
DEM (Digital Elevation Model)	NASA SRTM 30-meter data
NDVI (Normalized Difference Vegetation Index)	Sentinel-2 time-series data
Hail Municipality Data	https://webgis.amanathail.gov.sa/HailGeoExplorer/
Road network	The OpenStreetMap Foundation, 2022
Village, Fuel Stations, Service Sites, Urban Areas, Industrial Areas and Historic Sites	https://webgis.amanathail.gov.sa/HailGeoExplorer/

To perform an ecotourism suitability site study, datasets were utilized to establish nine criteria with varying scales of measurement that were then standardized for comparison.

3. METHODS

The criterion generation and geographical analysis, standardization, AHP, and suitability evaluation stages make up the study's methodology. Based on a literature analysis, field investigation, and local knowledge, every component and criterion were chosen. A suitability model was used to identify high-priority locations for monitoring ecotourism appropriateness in Hail province. In this study, the GIS-MCDA approach was applied using ESRI's ArcGIS Pro 2.8.4 software. GIS-MCDA is a prominent suit- ability analysis technique (Malczewski, 2006) that is often used to assist environmental decision-making (Eastman, 1999; Watson & Hudson, 2015; Shorabeh et al., 2022). The typical GIS-MCDA multi-attribute decision analysis (MADA) approach was utilized in this study, which contains a fixed, limited number of options and maintains spatial homogeneity of preferences for different levels of criterion values (Kiker et al., 2005; Wang et al., 2009; Malczewski & Rinner, 2015; Domazetović et al., 2019). The GAMA approach is created as an easy-to-use, three-step procedure that minimizes and streamlines needed processing to make the entire GIS-MCDA susceptibility modeling process simpler and more practical. The developed GAMA approach enables the automation of processes 3, 4, and 5, which are detailed below (Figure 2).

A suitability model was used to find the optimum position to put goods or regions to conserve, such as determining the best ecotourism site. Figure 2 depicts the various steps involved in land suitability assessment, which include data collection, pre-processing attribute and spatial data (including slope, vegetation, roads, fuel stations, historic sites, villages, urban areas, industrial sites, and service sites), and application of the suitability assessment functionality.

GIS-MCDA suitability mapping includes the following steps: (1) defining the objective; (2) determining the criteria; (3) harmonizing the criteria (value scaling); (4) criterion weighting; (5) criteria aggregation; and (6) assessing the accuracy of the suitability model (Malczewski, 1999; Greene et al., 2011; Atici et al., 2015). The decision-maker's judgment, the study's scope, and the availability of data all have a role in the first two stages (steps 1 and 2), but the availability of reference data is a major factor in step 6 (Stubelj Ars, 2014; Domazetović et al., 2019; Islam et al., 2022).
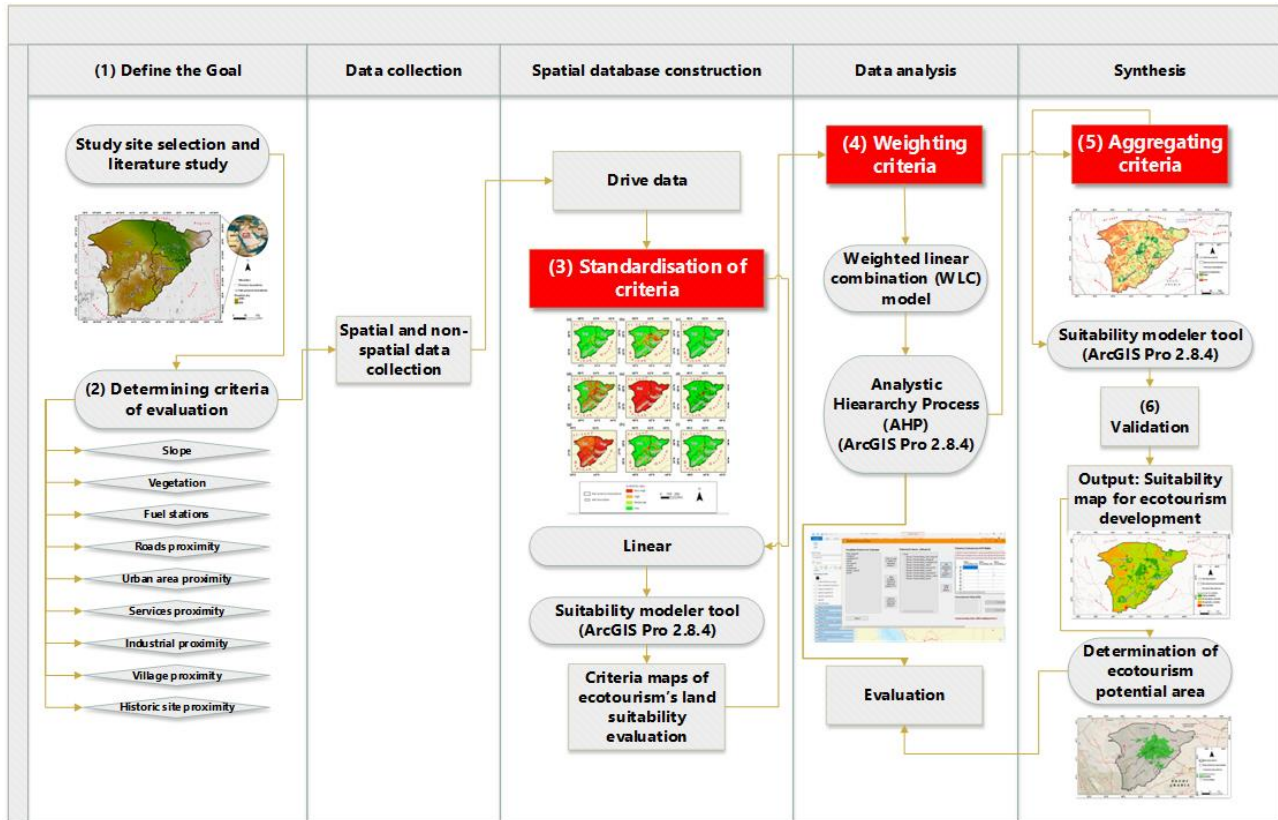
Figure 2. *Conceptual framework of the suitability model employed in this research. Red rectangle: GAMA technique automates three phases (3-5) of the GIS-MCDA cycle*

The score range process (Malczewski, 1999; Greene et al., 2011; Atici et al., 2015) is the most often used GIS-based method for standardizing assessment criteria (step 3) (Figure 2). The correctness of standardization is determined by the expert's judgment, experience, and knowledge (Stubelj Ars, 2014; Domazetović et al., 2019). In this particular attempt, criterion standardization was accomplished on the premise that the value function had a linear shape (equation 1):

$$xi = (R_i - R_{min})/(R_{max} - R_{min}) * SR \qquad (1)$$

where R_i denotes the raw score i, R_{min} the lowest score of each component, R_{max} the highest score of each factor, and SR the standardized range, which is set to 100 in this case (Voogd, 1983; Rinner, 2007; Drobne & Lisec, 2009; Bottero et al., 2018). When it comes to qualitative factors, the ordering of scores may be subjective. Criterion weighting (step 4) is the process of assigning a value to an assessment criterion in order to demonstrate its importance in contrast to the other criteria being considered (Malczewski, 1999; Greene et al., 2011; Atici et al., 2015) (Figure 2). In this work, the weighted linear combination (WLC) model was adopted, which is the most basic and extensively used GIS-MCDA model (Malczewski, 2011; Carter & Rinner, 2014; Zoghi et al., 2017).

The weighted linear combination (WLC) technique is a decision procedure used in geographic information systems (GIS) to build composite maps. It is a decision model that is often used in geographic information systems. However, the tactic is commonly used without a clear understanding of the assumptions behind this approach.

Weighted linear combination is a multi-criteria decision-making method that helps decision-makers to choose the best location from a range of possibilities. The local variant of the range-sensitivity concept considers the range of attribute values within a user-defined neighborhood (Carter & Rinner, 2014; Zoghi et al., 2017).

The decision rule in WLC assesses each option using the following value function, (equation 2):

$$S = \sum_j w_j v_j(x_i) = \sum_j w_j r_{ij}$$

(2)

where w_j is the normalized weight ($w_j = 1$), $v_j(x_i)$ is the value function for the j attribute, $x_i = x_{i1}, x_{i2}, \ldots x_{in}$, and r_{ij} is the attribute translated into the comparable scale (Drobne & Lisec, 2009; Zoghi et al., 2017). Criterion weighting was based on the pairwise comparisons approach in the context of the Analytic Hierarchy Process (AHP) (Saaty, 1977; 2001), which is an adaptation of WLC that depends on expert judgment to establish priority scales.

Saaty and Vargas (2012) recommended that the priority scales be produced by synthesizing their judgments using the geometric mean of the final outputs. AHP uses a basic scale of numbers ranging from 1 to 9 to express the intensities of judgments (Tables 2 and 3) (Saaty, 2002; 2006; Tjader et al., 2014).

Table 2. Values of preferences for paired Comparison (Gourabi & Rad, 2013)

Preferences (oral judgments)	Value
Extremely Preferred	9
Very Strongly Preferred	7
Strongly Preferred	5
Moderately Preferred	3
Equally Preferred	1
Preferences between the above intervals	2,4,6,8

Table 3. Random Consistency Index (RI) (Saaty & Vargas, 2012)

n	1	2	3	4	5	6	7	8	9
RI	0.00	0.00	0.52	0.89	1.11	1.25	1.35	1.40	1.45

All chosen criteria are compared to one another in a pairwise comparison matrix. Following the construction of the pairwise comparison matrix, $w = (w_1, w_2, \ldots, w_n)$ may be calculated as a vector of criteria weights. The weights are calculated based on the unique answer to:

$$C_w = \lambda_{max} w$$

(3)

where λ_{max} is the biggest eigenvalue of C. The consistency ratio CR of a pairwise comparison matrix describes the likelihood that the matrix ratings (ratings of each criterion against each other in terms of relative significance) were generated at random is described by the CR of a pairwise comparison matrix (Saaty, 1977). Here is how CR is defined:

$$CR = \lambda_{max} - n/RI(n-1)$$

(4)

where n is the number of criteria examined and RI denotes the random index, which is the consistency index of a randomly generated pairwise comparison matrix and is dependent on the number n of items being compared (Table 3). CR ratings less than 0.10, on the other hand, imply that the pairwise comparisons are reasonably consistent and that the adjustment is minor in relation to the actual values of the eigenvector entries (Saaty & Vargas, 2012). Pairwise judgments with CR ratings greater than 0.10 are almost randomly generated and unreliable (Fang et al., 2017; Xu & Zhang, 2017; Mansour et al., 2020; Tian & Yan, 2021). The initial weights should be revised if the value is larger than 0.10 since this indicates an inconsistent evaluation (Mansour et al., 2020).

The Suitability Modeler tool was used in ArcGIS Pro 2.8.4 to execute the criteria aggregation (step 5) and the suitability modeling technique. Finally, the correctness of the appropriateness model was validated (step 6) (Figure 2).

4. RESULTS AND DISCUSSION

The suitability model is a decision-making process with several criteria. It is applied in GIS, such as ArcGIS Pro, and provides for in-depth analytical answers to challenges in a variety of fields. Suitability modeling, in particular, is recommended for the location of ecotourism sites and selecting the best regions for them. The selection of the best ecotourism locations in this model is based on nine data layers (as presented in Table 4). The suitability model was created using ArcGIS Pro 2.8.4's Suitability Modeler Panel. All the data was converted to a 1–10 suitability scale. For weighing criteria, the multiplier method was utilized. The AHP Method (ArcGIS Pro Add-In tool) was used to allocate weights to the criteria (Mendadhala, 2018).

4.1. Criteria Maps Generation and Standardization

All of the attractions for performing nature-based activities, as well as the existence of infrastructure and equipment that allow for better use of the region, were taken into consideration when determining whether the territory in question was acceptable for the practice of ecotourism activities. The selection of the criteria was the result of a thorough review of the literature, and discussions with specialists who were aware of the objectives of the study (Table 4). The criteria were developed based on experience, professional views, and data from numerous sources. Many significant criteria are considered in ecotourism planning and site selection, such as attraction assets, services, and accessibility, which might be biological, cultural, physical, infrastructural, ecological, and environmental. Discussions with specialists in relevant areas of study, a search of authorized literature, and an examination of historical facts were used to acquire knowledge.

Table 4. Analyzing land suitability for ecotourism using certain criteria

Criteria	Unit	Suitability Rating				References
		High	Moderate	Marginal	Not	
Slope Criteria	Degree	0-5	5-15	15-20	>20	(Bunruamkaew & Murayam, 2011) (Tjiong et al., 2021) (Zabihi et al., 2020)
Vegetation Proximity Criteria	Meter	0-250	250-750	750-2000	>2000	(Bishop & Hulse, 1994) (Burkart et al., 2016) (Gourabi & Rad, 2013)
Industrial Proximity Criteria	Meter	>6000	6000-4000	4000-2000	2000-0	(Piran et al., 2013) (Al-Balawi & Ouerghi, 2022).
Road Proximity Criteria	Meter	0-1000	1000-2000	2000-3000	>3000	(Chakrabarty, 2011) (Suryabhagavan et al., 2015) (Sahani, 2020)
Urban Areas Proximity Criteria	Meter	0-3000	3000-6000	6000-9000	>9000	(Weaver, 2005) (Mahdavi & Niknejad, 2014) (Çetinkaya et al., 2018)
Villages Proximity Criteria	Meter	0-1000	1000-3000	3000-5000	>5000	(Sahani, 2019) (Sahani, 2020) (Al-Balawi & Ouerghi, 2022)
Historical Sites Proximity Criteria	Meter	0-5000	5000-10000	10000-15000	>150000	(El-Harami, 2014) (Deribew et al., 2022)
Service Sites Proximity Criteria	Meter	0-2000	2000-4000	4000-6000	>6000	(Suryabhagavan et al., 2015) (Nahuelhual et al., 2013)
Fuel Station Proximity Criteria	Meter	0-2000	2000-4000	4000-6000	>6000	(Gigović et al., 2016) (Ahmad et al., 2022)

This stage included the creation of a spatial database, which was then rasterized and converted into raster. This spatial database contained all vector and raster layers (maps), as well as data models like points, lines, and polygons. Euclidean distances and buffers were calculated using a variety of recommendations to identify characteristics and indicators of land suitable for ecotourism. All spatial layers were created using the ArcGIS

Pro program, and coordinate consistency was maintained. The elevation criterion was calculated using a DEM with a resolution of 30 m, and the slope criterion was classified using a degree measurement unit. A proximity analysis using the Euclidean distance classification tool was performed to divide regions into eligible areas for ecotourism based on the criteria of service locations, villages, historic sites, fuel stations, and metropolitan areas (Figure 3).

Similarly, the distance to the closest road for each place will then be shown using a distance raster that was created from the roads datasets. Using the Euclidean Distance tool, you will be able to extract the distance raster from the roads layer. In order to identify the best locations that are distant from industrial sites, proximity analysis utilizing Euclidean distance classification was also used to obtain the industrial factor (Figure 3).

The nine criteria, represented as nine grid layers (raster), are classified into four suit- ability classes: high suitability, moderate suitability, marginal suitability, and not suitable. The generated maps have all been standardized on a uniform scale from 1 to 4, in order to enable comparison. Values are arranged in ascending order according to their filling, with very proportional values receiving the highest value in weight (4) and disproportionate ones receiving the lowest weight (1) (Figure 3). Because each criteria have different measurement attributes, it is impossible to compare them with their raw scores. We noticed that the significance of the values in the definition of ranges of impact varied depending on the relevance of the effect of distance and closeness to each criterion. When evaluating closeness to urban agglomerations, for example, the agglomeration's proximity regions were represented by a larger value than the distant areas, whose ranges were represented by weak values, while the proximity range was represented. The industrial region criteria had low values, while the distant ranges had large values, and so on, depending on the nature of the criterion in terms of attraction or expulsion. GIS software such as ArcGIS provides various options for reclassification, depending on the Reclassify tool, with the goal of establishing standards and assigning a value that signifies a degree of completeness on a continuous scale ranging from one to four.

4.2. Criteria Weight Assignment Using AHP

The simple multi-attribute rating technique (SMART), the point allocation method, the direct rating method, the analytic hierarchy process (AHP), the best worst method (BWM), the full consistency method (FUCOM), and others are among the weight coefficient calculation (CWC) methods available. Depending on the research aims and purpose, all accessible CWC techniques offer benefits and limitations (Teknomo, 2006; Salabun et al., 2016; Pamučar et al., 2018). The analytical hierarchical process (AHP), which has been efficiently applied within the framework of the GAMA approach for gully erosion susceptibility modeling (Pamučar et al., 2018; Matić et al., 2019; Žižović & Pamučar, 2019), is one of the most often used CWC methodologies. In a paired approach, the AHP method offers a structural framework for quantifying the comparison of decision-making components and criteria (Laskar, 2003). Experts are asked to rate the value of a criteria map for a paired matrix using Saaty's scale (Saaty, 1977). The approach investigates the relative relevance of all factors by giving weight to each of them in a hierarchical sequence, with the suitability weight for each class of variables utilized at the top of the hierarchy. Expert suggestions often determine the relevance of each factor in the AHP study (Baniya, 2008). AHP also gives quantitative tools to evaluate judgment inconsistency to assure the legitimacy of the relative significance utilized. The consistency ratio index (CR), as indicated in Equation (4), may be determined using the characteristics of reciprocal matrices. According to Saaty (1977), the degree of consistency is sufficient if the CR is less than 0.10. If it is more than 0.10, the assessment process is incoherent, and the AHP technique may fail to provide appropriate results.

AHP was used to establish a hierarchy of selected criteria in order to find the best places for ecotourism activities. Each criterion layer was created using ArcGIS Pro Spatial Analyst, and the produced maps were then converted into raster models using weight values obtained from AHP. Table 5 shows the estimated and assigned weights and scores for the criteria for ecotourism appropriateness development in Hail province. The relevance, usefulness, and appropriateness rates for creating ecotourism are the rationales for assessing each sub-criterion. As a result of their importance and appropriateness for ecotourism, the priority scores and rankings for the criteria were determined. For example, in terms of closeness to industrial sites, low scores were assigned to locations that are near industrial sites, while higher priority values were assigned to locations that are far away from industrial sites (Figure 4).
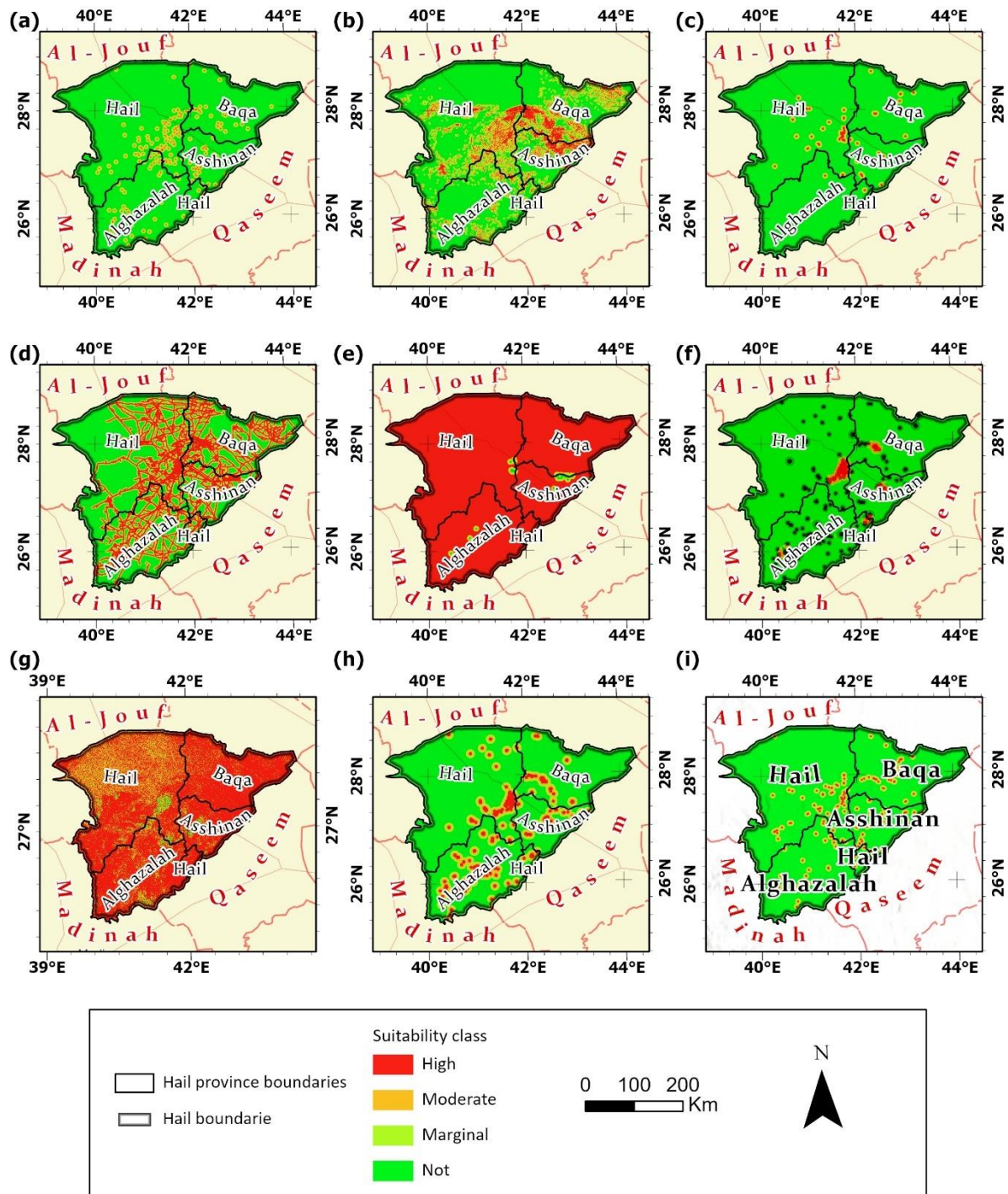
Figure 3. *Nine spatial criteria for ecotourism monitoring in Hail province.* ***a)*** *village,* ***b)*** *vegetation,* ***c)*** *service stations,* ***d)*** *Road's proximity,* ***e)*** *industrial,* ***f)*** *historic,* ***g)*** *slope,* ***h)*** *urban areas,* ***i)*** *fuel stations*

To find potential areas for ecotourism, all factors included in the study had to be standardized, using the AHP approach and the ArcGIS Pro suitability modeler. AHP makes it possible to compare qualitative and quantitative criteria consistently by integrating different input layer scales. Using the same measurement units across all spatial levels is ensured through standardization (Pereira & Duckstein, 1993; Bojórquez-Tapia et al., 2001; Chen et al., 2010). Therefore, the ArcGIS Pro suitability modeler tool was used to standardize and assign values to each criterion, after which all classed raster layers were converted to raster binary format. The most influential criteria are closeness to vegetation zones and distance from industrial regions, followed by proximity to the road network, historic places, and service locations.

The attribute factors are stored in the GIS database as map layers that include attribute values for each pixel in raster data (Kiker et al., 2005; Khalili & Duecker, 2013; Goyal et al., 2020). In the acquired data, there were nine key criteria in the form of nine GIS-based layers included for ecotourism (Figure 3). For criteria that may be expressed by continuous values, including slope, or distance from roads, the Continuous Functions technique works well. The values are continually transformed using this approach to the appropriateness scale by using a linear function. With each rise in the criteria value, the resultant appropriateness value continually changes since this technique applies a continuous function to the criteria values. With each step taken away from a road, for instance, the suitability can rapidly decline.

Table 5. *The Analytic Hierarchy Process (AHP) approach was used to create a pairwise comparison matrix with nine criteria*

Item Description	Slope	Village Proximity	Vegetation Proximity	Urban Areas Proximity	Service Sites Proximity	Road Proximity	Industrial Proximity	Historical Sites Proximity	Fuel Station Proximity	Weight
Slope	1	2	0.5	0.5	0.33	0.5	3	0.33	3	10%
Village Proximity	0.5	1	0.5	0.33	0.5	0.5	0.5	0.5	0.5	5%
Vegetation Proximity	2	2	1	2	2	3	0.5	0.5	2	15%
Urban Areas Proximity	2	3	0.5	1	2	0.5	0.5	0.33	2	10%
Service Sites Proximity	3	2	0.5	0.5	1	2	2	0.33	2	12%
Road Proximity	2	2	0.33	2	0.5	1	2	0.5	2	11%
Industrial Proximity	0.33	2	2	2	0.5	0.5	1	0.5	2	11%
Historical Sites Proximity	3	2	2	3	3	2	2	1	2	20%
Fuel Station Proximity	0.33	2	0.5	0.5	0.5	0.5	0.5	0.5	1	6%
Consistency Ratio CR										0.1

4.3. Suitability Map Generation

During this procedure, experts' opinions were sought to evaluate the relative importance of the factors and criteria at issue. The CR for ecotourism was assessed to be 0.1, which is appropriate for use in the suitability analysis. Table 5 ranks the nine (9) criteria used to determine the increasing requirement for ecotourism suitability monitoring in Hail province, which led to the creation of the maps shown in (Figure 4). As a result of data pre-processing, 9 raster layers are determined using GIS techniques (Figure 3). Figure 4 illustrates the suitability map that was developed by weighing and combining all of the aforementioned factors. The maximum model value was 900, while the lowest was 1. Higher values indicate appropriate and lower values indicate fewer ideal locations for ecotourism sites in the suitability map, which provides the summarized values of each raster datasets.

A spatial suitability map (Figure 4) was produced based on the results of the integration of raster maps of the nine criteria, demonstrating that Hail province is characterized by the presence of tourist sites that meet the conditions of the criteria of natural ecological tourist sites in varying degrees of suitability.

The suitability map was created using all procedure steps, and it shows four suitability classes: very suitable (0.75-1.00), moderately suitable (0.50-0.75), marginally suitable (0.25-0.50), and not suitable (0.00-0.25).

According to the ecotourism suitability map (Figure 4), the highly suitable region accounts for about 12.21% (14293.71871 km^2) of the total area and is largely located in the Hail province's center and eastern regions. Furthermore, two distinct zones are situated in the midwest and northeast, near the northern region. The moderately appropriate area accounts for about 58.50% of the overall region's size and is located in the province's southern and northeastern regions. Similarly, a larger proportion (28.21%) of the region is classified as marginally suitable. These locations are predominantly located in the island's north and center (Table 6). A small portion of the territory (1.07%) was labeled as Not suitable, with the majority of it located in and around Alghazalah's built-up regions and settlements in the south (Figure 4). Furthermore, small areas of the province's center and southern regions are unsuited for ecotourism and should be excluded from any successful tourist strategy (Figure 4).

Table 6. Land suitable for ecotourism coverage

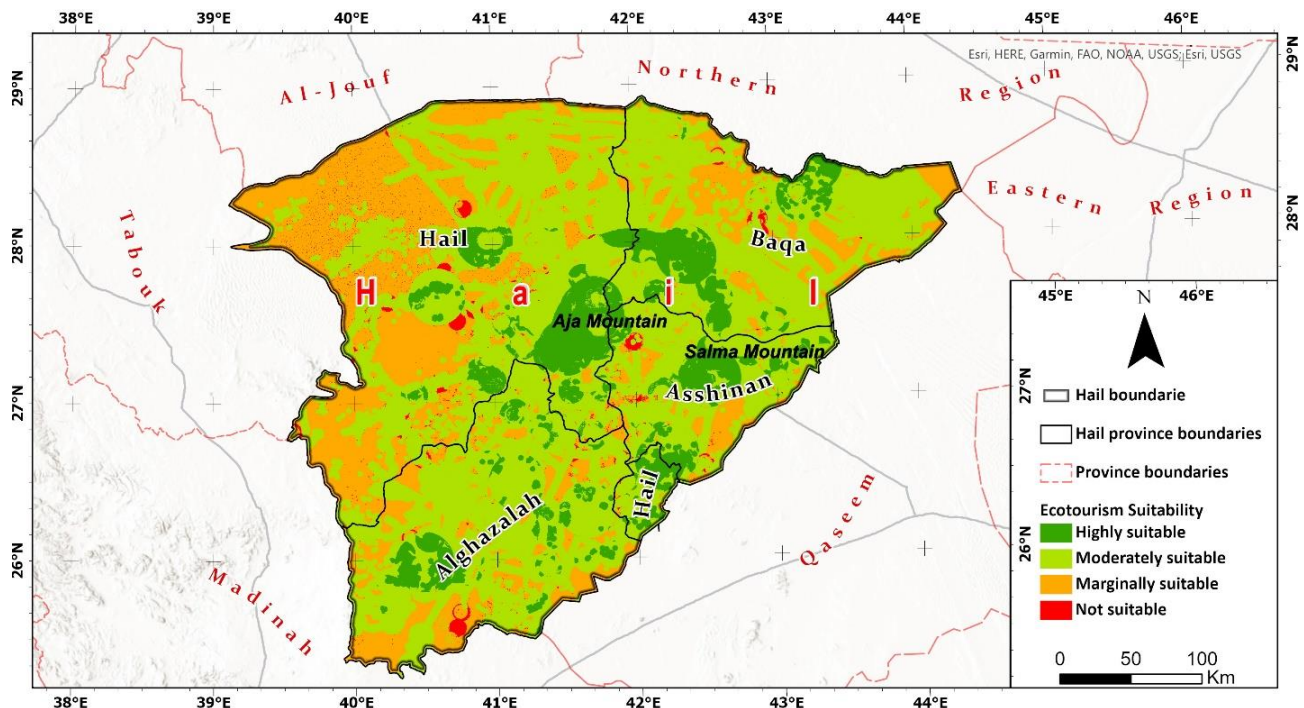| Category of suitability	Range of scores	Area coverage	
		(Km^2)	%
Highly suitable	0.75–1.00	14293.718	12.21
Moderately suitable	0.50–0.75	68459.627	58.50
Marginally suitable	0.25–0.50	33009.764	28.21
Not suitable	0.00–0.25	1252.037	1.07
Total area		117015.100	100

Figure 4. Ecotourism suitability map for Hail province

4.4. Locate the Areas for the Siting or to Preserve

The suitability map that results is the input data within the Suitability Modeler. The spatial requirements are specified by the Locate component of the suitability modeling technique. Within the suitability modeler tool, we defined the geographic criteria for the suitability model and selected the optimal area for the ecotourism region, which covers 24,5012 km^2 (20.93% of the total research area) (Figure 5).

372   Samera AL SALAH

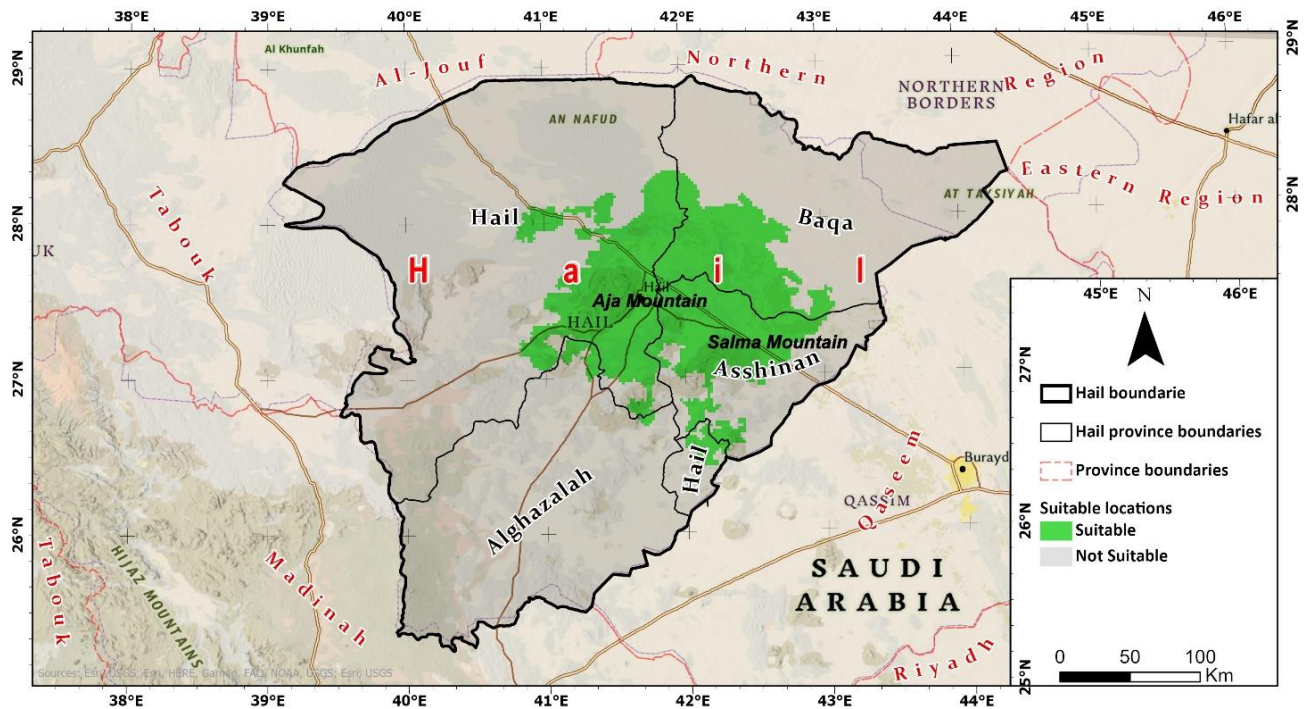GU J Sci, Part A   10(3) 361-377 (2023)   10.54287/gujsa.1328036

Figure 5. Ecotourism locations map for Hail province

4.5. Validation of the Methodological Approach

The overall area of the mountains in the Hail region is around 6818 square kilometers, accounting for 77.5% of the entire area of the region. These mountains are divided into two major mountain ranges, the Aja Mountains and the Salma Mountains, which extend parallel from the southwest to the northeast. The highest peak of Aja Mountain reaches more than 1400 meters above sea level and the Aja Mountain range extends over an area of 100 kilometers. The Salma mountains extend more than 60 square kilometers from the northeastern side of Hail city to the southwestern part. The highest peak stands at 1100 meters above sea level. ArcGIS Pro software was used as part of the test approach to check the validity of the model computations and output values. First, an Esri Mountain point feature class of 464 points, including lowlands, plateaus, and mountains, is applied to an input parameter. The Extract Values to Points tools (Spatial Analyst) were then used to save parameter values associated with each point position in the attribute table of an output feature class. As a result, the suitability pixel value for each mountain was derived by intersecting the mountain feature class with the ecotourism suitability map. Following this step, 64 mountains in the Locate area were chosen (Figure 6). The Hail region's mountains are distinguished by their pristine nature and lack of settlement, which exists in the form of small agricultural villages in the valleys and mountains such as Jebel Aja and Salma, and one of the most famous of these villages is the village of Oqda in the AJA mountains, as this village is beautiful for the residents of Hail and its surroundings, aided by its proximity to the city and its natural tourist importance. In addition, certain natural tourist activities, such as bird viewing, should be observed (Abdullah, 1996). According to the four levels of appropriateness, the existence of ecotourism sites that meet the requirements and criteria of environmental tourism sites defines the study area (high, moderate, marginal, and not).

Out of a total of 64 sites (including lowlands, plateaus, and mountains), 27 (Jabal Aja, Hazm ar Radum, Hazm ad Dab'ah, Jabal al 'Arfa', Jabal Si'aynin, Jabal al Qufayl, Jabal Dakhana, Ja'ad al Hamra', Jabal al Khubay, Jabal 'Itifah, Jibal Shatib, Jibal al 'Uqaylah, Humr al Qaltah, Jabal Ruwayyah, Jibal Minshar, Qarat as Sanduq, Huzum al Jithamiyah, Jabal Busrah, Huzum al Mukhtibi, Qarat ar Riha, Qur al Qish'ummah, Burqan al Ghidayyat, Qarat al Milayda', Jabal Malq, Jabal Salma, Hazm Eldhabaa, and Om Rkiba) show a high level of ecotourism suitability, making up 42.18% of all the sites. 37 locations were assigned a moderate appropriateness grade (Jabal Ghisil, Dulay' al Ashqar, Jabal al Muthalbat, Hadb 'Alya', Hazm Munayfah, Jabal Jidid, Hudaybat al 'Urayfa', Dulay'at ash Shighay, Jabal Sayid, Jabal Suwayqah, Jabal Thi'alabah, Jabal al Kaththanah, Burqan al Ajfar, Jibal as Sahabin, Abraq Abu Rijm, Jabal Sawa, Jabal Dab', Jibal Aja,

Kadis, Jabal ar Ra'ilah, Qarat Munaysifah, Jabal al Hamra', Qarat Munaysifah, Jabal Rukhaymah, Jibal ar Rawd, Jabal al Gharra', Jilan at Tayyim, Jabal 'Unayzah, Jabal al Ushayhib), accounting for 57.81% of all sites (Figure 6).
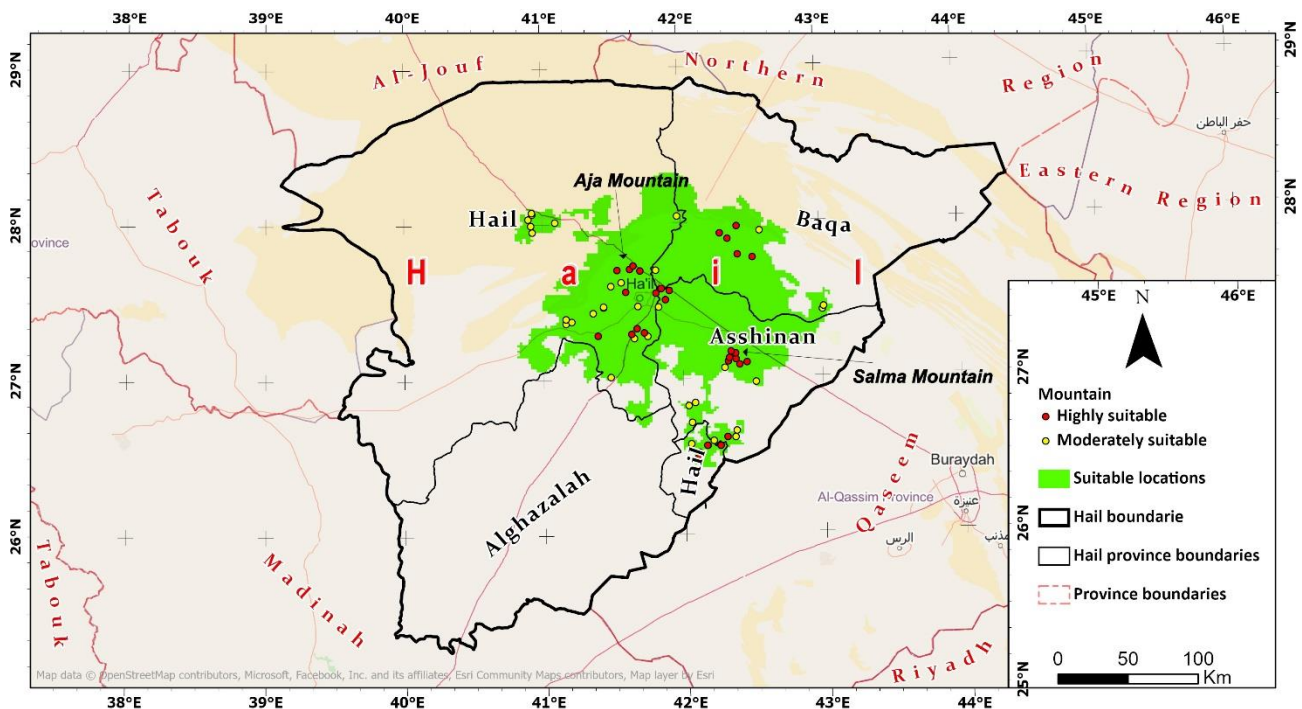

Figure 6. Mountains for ecotourism in Hail province

5. CONCLUSION

Ecotourism is certainly a major source of economic activity and rejuvenation in Hail province, as well as a means of preserving natural heritage assets. Ecotourism potential site selection criteria were developed with the input of nine raster datasets. The final ecotourism suitability map was created using a Geographic Information System's integrated weighted overlay approach. It aims to assess the potential of existing natural and rural characteristics in the Hail area, situated in the center of Saudi Arabia. The new suitability modeling tool in ArcGIS Pro optimizes site planning and suitability processes by allowing users to quickly perform suitability modeling with integrated tools. With the ability to manage, analyze, and display a variety of data related to tourism activity and produce maps that assist decision-making, geographic information systems technology, which provided advanced methods and mechanisms for analyzing spatial information, was used to assess the spatial suitability of natural ecotourism sites in the Hail province. The study's main contribution was the modern applied technical approach adopted. The study also used advanced methods and analysis methods, such as determining the weights of criteria, which is a very important process in the final model's results, and using the method of weighted superposition of all criteria within the framework of Multi-Criteria Analysis to integrate the values previously calibrated and unified by a common scale that allows giving one value to each point, where it processes all the inputs represented in the criteria. The outcome shows index values that enable categorization into four categories: unfit, slightly acceptable, moderately suitable, and highly suitable. These zones represent 24501.225 km² and 20.93% of the total research area, respectively. In order to reach an ideal solution for ecotourism site selection, comprehensive and regular monitoring in the appropriate and most suitable zones should be carried out.

CONFLICT OF INTEREST

The author declares no conflict of interest.

REFERENCES

Abdullah, N. W. (1996). *Geological and Geomorphological: Saudi Arabia: Forms of the Earth's Surface. Research in the Natural Geography of Saudi Arabia*. King Fahd National Library.

Ahmad, A. A., Hama, A. R., & Alawn, I. A. (2022). Ecotourist and Picnic Area Assessment Using AHP Analytical Tools in Sulaimani– Tourism Region, Iraq. *Engineering and Technology Journal*, *40*(11), 1560-1572.

Al-Balawi, A. B., & Ouerghi, S. A.-H. (2022). Assessment of spatial suitability of ecotourism sites in Al-Ahsa governorate, Saudi Arabia, by using GIS. *Journal of Humanities and Social Sciences*, *6*(1), 64-87. doi:10.26389/AJSRP.L180921

Atici, K. B., Simsek, A. B., Ulucan, A., & Tosun, M. U. (2015). A GIS-based Multiple Criteria Decision Analysis approach for wind power plant site selection. *Utilities Policy*, *37*, 86–96. doi:10.1016/j.jup.2015.06.001

Bakirman, T., & Gumusay, M. U. (2020). A novel GIS-MCDA-based spatial habitat suitability model for Posidonia oceanica in the Mediterranean. *Environmental Monitoring and Assessment*, *192*(4), 231. doi:10.1007/s10661-020-8198-1

Baniya, N. (2008). *Land Suitability Evaluation Using GIS for Vegetable Crops in Kathmandu Valley, Nepal*. PhD Thesis, Humboldt-Universitat zu Berlin.

Bishop, I. D., & Hulse, D. W. (1994). Prediction of scenic beauty using mapped data and geographic information systems. *Landscape and Urban Planning*, *30*(1-2), 59–70. doi:10.1016/0169-2046(94)90067-1

Bojórquez-Tapia, L. A., Diaz-Mondragón, S., & Ezcurra, E. (2001). GIS-based approach for participatory decision making and land suitability assessment. *International Journal of Geographical Information Science*, *15*(2), 129–151. doi:10.1080/13658810010005534

Bottero, M., D'Alpaos, C., & Oppio, A. (2018). Multicriteria Evaluation of Urban Regeneration Processes: An Application of PROMETHEE Method in Northern Italy. *Advances in Operations Research*, 9276075. doi:10.1155/2018/9276075

Bunruamkaew, K., & Murayam, Y. (2011). Site Suitability Evaluation for Ecotourism Using GIS & AHP: A Case Study of Surat Thani Province, Thailand. *Procedia-Social and Behavioral Sciences*, *21*, 269–278. doi:10.1016/j.sbspro.2011.07.024

Burkart, K., Meier, F., Schneider, A., Breitner, S., Canário, P., Alcoforado, M. J., Scherer, D., & Endlicher, W. (2016). Modification of Heat-Related Mortality in an Elderly Urban Population by Vegetation (Urban Green) and Proximity to Water (Urban Blue): Evidence from Lisbon, Portugal. *Environmental Health Perspectives*, *124*(7), 927–934. doi:10.1289/ehp.1409529

Carter, B., & Rinner, C. (2014). Locally weighted linear combination in a vector geographic information system. *Journal of Geographical Systems*, *16*(3), 343–361. doi:10.1007/s10109-013-0194-3

Çetinkaya, C., Kabak, M., Erbaş, M., & Özceylan, E. (2018). Evaluation of ecotourism sites: a GIS-based multi-criteria decision analysis. *Kybernetes*, 47(8), 1664-1686. doi:10.1108/K-10-2017-0392

Chakrabarty, A. (2011). Ecotourism Development and Security Restructuring: A GI Based Planning for Peaceful Dissuasion of Anarchism in Forest Provinces of India. *Procedia-Social and Behavioral Sciences*, *21*, 108–115. doi:10.1016/j.sbspro.2011.07.006

Chen, Y., Yu, J., & Khan, S. (2010). Spatial sensitivity analysis of multi-criteria weights in GIS-based land suitability evaluation. *Environmental Modelling & Software*, *25*(12), 1582–1591. doi:10.1016/j.envsoft.2010.06.001

Deribew, K. T., Mihretu, Y., Abreha, G., & Gemeda, D. O. (2022). Spatial analysis of potential ecological sites in the northeastern parts of Ethiopia using multi-criteria decision-making models. *Asia-Pacific Journal of Regional Science*, *6*(3), 961–991. doi:10.1007/s41685-022-00248-5

Doljak, D., Stanojević, G., & Miljanović, D. (2021). A GIS-MCDA based assessment for siting wind farms and estimation of the technical generation potential for wind power in Serbia. *International Journal of Green Energy*, *18*(4), 363–380. doi:10.1080/15435075.2020.1865363

Domazetović, F., Šiljeg, A., Lončar, N., & Marić, I. (2019). GIS automated multicriteria analysis (GAMA) method for susceptibility modelling. *MethodsX*, *6*, 2553–2561. doi:10.1016/j.mex.2019.10.031

Drobne, S., & Lisec, A. (2009). Multi-attribute Decision Analysis in GIS: Weighted Linear Combination and Ordered Weighted Averaging. *Informatica*, *33*(4), 459-474.

Eastman, J. R. (1999). Multi-criteria evaluation and GIS. In: P. A. Longley, M. F. Goodchild, D. J. Maguire, & D. W. Rhind (Eds.), *Geographical Information Systems* (pp. 493–502), John Wiley & Sons, New York.

El-Harami, J. (2014, December 9-11). The Diversity of Ecology and Nature Reserves as an Ecotourism Attraction in Jordan. In: M.A. Othuman Mydin & A. Marzuki (Eds.), 4th International Conference on Tourism Research (4ICTR), SHS Web of Conferences, (vol. 12, 01056), Kola Kinabalu, Malaysia. doi:10.1051/shsconf/20141201056

Fang, Q., Tong, Z., Qiao, M., & Ren, L. (2017). The Evaluation System of Online P2P Lending Platforms Based on AHP -- in the Perspective of Lenders. In: The Sixteenth Wuhan International Conference on E-Business－Social Network and Commerce (pp. 507-514).

Gigović, L., Pamučar, D., Lukić, D., & Marković, S. (2016). GIS-Fuzzy DEMATEL MCDA model for the evaluation of the sites for ecotourism development: A case study of "Dunavski ključ" region, Serbia. *Land Use Policy*, *58*, 348–365. doi:10.1016/j.landusepol.2016.07.030

Gourabi, B. R., & Rad, T. G. (2013). The analysis of ecotourism potential in Boujagh wetland with AHP method. *Life Science Journal*, *10*(2s), 251–258.

Goyal, P., Kumar, D., & Kumar, V. (2020). Application of multicriteria decision analysis (MCDA) in the area of sustainability: a literature review. *International Journal of the Analytic Hierarchy Process*, *12*(3), 512-545. doi:10.13033/ijahp.v12i3.720

Greene, R., Devillers, R., Luther, J. E., & Eddy, B. G. (2011). GIS-Based Multiple-Criteria Decision Analysis. *Geography Compass*, *5*(6), 412–432. doi:10.1111/j.1749-8198.2011.00431.x

Islam, N., Sarkar, B., Basak, A., Das, P., Paul, I., Debnath, M., & Roy, R. (2022). A novel GIS-based MCDM approach to identify the potential eco-tourism sites in the Eastern Dooars region (Himalayan foothill) of West Bengal, India. *Geocarto International*, *37*(26), 13145-13175. doi:10.1080/10106049.2022.2076917

Khalili, N. R., & Duecker, S. (2013). Application of multi-criteria decision analysis in design of sustainable environmental management system framework. *Journal of Cleaner Production*, *47*, 188–198. doi:10.1016/j.jclepro.2012.10.044

Kiker, G. A., Bridges, T. S., Varghese, A., Seager, T. P., & Linkov, I. (2005). Application of multicriteria decision analysis in environmental decision making. *Integrated Environmental Assessment and Management*, *1*(2), 95–108. doi:10.1897/IEAM_2004a-015.1

Laskar, A. (2003). *Integrating GIS and Multi-Criteria Decision Making Techniques for Land Resource Planning*. MSc Thesis, International Institute for Geo-Information Science and Earth Observation, Enschede.

Mahdavi, A., & Niknejad, M. (2014). Site suitability evaluation for ecotourism using MCDM methods and GIS: case study - Lorestan province, Iran. *Journal of Biodiversity and Environmental Sciences*, *4*(6), 425–437.

Malczewski, J. (1999). *GIS and Multicriteria Decision Analysis*. John Wiley & Sons.

Malczewski, J. (2006). GIS-based multicriteria decision analysis: a survey of the literature. *International Journal of Geographical Information Science*, *20*(7), 703–726. doi:10.1080/13658810600661508

Malczewski, J. (2011). Local weighted linear combination. *Transactions in GIS*, *15*(4), 439–455. doi:10.1111/j.1467-9671.2011.01275.x

Malczewski, J., & Rinner, C. (2015). *Multicriteria Decision Analysis in Geographic Information Science*. Springer. doi:10.1007/978-3-540-74757-4

Mansour, S., Al-Awhadi, T., & Al-Hatrushi, S. (2020). *Geospatial based multi-criteria analysis for ecotourism land suitability using GIS & AHP: a case study of Masirah Island, Oman*. *Journal of Ecotourism*, *19*(2), 148–167. doi:10.1080/14724049.2019.1663202

Matić, B., Jovanović, S., Das, D. K., Zavadskas, E. K., Stević, Ž., Sremac, S., & Marinković, M. (2019). *A New Hybrid MCDM Model: Sustainable Supplier Selection in a Construction Company*. *Symmetry*, *11*(3), 353. doi:10.3390/sym11030353

Mendadhala, R. G. (2018). *Automating Spatial Multi-Criteria Decision Analysis (MCDA) of housing development sites in Richardson, TX using ArcGIS Pro SDK for .Net - An accessibility level perspective*. MSc Thesis, The University of Texas at Dallas.

Mentzafou, A., Blagojević, M., & Dimitriou, E. (2021). A GIS-MCDA-Based Suitability Analysis for Meeting Targets 6.3 and 6.5 of the Sustainable Development Goals. *Sustainability*, *13*(8), 4153. doi:10.3390/su13084153

Modica, G., Laudari, L., Barreca, F., & Fichera, C. R. (2014). A GIS-MCDA Based Model for the Suitability Evaluation of Traditional Grape Varieties: The Case-Study of 'Mantonico' Grape (Calabria, Italy). *International Journal of Agricultural and Environmental Information Systems (IJAEIS)*, *5*(3), 1–16.

Nahuelhual, L., Carmona, A., Lozada, P., Jaramillo, A., & Aguayo, M. (2013). Mapping recreation and ecotourism as a cultural ecosystem service: An application at the local level in Southern Chile. *Applied Geography*, *40*, 71–82. doi:10.1016/j.apgeog.2012.12.004

Pamučar, D., Stević, Ž., & Sremac, S. (2018). A New Model for Determining Weight Coefficients of Criteria in MCDM Models: Full Consistency Method (FUCOM). *Symmetry*, *10*(9), 393. doi:10.3390/sym10090393

Pereira, J. M. C., & Duckstein, L. (1993). A multiple criteria decision-making approach to GIS-based land suitability evaluation. *International Journal of Geographical Information Systems*, *7*(5), 407–424. doi:10.1080/02693799308901971

Piran, H., Maleknia, R., Akbari, H., Soosani, J., & Karami O. (2013). Site selection for local forest park using analytic hierarchy process and geographic information system (case study: Badreh County). *International Research Journal of Applied and Basic Sciences*, *6*(7), 930–935.

Primavera, J. H., Friess, D. A., Van Lavieren, H., & Lee, S. Y. (2019). The Mangrove Ecosystem. In: C. Sheppard (Eds.), *World Seas: An Environmental Evaluation (Second Edition)*, (pp. 1-34). doi:10.1016/B978-0-12-805052-1.00001-2

Rinner, C. (2007). A geographic visualization approach to multi-criteria evaluation of urban quality of life. International *International Journal of Geographical Information Science*, *21*(8), 907–919. doi:10.1080/13658810701349060

Saaty, T. L. (1977). A scaling method for priorities in hierarchical structures. *Journal of Mathematical Psychology*, *15*(3), 234–281. doi:10.1016/0022-2496(77)90033-5

Saaty, T. L. (2001). *Decision Making for Leaders: The Analytic Hierarchy Process for Decisions in a Complex World*. RWS Publications.

Saaty, T. L. (2002). How to make and justify a decision: the analytic hierarchy process. Part 1. Examples and Applications *System Research and Information Technologies*, *2002*(1), 95-108.

Saaty, T. L. (2006). The Analytic Network Process. In: T. L. Saaty, & L. G. Vargas (Eds.), *Decision Making with the Analytic Network Process Economic, Political, Social and Technological Applications with Benefits, Opportunities, Costs and Risks* (pp. 1-26). Springer. doi:10.1007/0-387-33987-6_1

Saaty, T. L., & Vargas, L. (2012). *Models, Methods, Concepts & Applications of the Analytic Hierarchy Process*. Springer. doi:10.1007/978-1-4614-3597-6

Sahani, N. (2019). Assessment of ecotourism potentiality in GHNPCA, Himachal Pradesh, India, using remote sensing, GIS and MCDA techniques. *Asia-Pacific Journal of Regional Science*, *3*(2), 623–646. doi:10.1007/s41685-019-00116-9

Sahani, N. (2020). Application of analytical hierarchy process and GIS for ecotourism potentiality mapping in Kullu District, Himachal Pradesh, India. *Environment, Development and Sustainability*, *22*(7), 6187–6211. doi:10.1007/s10668-019-00470-w

Salabun, W., Ziemba, P., & Wątróbski, J. (2016, June 15-17). *The Rank Reversals Paradox in Management Decisions: The Comparison of the AHP and COMET Methods* In: I. Czarnowski, A. M. Caballero, R. J. Howlett, & L. C. Jain (Eds.), Proceedings of the 8th International KES Conference on INTELLIGENT DECISION TECHNOLOGIES KES-IDT-16 (pp. 181–191), Puerto de la Cruz, Tenerife, Spain. doi:10.1007/978-3-319-39630-9_15

Shorabeh, S. N., Firozjaei, H. K., Firozjaei, M. K., Jelokhani-Niaraki, M., Homaee, M., & Nematollahi, O. (2022). The site selection of wind energy power plant using GIS-multi-criteria evaluation from economic perspectives. *Renewable and Sustainable Energy Reviews*, *168*, 112778. doi:10.1016/j.rser.2022.112778

Stubelj Ars, M. (2014). Decision support in the implementation of sustainable development in protected areas regarding environmental education and ecotourism. PhD Thesis, Univerze v Novi Gorici.

Suryabhagavan, K. V., Tamirat, H., & Balakrishinan, M. (2015). Multi-criteria evaluation in identification of potential ecotourism sites in Hawassa town and its surroundings, Ethiopia. *Journal of Geomatics*, *9*(1), 86–92.

Teknomo, K. (2006). Analytic Hierarchy Process (AHP) Tutorial. URL

Tian, M., & Yan, S. (2021). Study on the Assessment of Internet-Financial Risk Based on Fuzzy Analytic Hierarchy Process. *Journal of Simulation*, *9*, 121-126.

Tjader, Y., May, J. H., Shang, J., Vargas, L. G., & Gao, N. (2014). Firm-level outsourcing decision making: A balanced scorecard-based analytic network process model. *International Journal of Production Economics*, *147, Part C*, 614–623. doi:10.1016/j.ijpe.2013.04.017

Tjiong, G. P., Supriatna, J., Takarina, N. D., & Tambunan, R. P. (2021). Mangrove diversity and suitability assessments for ecotourism in Cimalaya Wetan Coast, Karawang District, Indonesia. *Biodiversitas Journal of Biological Diversity*, *22*(2), 803-810. doi:10.13057/biodiv/d220234

Voogd, H. (1983). *Multicriteria Evaluation for Urban and Regional Planning*. Pion.

Wang, J.-J., Jing, Y.-Y., Zhang, C.-F., & Zhao, J.-H. (2009). Review on multi-criteria decision analysis aid in sustainable energy decision-making. *Renewable and Sustainable Energy Reviews*, *13*(9), 2263–2278. doi:10.1016/j.rser.2009.06.021

Watson, J. J. W., & Hudson, M. D. (2015). Regional Scale wind farm and solar farm suitability assessment using GIS-assisted multi-criteria evaluation. *Landscape and Urban Planning*, *138*, 20–31. doi:10.1016/j.landurbplan.2015.02.001

Weaver, D. B. (2005). Mass and Urban Ecotourism: New Manifestions of an Old Concept. *Tourism Recreation Research*, *30*(1), 19–26. doi:10.1080/02508281.2005.11081230

Xu, L., & Zhang, Y. (2017). A Credit Rating Model for Online P2P Lending Based on Analytic Hierarchy Process. In: J. Xu, A. Hajiyev, S. Nickel, & M. Gen (Eds.), Proceedings of the Tenth International Conference on Management Science and Engineering Management, (pp. 537–549). doi:10.1007/978-981-10-1837-4_46

Zabihi, H., Alizadeh, M., Wolf, I. D., Karami, M., Ahmad, A., & Salamian, H. (2020). A GIS-based fuzzy-analytic hierarchy process (F-AHP) for ecotourism suitability decision making: A case study of Babol in Iran. *Tourism Management Perspectives*, *36*, 100726. doi:10.1016/j.tmp.2020.100726

Žižović, M., & Pamučar, D. (2019). New model for determining criteria weights: Level Based Weight Assessment (LBWA) model. *Decision Making: Applications in Management and Engineering*, *2*(2), 126–137. doi:10.31181/dmame1902102z

Zoghi, M., Houshang Ehsani, A., Sadat, M., javad Amiri, M., & Karimi, S. (2017). Optimization solar site selection by fuzzy logic model and weighted linear combination method in arid and semi-arid region: A case study Isfahan-IRAN. *Renewable and Sustainable Energy Reviews*, *68, Part 2*, 986–996. doi:10.1016/j.rser.2015.07.014